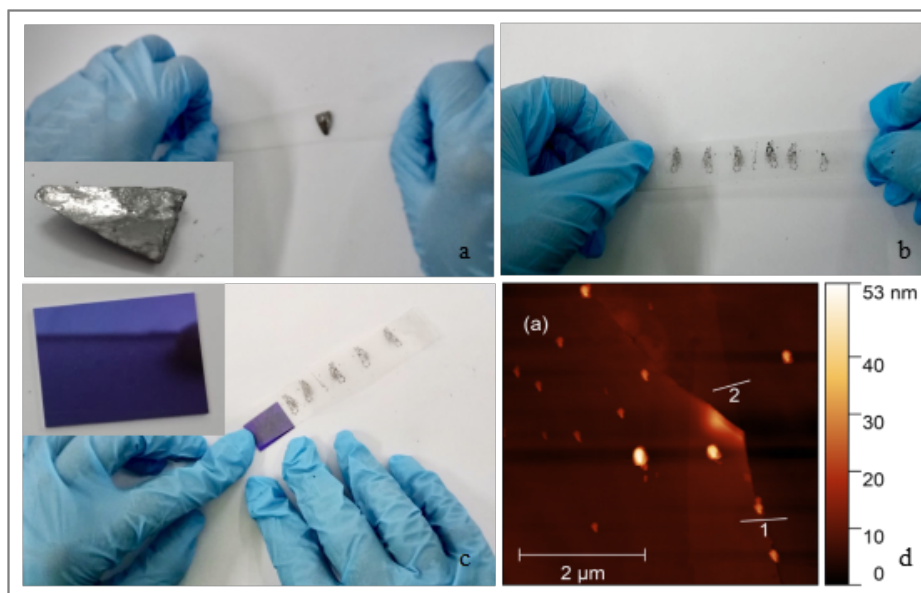


Journal of the National Science Foundation of Sri Lanka





JOURNAL OF THE NATIONAL SCIENCE FOUNDATION OF SRI LANKA

Editorial Board

Ajit Abeysekera (Editor in Chief)
A. Atputharajah
J.K.D.S. Jayanetti
L.P. Jayatissa
P. Prasad M. Jayaweera
Jagath Manatunge
S.S.N. Perera
Rohini de A. Seneviratne
Saman Seneweera
P. Wijekoon
M.J.S. Wijeyaratne

Language Editor

R.D. Guneratne

Editorial Office

Nadeeja Wickramarachchi (Principal Scientific Officer)
Uthpala T. Karunaratne (Senior Scientific Officer)
Upuli Ratnayake (Scientific Officer)

International Editorial Advisory Board

Chamil Abeykoon, UK
Dilanthi Amaratunga, UK
Dilantha Fernando, Canada
Leslie Gunatilaka, USA
Saman K. Halgamuge, Australia
Kithsiri W. Jayasena, Australia
Vassilios Kapaklis, Sweden
Wah Yun Low, Malaysia
Thomas Mathew, USA
Shanthi Mendis, Switzerland
Javier Francisco Ortega, USA
Malik Peiris, Hong Kong
Kamal Premaratne, USA
Nalin Samarasingha, USA
Ravi Silva, UK
Christopher C. Steel, Australia

Impact Factor: 0.682

Publication : Published quarterly (March, June, September and December) by the National Science Foundation of Sri Lanka.

Manuscripts: Research Articles, Research Communications, Reviews and Correspondences in all fields of Science and Technology may be submitted for consideration for publication. A guide to the preparation of manuscripts is provided in each issue. The guidelines may also be obtained by visiting the NSF website.

Disclaimer: No responsibility is assumed by the National Science Foundation of Sri Lanka for statement and opinions expressed by contributors to this Journal.

Manuscripts and all correspondence relating to them should be sent to the Editorial Office, National Science Foundation, 47/5, Maitland Place, Colombo 07, Sri Lanka.

Fax: 94-11- 2694754

E-mail: jnsf@nsf.gov.lk

JNSF home page: <http://www.nsf.gov.lk/index.php/nsfscience-magazine>

Publication : A publication fee of US\$ 250 will be levied for each manuscript except, when the corresponding author is affiliated to a Sri Lankan institution, in two stages.

- A processing fee of US\$ 20 will be levied for each manuscript at peer-review stage.
- Remaining US\$ 230 will be charged for accepted articles at the time of publication.

Copyright : © National Science Foundation of Sri Lanka

Articles in the Journal of the National Science Foundation of Sri Lanka are Open Access articles published under the Creative Commons CC-BY-ND License (<http://creativecommons.org/licenses/by/4.0/>). This license permits use, distribution and reproduction, commercial and non-commercial, provided that the original work is properly cited and is not changed anyway.

Indexing : The JNSF is indexed in Science Citation Index Expanded, Journal Citation Reports/Science Edition, BIOSIS Previews, Zoological Record, Biological Abstracts, Chemical Abstracts, Scopus, TEEAL, Ulrich's, AGRICOLA and EBSCOhost, CAB Abstracts

**JOURNAL OF THE
NATIONAL SCIENCE FOUNDATION
OF SRI LANKA**

Volume 51 Number 1

March 2023

C O N T E N T S

EDITORIAL

- 01 Predatory Journals; be aware of the spectrum!**
LP Jayatissa

RESEARCH ARTICLES

- 03 Effect of oviposition-site deprivation on reproductive performance and life history parameters of dengue vector *Aedes aegypti***
KM Gunathilaka and SM Ganehiarachchi
- 13 Quantification of metabolite cinnamic acid of cinnamon (*Cinnamomum zeylanicum*) in human plasma**
S Pigeera, P Ranasinghe, MN Kaumal and P Galappatthy
- 21 Temperature control in an exothermic continuous stirred tank reactor**
VA Rani, G Guna, D Prabhakaran and M Thirumarimurugan
- 37 On recurrence relations for moments of dual generalized order statistics for a general transmuted power function distribution with characterizations**
SH Shahbaz and MQ Shahbaz
- 53 Removal of methylene blue from aqueous solution using raw laterite: an adsorption study**
BM Gunathilake, D Jayawardana, PGH Pupulewatte, S Dissanayake and PM Manage
- 69 Comparison of physicochemical and sensory properties of African butter seed (*Pentadesma butyracea*) and cocoa fats for potential use in future food applications**
NPS Jayathissa, ABG Silva, WMT Madhujith, PGSM De Silva and R Jayatissa
- 81 Assessment of submergence stress responses and mining allelic variations of submergence tolerance gene *Sub1A* in Sri Lankan rice germplasm**
T Kariyawasam, D Nanayakkara, A Sumanarathna, D Weerasinghe, L Suriyagoda and D Jayatilake
- 93 A comparison of model parameter estimation methods for complex survey survival data**
IT Jayamanne, A Ramanayake and RV Jayatillake
- 105 Mechanically exfoliated graphene from Sri Lankan vein graphite for field effect transistor application**
M Thanishaichelvan, M Joy Karunya and U Sutharsini
- 113 Assessment of transverse thermal conductivity of coir fibre using experimental, analytical, and numerical methods**
LG Chamath, LKT Srimal and GA Sewvandi

129 Estimation of soil liquefaction potential in Colombo Port City (Sri Lanka) using several design earthquakes
IACC Ilangakoon and AMRG Athapaththu

149 Insights into the ecological roles of assembling genomes for stimulated methanogenic archaea *Methanoculleus* in coal seams
BJ Liu and Y Li

159 Analyzing the effects of quarantine, isolation, and vaccination on the spread of COVID-19 via a mathematical model
LW Somathilake

RESEARCH COMMUNICATION

175 Two new additions and one confirmation of the occurrence of Lamiaceae (Lamiales) species from Northern dry zone in Sri Lanka.
HD Jayasinghe and HT Gamhewa

Guidelines for Contributors



Cover: (a) Selected piece of graphite for graphene extraction; (b) successive scotch tape peeling of graphene layer (c) graphene transferred on to SiO₂/Si substrate; (d) AFM image of the transferred graphene layer

Editorial

Predatory Journals; be aware of the spectrum!

Academia the world over, are encouraged or coerced to conduct research in their fields as the new knowledge is instrumental and essential for the world to move ahead. The pressure for academics and researchers to author research publications is indicated by the popular aphorism 'publish or perish'. In some countries, like Sri Lanka, a monthly allowance is added to their salary as incentive if they have published at least one research paper within the relevant year modifying the above aphorism to 'publish as pay-off'. Such enforcements/incentives for research were strengthened throughout the world in the recent past.

In parallel to the above enforcements for research, a new threat to the honesty of research publications has emerged. It has become a global outbreak with a rising trend; it was initially named as predatory publications. Now there are many synonyms for the term 'Predatory' as 'bogus', 'deceptive', 'dubious', 'illegitimate' 'fake', 'fraudulent', 'parasitic', 'pseudo', 'questionable' etc. However, the term predatory is still widely used. The lack of a standard peer review process and the absence of good editorial services are the primary features of predatory Open Access (OA) journals.

The peer review process, actually the 'gate keeping' process for new knowledge, is defined as "*a process of subjecting an author's scholarly work, research or ideas to the scrutiny of others who are experts in the same field*". It was initiated few centuries ago in the UK and now it is being practiced in the world of academia. The two terms 'peer-reviewed' and 'refereed' are synonyms.

In predatory journals this peer review process is absent or minimal, and in some cases, it is 'modified' in unethical and unacceptable ways. Hence, 'the lack of proper peer review' in predatory journals shows a vast range. The funny 'manuscript' submitted to a predatory open access journal in the field of computer technology by Dr. Peter Vamplew in 2014, is the best example to represent the worst extreme of the above range of the review processes in predatory journals. The manuscript including a scatter plot and a flow chart was originally created by David Mazières and Eddie Kohler in 2005, using a single sentence of seven words (containing one obscene word), over and over again (<https://www.scs.stanford.edu/~dm/home/papers/remove.pdf>), and submitted to a conference as an annoyed response to frequent emails from the organizers of the conference inviting to submit papers. Later, Dr. Vamplew submitted a copy of the same 'manuscript' to the above predatory journal and it was accepted rating as 'excellent' by the 'journal's peer review process' with a request to pay the article processing charge (APC) of US\$150 to publish the paper. This indicates that some predatory journals accept any nonsense even without opening the file or reading at least the title. The journals which follow a modified version of the normal peer review process can be considered as the other end of the range of review processes in predatory journals. In this modification, the editors of the journal invite the corresponding author of one manuscript submitted to them, to review another manuscript submitted to the same journal, and vice versa, giving a bait of 25% reduction of their APC for a quick review of the manuscript assigned to them. In order to make sure a fast review, publishers of these journals impose a condition as 'the manuscript will be sent to more than two reviewers and 25% discount of the APC will be offered only to the reviewer who submitted the review report fast'. As the 25% discount is also a significantly high amount, the relevant 'author-reviewers' try to complete the job fast deviating from a thorough review. Moreover, in this scenario, these author-reviewers are not always experts in the subject; they could be juniors or even postgraduate students in the field. Due to all these facts, the standard of the review reports of such journals could vary in widely. Hence these types of reviews are non-standard, unethical, and questionable.

Between the above two extremes, there is a series of different types/levels of reviews among predatory journals as given below;

-tabulated review carry out using the words 'excellent', 'very good', 'satisfactory', 'need revision' etc.

- non-specific review report that is generally a pre-prepared one to suit with any manuscript and it is send with minor adjustments to fit with the manuscript submitted.
- incomplete editorial review; some predatory publishers, particularly those who publish a large number of predatory journals, assign a member of their journal staff having a basic knowledge in a related discipline eg. statistics, economics etc. to give a superficial and one-sided review.

Meanwhile, some predatory publishers run fake versions of reputed legitimate journals using the same title and same ISSN number. These are called ‘hijacked journals’. Knowledge on the above range of the review process could help to identify hijacked journals because unlike the original reputed journal, the highjacked journal does not maintain a thorough review process.

In all the above cases in predatory journals, the sole objective of the deviations from the proper peer review process and the lack of good editorial service is to minimize the time gap between the first submission to acceptance of the article as well as to reduce the rejection rate of manuscripts targeting easy and quick money.

However, all of the above reviews cannot be considered as ‘peer reviews’, because they are carried out by the journal staff. Moreover, some journals send emails to intellectuals in the relevant area and invite them to be reviewers of their journal(s). Whenever such intellectuals accept their invitations, the journal(s) send them manuscripts to review. But in many cases, the editors don’t send those genuine review reports to authors; instead, they follow their own predatory way to get manuscripts published after charging APCs. Only the reviewers can check whether this is happening by comparing the published papers, with the review reports they sent.

When the range of review practices in predatory journals are discussed, some exceptional cases also should be mentioned. Platinum or Diamond OA journals are one example. (In the Gold OA model, readers get free access and the authors pay the APC: In contrast, in the Platinum/Diamond OA model both the reader and author don’t pay, but an organization/Institute associated with the publisher, pays the APC to the publisher.) As an example, a private university may hire a publisher to run a journal under the name of the university. In such a case, if the publisher is given the responsibility for the whole process, the journal may run in predatory mode, but with the university name in cover pages misleading the readers as it is a ‘university journal’. Another example where confusion could arise is in cases where the ownership of the publisher is changed in the middle; in such a case, a reputed journal that maintained high standards could be sold and the buyer may run it from that point onwards in predatory mode taking advantage of the goodwill earned and maintained by the previous owner. Meanwhile some of the open access, non-predatory journals also could show some predatory features when it is managed in an irresponsible way. As an example, when some academic or professional body needs to publish a journal in their field as a marketing strategy, the organization assigns the responsibility of managing the journal to a person or a small team as an additional and voluntary task; then the journal could go ahead single-handedly as a business without paying much attention to norms and standards.

The above information could help researchers to learn about the broad range of predatory practices in journals and such an awareness should help to prevent being a prey of predatory journals. It is necessary to combat predatory journals as they create pseudo-knowledge that could ruin the credibility of the researcher as well as the relevant institute. Moreover, it may also negatively affect development programs if the policy makers and planners are not capable of identifying that the relevant knowledge base is coming from fake publications. Hence, researchers are advised to be aware of the above predatory practices, in addition to the identifying features which are visible on the websites and published papers of predatory journals.

L.P. Jayatissa

RESEARCH ARTICLE

Medical Entomology

Effect of oviposition-site deprivation on reproductive performance and life history parameters of dengue vector *Aedes aegypti*[†]

RAKM Gunathilaka and GASM Ganehiarachchi*

Department of Zoology and Environmental Management, Faculty of Science, University of Kelaniya, Kelaniya, Sri Lanka.

Submitted: 28 October 2021; Revised: 30 March 2022; Accepted: 27 May 2022

Abstract: Dengue and dengue haemorrhagic fever constitute one of the most significant arthropod-borne viral diseases that occur in tropical and subtropical regions in the world. Annually 390 million new dengue cases are being reported from the 128 dengue-endemic countries. *Aedes aegypti* is the primary vector that transmits the disease. Since the primary vector is a container breeder, source reduction appears to be a good vector control method. Source reduction limits the oviposition of females through oviposition-site deprivation. Therefore, the current study was conducted to determine the effect of oviposition-site deprivation on the fecundity, fertility, life-history parameters, and longevity of *Ae. aegypti*. Oviposition-site deprivation was enabled by delaying the access to the oviposition substrate. Female mosquitoes were allowed to access the oviposition substrate separately on the day of blood feeding and 2, 4, 6, and 8 days after blood feeding. The results showed that oviposition-site deprivation significantly increased fecundity with an increase in the number of egg retention days. The number of eggs laid by the female increased by 69% when the female was compelled to retain the eggs for 8 days. The highest recorded fecundity was 100 ± 5 . Nevertheless, fertility, percentage larval mortality, total larval duration, pupal duration, and longevity were not affected by the number of egg retention days. Thus, it is imperative to have a clear awareness about the effect of oviposition-site deprivation on the reproductive performance of the vector mosquitoes when adopting vector control strategies.

Keywords: *Aedes aegypti*, oviposition-site deprivation, reproductive performance.

INTRODUCTION

The first report, which was thought to be of a dengue epidemic, occurred in 1779 and 1780 in the three continents of Asia, Africa and North America (Hirsch, 1883). The disease was thought to be allied with an insect associated with water and the disease was called water poison by the Chinese people (McSherry, 1982). From 1780 to 1940, the dengue virus became endemic in urban tropical areas and World War II created ideal conditions for it to be converted into a global pandemic (Gubler, 1998). Dengue control measures used in many countries include source reduction through destruction of breeding places. However, an understanding of the reproductive performance and life history parameters is also essential eventually.

The virus is transmitted to humans through the bite of an infective mosquito. Vitarana *et al.* (1997) stated that *Aedes aegypti* is the primary vector while *Ae. albopictus* is the secondary vector of dengue in Sri Lanka. Early morning, 2 to 3 hours after daybreak and several hours before dusk are the peak biting hours of the vector (WHO, 2014a). During a single blood meal, they bite several people. Hence, it can transmit the virus to many people within a short period (Gubler & Rosen, 1976; Putnam & Scott, 1995; Platt *et al.*, 1997). That is why *Ae. aegypti* is considered to be an efficient epidemic vector (Gubler, 1998). It is predicted that by the year 2070 the

[†]An abstract of this research has been published in the Proceedings of the International Conference on Applied and Pure Sciences (ICAPS 2021-Kelaniya).

* Corresponding author (mangala@kln.ac.lk;  <https://orcid.org/0000-0002-9909-1437>)



This article is published under the Creative Commons CC-BY-ND License (<http://creativecommons.org/licenses/by-nd/4.0/>). This license permits use, distribution and reproduction, commercial and non-commercial, provided that the original work is properly cited and is not changed in anyway.

mean relative vectorial capacity of dengue fever transmission in Sri Lanka would increase (WHO, 2014b). Since *Ae. aegypti* is common in urban areas it prefers to breed in man-made containers which are commonly found in and around the houses (Gubler, 1998; WHO, 2014a). These include gutters, flower vases, old tires, buckets, water storage tanks, septic tanks etc. (Gubler, 1998). Kusumawathi and Fernando (2003) have stated that water storage tanks and barrels are the most productive breeding sites of *Ae. aegypti* in some areas of Sri Lanka. They attach the eggs to the walls of the containers just above the water level. *Ae. aegypti* females usually do not lay all the eggs in a single oviposition site. Instead, they deposit few eggs in several different oviposition sites (Harrington & Edman, 2001). This behaviour may increase the survival of the larvae and enable wider dispersal of the larvae. In addition, eggs of *Ae. aegypti* can remain viable for about 6 months without water in dry conditions. Usually, *Ae. aegypti* is an indoor breeder whereas *Ae. albopictus* is an outdoor breeder (Noordeen *et al.*, 2018). Both the *Ae. aegypti* and *Ae. albopictus* can survive in natural and artificial systems with clean or organically rich water (Kusumawathie & Fernando, 2003).

Generally, dengue outbreaks occur in Sri Lanka twice a year, which are seasonal followed by the monsoonal rains. They usually occur during June/July or October to December and are correlated with the increase of vector density (Sirisena & Noordeen, 2014). Since high rainfall causes flooding leading to increased breeding, the vector population density increases (Noordeen *et al.*, 2018).

Investigators have stated that female *Ae. albopictus* can retain mature eggs for a certain period until oviposition (Hitchcock, 1968). The egg retention and oviposition are affected by chemical and physical factors including visual, tactile, and olfactory responses (Bentley & Day, 1989; Dhileepan, 1997). Oviposition will be interrupted due to the lack of a suitable aquatic medium or due to oviposition deterrents (Xue *et al.*, 2005). This forced egg retention influences the oviposition patterns (Chadee, 1997) and vitellogenesis (Else & Judson, 1972) of *Ae. aegypti*. Once the female takes a blood meal, oogenesis begins, and it is followed by vitellogenesis (Else & Judson, 1972). These processes are governed by the hormones secreted from the neurosecretory cells of the brain and corpora allata (Lea, 1970). The duration of egg retention plays an important role in the reproductive performance and life history parameters of the mosquito. Judson (1967) has found that *Ae. aegypti* females can complete two gonotrophic cycles when the oviposition is prevented. Moreover, the amount of blood taken for the initiation of the second gonotrophic cycle was reported to be higher than the usual amount of blood required (Judson, 1967). Later, Else and Judson (1972) found that oviposition-site deprivation has prevented the initiation of the second gonotrophic cycle in many females and has significantly delayed the initiation time of the second gonotrophic cycle in other female *Ae. aegypti*. However, the study conducted by Meola and Lea (1972) has concluded that with the retention of a batch of mature eggs, a second gonotrophic cycle would not take place in *Ae. aegypti* because of the complete inhibition of vitellogenesis.

During dry seasons and dry spells during wet seasons, the oviposition sites may not be available for several days and weeks. Therefore, once female mosquitoes become gravid during these dry periods, there will not be oviposition sites to lay eggs on time. As a result, the female *Aedes* may retain eggs for more extended periods than usual.

Since there is no effective vaccine or drug against dengue fever, alternative strategies against *Aedes* vectors have been widely implemented. As *Ae. aegypti* is a container breeder, controlling dengue vectors through larval source reduction has become the most common and widely practised method. Such anthropogenic practice will create a similar situation to dry weather, where gravid mosquitoes will not find oviposition sites in the natural environment. This may lead to retention of eggs and may influence the reproductive performance of female vectors.

Thus, it is hypothesized that oviposition site deprivation created by natural and human influenced factors may affect the reproductive performance and life-history parameters of *Ae. aegypti*. In the absence of such knowledge on *Ae. aegypti* from Sri Lanka, a laboratory study was designed. The objective of the study was to determine the effect of oviposition site deprivation up to 8 days after blood feeding on the fecundity, fertility, larval mortality, total larval duration, pupal duration, and longevity of *Ae. aegypti*.

MATERIALS AND METHODS

Test insects and place of study

The eggs of *Ae. aegypti* used for the study were donated from the parent colony which has been maintained for 2 years at the Faculty of Medicine, University of Colombo. A pure colony of adult *Ae. aegypti* was maintained throughout the study period, in the insectary at the Department of Zoology and Environmental Management of the University of Kelaniya (6°58'20.91" N; 79°54'52.83" E) under the same temperature (27 ± 2 °C), relative humidity (75–80%), and photoperiod (12L : 12D) as provided for the parent colony at the University of Colombo.

Rearing of mosquitoes

A plastic tray (23.0 × 18.0 × 5.0 cm) was taken, and the egg sheet was placed in it. Two-third of the tray was filled with water boiled up to 100 °C and cooled to room temperature (Zheng *et al.*, 2015). The tray was covered with a 0.5 mm mesh net to prevent oviposition by other mosquitoes in the surroundings. After 24 h, the first instar larvae that hatched from the eggs were counted carefully under a light source. Then, 100 larvae were transferred to a 2 L plastic tray. A total of 6 trays were prepared with 100 larvae per each. The first, second, third, and fourth instar larvae were fed with 5, 6, 7 and 8 mL of the liquid diet of krill respectively, twice daily. The water quality of the larval rearing medium was maintained by carefully siphoning the water from the trays and replacing with new aged tap water daily. Once the larvae pupate, they were transferred into 500 mL beakers which contained aged tap water. The beakers were kept inside mosquito rearing cages until the adults emerged. A 10% sugar solution was used to feed the adults regularly (Helinski & Harrington, 2011; Zheng *et al.*, 2015). Human blood which was collected from the Central Blood Bank, Narahenpita was used to feed the female mosquitoes and they were starved for 24 hours before blood feeding. Blood-feeding was achieved using the membrane feeding technique (Owens, 1981).

Effect of oviposition site deprivation on fecundity, fertility, life-history parameters and adult longevity of *Aedes aegypti*

Four experiments were carried out to assess the effect of oviposition site deprivation on below parameters.

- (i) **Fecundity**
The number of eggs laid within 120 h (5 ds) after the females were allowed to oviposit, was counted under a low-power stereo microscope at 15X magnification.
- (ii) **Fertility**
After oviposition, a piece of egg sheet with 100 eggs was taken and was placed on a 2 L tray filled with water boiled up to 100 °C and cooled to room temperature. The number of first instar larvae that hatched out from the eggs after 24 h, were carefully counted under a light source and recorded. Another 24 h were spent in counting the number of 1st instar larvae.
- (iii) **Life-history parameters**
After oviposition, the egg sheet was taken and was placed on a 2 L tray filled with water boiled up to 100 °C and cooled to room temperature. Twenty-four hours later, 50 first instar larvae were counted and transferred to another 2 L tray. Larval mortality, total larval duration, and pupal duration were recorded.
- (iv) **Longevity**
After oviposition, the 10 females were transferred to a separate mosquito rearing cage. They were regularly fed with a 10% sugar solution (Helinski & Harrington, 2011; Zheng *et al.*, 2015). The average number of days that all the 10 females survived was recorded (Artis *et al.*, 2014).

Each experiment was repeated 3 times.

For these experiments, two hundred female mosquitoes were allowed to mate and were blood-fed for 30 min. Fully engorged 50 females were collected and 10 mosquitoes each were separately allowed for oviposition on the day of blood-feeding, and 2, 4, 6, and 8 ds after blood feeding. Black colour cylindrical plastic cups (200 mL) with a diameter of 7.0 cm and depth of 6.0 cm were used to prepare the oviposition substrates. The cups were soaked in a water bath for 1 wk to avoid the plastic odour. A filter paper stripe of length 22.0 cm and width 5.0 cm was placed along the interior circumference of the plastic cup which acted as the substrate for egg-laying. One-third of the cup was filled with aged tap water (Figure1).



Figure 1. Oviposition substrate with a filter paper stripe (22×5 cm)

Statistical analysis

Data obtained during the experiments were analysed using Minitab 18 software. All the data were tested for the Anderson-Darling normality test. As the data followed a normal distribution, one-way analysis of variance (ANOVA) was carried out to check whether there was a significant difference among the data obtained for the effect of oviposition site deprivation on the fecundity, fertility, and life history parameters of *Ae. aegypti* with the number of egg retention days. Tukey's test was used to test the differences among sample means for significance. Pearson correlation and regression analysis were applied to determine the functional relationship between the fecundity of *Ae. aegypti* mosquitoes and the number of egg retention days.

RESULTS AND DISCUSSION

Although several studies have been conducted to determine the effect of oviposition site deprivation on some lepidopterans and dipterans, limited studies have been conducted to determine the effect of oviposition site deprivation on the reproductive performances, life history parameters, and longevity of adult *Ae. aegypti*. According to the current study, the mean number of eggs laid by the females which were subjected to oviposition site deprivation had varied significantly (one-way ANOVA, $F = 12.19$, $DF = 4$, $p < 0.05$). Tukey's test showed that the fecundity of the females which were subjected to 6-day and 8-day egg retention periods were significantly different from the rest. The highest fecundity (100 ± 5) was observed once the females were subjected to an 8-day egg retention period and the lowest fecundity (59 ± 4) was observed when the females were subjected to a 0 day egg retention period (Figure 2a). The mean number of eggs laid was positively correlated with the number of egg retention days within the female (Pearson's correlation, $p < 0.05$, $R^2 = 0.986$; Figure 2b).

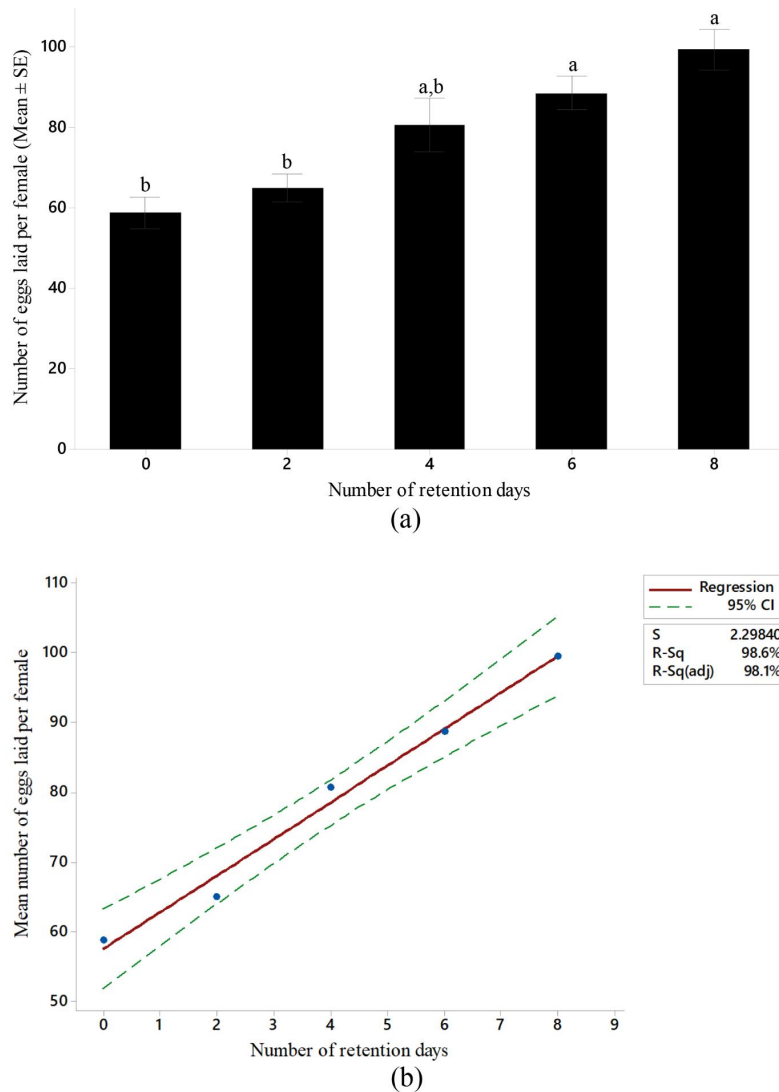


Figure 2: (a) Fecundity of female *Ae. aegypti* with number of egg retention days within the female. Bars with different letters are significantly different from each other ($p < 0.05$). (ANOVA, Tukey's test, $p < 0.05$). (b) Relationship between the fecundity of female *Ae. aegypti* with number of egg retention days within the female. (Pearson's correlation, $p < 0.05$)

Ae. aegypti is a container breeder. As such, the majority of the dengue elimination programmes are targeted at removing and destroying the breeding sites of the mosquitoes. Source reduction prevents or delays the oviposition of the females because of the limited number of available breeding sites. When the mosquitoes lack their preferred oviposition sites, they will be forced to retain eggs and lay them with a delay, in whatever the site available. However, the current study showed that there is an effect of oviposition site deprivation on fecundity. Fecundity increased by 69% compared to the 0 days, once the period of egg retention was increased by 8 days. Nevertheless, the exact physiology behind this phenomenon is unknown. It is assumed that the females utilize the food reserves that are available for general metabolism or reabsorb some egg rudiments and trigger a second gonotrophic cycle before the previous batch of eggs is laid. Some species such as *Anopheles pharoensis* (El-Akad & Humphreys, 1988) and *An. maculatus* (McDonald & Lu, 1972) respond to short-term oviposition site deprivation (2-5 days) while some other species like *Ae. albopictus* (Xue *et al.*, 2005) and *Culex quinquefasciatus* (Yang, 2008) respond to long-term oviposition site deprivation (10–70 days). Dieter *et al.* (2012) stated that the effect of oviposition site deprivation is modified by the nutritional condition of the diet taken before the egg retention period. When the females of *An. gambiae* were given a supplemental blood meal after long-term oviposition site deprivation, the fecundity increased compared to the fecundity of the females

which were not subjected to oviposition site deprivation (Dieter *et al.*, 2012). Therefore, in the wild condition mosquitoes may take another blood meal to increase their fecundity if they are subjected to oviposition site deprivation. This will lead to an increase in vector population. Ultimately the disease transmission intensity will also be increased due to the increased vector population.

Hatching rate of eggs represents the fertility of adult mosquitoes. The percentage of eggs hatched did not show any significant difference among the females which were subjected to different egg retention periods (one-way ANOVA, $F = 0.12$, $DF = 4$, $p > 0.05$; Table 1). The mean percentage of eggs hatched was 84.93 ± 0.47 . In contrast, the study conducted by Govoetchan *et al.* (2013) has shown a significant decline in egg hatch rate with the increase of the duration of oviposition site deprivation for a maximum of 15 days in both the KISUMU strain and wild strain of *An. gambiae*. The hatching rate was not increased when the oviposition site deprived females were treated with supplemental insemination. In addition to the waning in the hatching rate, some of the eggs of *An. gambiae* failed to tan (Dieter *et al.*, 2012). As all eggs tanned in the current study, there may not have been any effect of oviposition site deprivation on the tanning of *Ae. aegypti* eggs. Xue *et al.* (2005) stated that the number of eggs that failed to tan increased with the increase of duration of oviposition site deprivation. This may happen when the accumulation of L-tyrosine and other compounds necessary for the tanning of the chorion is prevented due to egg retention. When the eggs fail to fully tan within 6 to 8 hours after oviposition, the eggs may be exposed to dry conditions and they may collapse leading to a reduction in fertility (Clements, 1992). Yang (2008) has shown that both fecundity and fertility were high in wild-caught *Culex quinquefasciatus* females after 4 weeks of oviposition site deprivation.

Limited number of studies have been carried out to evaluate the effect of oviposition site deprivation or forced egg retention on larval mortality, total larval duration and pupal duration. The current study revealed that oviposition site deprivation has no impact on the life-history parameters of *Ae. aegypti*. The percentage larval mortality did not show a significant difference with the number of egg retention days within the female (one-way ANOVA, $F = 0.90$, $DF = 4$, $p > 0.05$; Table 1). The mean percentage larval mortality was 14.33 ± 1.16 . The total larval duration was measured by the sum of the larval duration of first, second, third, and the fourth instar larvae. The total larval duration did not show a significant difference with the number of egg retention days within the female (one-way ANOVA, $F = 0.60$, $DF = 4$, $p > 0.05$; Table 1). The mean total larval duration was 105.6 ± 2.4 hours. The pupal duration did not display a significant difference with number of egg retention days within the female (one-way ANOVA, $F = 0.30$, $DF = 4$, $p > 0.05$; Table 1). The mean pupal duration was 41.60 ± 0.98 hours. Similarly, adult female mosquitoes which were subjected to the different number of egg retention days did not show any significant difference in longevity (one-way ANOVA, $F = 0.40$, $DF = 4$, $p > 0.05$; Table 1). The mean adult longevity was 19.40 ± 0.29 days.

Table 1: Effect of oviposition site deprivation on fertility (number of eggs hatched), percentage larval mortality, total larval duration, pupal duration and adult longevity of female *Aedes aegypti* with different number of egg retention days within the female: 0, 2, 4, 6 and 8 days.

Parameter	Number of egg retention days within the female				
	0 days	2 days	4 days	6 days	8 days
Percentage of eggs hatched (Mean \pm SE)	86.0 \pm 1.5	84.7 \pm 2.7	85.7 \pm 3.9	83.3 \pm 2.9	85.0 \pm 3.5
Percentage larval mortality (Mean \pm SE)	10.3 \pm 1.5	15.0 \pm 3.2	16.7 \pm 3.5	16.3 \pm 3.0	13.3 \pm 2.0
Total larval duration in hours (Mean \pm SE)	100.0 \pm 4.0	108.0 \pm 6.9	100.0 \pm 4.0	112.0 \pm 4.0	108.0 \pm 12.0
Pupal duration in hours (Mean \pm SE)	40.0 \pm 4.0	44.0 \pm 4.0	44.0 \pm 4.0	40.0 \pm 4.0	40.0 \pm 4.0
Adult longevity in days (Mean \pm SE)	20.0 \pm 1.2	18.3 \pm 0.3	19.7 \pm 0.7	19.7 \pm 1.2	19.3 \pm 1.3

Although Govoetchan *et al.* (2013) has shown that the longevity of the gravid females of *An. gambiae* was higher than that of non-gravid females, oviposition site deprivation has not increased the survival of *An. gambiae*. The study conducted by Artis *et al.* (2014) showed that longevity and blood-feeding rate of *An. gambiae* have declined leading to a reduction in vectorial capacity. However, when the oviposition site deprived females receive access to a supplemental blood meal their survival is increased (Artis *et al.*, 2014).

Vector density is an important component of vectorial capacity (Dye, 1992). Climate, longevity, and fecundity of the females are the factors that determine the vector density (De Jesus & Reiskind, 2016). According to Ponlawat and Harrington (2009) vector control is the most successful way to control dengue and dengue haemorrhagic fever. Thus, it is important to know the reproductive biology and life history parameters of the vector mosquito.

The current study provides valuable information useful for planning vector control programmes. Dieter *et al.* (2012) has stated that vector control through source reduction would interrupt the oviposition of females and suppress the vector population. Consequently, source reduction leads to oviposition site deprivation due to the removal of breeding sites. In addition to source reduction, dry spells during wet seasons leads to the same. Therefore, gravid mosquitoes will retain the eggs due to the lack of breeding sites to lay them. The incidence of egg retention will significantly increase the fecundity of the females. Ultimately, increase in fecundity may lead to an increase in larval population that may contribute to an increase in the adult vector population. Thus, source reduction alone may not be an effective way to control vector population of *Ae. aegypti*. Hence, a focus on the early control of adult mosquitoes in control programmes is important to prevent large numbers of eggs being released to the environment.

Also, the current study revealed that the highest fecundity of the mosquitoes could occur when the mosquitoes were forced to retain eggs for 8 days. This knowledge can be applied in mass-rearing of mosquitoes to be used in the sterile insect technique. This is because the production of mosquitoes can be increased when the adults are allowed to oviposit at the most suitable age which will increase their fitness.

CONCLUSION

The present study indicates that delaying the oviposition of *Ae. aegypti* increases the fecundity of the female. However, parameters including fertility, percentage larval mortality, total larval duration, pupal duration, and longevity are not significantly affected. Early control of adult mosquitoes is important in the control programmes in view of the findings of the study. Furthermore, the study provides information on reproductive performance that is useful in mass rearing of mosquitoes, which is an essential procedure in sterile insect release and other methods currently experimented in Sri Lanka.

Acknowledgement

The authors thank Mr. Sudesh Ruvinda, Lecturer of the Department of Zoology and Environmental Management, University of Kelaniya for the support given for the statistical analysis and Mr. D. Sunil Shantha, Entomological Assistant, Faculty of Medicine, University of Colombo, for providing an egg sheet of *Ae. aegypti*.

REFERENCES

- Artis M.L., Huestis D.L. & Lehmann T. (2014). The effects of oviposition-site deprivation on longevity and blood feeding rate in *Anopheles gambiae*. *Parasites and Vectors* 7(1): 1–6.
DOI: <https://doi.org/10.1186/1756-3305-7-163>
- Bentley M.D. & Day J.F. (1989). Chemical ecology and behavioral aspects of mosquito oviposition. *Annual Review of Entomology* 34(1): 401–421.
DOI: <https://doi.org/10.1146/annurev.en.34.010189.002153>
- Chadee D.D. (1997). Effects of forced egg-retention on the oviposition patterns of female *Aedes aegypti* (Diptera: Culicidae). *Bulletin of Entomological Research* 87(6): 649–651.
DOI: <https://doi.org/10.1017/s000748530003875x>

- Clements A. (1992). The biology of mosquitoes: development, nutrition and reproduction, 1st edition, pp. 388. Chapman & Hall, London, UK.
- De Jesus C.E. & Reiskind M.H. (2016). The importance of male body size on sperm uptake and usage, and female fecundity in *Aedes aegypti* and *Aedes albopictus*. *Parasites and Vectors* **9**(1): 1–7.
DOI: <https://doi.org/10.1186/s13071-016-1734-8>
- Dhileepan K. (1997). Physical factors and chemical cues in the oviposition behavior of arboviral vectors *Culex annulirostris* and *Culex molestus* (Diptera: Culicidae). *Environmental Entomology* **26**(2): 318–326.
DOI: <https://doi.org/10.1093/ee/26.2.318>
- Dieter K.L., Huestis D.L. & Lehmann T. (2012). The effects of oviposition-site deprivation on *Anopheles gambiae* reproduction. *Parasites and Vectors* **5**(1): 1–8.
DOI: <https://doi.org/10.1186/1756-3305-5-235>
- Dye C. (1992). The analysis of parasite transmission by bloodsucking insects. *Annual Review of Entomology* **37**(1): 1–19.
DOI: <https://doi.org/10.1146/annurev.en.37.010192.000245>
- El-Akad A.S. & Humphreys J.G. (1988). Factors affecting oviposition and egg production in laboratory-reared *Anopheles pharoensis* Theobald. *Bulletin of the Society of Vector Ecologists* **13**(2): 243–247.
- Else J.G. & Judson C.L. (1972). Enforced egg-retention and its effects on vitellogenesis in the mosquito, *Aedes aegypti*. *Journal of Medical Entomology* **9**(6): 527–530.
DOI: <https://doi.org/10.1093/jmedent/9.6.527>
- Govoetchan R., Sovi A., Aikpon R., Salako A., Agbo F.O., Asidi A. & Akogbeto M. (2013). The impact of oviposition-site deprivation in gravid females of *Anopheles gambiae* (Diptera: Culicidae) on fecundity, trophic behaviour and life expectancy. *International Journal of Tropical Insect Science* **33**(4): 207–215.
DOI: <https://doi.org/10.1017/S1742758413000349>
- Gubler D.J. & Rosen L. (1976). A simple technique for demonstrating transmission of dengue virus by mosquitoes without the use of vertebrate hosts. *The American Journal of Tropical Medicine and Hygiene* **25**(1): 146–150.
DOI: <https://doi.org/10.4269/ajtmh.1976.25.146>
- Gubler D.J. (1998). The global pandemic of dengue/dengue haemorrhagic fever: current status and prospects for the future. *Annals of the Academy of Medicine, Singapore* **27**(2): 227–234.
- Harrington L.C. & Edman J.D. (2001). Indirect evidence against delayed "skip-oviposition" behavior by *Aedes aegypti* (Diptera: Culicidae) in Thailand. *Journal of Medical Entomology* **38**(5): 641–645.
DOI: <https://doi.org/10.1603/0022-2585-38.5.641>
- Helinski M.E. & Harrington L.C. (2011). Male mating history and body size influence female fecundity and longevity of the dengue vector *Aedes aegypti*. *Journal of Medical Entomology* **48**(2): 202–211.
DOI: <https://doi.org/10.1603/ME10071>
- Hirsch A. (1883). Dengue, a comparatively new disease: its symptoms. *Handbook of Geographical and Historical Pathology* **1**: 55–81.
- Hitchcock Jr J.C. (1968). Egg retention in *Anopheles quadrimaculatus* say in relation to the physiological age of the mosquito. *Journal of Medical Entomology* **5**(1): 8–8.
DOI: <https://doi.org/10.1093/jmedent/5.1.8>
- Judson C.L. (1967). Feeding and oviposition behavior in the mosquito *Aedes aegypti* (L.). I. Preliminary studies of physiological control mechanisms. *The Biological Bulletin* **133**(2): 369–377.
DOI: <https://doi.org/10.2307/1539832>
- Kusumawathi P.H.D. & Fernando W.P. (2003). Breeding habitats of *Aedes aegypti* Linnaeus and *Aedes albopictus* Skuse in a dengue transmission area in Kandy, Sri Lanka. *Ceylon Journal of Medical Science* **46**(2): 51–60.
DOI: <https://doi.org/10.4038/cjms.v46i2.4829>
- Lea A.O. (1970). Endocrinology of egg maturation in autogenous and anautogenous *Aedes taeniorhynchus*. *Journal of Insect Physiology* **16**(9): 1689–1696.
DOI: [https://doi.org/10.1016/0022-1910\(70\)90268-4](https://doi.org/10.1016/0022-1910(70)90268-4)
- McDonald J.L. & Lu L.C. (1972). Viability of mosquito eggs produced by female mosquitoes denied ovipositing sites. *Mosquito News* **32**(3): 463–466.
- McSherry J.A. (1982). Some medical aspects of the Darien scheme: was it dengue? *Scottish Medical Journal* **27**(2): 183–184.
DOI: <https://doi.org/10.1177/003693308202700215>
- Meola R. & Lea A.O. (1972). Humoral inhibition of egg development in mosquitoes. *Journal of Medical Entomology* **9**(1): 99–103.
DOI: <https://doi.org/10.1093/jmedent/9.1.99>
- Noordeen F. *et al.* (13 authors) (2018). Distribution of dengue vectors, *Aedes aegypti* and *Aedes albopictus*, in a few selected semi-urban areas of the Central Province of Sri Lanka. *Sri Lankan Journal of Infectious Diseases* **8**(1): 36–39.
DOI: <https://doi.org/10.4038/sljid.v8i1.8141>
- Owens L. (1981). A method for membrane feeding blood to Culicoides. *Australian Veterinary Journal* **57**(8): 396–397.
DOI: <https://doi.org/10.1111/j.1751-0813.1981.tb00538.x>

- Platt K.B., Linthicum K.J., Myint K.S., Innis B.L., Lerdthusnee K. & Vaughn D.W. (1997). Impact of dengue virus infection on feeding behavior of *Aedes aegypti*. *The American journal of Tropical Medicine and Hygiene* **57**(2): 119–125.
DOI: <https://doi.org/10.4269/ajtmh.1997.57.119>
- Ponlawat A. & Harrington L.C. (2009). Factors associated with male mating success of the dengue vector mosquito, *Aedes aegypti*. *The American Journal of Tropical Medicine and Hygiene* **80**(3): 395–400.
DOI: <https://doi.org/10.4269/ajtmh.2009.80.395>
- Putnam J.L. & Scott T.W. (1995). Blood-feeding behavior of dengue-2 virus-infected *Aedes aegypti*. *The American Journal of Tropical Medicine and Hygiene* **52**(3): 225–227.
DOI: <https://doi.org/10.4269/ajtmh.1995.52.225>
- Sirisena P.D.N.N. & Noordeen F. (2014). Evolution of dengue in Sri Lanka—changes in the virus, vector, and climate. *International Journal of Infectious Diseases* **19**: 6–12.
DOI: <https://doi.org/10.1016/j.ijid.2013.10.012>
- Vitarana T., Jayakuru W.S. & Withane N. (1997). Historical account of dengue haemorrhagic fever in Sri Lanka. *Dengue Bulletin* **21**: 177–118.
- World Health Organization (2014a). *Dengue and severe dengue* (pdf). World Health Organization. Regional Office for the Eastern Mediterranean. Available at <https://apps.who.int/iris/handle/10665/204161>, Accessed 9 January 2021.
- World Health Organization (2014b). *A Global Brief on Vector-Borne Diseases* (pdf). World Health Organization. Available at <https://apps.who.int/iris/handle/10665/111008>, Accessed 9 January 2021.
- Xue R.D., Ali A. & Barnard D.R. (2005). Effects of forced egg-retention in *Aedes albopictus* on adult survival and reproduction following application of DEET as an oviposition deterrent. *Journal of Vector Ecology* **30**(1): 45–48.
- Yang P. (2008). Effect of oviposition site deprivation on oviposition performance and egg hatch rate of naturally blood-fed gravid *Culex quinquefasciatus* (Diptera: Culicidae). *Hawaiian Entomological Society* **40**: 51–54.
- Zheng M.L., Zhang D.J., Damiens D.D., Lees R.S. & Gilles J.R. (2015). Standard operating procedures for standardized mass rearing of the dengue and chikungunya vectors *Aedes aegypti* and *Aedes albopictus* (Diptera: Culicidae)-II-Egg storage and hatching. *Parasites and Vectors* **8**(1): 1–7.
DOI: <https://doi.org/10.1186/s13071-015-0951-x>

RESEARCH ARTICLE

Biochemistry

Quantification of metabolite cinnamic acid of cinnamon (*Cinnamomum zeylanicum*) in human plasma

S Piger^{1*}, P Ranasinghe¹, MN Kaumal² and P Galappatthy¹

¹ Department of Pharmacology, Faculty of Medicine, University of Colombo, No.25, Kynsey Road, Colombo 08, Sri Lanka.

² Department of Chemistry, Faculty of Science, University of Colombo, Colombo 03, Sri Lanka.

Submitted: 02 December 2021; Revised: 05 April 2022; Accepted: 24 June 2022


Abstract: *Cinnamomum zeylanicum* (CZ) is known to have numerous beneficial medicinal effects. The mechanism of action and compounds which account for these effects are not yet clearly defined. The present study aims to develop and validate a method to quantify the metabolites of CZ in human plasma and study its pharmacokinetic profile. Cinnamic acid (CA) was identified as the main metabolites of CZ in human plasma and was used to develop and validate the method. HPLC with a UV-detector was used to identify and quantify CA. Linearity, precision, bias, repeatability, and lower limit of detection (LOD) were determined. CZ (5 g) was orally administered to 5 healthy volunteers and serial blood samples were taken, to determine maximal plasma concentration (C_{max}), time to reach maximal concentration (T_{max}) and elimination half-life ($T_{1/2}$) of CA. The precision, bias, and repeatability, of the method were 7.73%, 4.20%, and 5.63%, respectively. LOD was 1.11 $\mu\text{mol/L}$ and samples were stable up to five days at 4 °C. Recovery of the method was 95% -125%. The retention time of CA was 16 minutes at 254 nm. Concentrations of CA between 0.5 and 200.0 $\mu\text{mol/L}$ in a plasma matrix showed a linear response. C_{max} was $1.9 \pm 1.5 \mu\text{mol/L}$, while T_{max} and $T_{1/2}$ were 15 and 36 minutes respectively. The study developed a sensitive and specific HPLC method to detect CA, a key metabolite of CZ in humans, which is suitable for human pharmacokinetic studies. These pharmacokinetic parameters (C_{max} , T_{max} , $T_{1/2}$) would help in further development of CZ as a pharmaceutical agent for use in humans.

Keywords: Ceylon cinnamon, *Cinnamomum zeylanicum*, HPLC, humans, pharmacokinetics.

INTRODUCTION

Cinnamon, a spice mainly used as a flavouring agent, belongs to the Lauracea family. It has been a constituent of our food since ancient times. Cinnamon is also used in the aroma and essence industries due to its fragrance. Many parts of the cinnamon tree such as the bark, leaves, flowers, fruits, and roots, have some medicinal or culinary use. At present, there are approximately 250 different species identified in the cinnamon genus (Sangal *et al.*, 2011; Vangalapati & Prakash *et al.*, 2012) *Cinnamomum zeylanicum* (also known as *Cinnamomum verum*) and *Cinnamomum cassia* (*C. cassia* or *aromaticum*) are the two main species of cinnamon used all over the world (Ranasinghe *et al.*, 2013). *Cinnamomum zeylanicum* (*C. zeylanicum*), well known as Ceylon cinnamon (derived from its Latin name, zeylanicum) or also referred to as 'true cinnamon' is indigenous to Sri Lanka and southern parts of India. Sri Lanka produces the largest quantity and best quality Ceylon/true cinnamon in the world (Ranasinghe *et al.*, 2017).

In traditional Sri Lankan medicine, cinnamon is used as a remedy for respiratory, digestive, and gynaecological ailments (Ranasinghe *et al.*, 2013). In recent times, *in vitro* and *in vivo* studies using both *C. zeylanicum* and *C. cassia* have demonstrated numerous beneficial medicinal effects. These include antimicrobial, anti-inflammatory, anti-parasitic, antioxidant, anti-diabetic, anti-cancer, cholesterol lowering and blood pressure lowering activities (Wondrak *et al.*, 2010; Ranasinghe *et al.*, 2013; Rao & Gan, 2014). However, it

* Corresponding author (shehani54@gmail.com;  <https://orcid.org/0000-0003-4375-3240>)



This article is published under the Creative Commons CC-BY-ND License (<http://creativecommons.org/licenses/by-nd/4.0/>). This license permits use, distribution and reproduction, commercial and non-commercial, provided that the original work is properly cited and is not changed in anyway.

is important to note that most of the above effects were demonstrated *in vitro* and in animal studies, with few studies in humans (Khan *et al.*, 2003; Bernardo *et al.*, 2015). The mechanism of action and compounds which account for the medicinal effects are not yet clearly identified and require further study. Furthermore, since some of the demonstrated medicinal benefits include systemic effects, it is important to understand the pharmacokinetic profile of cinnamon in humans.

Cinnamon consists of a variety of resinous compounds, including cinnamaldehyde, cinnamate, cinnamic acid, and numerous essential oils (Senanayake *et al.*, 2002). The amount of compounds present varies according to the part of the plant, with the bark having mainly cinnamaldehyde (65–80%) and eugenol (5–10%) (Rao & Gan, 2014). Each compound in cinnamon may or may not follow different pathways in the body after oral administration, forming different metabolites. Cinnamaldehyde, cinnamyl acetate, and cinnamyl alcohol are converted into cinnamic acid by oxidation and hydrolysis, and subsequently β -oxidized to benzoate in the liver (El-Mawla *et al.*, 2001; Brahmachari *et al.*, 2009). Yuan *et al.* (1992) demonstrated that cinnamaldehyde follows first order kinetics with a half-life ($t_{1/2}$) of 9 min in rat blood and was almost completely metabolized into cinnamic acid before it was absorbed into blood. Several similar animal studies have been done to study the various pharmacokinetic parameters of cinnamon (Song *et al.*, 2002; Chen *et al.*, 2009). However, to date, there are no studies reporting the pharmacokinetic profile of *Cinnamomum zeylanicum* (CZ) in humans. Hence, the present study aims to develop and validate a method to quantify the metabolite of CZ in human plasma and study its pharmacokinetic profile after oral administration to healthy volunteers.

MATERIALS AND METHODS

Chemicals, reagents and instruments

Analytical grade cinnamic acid (purity $\geq 99\%$) (Sigma-Aldrich, St. Louis, MO, USA) was used for the study. In addition HPLC-grade acetonitrile (assay $\geq 99.8\%$) (Fisher Scientific, California, USA), methanol (assay $\geq 99.9\%$) (Sigma-Aldrich, St. Louis, MO, USA), ethyl acetate (assay $\geq 99.8\%$) (Sigma-Aldrich, St. Louis, MO, USA), and acetic acid (assay $\geq 99.8\%$) (Sigma-Aldrich, St. Louis, MO, USA) and hydrochloric acid (assay $\geq 37\%$) (Sigma-Aldrich, St. Louis, MO, USA) were used. The chromatographic system consisted of a PU-980 Jasco pump, a LC-800 series 802-SC system controller, LC-900 series CO-965 column, a UV-970 UV-vis detector set at 254 nm, a 20 μ L injection loop, a workstation for data collection and a C18 HPLC column 250 mm \times 4.6 mm \times 5 μ m. The mobile phase was methanol : acetonitrile : 2% acetic acid (20:25:70 v/v) at a flow rate of 1 mL/min and it was operated at room temperature.

Development of HPLC analysis method

A stock solution of standard cinnamic acid (0.021 mol/L) was prepared using methanol and it was diluted with methanol to prepare working solutions of cinnamic acid (0.5–800 μ mol/L). All prepared standard solutions were stored at 4 °C. Plasma samples were obtained from National Blood Transfusion Service at the National Hospital of Sri Lanka (Lot No: 15C008598). Aliquots of 25 mL from each one of the prepared serial dilutions of cinnamic acid (0.5–800 mmol/L) were added to each of the 250 mL samples of plasma to obtain the different concentrations of cinnamic acid in plasma. Plasma and cinnamic acid mixtures were vortexed for 2 min (Autovortex SA6 model, Stuart Scientific, UK).

Subsequently, for the purpose of extraction of cinnamic acid for HPLC analysis, each plasma sample with cinnamic acid was acidified with 75.0 μ L of 0.1 mol/L HCl and then vortexed for 1 min; subsequently, 1.5 mL of ethyl acetate was added and it was vortexed for another 2 min. Then it was centrifuged at 2500 rpm for 10 min (Kubota Laboratory Centrifuge 5100 model, Japan) at room temperature and the supernatant was collected into an Eppendorf tube. Then the collected solution was evaporated under a stream of nitrogen at 40 °C using a water bath. The same procedure was repeated two times with 1 mL of ethyl acetate. The residue was dissolved in 100.0 μ L of methanol and was injected to HPLC.

A mixture of methanol : acetonitrile : 2% acetic acid in water (20:25:70 v/v) was used as the mobile phase for all HPLC analyses, as it was found to be the ratio which gave the best resolution (Song *et al.*, 2002). The retention time of cinnamic acid was 16 min. The mobile phase was degassed using a sonicator (Sonorox, super

RK 1028 CH, Bandelin Electronics, Berlin) and it was filtered through 0.45 μ m pore size nylon membrane filter prior to use. The UV detector wavelength was set at 254 nm. First, the HPLC system without the column was washed with the mobile phase for 5 min to remove any air bubbles. Then the column (internal diameter 4.6 mm, particle size 5 μ m, length 250 mm) was placed and the system was washed for 20 min prior to the injection of analyte till a stable baseline was observed. Subsequently, the sample was injected manually using 0.025 mL syringe. Cinnamic acid was injected into the HPLC with changing mobile phase solvent ratios. This was done in triplicate, and then the optimum ratio with a greater resolution was selected for further analysis. The plasma series of cinnamic acid (0.5–25 μ mol/L) was injected (two injections per sample) into the HPLC after the extraction procedure. Two independently prepared samples were analysed from each concentration.

Statistical Analysis

A calibration plot was drawn, and the minimum level of detection, range, precision, recovery, linear range, and stability of the method were determined. The calibration curves for cinnamic acid were obtained for plasma series.

Limit of detection (LOD)

The LOD was determined using the standard deviation of the regression line and the slope of the calibration curve (cinnamic acid spiked plasma), using standard guidelines for method validation (Q2B Validation of Analytical Procedures: Methodology | FDA, 1996).

Precision, bias/accuracy, repeatability

To investigate precision, bias/accuracy, and repeatability ten independently prepared samples of cinnamic acid (25.0 μ mol/L) were extracted and injected into the HPLC. The cinnamic acid concentration was evaluated using the calibration curve, and repeatability, bias, and precision were calculated using standard equations (Q2B Validation of Analytical Procedures: Methodology | FDA, 1996).

Stability

To evaluate stability, plasma samples with cinnamic acid ($n = 5$) with the concentration of 200 μ mol/L were kept at 4 °C for 5 ds and then analysed using Student's t-test at the 95% confidence level, in order to evaluate the difference in absorbance with the time.

Recovery

In order to study recovery, three independent samples from 3 different concentrations with three replicated analyses were done. The mean absorbance value is given after the extraction was compared to the absorbance of corresponding concentration obtained from a standard cinnamic acid series in methanol.

Pharmacokinetics of cinnamic acid in healthy volunteers

Inclusion criteria

Pharmacokinetic parameters of cinnamic acid in blood were assessed in five healthy volunteers (>18 years). Ethical clearance for the study was obtained from the Ethics Review Committee, Faculty of Medicine, University of Colombo, Sri Lanka (EC/16/099). The participants were between 18 to 60 years, not on any other vitamin or mineral supplementations, having normal hepatic or renal functions, non-lactating, and non-pregnant.

Preparation of cinnamon extract for oral administration

To prepare the cinnamon powder for the study, CZ bark (Kosgoda, Sri Lanka) (3 g) was powdered and it was soaked in boiling water (250 mL) for 10 min in a closed cup. The entire extract along with undissolved parts was administered to volunteers.

Blood sample collection

The participants were asked to come after 10 h of overnight fasting. On the day of the study, initially, a baseline blood sample was taken at 8.00 am (0 h). Subsequently, the content of the above prepared CZ solution was given to study participants to drink. Subsequent blood samples were taken at 5 min, 15 min, 30 min, 60 min, 3 h and 6 hours. A 24-hour sample was taken in the morning of the following day at 8.00 am. Each blood sample was about 2–2.5 mL and was obtained from the ante-cubital fossa under sterile conditions. Subjects were given standard meals during the period of the study and CZ was avoided in the preparation of these meals.

Analysis of samples

The blood samples were separated by centrifugation and the supernatant (plasma) was collected. An aliquot (250.0 μ L) plasma sample was acidified with 75.0 μ L of 0.1 mol/L HCl and it was vortexed for 1 min. A 25.0 μ L portion of methanol was added to it. Then the same extraction procedure was followed as the cinnamic acid in the plasma sample described above. Finally, it was injected into the HPLC and the chromatograms were obtained. Using the calibration curve the plasma cinnamic acid concentrations were calculated. Then the concentration-time curve was drawn for extracted human plasma samples.

Pharmacokinetic parameters

Pharmacokinetic parameters were calculated using the non-compartment extra-vascular model applied for the cinnamic acid plasma disposition curves. The area under the plasma concentration-time curve (AUC) was calculated by the use of the mixed log-linear trapezoidal method. Values for the maximum plasma concentration (C_{max}) and time to peak plasma concentration (T_{max}) were directly determined from the plasma concentration-time curve. The elimination half-life ($T_{1/2}$ in minutes) was calculated as $0.693/K_e$, in which K_e was the elimination rate constant. Parametric and non-parametric statistical tests were done using SPSS version 14 (SPSS Inc., Chicago, IL, USA). Dichotomous variables are reported as numbers and percentages and compared using chi-square test. Continuous variables are presented as mean (\pm SD) and intergroup comparisons were conducted with Student's t-test or ANOVA with *post hoc* analysis. In all analyses, a $p < 0.05$ was considered as statistically significant.

RESULTS AND DISCUSSION

Development and validation of HPLC method

The plasma series of cinnamic acid (0.5–200 μ mol/L) were injected to HPLC. Within the concentration range, a linear calibration plot was obtained for cinnamic acid. The results of concentrations of 0.5–25 μ mol/L are shown in Figure 1.

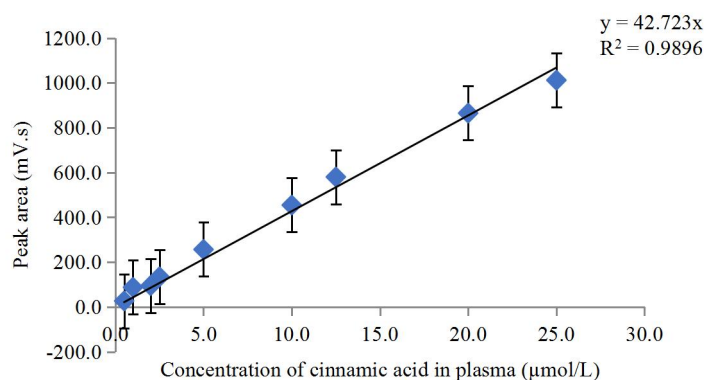


Figure 1: Calibration curve for cinnamic acid in plasma (0.5–25 μ mol/L)

Linear range

The linear range was from 0.5–200 $\mu\text{mol/L}$ in cinnamic acid spiked plasma series.

LOD, repeatability, bias, and precision

Repeatability, bias, and precision were evaluated by measuring the absorbance of ten independently prepared plasma samples with cinnamic acid (25.0 $\mu\text{mol/L}$) after the extraction procedure. The precision/relative standard deviation (RSD) of ten samples was 7.73%. The bias and repeatability of the method were 4.20% and 5.63, respectively. Using the function STEYX in MS-Excel the standard deviation of the regression line was found to be 15.013 and the slope of the line was 44.77. The LOD was 1.11 $\mu\text{mol/L}$ with 10 plasma samples.

Stability

The stability data of the cinnamic acid samples in plasma after 5 days at 4 °C were evaluated. The mean concentration of two data sets obtained on different days was tested using the two sample *t*-test at 95% confidence level. At 95% confidence level, there was no significant difference between the mean concentration of the two data series. Therefore, it was found the plasma samples with cinnamic acid are stable when stored at 4 °C up to 5 days. The stability of CA and hippuric acid in rat plasma samples were previously reported as 12 hours at room temperature, 24 hours at 4 °C and 7 days at -70 °C (Chen *et al.*, 2009).

Recovery

The recovery of the extraction method is 95–125% which indicates the efficiency of the extraction method. According to FDA, the mean recovery should be 100 ± 2 at each concentration over the range of 80–120% of the target concentration. Therefore the recovery of the method is acceptable and it has been also recorded the recovery of cinnamic acid as 71.5–85.0% in previous studies (Chen *et al.*, 2009).

Pharmacokinetics study

The sample size was 5, of which three participants were males. Mean (\pm SD) age, height, weight and BMI were 26.2 ± 3.0 years, 169.8 ± 8.9 cm, 70.6 ± 12.8 kg and 24.3 ± 2.7 kg/m², respectively. The change in mean plasma cinnamic acid concentration (\pm SD) with time, using time zero as the reference point is shown in Figure 2. Plasma cinnamic acid concentration increased from baseline (0 h) and the maximal concentration achieved in the blood (C_{max}) was 1.9 ± 1.5 $\mu\text{mol/L}$. The time taken to reach the maximal concentration (T_{max}) was 15 minutes. Subsequently, the concentration gradually decreased (Figure 2). The area under the curve (AUC) from time of administration to the time of last observation was 588 $\mu\text{mol} \cdot \text{min/L}$. The elimination rate constant (K_e) was 0.019 min^{-1} . The elimination half-life ($T_{1/2}$) was 36 minutes.

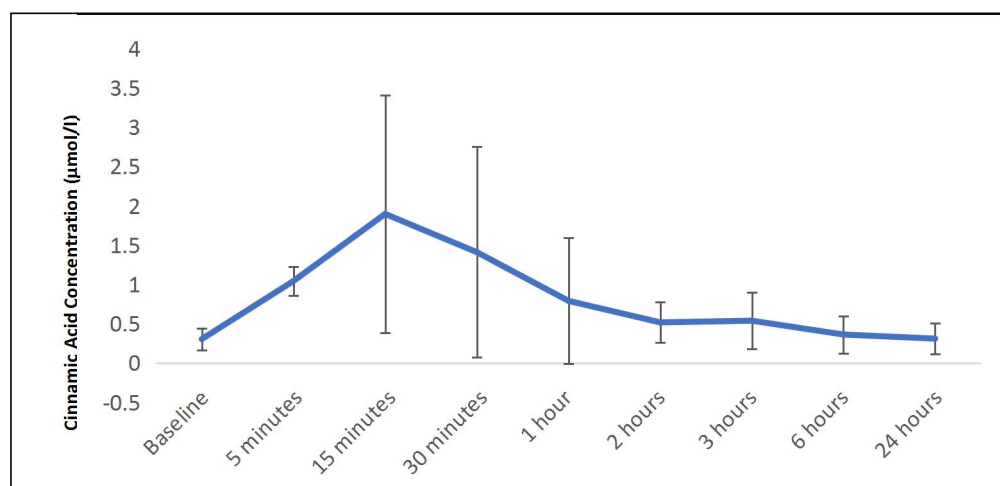


Figure 2: Change in mean cinnamic acid concentration (\pm SD) with time

The present study is the first to describe a sensitive, specific, and rapid HPLC method with UV detection for the determination of metabolites (cinnamic acid) of *Cinnamomum zeylanicum* in human plasma. Our results show that this validated method is suitable for pharmacokinetic studies of *Cinnamomum zeylanicum* in humans, with advanced HPLC using high sensitivity detectors. These findings will help further studies on *Cinnamomum zeylanicum*, which is now emerging as a potential pharmaceutical agent for the treatment of several diseases, including diabetes, hyperlipidaemia, hypertension, cardiovascular disease and Alzheimer's disease (Ranasinghe et al., 2013). Obtaining human pharmacokinetic information is an essential step in the new drug development process, which helps to ensure the appropriate usage of medicines. The current method will be effective in detecting metabolites of cinnamon in plasma. Furthermore, identification of metabolites of *Cinnamomum zeylanicum* detectable in human plasma would help in the identification of active compounds responsible for the observed pharmacodynamic properties.

The metabolites of *Cinnamomum zeylanicum* identified for the purpose of the present study were cinnamaldehyde, benzoic acid, and cinnamic acid, based on evidence from previous animal studies (Yuan et al., 1992; Song et al., 2002; Chen et al., 2009). However, at the initial screening, cinnamaldehyde was excluded from further analysis due to the tailing nature of the peak irrespective of the concentration. Furthermore, only cinnamic acid was identified to be present in the blood after oral administration of *Cinnamomum zeylanicum* in humans. The standards used in the present study were prepared in methanol due to the higher solubility of these compounds in methanol than in water. The developed method was linear for cinnamic acid in the plasma matrix from 0.5–200.0 $\mu\text{mol/L}$. Chen et al. (2009) have recorded a linear range of 0.34–33.78 $\mu\text{mol/L}$ in rat plasma. The linear range of cinnamic acid will permit the use of this method for future pharmacokinetic studies. Furthermore, the method was specific for cinnamic acid and the precision/relative standard deviation (RSD), bias, and repeatability of the method were 7.73%, 4.20% and 5.63 respectively. The sample was stable up to five days at 4 °C. The recovery of the method was 95–125% and the LOD was 1.11 $\mu\text{mol/L}$. All these validation parameters are in satisfactory levels. According to Song et al. (2002) within day precision was approximately 3.7–9.3% and day to day precision was 2.4–5.8% in animal studies.

As per the results, the maximal concentration reached in plasma (C_{max}) was $1.9 \pm 1.5 \mu\text{mol/L}$. The time taken to reach maximum plasma concentration (T_{max}) and elimination half-life ($T_{1/2}$) of cinnamic acid in humans was 15 minutes and 36 minutes, respectively. In animal studies involving Sprague-Dawley rats with *Cinnamomum cassia*, the T_{max} and $T_{1/2}$ of cinnamic acid was 7 ± 6 minutes and 20 ± 7 minutes respectively after intragastric administration (Chen et al., 2009). Li et al. (2008) reported that the plasma concentration of cinnamic acid (from *Cinnamomum zeylanicum*) reached the maximum at 1.8 hours and the $T_{1/2}$ was 3.1 hours after intragastric administration in rabbits while Yang et al. (1994) reported a T_{max} of 53 minutes and a $T_{1/2}$ of 5.7 hours after intragastric administration of Baoxin pill (a pill containing *Cinnamomum cassia* and several other herbal ingredients) in rats. The observed differences are likely due to differences in cinnamon species used (*Cinnamomum cassia* or *Cinnamomum zeylanicum*), animal species tested (rats, rabbits, or humans), dosage forms utilized (powder or capsules) or the composition of the dosage form (cinnamon only or cinnamon mixed with other ingredients). Hence, further studies are required to replicate these findings from this first study using Ceylon cinnamon in healthy humans and conclusively determine the pharmacokinetic parameters of cinnamic acid after oral administration of *Cinnamomum zeylanicum* in humans.

CONCLUSION

In conclusion, the present study developed a sensitive and specific HPLC method to detect cinnamic acid, a key metabolite of *Cinnamomum zeylanicum* in humans. This method is suitable for pharmacokinetic studies of *Cinnamomum zeylanicum* in humans. The study also determined the maximal concentration reached in plasma (C_{max}), time taken to reach maximum concentration (T_{max}) and elimination half-life ($T_{1/2}$) of cinnamic acid in humans. The identified pharmacokinetic parameters (C_{max} , T_{max} , and $T_{1/2}$) would help in the further development of CZ as a pharmaceutical agent for use in humans.

REFERENCES

- FDA (1996). Q2B Validation of Analytical Procedures: Methodology. Available at <https://www.fda.gov/regulatory-information/search-fda-guidance-documents/q2b-validation-analytical-procedures-methodology>, Accessed 1 December 2021.
- Bernardo M.A., Silva M.L., Santos E., Moncada M.M., Brito J., Proença L., Singh J. & de Mesquita M. F. (2015). Effect of cinnamon tea on postprandial glucose concentration. *Journal of Diabetes Research* **2015**: 913651. DOI: <https://doi.org/10.1155/2015/913651>
- Brahmachari S., Jana A. & Pahan K. (2009). Sodium benzoate, a metabolite of cinnamon and a food additive, reduces microglial and astroglial inflammatory responses. *The Journal of Immunology* **183**(9): 5917–5927. DOI: <https://doi.org/10.4049/jimmunol.0803336>
- Chen Y., Ma Y. & Ma W. (2009). Pharmacokinetics and bioavailability of cinnamic acid after oral administration of *Ramulus Cinnamomi* in rats. *European Journal of DRUG Metabolism and Pharmacokinetics* **34**(1): 51–56. DOI: <https://doi.org/10.1007/BF03191384>
- El-Mawla A., Schmidt W. & Beerhues L. (2001). Cinnamic acid is a precursor of benzoic acids in cell cultures of *Hypericum androsaemum* L. but not in cell cultures of *Centaurium erythraea* RAFN. *Planta* **212**: 288–293. DOI: <https://doi.org/10.1007/s004250000394>
- Khan A., Safdar M., Ali Khan M.M., Khattak K.N. & Anderson R.A. (2003). Cinnamon improves glucose and lipids of people with type 2 diabetes. *Diabetes Care* **26**(12): 3215–3218. DOI: <https://doi.org/10.2337/diacare.26.12.3215>
- Ranasinghe P., Galappaththy P., Constantine G.R., Jayawardena R., Weeratunga H.D., Premakumara S. & Katulanda P. (2017). *Cinnamomum zeylanicum* (Ceylon cinnamon) as a potential pharmaceutical agent for type-2 diabetes mellitus: study protocol for a randomized controlled trial. *Trials* **18**(1): 1–8. DOI: <https://doi.org/10.1186/s13063-017-2192-0>
- Ranasinghe P., Pigerá S., Premakumara G.A., Galappaththy P., Constantine G.R. & Katulanda P. (2013). Medicinal properties of ‘true’ cinnamon (*Cinnamomum zeylanicum*): a systematic review. *BMC Complementary and Alternative Medicine* **13**(1): 1–10. DOI: <https://doi.org/10.1186/1472-6882-13-275>
- Rao P.V. & Gan S.H. (2014). Cinnamon: a multifaceted medicinal plant. *Evidence-Based Complementary and Alternative Medicine* **2014**. DOI: <https://doi.org/10.1155/2014/642942>
- Sangal A. (2011). Role of cinnamon as beneficial antidiabetic food adjunct: A review. *Advances in Applied Science Research* **2**(4): 440–450.
- Senanayake U.M., Lee T.H. & Wills R.B. (1978). Volatile constituents of cinnamon (*Cinnamomum zeylanicum*) oils. *Journal of Agricultural and Food Chemistry* **26**(4): 822–824. DOI: <https://doi.org/10.1021/jf60218a031>
- Song Z., Bi K. & Luo X. (2002). An HPLC method for the determination and pharmacokinetic study of cinnamic acid in the plasma of rats having taken the traditional Chinese medicinal preparation Ling-Gui-Zhu-Gan decoction. *Journal of Chromatographic Science* **40**(4): 198–200. DOI: <https://doi.org/10.1093/chromsci/40.4.198>
- Vangalapati M., Satya N.S., Prakash D.S. & AvaniGadda S. (2012). A review on pharmacological activities and clinical effects of cinnamon species. *Research Journal of Pharmaceutical, Biological and Chemical Sciences* **3**(1): 653–663.
- Li W.L., Whang X.D., Ji Y.B., Hu Z.T., Ren X.L. & Whang J. (2008). Comparison study pharmacokinetics of different source cinnamon acid. *China Journal of Chinese Materia Medica* **33**(10): 1192–1195.
- Wondrak G.T., Villeneuve N.F., Lamore S.D., Bause A.S., Jiang T. & Zhang D.D. (2010). The cinnamon-derived dietary factor cinnamic aldehyde activates the Nrf2-dependent antioxidant response in human epithelial colon cells. *Molecules* **15**: 3338–3355. DOI: <https://doi.org/10.3390/molecules15053338>
- Yang C., Hou S., Sun Y. & Li C. (1994). Pharmacokinetics of cinnamic acid of BAOXIN PILL in rat. *Chinese Traditional and Herbal Drugs* **32**: 616–618.
- Yuan J., Bucher J.R., Goehl T.J., Dieter M.P. & Jameson C.W. (1992). Quantitation of cinnamaldehyde and cinnamic acid in blood by HPLC. *Journal of Analytical Toxicology* **16**(6): 359–362. DOI: <https://doi.org/10.1093/jat/16.6.359>

RESEARCH ARTICLE

Process Control Engineering

Temperature control in an exothermic continuous stirred tank reactor

VA Rani*, G Guna, D Prabhakaran and M Thirumarimurugan

Department of Chemical Engineering, Coimbatore Institute of Technology, Coimbatore, Tamil Nadu 641014, India.


Submitted: 27 December 2021; Revised: 15 April 2022; Accepted: 24 June 2022

Abstract: A continuous stirred tank reactor (CSTR) is a batch reactor fortified with an impeller or additional mixing device to provide resourceful mixing. In chemical engineering, the name CSTR is often used to describe an idealised agitated tank reactor used to model manoeuvre variables necessary to achieve a specified output. Most chemical plants have a process involving a continuous stirred tank reactor (CSTR), and it has more nonlinearity in real-world implementation due to disturbances like change in surrounding temperature, non-uniformity in mixing, and change in the temperature of the coolant. The aim of the work is to study the dynamic behaviour of a continuous stirred tank reactor with coolant flow rate as input and reactor temperature as output and to design a suitable controller to control the temperature of the continuous stirred tank reactor by conducting an exothermic reaction in real-time. A continuous stirred tank reactor was modelled with the help of a transfer function model in the MATLAB environment. For controlling the temperature of the reactor fluid, the design of proportional integral derivative, proportional integral derivative (PID) – particle swarm optimization (PSO), proportional integral derivative (PID) – artificial bee colony optimization (ABC) and model predictive control (MPC) controller were carried out. The simulation results show that model predictive control has better tracking performance compared to conventional PID, PID–PSO or PID–ABC.

Keywords: Controller tuning, exothermic reaction, optimization algorithms, temperature control, transfer function.

INTRODUCTION

Continuous stirred tank reactors are important in industries such as construction materials, biofuels, pharmaceuticals and wastewater treatment (Rani *et al.*, 2020). The reaction in a CSTR can be exothermic or endothermic. On the occurrence of an exothermic reaction, heat is liberated. Under such conditions, a coolant stream will be transported through the jacket that surrounds the reactor to remove the extra heat. On the other hand, if an endothermic reaction occurs in the system, a heating medium has to be provided through the jacket for regulating the temperature in the reactor. A reactor operating at a constant temperature is called an isothermal reactor (Ahmed *et al.*, 2016). When exothermic or endothermic reactions take place, heat is either liberated or absorbed. This leads to a change in the temperature of the reactor at various points in time. Since the temperature of the reaction in the reactor is not constant throughout, it is called a non-isothermal reactor. Regulating the temperature in the non-isothermal CSTR is an important control problem. Various controller schemes such as classical controllers (Dey & Roy, 2014), optimal controllers (Da & Shu-Cai, 2018), and robust controllers (Monika Bakošová *et al.*, 2005) are used to overcome the temperature control problem. In order to achieve better performance of the controller, there is a need for proper adjustment of the parameters of the controller. The procedure for adjustment of the controller parameters is called ‘tuning’ or ‘design’ of the controller. The most widely accepted practical tuning methods are the Ziegler and Nichols (1942) method and Cohen and Coon (1953) method (Agarwal *et al.*, 2015). These methods are compatible only with an open loop, stable and single input single output (SISO) system, and it is not suitable for a complex and highly unstable process. Hence, tuning a higher order for a complex process is very difficult using conventional approaches.

* Corresponding author (anusharani151@gmail.com;  <https://orcid.org/0000-0001-7290-9086>)



This article is published under the Creative Commons CC-BY-ND License (<http://creativecommons.org/licenses/by-nd/4.0/>). This license permits use, distribution and reproduction, commercial and non-commercial, provided that the original work is properly cited and is not changed in anyway.

Thus, the control society has shifted its focus to stochastic approaches, which offer a heuristic searching method for the tuning mechanism. The optimal controller parameters, which are obtained from the evolutionary optimization techniques, are fed into the controller. Then, the closed loop system is simulated to find the desired response. From the output response of the process, the objective function is evaluated based on the set point value, and it is processed by the evolutionary optimizer. There are numerous evolutionary optimization techniques used in the literature to tune the parameters of a PID controller, such as particle swarm optimization (PSO) (Bonyadi & Michalewicz, 2017), bacterial foraging optimization (BFO) (Das *et al.*, 2009) and atom search optimization (Zhao *et al.*, 2019). Apart from the optimization techniques, the formulation of the objective function is the significant part of the optimization. The most widely employed objective function is the summation of errors between the set point and the actual output. In PID controller design methods, the most common performance criteria are integrated absolute error (IAE), integrated time weight square error (ITWSE), integrated squared error (ISE), and mean square error (MSE). These four integral performance criteria have their own advantages and disadvantages.

In Swapnadeep and Lillie (2017), the temperature control of CSTR was performed using the PID tuned by the Ziegler-Nichols method, genetic algorithm (GA), and the PSO. The mathematical model of the CSTR was considered, and the objective function used for the optimization was the ISE. The transient and steady-state analysis was carried out on the closed loop system, and it was found that the PID-PSO performed better while ISE was used as the objective function. In Thulasi Dharan *et al.* (2017), a multi input multi output (MIMO) model of the CSTR was considered for temperature control. Here the objective function used was the ITAE. The PSO had better closed-loop performance compared to the other optimization algorithms. Masilamani *et al.* (2015) computed a model predictive controller for the temperature and concentration control of the CSTR. Here the state space model of the CSTR was considered for the implementation of the controller. The MPC toolbox of the MATLAB environment was used to provide the plant inputs and initial values to the state space model of the CSTR. The MPC predicts the value of the temperature and concentration and controls the same. In this study, the model required for the control of the CSTR was obtained from the experimentation. The performance criterion obtained from various models of CSTR is to be compared with the experimental model. The novelty of the study lies in the usage of the experimental model for controller implementation. From the literature, it is seen that the objective function mainly used was the ITAE and ISE. In this study, a new objective function, which is the combination of the ITAE and the overshoot, was used.

MATERIALS AND METHODS

Process description

Experimental setup

A non-isothermal CSTR consists of inlet streams, an outlet stream, and the jacket through which the coolant is passed in order to remove the heat generated due to the exothermic reaction inside the reactor. The temperature of the reaction mixture, the concentration of the reaction mixture and the level of fluid inside the tank are the important process variables. Actual values of these variables are measured using appropriate instruments and controlled to the desired value using controllers. The setup is pictured in Figure 1 and consists of a resistance temperature detector (RTD), variable frequency drive (VFD), motor, pumps, programmable logic controller (PLC), emergency shutdown, stirrer, and tanks. The reactor vessel is insulated with glass wool to prevent the heat from escaping into the surrounding. The capacity of the reactor vessel is 50 L, the hold up inside the reactor is 25 L, and the reactants are stored in tanks of volume 25 L. From the tanks, the reactants can be transferred to the reactor using a pump (12 Volt DC, maximum pressure 0.65 MPa) which operates at a flow rate of 4 LPM. Ball valves are used to reduce the flow of reactant. The equipment is made of steel and coated with anti-corrosion paint. The stirrer speed is kept constant. In this process, the input variable is the flow rate of coolant, and the output variable is the temperature of the reactor fluid. The range of the variables is tabulated in Table 1.

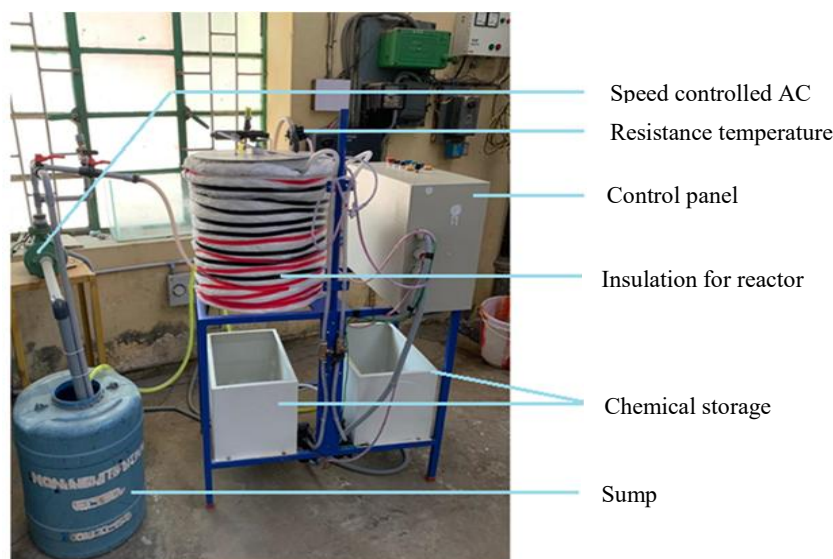


Figure 1: Experimental set up of CSTR

Table 1: Process variables and their value range

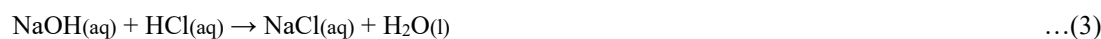
Variables	Symbols	Values range
Feed flow rate of each reactant	F_1, F_2	0.75 LPM
Jacket feed flow rate	$F_j(t)$	0–2 LPM
Inlet temperature of reactor fluid	T_i	30 °C
Outlet temperature of reactor fluid	$T_{io}(t)$	35–50 °C
Jacket inlet temperature	T_{ji}	29 °C
Jacket outlet temperature	T_{jo}	30–45 °C

Study of the setup with chemicals and reaction kinetics

In this study, the reaction between a strong acid, hydrochloric acid (HCl), and a strong base, sodium hydroxide (NaOH), is considered.



The neutralization reaction is an exothermic reaction, and it is carried out inside the reactor:



Design of conventional PID controller

Fundamentals and theory of PID

A block diagram of a simple closed-loop system consisting of a plant and a controller with unity feedback is diagrammed in Figure 2. The purpose of the system is to keep the process output (Y) closest to the desired output (Y_d) regardless of disturbances. This is achieved by manipulating the process input (U) through the controller (Dong *et al.*, 2021). The performance of the closed loop system is defined by the performance criteria of mean square error (MSE), rise time (T_r), settling time (T_s) and steady state error (E_{ss}) of the transient response.

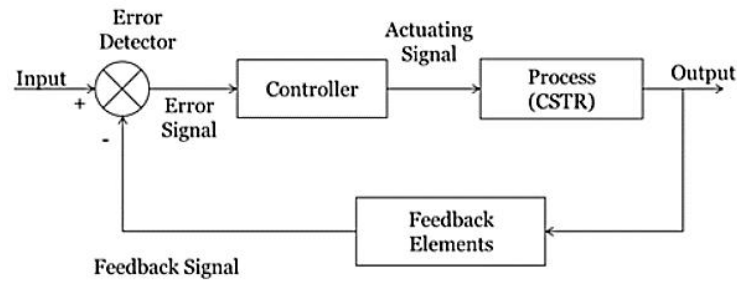


Figure 2: PID controller block diagram

The PID controller is commonly used in industries because of its simplicity in implementation, and it is a linear feedback controller whose control action is based on the error signal $e(t)$, which is a difference between the set point and the model output value. Mathematically the PID controller is given as:

$$u(t) = K_p e(t) + K_i \int e(t) dt + K_d (de(t)/dt) \quad \dots(4)$$

where K_p = Proportional gain
 K_i = Integral gain
 K_d = Derivative gain

The proportional gain of the controller reduces error responses to disturbances (Aslam & Kaur, 2011). The integral of the error eliminates steady-state offsets, and the derivative of the error dampens the dynamic response. Thereby, the stability of the system is improved.

Tuning of PID

Tuning of the independent/tunable parameters is an important step in controller design. In this study, MSE is chosen as the objective function to achieve minimal control errors. It squares the error to remove the negative error components and discriminates between over-damped and under-damped systems.

$$MSE = \frac{1}{2} \int_{t=0}^T e^2(t) dt \quad \dots(5)$$

Lower values of the objective function will give a better closed-loop performance. During the tuning of the controller, MSE, rise time (T_r), settling time (T_s), and steady-state error (E_{ss}) are taken as performance indices.

Rise time (T_r) is the time required for the response to rise from 10 to 90% or 0 to 100% of its final value. For an under-damped system, a second-order system with 0 to 100% rise time is commonly used.

For an over-damped system, 10 to 90% rise time is commonly used.

$$Rise\ Time\ (T_r) = \frac{\pi - \beta}{\omega_d}, \beta = \cos^{-1} \varepsilon \quad \dots(6)$$

where ε is the damping ratio, and ω_d is the damped natural frequency.

Settling time (T_s) is the time required for the response curve to reach and stay within a range about the final value of size specified by an absolute percentage of the final value (usually 5 to 2%).

$$Settling\ Time\ (T_s) = \frac{4}{\varepsilon \omega_n} \quad \dots(7)$$

where ε is the damping ratio, and ω_n is the natural frequency.

Steady-state error (E_{ss}) is the difference between the measured constant output and the input constituents or a set point in a steady-state condition.

Ziegler-Nichols open loop tuning method

In this study, the conventional Ziegler-Nichols method has been used to find the approximate values of the parameters of the PID controller.

- We first plot the Bode diagram for the final control element, the process, and the measuring element in series, $G_i, G_p, H(j\omega)$.
- At the crossover frequency, the overall gain is A . As per the Bode criterion, the gain of a proportional controller causing the system to be on the verge of instability is $1/A$.
- We define this quantity to be the ultimate gain K_u .

$$\text{Thus } K_u = 1/A \tag{8}$$

- The ultimate period P_u is defined as the period of the sustained cycling that would occur if a proportional controller with gain K_u , were used.

$$P_u = 2\pi/\omega_{co} \text{ time/cycle} \tag{9}$$

- The value of the controller gains is calculated as in Table 2.

Table 2: Ziegler-Nichols controller settings

Type of control	$G_c(s)$	K_c	τ_I	τ_D
Proportional (P)	K_c	$0.5K_u$		
Proportional-integral (PI)	$K_c (1 + \frac{1}{\tau_I s})$	$0.45K_u$	$\frac{P_u}{1.2}$	
Proportional-integral-derivative (PID)	$K_c (1 + \frac{1}{\tau_I s} + \tau_D s)$	$0.6K_u$	$\frac{P_u}{2}$	$\frac{P_u}{8}$

Tuning of PID controller using evolutionary algorithms

In Li *et al.* (2015), a hybrid algorithm which is the combination of the PSO and the ABC, was proposed for the optimization of the higher dimensional objective functions and to improve the performance of the optimization algorithm. The algorithm uses the local search space of the PSO and the global search space of the ABC. This hybrid algorithm was applied to various benchmark functions and was compared to other optimization algorithms, such as the ABC and PSO. Saravanakumar *et al.* (2017) used the state transition algorithm (STA) for the tuning of the controller used in the MIMO distillation column. The STA is a heuristic random search algorithm working on the principle of state transition. The objective function used for this optimization is the ITAE and the IAE. From the simulation results, it was understood that the STA is a powerful algorithm with good search capability and improves the performance of the system. In this study, two methods are exploited for obtaining the tunable parameters of the controllers, namely, the conventional tuning methods and the evolutionary algorithms such as PSO and ABC. The evolutionary methods require an objective function that has to be minimized in order to obtain the optimal values of the tunable parameters. In this work, MSE is used as the objective function. The maximum and minimum values of the tunable parameters are obtained from the conventional tuning method (Ziegler-Nichols). Random generation of the initial population within the bounds of the tunable parameters is employed.

Particle swarm optimization (PSO)

PSO is one of the most recent evolutionary algorithms based on the searching behaviour of animals, such as fish schooling and bird flocking (Sultaniya & Gupta, 2014). In the PSO model, each particle is composed of three vectors: the velocity v_i , the current position x_i , and the previous best position $pbest_i$. The velocity in this application is the speed at which or how fast the tunable parameters (K_p , K_i , K_d) of the PID controller reach the optimal values within the search space. Suppose that the objective function is D-dimensional, then the velocity and position of the i^{th} particle are represented as $v_i = (v_{i1}, v_{i2}, v_{i3}, \dots, v_{iD})$ and $x_i = (x_{i1}, x_{i2}, x_{i3}, \dots, x_{iD})$, respectively, while its previous best position is stored in $pbest_i = (pbest_{i1}, pbest_{i2}, pbest_{i3}, \dots, pbest_{iD})$. In each generation, the best position discovered from all $pbest$ positions is known as the global best position, $gbest = (gbest_1, gbest_2, gbest_3 \dots gbest_D)$. The process of PSO is presented below:

Step 1: Initialization

Assign parameters and create populations of size $N = 50$

Set $iter = 0$

Step 2: Reproduction and updating loop

for $i = 1, 2, \dots, N$ do

Update the velocity v_i of particle x_i by using velocity equation

Update the position of particle x_i by using position equation

Evaluate the fitness value of the new particle x_i

if x_i is better than $pbest_i$ then

Set x_i to be $pbest_i$

end (if)

end (for)

Set the particle with the best fitness value to be $gbest$

$iter = iter + 1$

Step 3: If the iteration is greater than the maximum iteration, the process is terminated.

Else, go back to Step 2.

The velocity equation in PSO is

$$v_i^{t+1} = w \cdot v_i^t + c_1 \cdot r_1 \cdot (pbest_i^t - x_i^t) + c_2 \cdot r_2 \cdot (gbest^t - x_i^t) \quad \dots(10)$$

and the position equation is

$$x_i^{t+1} = x_i^t + v_i^{t+1} \quad \dots(11)$$

where c_1 and c_2 are two positive constants that indicate the relative influence of the cognition and social components, respectively; w is inertia weight that provides a balance between local exploitation and global exploration; r_1 and r_2 are random real values in the interval $[0, 1]$. For this application, the values of $c_1 = 2$, $c_2 = 4.05$ and $w = 0.6$. The velocity of the particles on each dimension is clamped to the range $[-V_{max}, V_{max}]$. If the terminate criterion is satisfied, the algorithm produces the best solution ($gbest$). Otherwise, the iteration stage is repeated.

Artificial bee colony optimization (ABC)

In 2005, Karaboga proposed an ABC algorithm which is a swarm intelligence based on the foraging behaviour of honeybee swarms. The colony of artificial bees in the ABC algorithm consists of three groups of bees: employed bees, onlookers and scouts. Employed bees are responsible for searching for a food source and for sharing this information to recruit onlooker bees. Onlooker bees tend to choose better food sources than the employed bees, and search for food further around the nominated food source (Muske & Rawlings, 1993). If a food source is not improved by a predetermined number of trials (denoted by the limit), this employed bee will become a scout bee to search randomly for new food sources.

The main steps of ABC algorithm are given below:

Step 1: Initialization

Allot parameters and populations of size $N_p = 50$, $S_N = N_p/2$.

Set trial = 0 for each population

Step 2: The employed bee phase for $i = 1, 2, \dots, S_N$ do

Update a new candidate solution v_i by using update equation for the employed bees. Evaluate the fitness value of the candidate solution v_i .

Apply a greedy selection process between v_i and x_i to select the better one.

If solution x_i does not improve, $trial_i = trial_i + 1$, otherwise $trial_i = 0$.

end (for)

Step 3: Calculate the probability P_i by using the probability equation for the solutions x_i using fitness values

Step 4: The onlooker bee phase for $i = 1, 2, \dots, S_N$

do if $rand(0, 1) \leq P_i$ then

Update a new candidate solution v_i by using update equation for the onlooker bees.

Evaluate the fitness value of the candidate solution v_i .

Apply a greedy selection process between v_i and x_i to select the better one.

If solution x_i does not improve, $trial_i = trial_i + 1$, otherwise $trial_i = 0$.

end (if)

end (for)

Step 5: The scouts bee phase

if $\max(trial_i) > limit$ then

Replace x_i with a new randomly produced candidate solution by using the replacing equation

end (if)

Step 6: If the iteration is greater than maximum iteration, stop and output the best solution achieved so far.

Otherwise, return to **Step 2**.

A new food source v_i can be produced from the old food source using the update equation (12),

$$v_i^{t+1} = x_i^t + r \cdot (x_i^t - x_k^t) \quad \dots(12)$$

where $k \in \{1, 2, \dots, S_N\}$ is randomly chosen indexes and must be altered from i

The new random food source position (scout bee) will be calculated from the following replacing equation (13),

$$x_{t+1} = x_{max} + rand \cdot (x_{max} - x_{min}) \quad \dots(13)$$

where x_{min} and x_{max} are the lower and upper bound of the food source position, respectively. The candidate solution is compared with the old one. If the new food source has a better quality compared to the old source, then the new one replaces the latter. Otherwise, the old source is retained.

Design of model predictive controller (MPC)

Model Predictive Control is an optimization-based controller in which constraints to input and output signals can be given. For the design of MPC, it uses a dynamic process model, a cost function (J) over the horizon, and optimization of the cost function using the control input (u). The cost function of the process is,

$$J = \sum_{j=N_1}^{N_2} w_e [\hat{y}(t+j) - w(t+j)]^2 + \sum_{j=N_1}^{N_2} w_u [\Delta u(t+j-1)]^2 \quad \dots(14)$$

where N_1 = Minimum costing prediction horizon
 N_2 = maximum costing prediction
 N_u = length of control horizon
 \hat{y} = predicted output
 w = reference trajectory
 u = manipulated input
 w_e = weight to the error of prediction
 w_u = weight to the change in control action

In MPC, future control input and future process output are predicted using the process model, and the cost function of the system has been optimized over the prediction horizon while emulating the constraints provided. At the current time step, MPC applies only the first step of the optimal solution as a control signal; then, the prediction horizon shifts forward one step at a time, and the same method continues. Based on the control horizon given, the numbers of control action values are considered as free variables to be optimized. The basic structure of MPC is integrated in Figure 3.

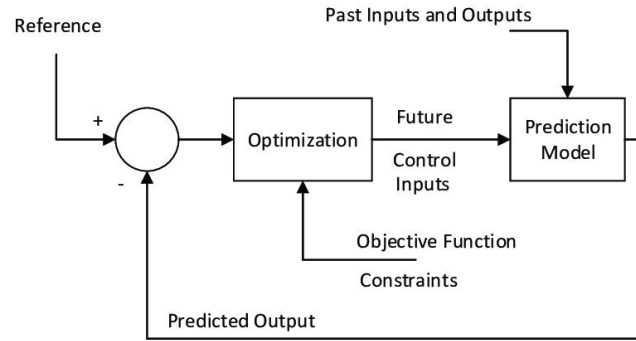


Figure 3: Structure of MPC

The performance of the controller is measured in terms of:

1. Overshoot: It is a measure of how much the response exceeds the ultimate value following a step change.
Overshoot = $A/B = \exp(-\pi\varepsilon/\sqrt{1-\varepsilon^2})$
2. Rise time (T_r) is the time required for the response to rise from 10% to 90% of its final value.
3. Settling time (T_s) is the time required for the response curve to reach and stay within a range about the final value of size specified by the absolute percentage of the final value (given as 2%).
4. Mean square error, $MSE = 1/T \int_{t=0}^T e^2 dt$
5. Integral of the square of the error (ISE), $ISE = \int_{t=0}^T e^2 dt$
6. Integral of the absolute value of error (IAE), $IAE = \int_{t=0}^T |e| dt$
7. Integral of time-weighted absolute error (ITAE), $ITAE = \int_{t=0}^T |e| t dt$

RESULTS AND DISCUSSION

A non-isothermal CSTR experimental setup was designed and studied by conducting a neutralization reaction, which is exothermic, with strong acid and strong base. The data acquired were plotted in Figure 4, which shows that the temperature of the reactor fluid depends on the flow rate and temperature of the coolant. For implementing temperature control in the CSTR, an experimental model is required. The transfer function model is obtained using system identification methods in the MATLAB environment. The transfer function model obtained using experimental data is given by equation 16, and the estimated transfer function, along with the measured data, is represented in Figure 5. In this section, the response of the experimental models to the other models, such as the MIMO (Thulasi Dharan *et al.*, 2017), State-space (Masilamani *et al.*, 2015), and mathematical models (Swapnadeep & Lillie, 2017) are considered for the sake of comparison.

$$G_p = \frac{(0.02375 s + 4.19 e^{-5})}{(s^2 + 0.002181 s + 1.917 e^{-6})} \quad \dots(15)$$

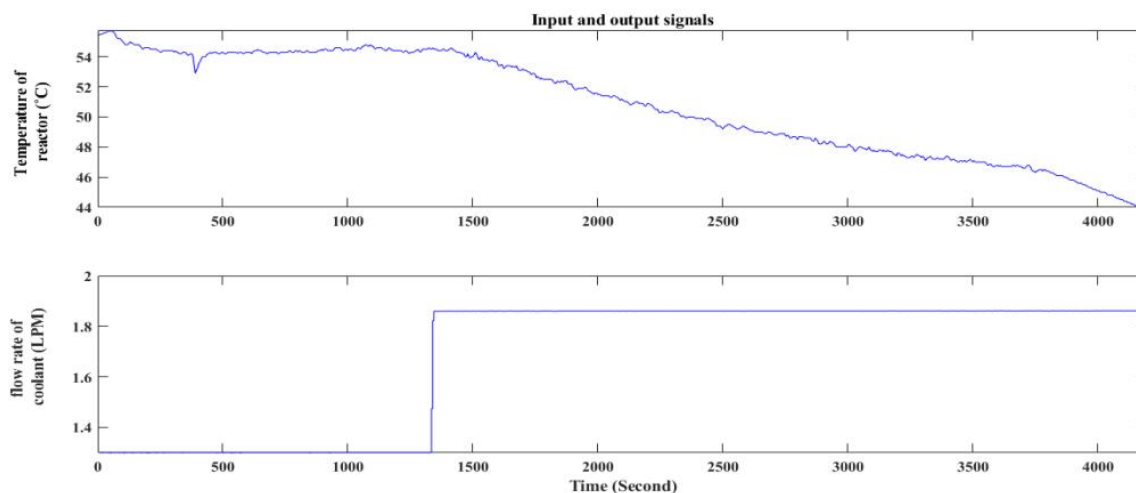


Figure 4: Data acquired by conducting an exothermic reaction

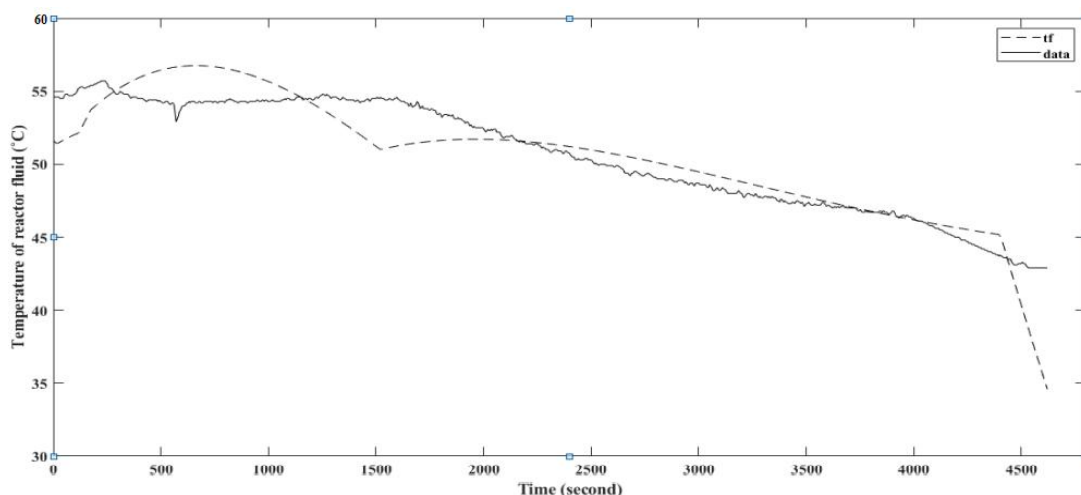


Figure 5: Transfer function model response

In the PID controller for the ZN method, the Bode diagram was plotted as in Figure 6, and the gain margin is 1.459 (Abs), the crossover frequency is 0.0421(rad/s), and the phase margin is 53.8884 (deg). Then the ultimate gain $K_u = 0.685$, and the ultimate period $P_u = 149.2443$ are calculated. Using the ZN controller setting, $K_p = 0.411$, $K_i = 0.0055$, and $K_d = 7.6674$ were found, and the step response of the temperature control system using various models is displayed in Figure 7.

In tuning PID parameters using PSO, the PSO parameters are as follows: iteration (N) = 100, number of particles (i) = 50, problem dimension = 3 (K_p , K_i , K_d), upper and lower boundary to K_p , K_i , and K_d values are $LB = 0.0001, 0.0001, 0.0001$, respectively, $UB = 10, 2, 30$, respectively, constant values are $c_1 = 2$ and $c_2 = 4.05$, and inertia weight, $w = 0.6$. The inertia weight plays an important role in the convergence behaviour of the algorithm, which in turn affects the time domain response of the closed loop system, as seen in Table 3. The objective function for this is given as the summation of ITAE and overshoot,

$$Obj = 20 \times \sum (t. |e|dt) + 80 \times (\max (y) - y_d) \times 100 \quad \dots(16)$$

The PSO takes equation (16) as the objective function and aims to minimize it. The values of K_p , K_i , K_d corresponding to the minimized value of the objective function are the optimized values. These optimized values are used as the controller parameters of the PID controller used in the temperature control system. The particles, in this case is a 50×3 matrix as the number of particles is 50 and the dimension is 3. For each particle in the matrix, the value of the fitness function is calculated using equation (16), and the velocity and position of the particle are also obtained using equations (11) and (12), respectively. The evaluated fitness function values

are stored and compared to the global best fitness function. There is updating of the velocity, position and the local best if the evaluated fitness function is better than the global best.

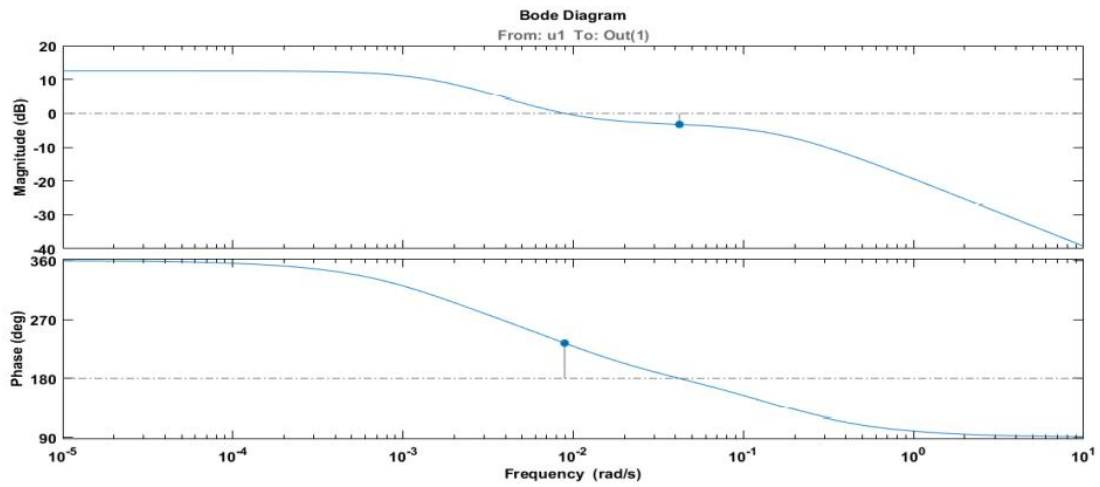


Figure 6: Bode diagram using transfer function model

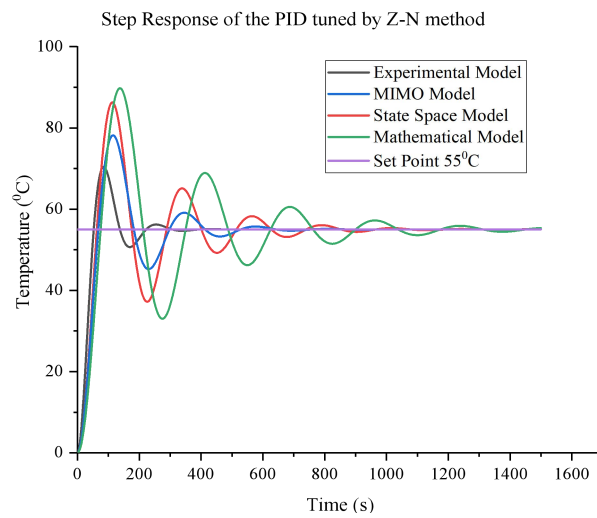


Figure 7: Step response of temperature control system with ZN tuning method

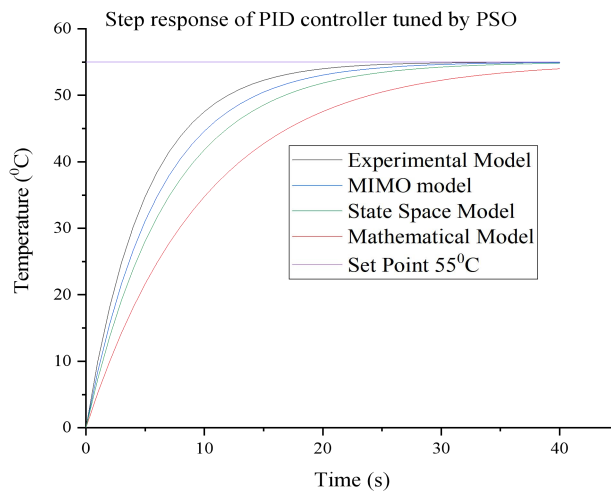


Figure 8: Step response of temperature control system with PSO technique for tuning

The parameters of ABC are assigned as follows: maximum number of iterations = 50, problem dimension (D) = 3 [K_p , K_i , K_d], size of the population (N_p) = 50, the number of food sources (SN) = $N_p/2$, and the boundary condition for K_p , K_i , K_d are as follows: $x_{min} = 0, 0, 0$ and $x_{max} = 10, 2, 30$, respectively. The objective function of this problem is considered as the combination of ITAE and overshoot as in equation (16),

In the system considered, the bees are a 50×3 matrix containing the possible values of K_p , K_i , K_d , aiming to minimize the objective function in equation (16). The food, in this case, is the minimum value of the objective function among the values of the objective functions obtained for each bee. In ABC, the bees are in search of the optimal solution, and the solutions are updated frequently as a result of the neighbourhood search. When the optimal solution is achieved, the objective function is at its minimum. The optimal solution is the tuned values of the K_p , K_i , and K_d ; these values are used in the PID controller applied in the temperature control loop of the CSTR.

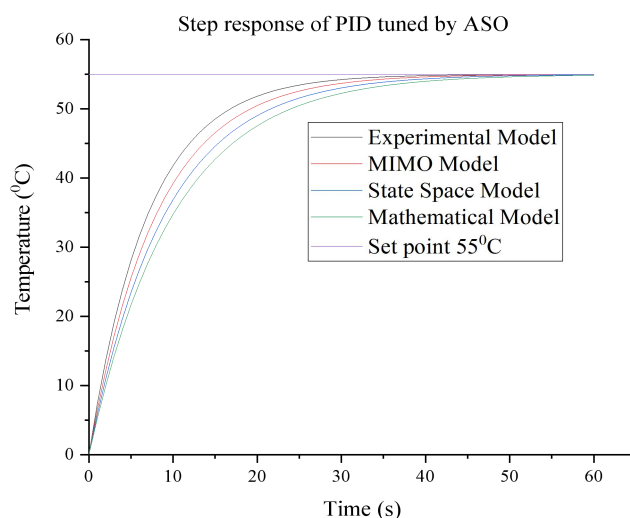


Figure 9: Step response of temperature control system with ABC optimization technique for tuning

In equation 18, e = error, y = output response, and y_d = desired output. By following the appropriate steps mentioned above, tunable PID parameters can be obtained and are categorized in Table 3.

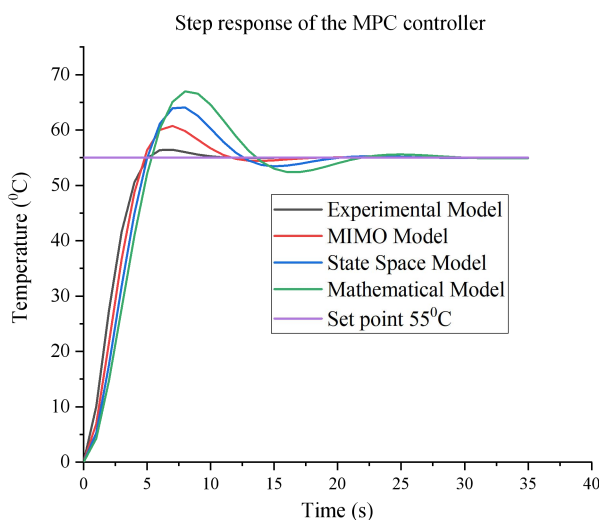


Figure 10: Step response of temperature control system using MPC

The step response of PSO-based PID tuning is depicted in Figure 8, and the step response of ABC-based PID tuning is shown in Figure 9, and from the plots, the time domain specifications are obtained. The model predictive controller was designed with transfer function model, length of prediction horizon (N_p) given as 10, length of control (N_u) given as 2, weight to the error of prediction (w_e) given as 1, and weight to the change in control action (w_u) given as 0.1.

The step response of the temperature control system using MPC is shown in Figure 10. The performance of the controller for various models was accessed and enumerated in Tables 3 and 4.

Table 3: Comparison of tuning methods considering various models

Model of CSTR	Set point (°C)	Tuning algorithm	K_p	K_i	K_d	Overshoot %	T_r (second)	T_s (second)
Experimental	55	Z-N	0.411	0.0055	7.6674	28.4	96.6	734
		PSO	10	0.0076	1.4734	0	9.53	21.2
		ABC	6.567	0.0164	2.5477	0	14.4	23.5
		MPC	4.488	0.0172	1.5678	0	6.48	16.8
MIMO (Thulasi Dharan et al., 2017)	55	Z-N	1.201	0.0155	8.2458	29.25	98.54	746
		PSO	12.35	0.0865	2.3458	0	9.95	23.3
		ABC	6.567	0.0164	2.5477	0	15.6	25.4
		MPC	4.488	0.0172	1.9867	5	7.63	17.2
State-space (Masilamani et al., 2015)	55	Z-N	3.258	0.0824	9.5687	32.64	98.99	1000
		PSO	14.02	0.1065	3.6547	0	15.24	25.1
		ABC	7.368	0.1168	3.0058	0	17.68	27.6
		MPC	5.006	0.1358	2.257	8.26	8.66	19.3
Mathematical (Swapnadeep & Lillie, 2017)	55	Z-N	5.258	0.0992	12.358	35.45	100.3	1500
		PSO	16.38	0.2058	4.6587	0	18.41	27.2
		ABC	8.467	0.2587	4.8794	0	19.64	30.5
		MPC	7.05	0.3687	3.5042	10.35	9.25	22.4

Table 4: Performance of controllers considering various models

Model of CSTR	Set point (°C)	Controller	MSE	ISE	IAE	ITAE
Experimental	55	Z-N	0.411	0.0055	7.6674	28.4
		PSO	10	0.0076	1.4734	0
		ABC	6.567	0.0164	2.5477	0
		MPC	4.488	0.0172	1.5678	0
MIMO (Thulasi Dharan et al., 2017)	55	Z-N	0.995	0.0089	8.3679	30.5
		PSO	12.358	0.0093	2.9658	0
		ABC	8.367	0.0568	3.5687	0
		MPC	5.368	0.0639	2.6879	0
State-space (Masilamani et al., 2015)	55	Z-N	1.384	0.0100	10.3574	32.5
		PSO	13.587	0.0158	3.6789	0
		ABC	9.367	0.0985	5.0010	0
		MPC	6.3487	0.0109	4.0068	0
Mathematical (Swapnadeep & Lillie, 2017)	55	Z-N	2.258	0.0258	11.3681	34.2
		PSO	14.3687	0.0518	4.6897	0
		ABC	10.3658	0.1025	6.9387	0
		MPC	8.3679	0.0912	5.2581	0

Set point tracking

The set point tracking responses of the temperature of the reactor fluid with PID, PID-PSO, PID-ABC and MPC with the positive step change of amplitude 5, given at 800 seconds, are plotted in Figure 11.

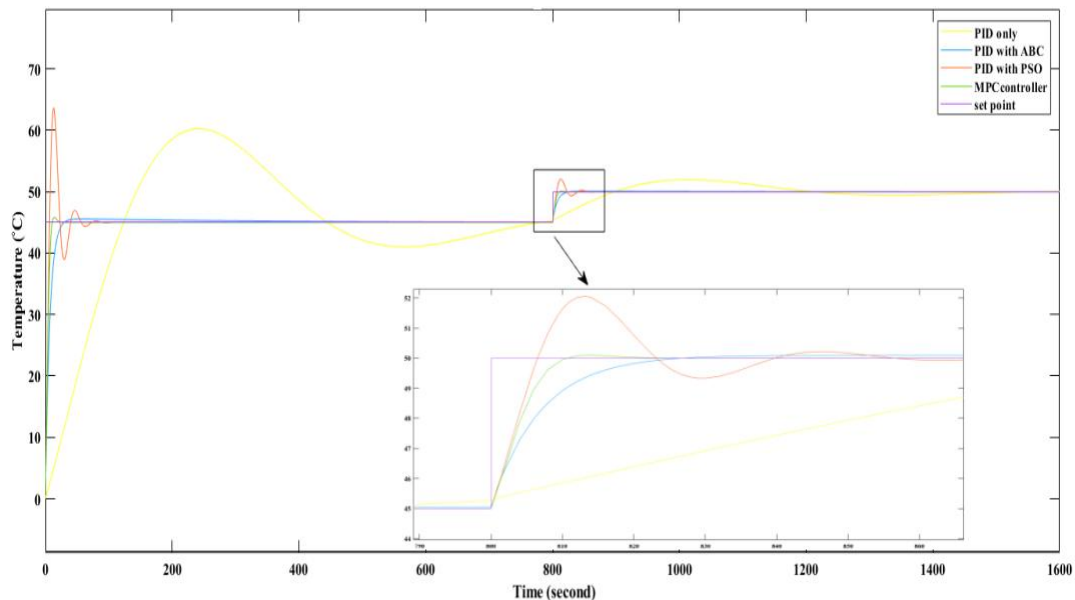


Figure 11: Set point tracking of PID, PID-PSO, PID-ABC and MPC

Disturbance rejection

The disturbance rejection of the response of the temperature of reactor fluid with PID, PID-PSO, PID-ABC and MPC with the negative step change of amplitude 5, given at 800 seconds, are graphed in Figure 12.

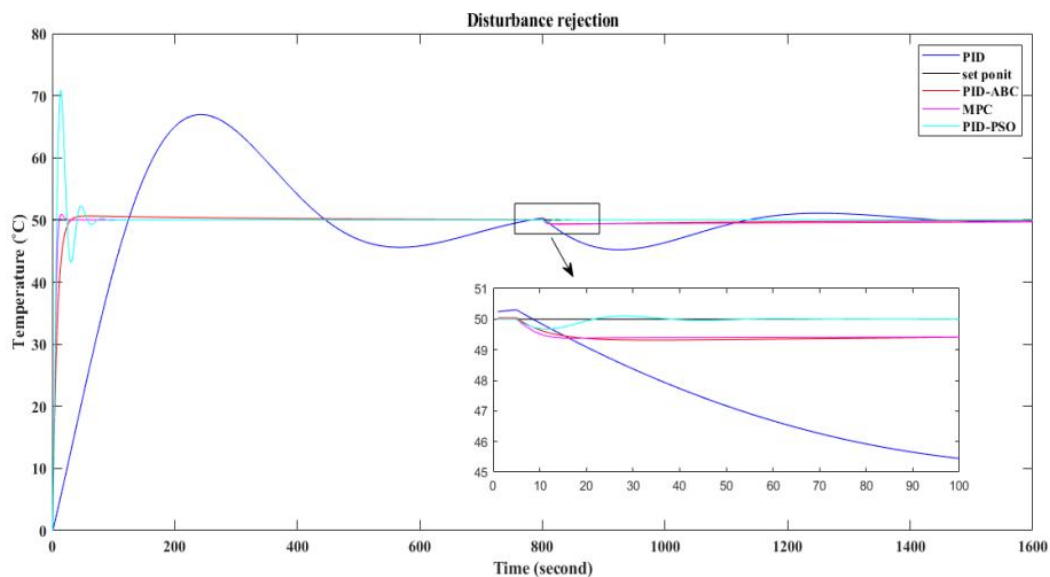


Figure 12: Disturbance rejection of PID, PID-PSO, PID-ABC and MPC

CONCLUSION

The experimental model of the CSTR system was considered to develop the controllers. Various models from the literature were used for the controller design alongside the experimental model for the sake of comparison. The PID, PID-PSO, PID-ABC, and MPC controllers were developed using the various models and compared in terms of MSE, ISE, IAE, ITAE and time domain specifications such as overshoot, rise time, and settling time. The objective function used was the combination of ITAE and overshoot for the optimization algorithms PSO and ABC. From the simulation results, the experimental model performed better than the other models in all the cases of tuning methods. PID-PSO using the experimental model has minimized the overshoot (0%), rise time (9.53 seconds), and settling time (21.2 seconds). However, the MPC is better than the PID controller with evolutionary algorithms. The time domain specifications of MPC are overshoot (0%), rise time (6.48 seconds) and settling time (16.8 seconds). The values of MSE, ISE, IAE, and ITAE are 7.307, 0.7307×10^4 , 219.5 and 712.9 for MPC, respectively. With the set point tracking studies, the MPC controller has better tracking performance, and in disturbance rejection, the PID controller with PSO has improved rejection compared to the MPC controller. For future studies, the evolutionary algorithms can be hybridized by exploiting the best parts of each algorithm to form a more effective algorithm. Models for the CSTR systems can be improved by using non-linear models such as the Hammerstein-Wiener models.

REFERENCES

- Agarwal V., Deo A. & Kumar N. (2015). Temperature control of CSTR using PID controller. *International Journal of Engineering and Computer Science* **5**(04): 11902–11905.
- Ahmed A.O., Gasmelseed G.A., Karama A. & Musa A.E. (2016). Cascade control of a continuous stirred tank reactor (CSTR). *Journal of Applied and Industrial Sciences* **1**(04): 16–23.
- Aslam F. & Kaur G. (2011). Comparative analysis of conventional, P, PI, PID and fuzzy logic controllers for the efficient control of concentration in CSTR. *International Journal of Computer Applications* **6**(17): 12–16.
DOI: <https://doi.org/10.5120/2226-2836>
- Bakošová M., Puna, D. & Mészáros A. (2005). Robust controller design for a chemical reactor. *Computer Aided Chemical Engineering* **20**: 1303–1308.
DOI: [https://doi.org/10.1016/S1570-7946\(05\)80059-8](https://doi.org/10.1016/S1570-7946(05)80059-8)
- Bonyadi M.R. & Michalewicz Z. (2017). Particle swarm optimization for single objective continuous space problems: a review. *Evolutionary Computation* **25**(1): 1–54.
DOI: https://doi.org/10.1162/EVCO_r_00180
- Da H. & Shu-cai H. (2018). Optimal controller design based on minimum principle. *MATEC Web of Conferences* **173**(1): 01001.
DOI: <https://doi.org/10.1051/mateconnf/201817301001>
- Das S., Biswas A., Dasgupta S. & Abraham A. (2009). Bacterial foraging optimization algorithm: theoretical foundations, analysis, and applications. In: *Foundations of Computational Intelligence*, volume 3. Studies in Computational Intelligence, vol 203. Springer, Berlin, Heidelberg, Germany.
DOI: https://doi.org/10.1007/978-3-642-01085-9_2
- Dey B.K. & Roy L. (2014). A comparative study on temperature control of CSTR using PI controller, PID controller and PID (two degree of freedom) controller. *International Journal of Electronics and Computer Science Engineering* **52**(01): 62–68.
- Dong S., Wang Y., Hu W., Zhang G. & Zhan J. (2021). Constant temperature control system of building energy system. *Thermal Science* **25**(4B): 2853–2860.
DOI: <https://doi.org/10.2298/TSCI2104853D>
- Gao D.X. & Liu H. (2015). Optimal dynamic control for CSTR nonlinear system based on feedback linearization. *27th Chinese Control and Decision Conference*, pp.1298–1302.
DOI: <https://doi.org/10.1109/CCDC.2015.7162119>
- Masilamani A., Panda R., Sivamani R. & Dheepak R. (2015). Design of MPC controller for CSTR. *International Journal of Applied Engineering Research* **10**(33): 1303–1308.
- Muske K.R. & Rawlings J.B. (1993). Model predictive control with linear models. *AIChE Journal- Process Systems Engineering* **39**(02): 262–287.
DOI: <https://doi.org/10.1002/aic.690390208>
- Rani V.A., Prabhakaran D. & Thirumarimurugan M. (2020). Modelling and control of pH in a continuous stirred tank Reactor (CSTR). *Journal of Environmental Protection and Ecology* **21**(02): 413–422.
- Saravanakumar G., Valarmathi K., Pallikonda M.R. & Seshadhri S. (2015). Tuning of multivariable decentralized PID controller using state transition algorithm. *Studies in Informatics and Control* **24**(4): 367–378.
DOI: <https://doi.org/10.24846/v24i4y201501>

- Sultaniya S. & Gupta R. (2014). Design of PID controller using PSO algorithm for CSTR. *International Journal of Electronic and Electrical Engineering* **07**(09): 971–977.
- Swapnadeep B. & Lillie D. (2017). A comparative study of PID based temperature control of CSTR using genetic algorithm and particle swarm optimization. In: *International Conference on Emerging Trends in Computing and Communication Technologies*, pp. 1–6.
DOI: <https://doi.org/10.1109/ICETCCT.2017.8280312>
- Thulasi Dharan S., Kavyarasan K. & Bagyaveereswaran V. (2017). Tuning of PID controller using optimization techniques for a MIMO process. IOP Conference Series: *Materials Science and Engineering* **263**(5).
DOI: <https://doi.org/10.1088/1757-899X/263/5/052019>
- Weiguo Z., Liying W. & Zhenxing Z. (2019). Atom search optimization and its application to solve a hydrogeologic parameter estimation problem. *Knowledge-Based Systems* **163**: 283–304.
DOI: <https://doi.org/10.1016/j.knosys.2018.08.030>.
- Zhiyong L., Weiyong W., Yanyan Y. & Zheng L. (2015). A hybrid algorithm based on particle swarm and artificial bee colony for high-dimensional optimization problems. *Expert Systems with Applications* **42**(22): 8881–8895.
DOI: <https://doi.org/10.1016/j.eswa.2015.07.043>

RESEARCH ARTICLE

Ordered Random Variables

On recurrence relations for moments of dual generalized order statistics for a general transmuted power function distributions with characterizations

SH Shahbaz and MQ Shahbaz*

Department of Statistics, King Abdulaziz University, Jeddah, Kingdom of Saudi Arabia.

Submitted: 18 March 2021; Revised: 08 July 2022; Accepted: 22 July 2022

Abstract: Dual generalized order statistics is a unified method for random variables that are arranged in decreasing order. The moments of dual generalized order statistics are helpful to study the properties of any distribution. Often, the moments of dual generalized order statistics are not easy to compute and recursive computation is done. The recurrence relations for moments of generalized and dual generalized order statistics are helpful to compute the higher order moments from the lower order moments. In this paper the methods for recursive computation of moments of dual generalized order statistics for general transmuted power function distributions are presented. The general transmuted power function distributions are first defined and then the recurrence relations are obtained. These recurrence relations include relations for single, inverse, product, and ratio moments. The recurrence relations are used to obtain the relations for moments of special cases, which include lower record values and reversed order statistics. Some characterizations of the general transmuted power function distributions are also presented based on the basis of single and product moments of dual generalized order statistics. These characterizations are unique results for the general transmuted power function distributions. The results given in the paper are useful to obtain the results for special cases of general transmuted power function distribution which includes power function and transmuted power function distributions.


Keywords: Dual generalized order statistics, general transmuted distributions, moments, power function distribution.

INTRODUCTION

The study of ordered random variables has been an area of interest for several authors. The classical method for increasingly arranged random variables is order statistics and has been a very useful method in studies of extreme events. This method has been extensively discussed by various authors; see for example David and Nagaraja (2003) and Arnold *et al.* (2008). Chandler (1952) and Dziubdzziel and Kopociski (1976) have introduced record values as another method for the modelling of extreme records – lower as well as upper records.

Kamps (1995) has introduced generalized order statistics (gos) as a unified model for random variables which are arranged in increasing order. Kamps (1995) has argued that several models for increasingly arranged random variables, including order statistics and upper record values, appear as special cases of the generalized order statistics.

In several situations we need to study the distributional behaviour of random variables which are arranged in decreasing order of importance. Reflected order statistics and lower record values are two classical methods for such random variables. The dual generalized order statistics (dgos), introduced by Burkschat *et al.* (2003), is a unified method for random variables arranged in decreasing order.

* Corresponding author (qshahbaz@gmail.com;  <https://orcid.org/0000-0002-0695-1216>)



Burkschat *et al.* (2003) have shown that the joint distribution of $dgos$ for a sample of size n is

$$f_{1,2,\dots,n;n,m,k}(x_1, \dots, x_n) = k \left(\prod_{j=1}^{n-1} \gamma_j \right) [F(x_n)]^{k-1} f(x_n) \left[\prod_{i=1}^{n-1} \{F(x_i)\}^m f(x_i) \right], x \in \mathfrak{R}, \quad \dots(1)$$

where $k \geq 1$, $m \in \mathbb{R}$, $\gamma_j = k + (n-j)(m+1)$ and $F(x_i)$ is cumulative distribution function of i^{th} random variable. Burkschat *et al.* (2003) have further shown that the marginal distribution of a single $dgos$ and joint distribution of two $dgos$ are given as

$$f_{r;n,m,k}(x) = \frac{C_{r-1}}{(r-1)!} f(x) [F(x)]^{\gamma_{r-1}} g_m^{r-1} [F(x)], x \in \mathfrak{R}, \quad \dots(2)$$

and

$$f_{r,s;n,m,k}(x_1, x_2) = \frac{C_{s-1}}{(r-1)!(s-r-1)!} f(x_1) f(x_2) [F(x_1)]^m g_m^{r-1} [F(x_1)] \\ \times [F(x_2)]^{\gamma_{s-1}} [h_m \{F(x_1)\} - h_m \{F(x_2)\}]^{s-r-1}, x \in \mathfrak{R} \quad \dots(3)$$

where $C_{r-1} = \prod_{j=1}^r \gamma_j$ and

$$h_m(x) = \begin{cases} (m+1)^{-1} (x^{m+1}); & m \neq -1 \\ \ln x; & m = -1. \end{cases}; \quad g_m(x) = \begin{cases} (m+1)^{-1} (1-x^{m+1}); & m \neq -1 \\ -\ln x; & m = -1. \end{cases}$$

Different models of decreasingly arranged random variables appear as special cases of $dgos$. For example, the reflected order statistics appears as a special case of $dgos$ for $m = 0$ and $k = 1$. The lower record values appear as special case of $dgos$ for $m = -1$. For further discussion about $dgos$ see, for example, Ahsanullah and Nevzorov (2001) and Shahbaz *et al.* (2016)

Most of the work in the field of $dgos$ is based upon obtaining recurrence relations for moments of $dgos$, when the sample is available from some probability distribution, and proposing some characterizations of the distributions using moments of $dgos$. Athar and Faizan (2011) have obtained the relations for moments of lower record values for power function distribution and have also obtained some characterizations. The recurrence relations for moments of $dgos$ for a general class of inverted distributions have been obtained by Kotb *et al.* (2013). Ahsanullah *et al.* (2013) have given some characterizations for the power function distribution using moments of lower record values.

The recurrence relations for moments of gos and $dgos$ for transmuted distributions have not been explored. Al-Sobhi *et al.* (2021) have obtained the recurrence relations for moments of gos for a transmuted exponential distribution. In this paper we have obtained the recurrence relations for moments of $dgos$ for a general transmuted power function distribution. We will first introduce the general transmuted power function distribution.

MATERIALS AND METHODS

In this section the general transmuted power function distributions have been introduced.

General transmuted power function distributions

The transmuted family of distributions has been introduced by Shaw and Buckley (2007) as a method of obtaining new probability distributions from the available ones. This family has been explored by several authors. Recently, Rehman *et al.* (2018; 2018b) have extended the transmuted family of distributions to the general case and have proposed two methods to extend them. The distribution functions of the general transmuted family of distributions, proposed by Rehman *et al.* (2018a; 2018b), are

$$F_1(x) = G(x) + \sum_{h=1}^t \lambda_h G^h(x) [1 - G(x)], x \in \mathfrak{R} \quad \dots(4)$$

and

$$F_2(x) = G(x) + \sum_{h=1}^t \lambda_h G(x) [1 - G(x)]^h, x \in \mathfrak{R}, \quad \dots(5)$$

where $G(x)$ is cumulative distribution function (*cdf*) of the baseline distribution. The density functions corresponding to (4) and (5) are, respectively,

$$f_1(x) = g(x) \left[1 - \sum_{h=1}^t (h+1) \lambda_h G^h(x) + \sum_{h=1}^t h \lambda_h G^{h-1}(x) \right], x \in \mathfrak{R} \quad \dots(6)$$

and

$$f_2(x) = g(x) \left[1 + \sum_{h=1}^t \lambda_h \{1 - G(x)\}^h - \sum_{h=1}^t h \lambda_h G(x) \{1 - G(x)\}^{h-1} \right], x \in \mathfrak{R}, \quad \dots(7)$$

where $g(x)$ is the density function corresponding to $G(x)$. Also, the λ 's are the transmutation parameters. These parameters require certain conditions that are given below.

For (4) and (6): $-1 \leq \lambda_h \leq 1 \ \& \ -t \leq \sum_{h=1}^t \lambda_h \leq 1$

For (5) and (7): $-1 \leq \lambda_h \leq 1 \ \& \ -1 \leq \sum_{h=1}^t \lambda_h \leq t$.

The transmuted family of distributions, proposed by Shaw and Buckley (2007), appears as a special case of the general transmuted family of distributions for $t = 1$. The general transmuted family of distributions can be used to generate transmuted distributions for different $G(x)$. In the following we have proposed two general transmuted power function distributions by using the following density and distribution functions of power function distribution, with parameters $(\alpha, c) > 0$,

$$g(x) = \frac{\alpha x^{\alpha-1}}{c^\alpha}, 0 < x < c, (\alpha, c) > 0 ; G(x) = \frac{x^\alpha}{c^\alpha}, 0 < x < c, (\alpha, c) > 0. \quad \dots(8)$$

in (4) and (5). These distributions are defined in the following subsections.

The general transmuted power function distribution-I

The general transmuted power function distribution-I (GTPF-I) is obtained by using (8) in (4) and (6). The distribution and density function of the GTPF-I are

$$F_1(x) = \frac{x^\alpha}{c^\alpha} + \sum_{h=1}^t \lambda_h \frac{x^{\alpha h}}{c^{\alpha h}} \left(1 - \frac{x^\alpha}{c^\alpha} \right) = \frac{x^\alpha}{c^\alpha} \left[1 + \sum_{h=1}^t \lambda_h \frac{x^{\alpha(h-1)}}{c^{\alpha(h-1)}} - \sum_{h=1}^t \lambda_h \frac{x^{\alpha h}}{c^{\alpha h}} \right], 0 < x < c \quad \dots(9)$$

and

$$f_1(x) = \frac{\alpha x^{\alpha-1}}{c^\alpha} \left[1 + \sum_{h=1}^t h \lambda_h \frac{x^{\alpha(h-1)}}{c^{\alpha(h-1)}} - \sum_{h=1}^t (h+1) \lambda_h \frac{x^{\alpha h}}{c^{\alpha h}} \right], 0 < x < c. \quad \dots(10)$$

It is to be noted that the transmuted power function distribution, proposed by Haq *et al.* (2016), appears as a special case of GTPF-I for $t = 1$. The density and distribution functions of GTPF-I are related as

$$F_1(x) = \frac{x}{\alpha} f_1(x) - \sum_{h=1}^t (h-1) \lambda_h \frac{x^{\alpha h}}{c^{\alpha h}} + \sum_{h=1}^t h \lambda_h \frac{x^{\alpha(h+1)}}{c^{\alpha(h+1)}}, 0 < x < c. \quad \dots(11)$$

This relation is useful in obtaining recurrence relations for moments of $dgos$ for $GTPF-I$ which we will give in the coming sections.

The general transmuted power function distribution-II

The general transmuted power function distribution-II ($GTPF-II$) is obtained by using (8) in (5) and (7). The distribution and density function of the $GTPF-II$ are

$$F_2(x) = \frac{x^\alpha}{c^\alpha} + \sum_{h=1}^t \lambda_h \frac{x^\alpha}{c^\alpha} \left(1 - \frac{x^\alpha}{c^\alpha}\right)^h, \quad 0 < x < c \quad \dots(12)$$

and

$$f_2(x) = \frac{\alpha x^{\alpha-1}}{c^\alpha} \left[1 + \sum_{h=1}^t \lambda_h \left(1 - \frac{x^\alpha}{c^\alpha}\right)^h - \sum_{h=1}^t h \lambda_h \frac{x^\alpha}{c^\alpha} \left(1 - \frac{x^\alpha}{c^\alpha}\right)^{h-1} \right], \quad 0 < x < c. \quad \dots(13)$$

The distribution and density functions, given in (12) and (13) are related as

$$F_2(x) = \frac{x}{\alpha} f_2(x) + \sum_{h=1}^t h \lambda_h \sum_{j=0}^{h-1} (-1)^j \binom{h-1}{j} \frac{x^{\alpha(j+2)}}{c^{\alpha(j+2)}}, \quad 0 < x < c. \quad \dots(14)$$

The relation (14) is useful in obtaining recurrence relations for moments of $dgos$ for $GRPF-II$ which will be obtained in the coming sections.

RESULTS AND DISCUSSION

In this section the main results of the paper are discussed.

Recurrence relations for single and inverse moments

In this section we will obtain the recurrence relations for single and inverse moments of $dgos$ for the general transmuted power function distributions, introduced in the previous section. For this we will consider following relation between moments of $dgos$, see for example Kotb *et al.* (2003) and Shahbaz *et al.* (2016).

$$\mu_{r:n,m,k}^p - \mu_{r-1:n,m,k}^p = -\frac{p C_{r-1}}{\gamma_r (r-1)!} \int_{-\infty}^{\infty} x^{p-1} [F(x)]^{\gamma_r} g_m^{r-1} [F(x)] dx, \quad \dots(15)$$

where $\mu_{r:n,m,k}^p = E(X_{r:n,m,k}^p)$ and $X_{r:n,m,k}$ is the r^{th} $dgos$.

The recurrence relations for general transmuted power function distributions are obtained in the following subsections.

General transmuted power function distribution-I

In this section we will obtain the recurrence relations for single and inverse moments of $dgos$ for $GTPF-I$. The recurrence relation for single moments of $dgos$ from $GTPF-I$ is given in the following Theorem.

Theorem 1: The single moments of general transmuted power function distribution-I are related as

$$\begin{aligned} \mu_{r:n,m,k}^p &= \left(\frac{\alpha \gamma_r}{\alpha \gamma_r + p} \right) \left[\mu_{r-1:n,m,k}^p + \sum_{h=1}^t \frac{\lambda_h p \gamma_r C_{r-1}}{c^{\alpha(h+1)} \gamma_r C_{r-1(k-1)}} \left\{ \frac{h}{p + \alpha(h+1)} \right. \right. \\ &\quad \left. \left. \times \left[\mu_{r:n,m,k-1}^{p+\alpha(h+1)} - \mu_{r-1:n,m,k-1}^{p+\alpha(h+1)} \right] - \frac{c^\alpha (h-1)}{p + \alpha h} \left[\mu_{r:n,m,k-1}^{p+\alpha h} - \mu_{r-1:n,m,k-1}^{p+\alpha h} \right] \right\} \right], \quad \dots(16) \end{aligned}$$

where $\gamma_{r(k-1)} = (k-1) + (n-r)(m+1)$ and $C_{r-1(k-1)} = \prod_{j=1}^r \gamma_{j(k-1)}$.

Proof: Using (11) in (15) we have

$$\begin{aligned} \mu_{r:n,m,k}^p - \mu_{r-1:n,m,k}^p &= -\frac{pC_{r-1}}{\gamma_r(r-1)!} \int_0^c x^{p-1} \left\{ \frac{x}{\alpha} f_1(x) - \sum_{h=1}^t (h-1) \lambda_h \frac{x^{\alpha h}}{c^{\alpha h}} + \sum_{h=1}^t h \lambda_h \frac{x^{\alpha(h+1)}}{c^{\alpha(h+1)}} \right\} \\ &\quad \times [F(x)]^{\gamma_{r-1}} g_m^{r-1} [F(x)] dx \\ &= -\frac{p}{\alpha \gamma_r} \mu_{r:n,m,k}^p + \sum_{h=1}^t (h-1) \lambda_h \frac{pC_{r-1}}{\gamma_r c^{\alpha h} (r-1)!} \int_0^c x^{p+\alpha h-1} [F(x)]^{\gamma_{r-1}} g_m^{r-1} [F(x)] dx \\ &\quad - \sum_{h=1}^t h \lambda_h \frac{pC_{r-1}}{\gamma_r c^{\alpha(h+1)} (r-1)!} \int_0^c x^{p+\alpha(h+1)-1} [F(x)]^{\gamma_{r-1}} g_m^{r-1} [F(x)] dx \\ &= -\frac{p}{\alpha \gamma_r} \mu_{r:n,m,k}^p - \sum_{h=1}^t (h-1) \frac{\lambda_h p \gamma_{r(k-1)} C_{r-1}}{\gamma_r c^{\alpha h} (p+\alpha h) C_{r-1(k-1)}} \left\{ \mu_{r:n,m,k-1}^{p+\alpha h} - \mu_{r-1:n,m,k-1}^{p+\alpha h} \right\} \\ &\quad + \sum_{h=1}^t h \frac{\lambda_h p \gamma_{r(k-1)} C_{r-1}}{\gamma_r c^{\alpha(h+1)} \{p+\alpha(h+1)\} C_{r-1(k-1)}} \left\{ \mu_{r:n,m,k-1}^{p+\alpha(h+1)} - \mu_{r-1:n,m,k-1}^{p+\alpha(h+1)} \right\}. \end{aligned}$$

Rearranging, we have (16) and hence the theorem.

It is to be noted that the recurrence relation (16) reduces to the recurrence relations for moments of *dgos* for power function distribution for $\lambda_h = 0; h = 1, 2, \dots, t$ as obtained by Athar and Faizan (2011). The following corollaries immediately follow from Theorem 1.

Corollary 1: Using “ $-p$ ” in place of p the following relation for inverse moments of *dgos* for *GTPF-I* is obtained

$$\begin{aligned} \mu_{r:n,m,k}^{-p} &= \left(\frac{\alpha \gamma_r}{\alpha \gamma_r - p} \right) \left[\mu_{r-1:n,m,k}^{-p} - \sum_{h=1}^t \frac{\lambda_h p \gamma_{r(k-1)} C_{r-1}}{c^{\alpha(h+1)} \gamma_r C_{r-1(k-1)}} \left\{ \frac{h}{\alpha(h+1) - p} \right. \right. \\ &\quad \left. \left. \times \left[\mu_{r:n,m,k-1}^{\alpha(h+1)-p} - \mu_{r-1:n,m,k-1}^{\alpha(h+1)-p} \right] - \frac{c^\alpha (h-1)}{\alpha h - p} \left[\mu_{r:n,m,k-1}^{\alpha h - p} - \mu_{r-1:n,m,k-1}^{\alpha h - p} \right] \right\} \right]. \end{aligned} \quad \dots (17)$$

Corollary 2: Using $m = -1$ in (16) and (17) the following relations for single and inverse moments of lower record values for *GTPF-I* are obtained

$$\begin{aligned} \mu_{K(r)}^p &= \left(\frac{\alpha k}{\alpha k + p} \right) \left[\mu_{K(r-1)}^p + \sum_{h=1}^t \frac{\lambda_h p}{c^{\alpha(h+1)}} \left(\frac{k}{k-1} \right)^{r-1} \left\{ \frac{h}{p + \alpha(h+1)} \right. \right. \\ &\quad \left. \left. \times \left[\mu_{K-1(r)}^{p+\alpha(h+1)} - \mu_{K-1(r-1)}^{p+\alpha(h+1)} \right] - \frac{c^\alpha (h-1)}{p + \alpha h} \left[\mu_{K-1(r)}^{p+\alpha h} - \mu_{K-1(r-1)}^{p+\alpha h} \right] \right\} \right]. \end{aligned} \quad \dots (18)$$

$$\begin{aligned} \mu_{K(r)}^{-p} &= \left(\frac{\alpha k}{\alpha k - p} \right) \left[\mu_{K(r-1)}^{-p} - \sum_{h=1}^t \frac{\lambda_h p}{c^{\alpha(h+1)}} \left(\frac{k}{k-1} \right)^{r-1} \left\{ \frac{h}{\alpha(h+1) - p} \right. \right. \\ &\quad \left. \left. \times \left[\mu_{K-1(r)}^{\alpha(h+1)-p} - \mu_{K-1(r-1)}^{\alpha(h+1)-p} \right] - \frac{c^\alpha (h-1)}{\alpha h - p} \left[\mu_{K-1(r)}^{\alpha h - p} - \mu_{K-1(r-1)}^{\alpha h - p} \right] \right\} \right]. \end{aligned} \quad \dots (19)$$

Corollary 3: Using $m = 0$ and $k = 1$ in (16) and (17) the following relations for single and inverse moments of reversed order statistics for GTPF-I are obtained.

$$\mu_{r:n}^p = \left[\frac{\alpha(n-r+1)}{\alpha(n-r+1)+p} \right] \left[\mu_{r-1:n}^p + \sum_{h=1}^t \frac{\lambda_h p}{c^{\alpha(h+1)}} \frac{n}{n-r+1} \left\{ \frac{h}{p+\alpha(h+1)} \right. \right. \\ \left. \left. \times \left[\mu_{r:n}^{p+\alpha(h+1)} - \mu_{r-1:n}^{p+\alpha(h+1)} \right] - \frac{c^\alpha(h-1)}{p+\alpha h} \left[\mu_{r:n}^{p+\alpha h} - \mu_{r-1:n}^{p+\alpha h} \right] \right\} \right]. \quad \dots(20)$$

$$\mu_{r:n}^{-p} = \left[\frac{\alpha(n-r+1)}{\alpha(n-r+1)-p} \right] \left[\mu_{r-1:n}^{-p} - \sum_{h=1}^t \frac{\lambda_h p}{c^{\alpha(h+1)}} \frac{n}{n-r+1} \left\{ \frac{h}{\alpha(h+1)-p} \right. \right. \\ \left. \left. \times \left[\mu_{r:n}^{\alpha(h+1)-p} - \mu_{r-1:n}^{\alpha(h+1)-p} \right] - \frac{c^\alpha(h-1)}{\alpha h - p} \left[\mu_{r:n}^{\alpha h - p} - \mu_{r-1:n}^{\alpha h - p} \right] \right\} \right]. \quad \dots(21)$$

General transmuted power function distribution-II

In the following we will obtain the recurrence relations for single and inverse moments of $dgos$ for $GTPF-II$. The recurrence relation for single moments of $dgos$ from $GTPF-II$ is given in the following Theorem.

Theorem 2: The single moments of general transmuted power function distribution-II are related as

$$\mu_{r:n,m,k}^p = \left(\frac{\alpha \gamma_r}{\alpha \gamma_r + p} \right) \left[\mu_{r-1:n,m,k}^p + \sum_{h=1}^t h \lambda_h \sum_{j=0}^{h-1} \frac{(-1)^j}{c^{\alpha(j+2)}} \binom{h-1}{j} \right. \\ \left. \times \frac{p \gamma_{r(k-1)} C_{r-1}}{\{p+\alpha(j+2)\} \gamma_r C_{r-1(k-1)}} \left\{ \mu_{r:n,m,k-1}^{p+\alpha(j+2)} - \mu_{r-1:n,m,k-1}^{p+\alpha(j+2)} \right\} \right]. \quad \dots(22)$$

Proof: The recurrence relation for single moments of $dgos$ for $GTPF-II$ is obtained by using (14) in (15) as

$$\mu_{r:n,m,k}^p - \mu_{r-1:n,m,k}^p = -\frac{p C_{r-1}}{\gamma_r (r-1)!} \int_0^c x^{p-1} \left\{ \frac{x}{\alpha} f_2(x) + \sum_{h=1}^t h \lambda_h \sum_{j=0}^{h-1} \frac{(-1)^j}{c^{\alpha(j+2)}} \binom{h-1}{j} \frac{x^{\alpha(j+2)}}{c^{\alpha(j+2)}} \right\} \\ \times [F(x)]^{\gamma_r-1} g_m^{r-1} [F(x)] dx \\ = -\frac{p C_{r-1}}{\alpha \gamma_r (r-1)!} \int_0^c x^p f_2(x) [F(x)]^{\gamma_r-1} g_m^{r-1} [F(x)] dx - \frac{p C_{r-1}}{\gamma_r (r-1)!} \\ \times \sum_{h=1}^t h \lambda_h \sum_{j=0}^{h-1} \frac{(-1)^j}{c^{\alpha(j+2)}} \binom{h-1}{j} \int_0^c x^{p+\alpha(j+2)-1} [F(x)]^{\gamma_r-1} g_m^{r-1} [F(x)] dx \\ = -\frac{p}{\alpha \gamma_r} \mu_{r:n,m,k}^p + \sum_{h=1}^t h \lambda_h \sum_{j=0}^{h-1} \frac{(-1)^j}{c^{\alpha(j+2)}} \binom{h-1}{j} \frac{p \gamma_{r(k-1)} C_{r-1}}{\{p+\alpha(j+2)\} \gamma_r C_{r-1(k-1)}} \\ \times \left[\mu_{r:n,m,k-1}^{p+\alpha(j+2)} - \mu_{r-1:n,m,k-1}^{p+\alpha(j+2)} \right].$$

Rearranging the above we have (22) and hence the Theorem.

The relation (22) reduces to the recurrence relations for single moments of $dgos$ for power function distribution for $\lambda_h = 0$; $h = 1, 2, \dots, t$. The following are some corollaries which immediately follow from Theorem 2.

Corollary 4: Using “ $-p$ ” in place of p the following relation for inverse moments of $dgos$ for $GTPF-II$ is obtained

$$\begin{aligned} \mu_{r:n,m,k}^{-p} &= \left(\frac{\alpha \gamma_r}{\alpha \gamma_r - p} \right) \left[\mu_{r-1:n,m,k}^{-p} - \sum_{h=1}^t h \lambda_h \sum_{j=0}^{h-1} \frac{(-1)^j}{c^{\alpha(j+2)}} \binom{h-1}{j} \right. \\ &\quad \left. \times \frac{p \gamma_{r(k-1)} C_{r-1}}{\{\alpha(j+2) - p\} \gamma_r C_{r-1(k-1)}} \left\{ \mu_{r,n,m,k-1}^{\alpha(j+2)-p} - \mu_{r-1,n,m,k-1}^{\alpha(j+2)-p} \right\} \right]. \end{aligned} \quad \dots(23)$$

Corollary 5: Using $m = -1$ in (22) and (23) the following relations for single and inverse moments of lower record values for $GTPF-II$ are obtained

$$\begin{aligned} \mu_{K(r)}^p &= \left(\frac{\alpha k}{\alpha k + p} \right) \left[\mu_{K(r-1)}^p + \sum_{h=1}^t h \lambda_h \sum_{j=0}^{h-1} \frac{(-1)^j p}{c^{\alpha(j+2)} \{p + \alpha(j+2)\}} \binom{h-1}{j} \right. \\ &\quad \left. \times \left(\frac{k}{k-1} \right)^{r-1} \left\{ \mu_{K-1(r)}^{p+\alpha(j+2)} - \mu_{K-1(r-1)}^{p+\alpha(j+2)} \right\} \right]. \end{aligned} \quad \dots(24)$$

$$\begin{aligned} \mu_{K(r)}^{-p} &= \left(\frac{\alpha k}{\alpha k - p} \right) \left[\mu_{K(r-1)}^{-p} - \sum_{h=1}^t h \lambda_h \sum_{j=0}^{h-1} \frac{(-1)^j p}{c^{\alpha(j+2)} \{\alpha(j+2) - p\}} \binom{h-1}{j} \right. \\ &\quad \left. \times \left(\frac{k}{k-1} \right)^{r-1} \left\{ \mu_{K-1(r)}^{\alpha(j+2)-p} - \mu_{K-1(r-1)}^{\alpha(j+2)-p} \right\} \right]. \end{aligned} \quad \dots(25)$$

Corollary 6: Using $m = 0$ and $k = 1$ in (22) and (23) the following relations for single and inverse moments of reversed order statistics for $GTPF-I$ are obtained

$$\begin{aligned} \mu_{r:n}^p &= \left[\frac{\alpha(n-r+1)}{\alpha(n-r+1) + p} \right] \left[\mu_{r-1:n}^p + \sum_{h=1}^t h \lambda_h \sum_{j=0}^{h-1} \frac{(-1)^j}{c^{\alpha(j+2)}} \binom{h-1}{j} \right. \\ &\quad \left. \times \frac{p}{\{p + \alpha(j+2)\}} \frac{n}{n-r+1} \left\{ \mu_{r,n}^{p+\alpha(j+2)} - \mu_{r-1,n}^{p+\alpha(j+2)} \right\} \right]. \end{aligned} \quad \dots(26)$$

$$\begin{aligned} \mu_{r:n}^{-p} &= \left[\frac{\alpha(n-r+1)}{\alpha(n-r+1) - p} \right] \left[\mu_{r-1:n}^{-p} - \sum_{h=1}^t h \lambda_h \sum_{j=0}^{h-1} \frac{(-1)^j}{c^{\alpha(j+2)}} \binom{h-1}{j} \right. \\ &\quad \left. \times \frac{p}{\{\alpha(j+2) - p\}} \frac{n}{n-r+1} \left\{ \mu_{r,n}^{\alpha(j+2)-p} - \mu_{r-1,n}^{\alpha(j+2)-p} \right\} \right]. \end{aligned} \quad \dots(27)$$

We will now obtain the recurrence relations for product and ratio moments of $dgos$ for general transmuted power function distributions in the following section.

Recurrence relations for product and ratio moments

In this section the recurrence relations for product and ratio moments of $dgos$ for the general transmuted power function distributions will be given. These relations are obtained by considering the following relation between product moments of $dgos$, see for example Kotb *et al.* (2003) and Shahbaz *et al.* (2016).

$$\begin{aligned} \mu_{r,s;n,m,k}^{p,q} - \mu_{r,s-1;n,m,k}^{p,q} &= - \frac{q C_{s-1}}{\gamma_s (r-1)! (s-r-1)!} \int_{-\infty}^{\infty} \int_{-\infty}^{x_1} x_1^p x_2^{q-1} f(x_1) [F(x_1)]^m \\ &\quad \times g_m^{r-1} [F(x_1)] [h_m(x_1) - h_m(x_2)]^{s-r-1} [F(x_2)]^{\gamma_s} dx_2 dx_1, \end{aligned} \quad \dots(28)$$

where $\mu_{r,s;n,m,k}^{p,q} = E(X_{r,n,m,k}^p X_{s,n,m,k}^q)$. The recurrence relations for general transmuted power function distributions are obtained in the following subsections.

General transmuted power function distribution-I

In the following we will obtain the recurrence relations for product and ratio moments of *dgos* for *GTPF-I*. The recurrence relation for product moments of *dgos* from *GTPF-I* is given in the following Theorem.

Theorem 3: The product moments of general transmuted power function distribution-I are related as

$$\mu_{r,s;n,m,k}^{p,q} = \left(\frac{\alpha\gamma_s}{\alpha\gamma_s + q}\right) \left[\mu_{r,s-1;n,m,k}^{p,q} + \sum_{h=1}^t \frac{\lambda_h q \gamma_{s(k-1)} C_{s-1}}{c^{\alpha(h+1)} \gamma_s C_{s-1(k-1)}} \left\{ \frac{h}{q + \alpha(h+1)} \right. \right. \\ \left. \left. \times \left[\mu_{r,s;n,m,k-1}^{p,q+\alpha(h+1)} - \mu_{r,s-1;n,m,k-1}^{p,q+\alpha(h+1)} \right] - \frac{c^\alpha (h-1)}{q + \alpha h} \left[\mu_{r,s;n,m,k-1}^{p,q+\alpha h} - \mu_{r,s-1;n,m,k-1}^{p,q+\alpha h} \right] \right\} \right] \dots(29)$$

Proof: Using (11) in (28) we have

$$\mu_{r,s;n,m,k}^{p,q} - \mu_{r,s-1;n,m,k}^{p,q} = -\frac{q C_{s-1}}{\gamma_s (r-1)! (s-r-1)!} \int_0^c \int_0^{x_1} x_1^p x_2^{q-1} f(x_1) [F(x_1)]^m g_m^{r-1} [F(x_1)] \\ \times [h_m(x_1) - h_m(x_2)]^{s-r-1} [F(x_2)]^{\gamma_s-1} \\ \times \left\{ \frac{x}{\alpha} f_1(x_2) - \sum_{h=1}^t (h-1) \lambda_h \frac{x_2^{\alpha h}}{c^{\alpha h}} + \sum_{h=1}^t h \lambda_h \frac{x_2^{\alpha(h+1)}}{c^{\alpha(h+1)}} \right\} dx_2 dx_1$$

or

$$\mu_{r,s;n,m,k}^{p,q} - \mu_{r,s-1;n,m,k}^{p,q} = -\frac{q}{\alpha\gamma_s} \mu_{r,s;n,m,k}^{p,q} + \sum_{h=1}^t \frac{(h-1)\lambda_h q C_{s-1}}{\gamma_s c^{\alpha h} (r-1)! (s-r-1)!} \int_0^c \int_0^{x_1} x_1^p x_2^{q+\alpha h-1} f(x_1) \\ \times [F(x_1)]^m g_m^{r-1} [F(x_1)] [h_m(x_1) - h_m(x_2)]^{s-r-1} [F(x_2)]^{\gamma_s-1} dx_2 dx_1 \\ - \sum_{h=1}^t \frac{h\lambda_h q C_{s-1}}{\gamma_s c^{\alpha h} (r-1)! (s-r-1)!} \int_0^c \int_0^{x_1} x_1^p x_2^{q+\alpha(h+1)-1} f(x_1) [F(x_1)]^m \\ \times g_m^{r-1} [F(x_1)] [h_m(x_1) - h_m(x_2)]^{s-r-1} [F(x_2)]^{\gamma_s-1} dx_2 dx_1$$

or

$$\mu_{r,s;n,m,k}^{p,q} - \mu_{r,s-1;n,m,k}^{p,q} = -\frac{q}{\alpha\gamma_s} \mu_{r,s;n,m,k}^{p,q} - \sum_{h=1}^t \frac{(h-1)\lambda_h q \gamma_{s(k-1)} C_{s-1}}{\gamma_s c^{\alpha h} (q + \alpha h) C_{s-1(k-1)}} \left\{ \mu_{r,s;n,m,k-1}^{p,q+\alpha h} - \mu_{r,s-1;n,m,k-1}^{p,q+\alpha h} \right\} \\ + \sum_{h=1}^t \frac{h\lambda_h q \gamma_{s(k-1)} C_{s-1}}{\gamma_s c^{\alpha(h+1)} \{q + \alpha(h+1)\} C_{s-1(k-1)}} \left\{ \mu_{r,s;n,m,k-1}^{p,q+\alpha(h+1)} - \mu_{r,s-1;n,m,k-1}^{p,q+\alpha(h+1)} \right\}$$

Re-arranging the above equation we have (29) and hence the Theorem.

It is to be noted that the recurrence relations for product moments for *GTPF-I*, given in (29), reduces to the recurrence relations for product moments of *dgos* for power function distribution, given by Athar and Faizan (2011), for $\lambda_h = 0; h = 1, 2, \dots, t$.

Some useful corollaries which are immediate from the above Theorem are given below.

Corollary 7: Using “ $-q$ ” in place of q in (28) the following relation for ratio moments of $dgos$ for $GTPF-I$ is obtained

$$\begin{aligned} \mu_{r,s;n,m,k}^{p,-q} &= \left(\frac{\alpha\gamma_s}{\alpha\gamma_s - q} \right) \left[\mu_{r,s-1;n,m,k}^{p,-q} - \sum_{h=1}^t \frac{\lambda_h q \gamma_{s(k-1)} C_{s-1}}{c^{\alpha(h+1)} \gamma_s C_{s-1(k-1)}} \left\{ \frac{h}{\alpha(h+1) - q} \right. \right. \\ &\quad \left. \left. \times \left[\mu_{r,s;n,m,k-1}^{p,\alpha(h+1)-q} - \mu_{r,s-1;n,m,k-1}^{p,\alpha(h+1)-q} \right] - \frac{c^\alpha (h-1)}{\alpha h - q} \left[\mu_{r,s;n,m,k-1}^{p,\alpha h - q} - \mu_{r,s-1;n,m,k-1}^{p,\alpha h - q} \right] \right\} \right]. \end{aligned} \quad \dots(30)$$

Corollary 8: Using $m = -1$ in (29) and (30) the following relations for product and ratio moments of lower record values for $GTPF-I$ are obtained

$$\begin{aligned} \mu_{K(r,s)}^{p,q} &= \left(\frac{\alpha k}{\alpha k + q} \right) \left[\mu_{K(r,s-1)}^{p,q} + \sum_{h=1}^t \frac{\lambda_h q}{c^{\alpha(h+1)}} \left(\frac{k}{k-1} \right)^{s-1} \left\{ \frac{h}{q + \alpha(h+1)} \right. \right. \\ &\quad \left. \left. \times \left[\mu_{K-1(r,s)}^{p,q+\alpha(h+1)} - \mu_{K-1(r,s-1)}^{p,q+\alpha(h+1)} \right] - \frac{c^\alpha (h-1)}{q + \alpha h} \left[\mu_{K-1(r,s)}^{p,q+\alpha h} - \mu_{K-1(r,s-1)}^{p,q+\alpha h} \right] \right\} \right]. \end{aligned} \quad \dots(31)$$

$$\begin{aligned} \mu_{K(r,s)}^{p,-q} &= \left(\frac{\alpha k}{\alpha k + q} \right) \left[\mu_{K(r,s-1)}^{p,-q} - \sum_{h=1}^t \frac{\lambda_h q}{c^{\alpha(h+1)}} \left(\frac{k}{k-1} \right)^{s-1} \left\{ \frac{h}{\alpha(h+1) - q} \right. \right. \\ &\quad \left. \left. \times \left[\mu_{K-1(r,s)}^{p,\alpha(h+1)-q} - \mu_{K-1(r,s-1)}^{p,\alpha(h+1)-q} \right] - \frac{c^\alpha (h-1)}{\alpha h - q} \left[\mu_{K-1(r,s)}^{p,\alpha h - q} - \mu_{K-1(r,s-1)}^{p,\alpha h - q} \right] \right\} \right]. \end{aligned} \quad \dots(32)$$

Corollary 9: Using $m = 0$ and $k = 1$ in (29) and (30) the following relations for product and ratio moments of reversed order statistics for $GTPF-I$ are obtained

$$\begin{aligned} \mu_{r,s;n}^{p,q} &= \left[\frac{\alpha(n-s+1)}{\alpha(n-s+1) + q} \right] \left[\mu_{r,s-1;n}^{p,q} + \sum_{h=1}^t \frac{\lambda_h q}{c^{\alpha(h+1)}} \frac{n}{n-s+1} \left\{ \frac{h}{q + \alpha(h+1)} \right. \right. \\ &\quad \left. \left. \times \left[\mu_{r,s;n}^{p,q+\alpha(h+1)} - \mu_{r,s-1;n}^{p,q+\alpha(h+1)} \right] - \frac{c^\alpha (h-1)}{q + \alpha h} \left[\mu_{r,s;n}^{p,q+\alpha h} - \mu_{r,s-1;n}^{p,q+\alpha h} \right] \right\} \right]. \end{aligned} \quad \dots(33)$$

$$\begin{aligned} \mu_{r,s;n}^{p,-q} &= \left[\frac{\alpha(n-s+1)}{\alpha(n-s+1) - q} \right] \left[\mu_{r,s-1;n}^{p,-q} - \sum_{h=1}^t \frac{\lambda_h q}{c^{\alpha(h+1)}} \frac{n}{n-s+1} \left\{ \frac{h}{\alpha(h+1) - q} \right. \right. \\ &\quad \left. \left. \times \left[\mu_{r,s;n}^{p,\alpha(h+1)-q} - \mu_{r,s-1;n}^{p,\alpha(h+1)-q} \right] - \frac{c^\alpha (h-1)}{\alpha h - q} \left[\mu_{r,s;n}^{p,\alpha h - q} - \mu_{r,s-1;n}^{p,\alpha h - q} \right] \right\} \right]. \end{aligned} \quad \dots(34)$$

We will now give recurrence relations for product and ratio moments of $dgos$ for $GTPF-II$ in the following.

General transmuted power function distribution-II

In the following Theorem the recurrence relations for product and ratio moments of $dgos$ for $GTPF-II$ are given.

Theorem 4: The product moments of general transmuted power function distribution-II are related as

$$\begin{aligned} \mu_{r,s;n,m,k}^{p,q} &= \left(\frac{\alpha\gamma_s}{\alpha\gamma_s + q} \right) \left[\mu_{r,s-1;n,m,k}^{p,q} + \sum_{h=1}^t h \lambda_h \sum_{j=0}^{h-1} (-1)^j \binom{h-1}{j} \right. \\ &\quad \left. \times \frac{q \gamma_{s(k-1)} C_{s-1}}{\gamma_s c^{\alpha(j+2)} \{q + \alpha(j+2)\} C_{s-1(k-1)}} \left\{ \mu_{r,s;n,m,k-1}^{p,q+\alpha(j+2)} - \mu_{r,s-1;n,m,k-1}^{p,q+\alpha(j+2)} \right\} \right]. \end{aligned} \quad \dots(35)$$

Proof: Using (14) in (28) we have

$$\begin{aligned} \mu_{r,s;n,m,k}^{p,q} - \mu_{r,s-1;n,m,k}^{p,q} &= -\frac{qC_{s-1}}{\gamma_s(r-1)!(s-r-1)!} \int_0^c \int_0^{x_1} x_1^p x_2^{q-1} f(x_1) [F(x_1)]^m g_m^{r-1} [F(x_1)] \\ &\quad \times [h_m(x_1) - h_m(x_2)]^{s-r-1} [F(x_2)]^{\gamma_s-1} \\ &\quad \times \left\{ \frac{x}{\alpha} f_2(x_2) + \sum_{h=1}^t h\lambda_h \sum_{j=0}^{h-1} (-1)^j \binom{h-1}{j} \frac{x_2^{\alpha(j+2)}}{c^{\alpha(j+2)}} \right\} dx_2 dx_1 \\ &= -\frac{q}{\alpha\gamma_s} \mu_{r,s;n,m,k}^{p,q} + \sum_{h=1}^t h\lambda_h \sum_{j=0}^{h-1} (-1)^j \binom{h-1}{j} \frac{qC_{s-1}}{\gamma_s c^{\alpha(j+2)} (r-1)!(s-r-1)!} \\ &\quad \times \int_0^c \int_0^{x_1} x_1^p x_2^{q+\alpha(j+2)-1} f(x_1) [F(x_1)]^m g_m^{r-1} [F(x_1)] \\ &\quad \times [h_m(x_1) - h_m(x_2)]^{s-r-1} [F(x_2)]^{\gamma_s-1} dx_2 dx_1 \end{aligned}$$

or

$$\begin{aligned} \mu_{r,s;n,m,k}^{p,q} - \mu_{r,s-1;n,m,k}^{p,q} &= -\frac{q}{\alpha\gamma_s} \mu_{r,s;n,m,k}^{p,q} + \sum_{h=1}^t h\lambda_h \sum_{j=0}^{h-1} (-1)^j \binom{h-1}{j} \\ &\quad \times \frac{q\gamma_{s(k-1)} C_{s-1}}{\gamma_s c^{\alpha(j+2)} \{q + \alpha(j+2)\} C_{s-1(k-1)}} \left\{ \mu_{r,s;n,m,k-1}^{p,q+\alpha(j+2)} - \mu_{r,s-1;n,m,k-1}^{p,q+\alpha(j+2)} \right\}. \end{aligned}$$

Re-arranging, we have (35) and hence the theorem.

The relation (35) again reduces to the recurrence relation for product moments of *dgos* for power function distribution, given by Athar and Faizan (2011), for $\lambda_h = 0; h = 1, 2, \dots, t$. The corollaries which follow from Theorem 4 are given below.

Corollary 10: Using “ $-q$ ” in place of q in (35) the following relation for ratio moments of *dgos* for *GTPF-II* is obtained

$$\begin{aligned} \mu_{r,s;n,m,k}^{p,-q} &= \left(\frac{\alpha\gamma_s}{\alpha\gamma_s - q} \right) \left[\mu_{r,s-1;n,m,k}^{p,-q} - \sum_{h=1}^t h\lambda_h \sum_{j=0}^{h-1} (-1)^j \binom{h-1}{j} \right. \\ &\quad \left. \times \frac{q\gamma_{s(k-1)} C_{s-1}}{\gamma_s c^{\alpha(j+2)} \{q + \alpha(j+2)\} C_{s-1(k-1)}} \left\{ \mu_{r,s;n,m,k-1}^{p,\alpha(j+2)-q} - \mu_{r,s-1;n,m,k-1}^{p,\alpha(j+2)-q} \right\} \right]. \end{aligned} \quad (36)$$

Corollary 11: Using $m = -1$ in (35) and (36) the following relations for product and ratio moments of lower record values for *GTPF-II* are obtained

$$\begin{aligned} \mu_{K(r,s)}^{p,q} &= \left(\frac{\alpha k}{\alpha k + q} \right) \left[\mu_{K(r,s-1)}^{p,q} + \sum_{h=1}^t h\lambda_h \sum_{j=0}^{h-1} (-1)^j \binom{h-1}{j} \right. \\ &\quad \left. \times \frac{q}{c^{\alpha(j+2)} \{q + \alpha(j+2)\}} \left(\frac{k}{k-1} \right)^{s-1} \left\{ \mu_{K-1(r,s)}^{p,q+\alpha(j+2)} - \mu_{K-1(r,s-1)}^{p,q+\alpha(j+2)} \right\} \right]. \end{aligned} \quad \dots(37)$$

$$\begin{aligned} \mu_{K(r,s)}^{p,-q} &= \left(\frac{\alpha k}{\alpha k - q} \right) \left[\mu_{K(r,s-1)}^{p,-q} - \sum_{h=1}^t h\lambda_h \sum_{j=0}^{h-1} (-1)^j \binom{h-1}{j} \right. \\ &\quad \left. \times \frac{q}{c^{\alpha(j+2)} \{q + \alpha(j+2)\}} \left(\frac{k}{k-1} \right)^{s-1} \left\{ \mu_{K-1(r,s)}^{p,\alpha(j+2)-q} - \mu_{K-1(r,s-1)}^{p,\alpha(j+2)-q} \right\} \right]. \end{aligned} \quad \dots(38)$$

Corollary 12: Using $m = 0$ and $k = 1$ in (35) and (36) the following relations for product and ratio moments of reversed order statistics for *GTPF-II* are obtained

$$\begin{aligned} \mu_{r,s:n}^{p,q} &= \left[\frac{\alpha(n-s+1)}{\alpha(n-s+1)+q} \right] \left[\mu_{r,s-1:n}^{p,q} + \sum_{h=1}^t h \lambda_h \sum_{j=0}^{h-1} (-1)^j \binom{h-1}{j} \right. \\ &\quad \left. \times \frac{q}{c^{\alpha(j+2)} \{q + \alpha(j+2)\}} \frac{n}{n-s+1} \left\{ \mu_{r,s:n}^{p,q+\alpha(j+2)} - \mu_{r,s-1:n}^{p,q+\alpha(j+2)} \right\} \right]. \end{aligned} \tag{39}$$

$$\begin{aligned} \mu_{r,s:n}^{p,-q} &= \left[\frac{\alpha(n-s+1)}{\alpha(n-s+1)-q} \right] \left[\mu_{r,s-1:n}^{p,-q} - \sum_{h=1}^t h \lambda_h \sum_{j=0}^{h-1} (-1)^j \binom{h-1}{j} \right. \\ &\quad \left. \times \frac{q}{c^{\alpha(j+2)} \{\alpha(j+2) - q\}} \frac{n}{n-s+1} \left\{ \mu_{r,s:n}^{p,\alpha(j+2)-q} - \mu_{r,s-1:n}^{p,\alpha(j+2)-q} \right\} \right]. \end{aligned} \tag{40}$$

We will now give some characterizations of general transmuted power function distributions based upon single and product moment of *dgos*.

Characterizations

In this section some characterization results will be presented for general transmuted power function distributions. These characterization results are based upon single and product moments of *dgos*.

General transmuted power function-I

The characterization results for *GTPF-I* are given in the following. These characterizations are given in the following Theorems.

Theorem 5: A necessary and sufficient condition for a random variable X to have density and distribution functions (9) and (10), respectively, is that the moments of its *dgos* are related as

$$\begin{aligned} \mu_{r:n,m,k}^p &= \left(\frac{\alpha \gamma_r}{\alpha \gamma_r + p} \right) \left[\mu_{r-1:n,m,k}^p + \sum_{h=1}^t \frac{\lambda_h p \gamma_{r(k-1)} C_{r-1}}{c^{\alpha(h+1)} \gamma_r C_{r-1(k-1)}} \left\{ \frac{h}{p + \alpha(h+1)} \right. \right. \\ &\quad \left. \left. \times \left[\mu_{r:n,m,k-1}^{p+\alpha(h+1)} - \mu_{r-1:n,m,k-1}^{p+\alpha(h+1)} \right] - \frac{c^\alpha (h-1)}{p + \alpha h} \left[\mu_{r:n,m,k-1}^{p+\alpha h} - \mu_{r-1:n,m,k-1}^{p+\alpha h} \right] \right\} \right]. \end{aligned}$$

Proof: The necessary condition immediately follows from Theorem 1. For a sufficient condition consider (15) as

$$\mu_{r:n,m,k}^p - \mu_{r-1:n,m,k}^p = - \frac{p C_{r-1}}{\gamma_r (r-1)!} \int_{-\infty}^{\infty} x^{p-1} [F(x)]^{\gamma_r} g_m^{r-1} [F(x)] dx.$$

Using the above equation with (11) we have

$$\begin{aligned} - \frac{p C_{r-1}}{\gamma_r (r-1)!} \int_{-\infty}^{\infty} x^{p-1} [F(x)]^{\gamma_r} g_m^{r-1} [F(x)] dx &= - \frac{p C_{r-1}}{\gamma_r (r-1)!} \int_{-\infty}^{\infty} x^{p-1} \\ &\quad \times \left\{ \frac{x}{\alpha} f_1(x) - \sum_{h=1}^t (h-1) \lambda_h \frac{x^{\alpha h}}{c^{\alpha h}} + \sum_{h=1}^t h \lambda_h \frac{x^{\alpha(h+1)}}{c^{\alpha(h+1)}} \right\} [F(x)]^{\gamma_r-1} g_m^{r-1} [F(x)] dx \end{aligned}$$

or

$$-\frac{pC_{r-1}}{\gamma_r(r-1)!} \int_{-\infty}^{\infty} x^{p-1} [F(x)]^{\gamma_r-1} g_m^{r-1} [F(x)] \\ \times \left[F(x) - \left\{ \frac{x}{\alpha} f(x) - \sum_{h=1}^t (h-1) \lambda_h \frac{x^{\alpha h}}{c^{\alpha h}} + \sum_{h=1}^t h \lambda_h \frac{x^{\alpha(h+1)}}{c^{\alpha(h+1)}} \right\} \right] = 0.$$

Applying the Müntz–Szász theorem—see Hwang and Lin (1984)—to the above equation we have

$$F(x) = \frac{x}{\alpha} f(x) - \sum_{h=1}^t (h-1) \lambda_h \frac{x^{\alpha h}}{c^{\alpha h}} + \sum_{h=1}^t h \lambda_h \frac{x^{\alpha(h+1)}}{c^{\alpha(h+1)}}$$

and this relation holds between the density and distribution function of *GTPF-I* distribution and hence the theorem.

Theorem 6: A necessary and sufficient condition for a random variable X to have density and distribution functions (9) and (10), respectively, is that the joint moments of its *dgos* are related as

$$\mu_{r,s;n,m,k}^{p,q} = \left(\frac{\alpha \gamma_s}{\alpha \gamma_s + q} \right) \left[\mu_{r,s-1;n,m,k}^{p,q} + \sum_{h=1}^t \frac{\lambda_h q \gamma_{s(k-1)} C_{s-1}}{c^{\alpha(h+1)} \gamma_s C_{s-1(k-1)}} \left\{ \frac{h}{q + \alpha(h+1)} \right. \right. \\ \left. \left. \times \left[\mu_{r,s;n,m,k-1}^{p,q+\alpha(h+1)} - \mu_{r,s-1;n,m,k-1}^{p,q+\alpha(h+1)} \right] - \frac{c^\alpha (h-1)}{q + \alpha h} \left[\mu_{r,s;n,m,k-1}^{p,q+\alpha h} - \mu_{r,s-1;n,m,k-1}^{p,q+\alpha h} \right] \right\} \right].$$

Proof: The necessary condition immediately follows from Theorem 3. For a sufficient condition consider (28) as

$$\mu_{r,s;n,m,k}^{p,q} - \mu_{r,s-1;n,m,k}^{p,q} = -\frac{qC_{s-1}}{\gamma_s(r-1)!(s-r-1)!} \int_{-\infty}^{\infty} \int_{-\infty}^{x_1} x_1^p x_2^q f(x) [F(x)]^m \\ \times g_m^{r-1} [F(x_1)] [h_m(x_1) - h_m(x_2)]^{s-r-1} [F(x_2)]^s dx_2 dx_1$$

Using the above with (11) we have

$$-\frac{qC_{s-1}}{\gamma_s(r-1)!(s-r-1)!} \int_0^{\infty} \int_0^{x_1} x_1^p x_2^{q-1} f(x_1) [F(x_1)] g_m^{r-1} [F(x_1)]^m \\ \times [h_m(x_1) - h_m(x_2)]^{s-r-1} [F(x_2)]^s dx_2 dx_1 = -\frac{qC_{s-1}}{\gamma_s(r-1)!(s-r-1)!} \\ \times \int_0^{\infty} \int_0^{x_1} x_1^p x_2^{q-1} f(x_1) [F(x_1)] g_m^{r-1} [F(x_1)]^m [h_m(x_1) - h_m(x_2)]^{s-r-1} \\ \times [F(x_2)]^{\gamma_s-1} \left\{ \frac{x}{\alpha} f(x_2) - \sum_{h=1}^t (h-1) \lambda_h \frac{x_2^{\alpha h}}{c^{\alpha h}} + \sum_{h=1}^t h \lambda_h \frac{x_2^{\alpha(h+1)}}{c^{\alpha(h+1)}} \right\} dx_2 dx_1$$

or

$$-\frac{qC_{s-1}}{\gamma_s(r-1)!(s-r-1)!} \int_0^{\infty} \int_0^{x_1} x_1^p x_2^{q-1} f(x_1) [F(x_1)] g_m^{r-1} [F(x_1)]^m [h_m(x_1) - h_m(x_2)]^{s-r-1} \\ \times [F(x_2)]^{\gamma_s-1} \left[F(x) - \left\{ \frac{x}{\alpha} f(x_2) - \sum_{h=1}^t (h-1) \lambda_h \frac{x_2^{\alpha h}}{c^{\alpha h}} + \sum_{h=1}^t h \lambda_h \frac{x_2^{\alpha(h+1)}}{c^{\alpha(h+1)}} \right\} \right] dx_2 dx_1 = 0.$$

Applying the Müntz–Szász theorem—see Hwang and Lin (1984)—to the above equation we have

$$F(x_2) = \frac{x_2}{\alpha} f(x_2) - \sum_{h=1}^t (h-1) \lambda_h \frac{x_2^{\alpha h}}{c^{\alpha h}} + \sum_{h=1}^t h \lambda_h \frac{x_2^{\alpha(h+1)}}{c^{\alpha(h+1)}}$$

and this relation holds between density and distribution function of *GTPF-I* distribution and hence the theorem.

General transmuted power function-II

The characterization results for *GTPF-II* are given in following Theorems

Theorem 7: A necessary and sufficient condition for a random variable X to have density and distribution functions (12) and (13), respectively, is that the moments of its *dgos* are related as

$$\mu_{r:n,m,k}^p = \left(\frac{\alpha\gamma_r}{\alpha\gamma_r + p} \right) \left[\mu_{r-1:n,m,k}^p + \sum_{h=1}^t h\lambda_h \sum_{j=0}^{h-1} \frac{(-1)^j}{c^{\alpha(j+2)}} \binom{h-1}{j} \right. \\ \left. \times \frac{p\gamma_{r(k-1)}C_{r-1}}{\{p + \alpha(j+2)\}\gamma_r C_{r-1(k-1)}} \left\{ \mu_{r:n,m,k-1}^{p+\alpha(j+2)} - \mu_{r-1:n,m,k-1}^{p+\alpha(j+2)} \right\} \right]$$

Proof: The necessary condition immediately follow from Theorem 2. For a sufficient condition consider (15) as

$$\mu_{r:n,m,k}^p - \mu_{r-1:n,m,k}^p = - \frac{pC_{r-1}}{\gamma_r(r-1)!} \int_{-\infty}^{\infty} x^{p-1} [F(x)]^{\gamma_r} g_m^{r-1} [F(x)] dx.$$

Using the above equation with (14) we have

$$- \frac{pC_{r-1}}{\gamma_r(r-1)!} \int_{-\infty}^{\infty} x^{p-1} [F(x)]^{\gamma_r} g_m^{r-1} [F(x)] dx = - \frac{pC_{r-1}}{\gamma_r(r-1)!} \int_{-\infty}^{\infty} x^{p-1} [F(x)]^{\gamma_r-1} \\ \times \left\{ \frac{x}{\alpha} f_2(x) + \sum_{h=1}^t h\lambda_h \sum_{j=0}^{h-1} (-1)^j \binom{h-1}{j} \frac{x^{\alpha(j+2)}}{c^{\alpha(j+2)}} \right\} g_m^{r-1} [F(x)] dx$$

or

$$- \frac{pC_{r-1}}{\gamma_r(r-1)!} \int_{-\infty}^{\infty} x^{p-1} [F(x)]^{\gamma_r-1} g_m^{r-1} [F(x)] \\ \times \left[F(x) - \left\{ \frac{x}{\alpha} f(x) + \sum_{h=1}^t h\lambda_h \sum_{j=0}^{h-1} (-1)^j \binom{h-1}{j} \frac{x^{\alpha(j+2)}}{c^{\alpha(j+2)}} \right\} \right] dx = 0.$$

Applying the Müntz–Szász theorem—see Hwang and Lin (1984)—to the above equation we have

$$F(x) = \frac{x}{\alpha} f(x) + \sum_{h=1}^t h\lambda_h \sum_{j=0}^{h-1} (-1)^j \binom{h-1}{j} \frac{x^{\alpha(j+2)}}{c^{\alpha(j+2)}}$$

and this relation holds between density and distribution function of *GTPF-II* distribution and hence the theorem.

Theorem 8: A necessary and sufficient condition for a random variable X to have density and distribution functions (12) and (13), respectively, is that the joint moments of its *dgos* are related as

$$\mu_{r:s:n,m,k}^{p,q} = \left(\frac{\alpha\gamma_s}{\alpha\gamma_s + q} \right) \left[\mu_{r,s-1:n,m,k}^{p,q} + \sum_{h=1}^t h\lambda_h \sum_{j=0}^{h-1} (-1)^j \binom{h-1}{j} \right. \\ \left. \times \frac{q\gamma_{s(k-1)}C_{s-1}}{\gamma_s c^{\alpha(j+2)} \{q + \alpha(j+2)\} C_{s-1(k-1)}} \left\{ \mu_{r,s:n,m,k-1}^{p,q+\alpha(j+2)} - \mu_{r,s-1:n,m,k-1}^{p,q+\alpha(j+2)} \right\} \right].$$

Proof: The necessary condition immediately follow from Theorem 3. For a sufficient condition consider (28) as

$$\mu_{r,s:n,m,k}^{p,q} - \mu_{r,s-1:n,m,k}^{p,q} = - \frac{qC_{s-1}}{\gamma_s(r-1)!(s-r-1)!} \int_{-\infty}^{\infty} \int_{-\infty}^{x_1} x_1^p x_2^{q-1} f(x_1) [F(x_1)]^m \\ \times g_m^{r-1} [F(x_1)] [h_m(x_1) - h_m(x_2)]^{s-r-1} [F(x_2)]^{\gamma_s} dx_2 dx_1.$$

Using the above with (14) we have

$$\begin{aligned} & -\frac{qC_{s-1}}{\gamma_s(r-1)!(s-r-1)!} \int_{-\infty}^{\infty} \int_{-\infty}^{x_1} x_1^p x_2^{q-1} f(x_1) [F(x_1)]^m g_m^{r-1} [F(x_1)] \\ & \quad \times [h_m(x_1) - h_m(x_2)]^{s-r-1} [F(x_2)]^{\gamma_s} dx_2 dx_1 = -\frac{qC_{s-1}}{\gamma_s(r-1)!(s-r-1)!} \\ & \quad \times \int_{-\infty}^{\infty} \int_{-\infty}^{x_1} x_1^p x_2^{q-1} f(x_1) [F(x_1)]^m g_m^{r-1} [F(x_1)] [h_m(x_1) - h_m(x_2)]^{s-r-1} \\ & \quad \times [F(x_2)]^{\gamma_s-1} \left\{ \frac{x_2}{\alpha} f(x_2) + \sum_{h=1}^t h \lambda_h \sum_{j=0}^{h-1} (-1)^j \binom{h-1}{j} \frac{x_2^{\alpha(j+2)}}{c^{\alpha(j+2)}} \right\} dx_2 dx_1 \end{aligned}$$

or

$$\begin{aligned} & -\frac{qC_{s-1}}{\gamma_s(r-1)!(s-r-1)!} \int_{-\infty}^{\infty} \int_{-\infty}^{x_1} x_1^p x_2^{q-1} f(x_1) [F(x_1)]^m g_m^{r-1} [F(x_1)] [h_m(x_1) - h_m(x_2)]^{s-r-1} \\ & \quad \times [F(x_2)]^{\gamma_s-1} \left[F(x_2) - \left\{ \frac{x_2}{\alpha} f(x_2) + \sum_{h=1}^t h \lambda_h \sum_{j=0}^{h-1} (-1)^j \binom{h-1}{j} \frac{x_2^{\alpha(j+2)}}{c^{\alpha(j+2)}} \right\} \right] dx_2 dx_1. \end{aligned}$$

Applying the Müntz–Szász theorem—see Hwang and Lin (1984)—to above equation we have

$$F(x_2) = \frac{x_2}{\alpha} f(x_2) + \sum_{h=1}^t h \lambda_h \sum_{j=0}^{h-1} (-1)^j \binom{h-1}{j} \frac{x_2^{\alpha(j+2)}}{c^{\alpha(j+2)}}$$

and this relation holds between density and distribution function of *GTPF-II* distribution and hence the theorem.

CONCLUSION

In this paper some recurrence relations for single, inverse, product and ratio moments of *dgos* for the general transmuted power function distribution are obtained. These relations are helpful for computing higher order moments from the lower order moments. These relations also enable us to compute moments of special cases of *dgos* from the general transmuted power function distribution. These relations are also helpful to compute moments of *dgos* and its special cases for any order transmuted distribution for power function baseline distribution.

REFERENCES

- Ahsanullah M. & Nevzorov V.B. (2001). *Ordered Random Variables*. Nova Science Publishers, USA.
- Ahsanullah M., Shakil M. & Kibria B.M.G. (2013). A characterization of power function distribution based on lower record values. *ProbStat Forum* **6**(08): 68–72.
- Al-Sobhi M., Hanif Shahbaz S. & Sherwani R.A.K. (2021). Relations for moments of generalized order statistics for transmuted exponential distribution and characterization. *Pakistan Journal of Statistics and Operation Research* **17**(1): 43–50.
DOI: <https://doi.org/10.18187/pjsor.v17i1.3517>
- Arnold B.C., Balakrishnan N. & Nagaraja H.N. (2008). *A First Course in Order Statistics*. SIAM, USA.
- Athar H. & Faizan M. (2011). Moments of lower generalized order statistics for power function distribution and a characterization. *International Journal of Statistical Sciences* **11**: 125–134.
- Burkschat M., Cramer E. & Kamps U. (2003). Dual generalized order statistics. *Metron* **61**(01): 13–26.
- Chandler K.N. (1952). The distribution and frequency of record values. *Journal of Royal Statistics Society B* **14**(02): 220–228.
DOI: <https://doi.org/10.1111/j.2517-6161.1952.tb00115.x>
- David H.A. & Nagaraja H.N. (2003). *Order Statistics*. John Wiley Inc., USA.
- Dziubdział W.A. & Kopociski B. (1976). Limiting properties of the k-th record value. *Applied Mathematics* **15**(02):187–190.
DOI: <https://doi.org/10.4064/am-15-2-187-190>
- Haq M.A., Butt N.S., Usman R.M. & Fattah A.A. (2016). Transmuted power function distribution. *Gazi University Journal of Science* **29**(01): 177–185.

- Hwang J.S. & Lin G.D. (1984). Extensions of Müntz–Szász theorems and application. *Analysis* **4**(12): 143–160.
DOI: <https://doi.org/10.1524/anly.1984.4.12.143>
- Kamps U. (1995). A concept of generalized order statistics. *Journal of Statistical Planning and Inference* **48**(01): 1–23.
DOI: [https://doi.org/10.1016/0378-3758\(94\)00147-N](https://doi.org/10.1016/0378-3758(94)00147-N)
- Kotb M.S., El-Din M.M.M. & Newer H.A. (2013). Recurrence relations for single and product moments of lower generalized order statistics from a general class of distributions and its characterizations. *International Journal of Pure and Applied Mathematics* **87**(02): 229–247.
DOI: <http://dx.doi.org/10.12732/ijpam.v87i2.4>
- Rahman M.M., Al-Zahrani B. & Shahbaz M.Q. (2018a). A general transmuted family of distributions. *Pakistan Journal of Statistics and Operation Research* **14**(02): 451–469.
DOI: <https://doi.org/10.18187/pjsor.v14i2.2334>
- Rahman M.M., Al-Zahrani B. & Shahbaz M.Q. (2018b). New general transmuted family of distributions with applications. *Pakistan Journal of Statistics and Operation Research* **14**(04): 807–829.
DOI: <https://doi.org/10.18187/pjsor.v14i4.2655>
- Shahbaz M.Q., Ahsanullah M., Hanif Shahbaz S. & Al-Zahrani B. (2016). *Ordered Random Variables: Theory and Applications*, Atlantis Press and Springer.
- Shaw W.T. & Buckley I.R.C. (2007). The alchemy of probability distributions: beyond Gram-Charlier expansions, and a skew-kurtotic-normal distribution from a rank transmutation map. *Research Report*.
DOI: <https://doi.org/10.48550/arXiv.0901.0434>

RESEARCH ARTICLE

Environmental Science

Removal of methylene blue from aqueous solution using raw laterite: an adsorption study

BM Gunathilake¹, D Jayawardana^{1*}, PGH Pupulewatte¹, S Dissanayake¹ and PM Manage²

¹Department of Forestry and Environmental Science, Faculty of Applied Sciences, University of Sri Jayewardenepura, Gangodawila, Nugegoda, Sri Lanka.

²Department of Zoology, Faculty of Applied Sciences, University of Sri Jayewardenepura, Gangodawila, Nugegoda, Sri Lanka.

Submitted: 10 January 2022; Revised: 30 June 2022; Accepted: 26 August 2022

Abstract: Existing methods for dye removal have their limitations and can be expensive and not very effective. Therefore, the search for efficient, effective, less expensive, and environmentally-friendly ways to remove industrial dyes from water remains open. Methylene blue (MB) removal from aqueous solutions is studied using raw laterite soil as a low-cost adsorbent. The physico-chemical properties and surface area were determined. Effects of parameters such as contact time, laterite dosage, pH, and ionic salts on MB adsorption by raw laterite were examined. The results showed that the maximum removal efficiency of MB adsorption was observed at pH values above 10, after 60 min of contact time, and with an adsorbent (raw Laterite) dose of 1.00 g in 100mL of dye solution. Increasing the salt concentration decreased the absorption of dye from solution. Ionic salt media containing, CaCl₂ and KCl have shown maximum and minimum influence, respectively, on the adsorption of MB by raw laterite soil. At the optimum conditions, the experimental adsorption capacity of raw laterite was 2.930 mg/g. The experimental data fitted the pseudo-second order kinetic model ($R^2 = 0.99$). The Freundlich adsorption isotherm model ($R^2 = 0.99$) showed the best fit to the experimental adsorption data. According to the Freundlich isotherm model, the calculated adsorption capacity of raw laterite was 2.949 mg/g. Desorption studies with several solvents revealed that the adsorbent could successfully retain MB, up to 33.89%. Therefore, it can be considered that raw laterite soil is effective in removing MB from aqueous solutions.

Keywords: Adsorbent, contamination, laterite, methylene blue.

INTRODUCTION

The presence of dyes in industrial effluents is a significant concern due to their adverse effects on many life forms (Shooto *et al.*, 2020). Synthetic dyes have harmful characteristics such as toxicity, carcinogenicity, poor biodegradability, and a tendency to bio-accumulate (Duman *et al.*, 2018). About 15% of the total world production of dyes is lost as textile effluents, generating large volumes of coloured wastewater (Hameed *et al.*, 2007; Lassoued *et al.*, 2018). The abundant dye effluent causes aesthetic pollution, and eutrophication harms aquatic life (Houas *et al.*, 2001; Hameed *et al.*, 2007; Awomeso *et al.*, 2010). However, even after industrial wastewater treatment, the final effluent exhibits a certain degree of colour intensity, indicating further contamination (Rafatullah *et al.*, 2010). Therefore, there is a high demand for colour-free industrial effluent (Hao *et al.*, 2000).

Methylene blue (MB) is one of the most widely used dyes in the textile industry. It can cause several adverse health effects; eye burns, breathing difficulties, nausea, vomiting, diarrhoea, and gastritis can be caused by ingestion and inhalation of MB. Also, the accidental intake of large doses of MB would cause abdominal and chest pain, severe headache, profuse sweating, mental confusion, and methaemoglobinaemia (Ghosh & Bhattacharyya, 2002; Hameed *et al.*, 2007; Rafatullah *et al.*, 2010). As a result, removing MB from contaminated water is critical. Several physical, chemical, and biological methods to remove dyes from solutions, such as chemical oxidation, ozonation, membrane filtration, flotation, and adsorption, have been identified (Hao *et al.*, 2000). However, these dye removal methods have limits and are costly and ineffective. As

* Corresponding author (daham@sci.sjp.ac.lk;  <https://orcid.org/0000-0001-9328-2729>)



This article is published under the Creative Commons CC-BY-ND License (<http://creativecommons.org/licenses/by-nd/4.0/>). This license permits use, distribution and reproduction, commercial and non-commercial, provided that the original work is properly cited and is not changed in anyway.

a result, seeking efficient, effective, low-cost, and environmentally acceptable technologies to remove industrial dyes from water continues.

In general, adsorption is defined as the enrichment of molecules, atoms, or ions in the vicinity of an interface (Thommes *et al.*, 2015). Adsorption is considered better in water treatment because of its convenience, ease of operation, and simplicity of design (Rafatullah *et al.*, 2010). As adsorption has broader applicability in removing different types of pollutants from water, it is extensively used in water pollution control (Pollard *et al.*, 1992). Recently, an increasing interest in utilizing clay minerals to remove dyes has been seen. Adsorption of MB with the clay minerals kaolinite and bentonite has been studied successfully (Ghosh & Bhattacharyya, 2002; Hong *et al.*, 2009; Mouni *et al.*, 2018). These studies reveal that clay minerals exhibit a strong affinity for MB, which is mainly dominated by ion-exchange processes (Rafatullah *et al.*, 2010). There have been few studies in which laterite has been utilized as an adsorbent. Laterite soil contains SiO₂, Fe₂O₃, and Al₂O₃. These ions can create both positive and negative charges on the surface at neutral pH. This makes the soil a suitable adsorbent for both cations and anions. Further, the high porosity and the availability of anion exchange sites are useful (Ranasinghe *et al.*, 2014; Mitra *et al.*, 2015). Previous studies related to laterite led to positive results in removing anions, such as fluoride (Sarkar *et al.*, 2006; Vithanage *et al.*, 2012). Further, laterite is used for the removal of phosphate (Zhang *et al.*, 2011), arsenite (Maiti *et al.*, 2013; Ranasinghe *et al.*, 2014), and metals such as copper (Pham *et al.*, 2017), lead, and chromium (Mitra *et al.*, 2015).

Laterite soil is widespread in the southwestern area of Sri Lanka, where it is known as ‘cabook’ in Sinhala. It is typically classified as a mottled earthy mass enriched in iron and aluminium hydroxides, that is somewhat dense but reasonably rapidly handled (Nayanthika *et al.*, 2018). Besides, laterite contains significant amounts of kaolinite and gibbsite, filling the cells of the kaolinite-sesquioxide matrix (Dissanayake, 1980). Raw laterite has not been investigated to remove industrial dyes from wastewater. As a result, this study aims to evaluate the optimal laterite soil parameters for MB-related sorption processes using kinetic modeling. This research aims to develop alternative dye removal systems that will not depend on chemicals to reduce the cost of wastewater treatment processes and introduce environmentally friendly, low-cost methods to treat industrial dyes.

MATERIALS AND METHODS

Material selection

Laterite soil forms from metamorphic rock in Sri Lanka, containing primary and secondary minerals (Herath & Pathirana, 1983). Naturally available pristine laterite soil was collected from the southwest zone of Sri Lanka using the soil auger and air-dried to a constant mass. The air-dried samples were ground to a powder using the mortar and pestle and were mechanically sieved through a 53 µm standard sieve. Analytical grade Sigma Aldrich MB (tetramethylthionine chloride) was used as the adsorbate for batch experiments and was not purified before use in experimental studies.

Characterization of laterite

The cation exchange capacity (CEC) of laterite soil was determined using the BaCl₂ Compulsive Exchange Method (Gillman & Sumpter, 1986). The pH of the laterite soil was measured using the SoilStik-2105 FieldScout pH Meter. The laterite soil's redox potentials (ORP) were measured using the WTW ProfiLine pH 3110 pH/mV meter. The conductivity of soil samples was measured using a WTW ProfiLine cond3210 conductivity meter. The loss on ignition (LOI) test was carried out to determine the organic matter (OM) and total organic carbon (TOC) contents in laterite (Wang *et al.*, 2011). The moisture content of laterite soil was measured by the direct percentage mass difference method (Nayanthika *et al.*, 2018).

$$\text{Moisture content \%} = \frac{W_{Wet} - W_{Dry}}{W_{Wet}} \times 100 \quad \dots(1)$$

where W_{wet} is the initial mass of the sample and W_{dry} is the mass of the dried sample at 105 °C until the samples reach constant weights.

The surface morphology and the structure of the laterite sample prepared were obtained with a scanning electron microscopy (SEM) using the Hitachi S-4200 field emission SEM (Zhu *et al.*, 2009). The powdered sample was analyzed for specific surface area and pore size distributions by N₂ adsorption at 77 K using the Autosorb IQ-MP (1 Stat.) Viton BET surface area analyzer (Gibson *et al.*, 2020). Parameters of the instrument were set according to 12.4 hours of approximate outgas time, and 300 °C final outgas temperature. Analysis was carried out for 3.25 hours using the standard analysis mode. Laterite soils were analyzed using X-Ray diffraction (XRD) using the Rigaku TTRAX III XRD instrument. The powdered samples were analyzed using Cu K-alpha radiation and wavelength 1.54 Å over 2θ ranging from 5° to 70° incremented by a step size of 0.02°, which are relevant parameters for the clay mineral observations (Zhao & Tan, 2018). FTIR (Fourier-transform infrared spectroscopy) analysis was used to identify and study the behavior of adsorption sites in laterite soil. Thus, investigations were carried out using a Nicolet iS10 spectrometer before and after adsorption, using the KBr-pellet method, and spectra were obtained in the range 4000–400 cm⁻¹ (Smidt *et al.*, 2005).

Adsorption experiment

The stock solutions of MB were prepared by dissolving weighed dye powder to produce a concentration of 1000 mg/L. The solutions used in batch experiments were produced by diluting the stock solution to different initial concentrations. All solutions were prepared using distilled water. The adsorption studies of MB with laterite soil were carried out using a series of batch experiments using 100.0 mL solutions of 30.0 mg/L initial MB concentration. The equilibrium concentrations were analyzed using the Shimadzu UV-1900 spectrometer at the maximum wavelength of MB, 663 nm. The adsorbent dosage, contact time, effect of pH, and effect of salts on adsorption were studied to investigate the optimum conditions.

The amount of MB absorbed per unit weight of adsorbent (q_e in mg/g) was calculated as equation (2)

$$q_e = \frac{(C_0 - C_e) \times V}{m} \quad \dots(2)$$

where C_0 is the initial concentration of MB dye (mg/L), C_e is the equilibrium concentration of the dye (mg/L), V is the volume of MB solution (L), and m is the dry laterite mass (g).

The percentage removal efficiency of MB from aqueous solutions was calculated using the following equation.

$$\text{Percentage removal Efficiency} = \frac{(C_0 - C_e) \times 100}{C_0} \quad \dots(3)$$

The experiments were conducted in triplicates under similar conditions.

Adsorption kinetic studies

Kinetic adsorption experiments were conducted using a series of solutions, with an initial dye concentration of 30 mg/L, optimum equilibrium pH, and optimum adsorbent dosage at ambient temperature by varying the contact time with an agitation speed of 120 rpm. Dosages 0.5 g and 1.0 g attained equilibrium within a short period, and as it is essential to give appropriate time to analyze the equilibrium kinetics. The dosage of 0.1 g was selected for further testing since it takes 60 minutes to saturate. After completing the predetermined time interval, the solids phase was removed from the solutions by centrifugation, and MB concentrations were determined. The amount of MB adsorbed per unit mass of adsorbent (q_e in mg/g) was calculated using equation (2). Adsorption kinetic parameters can predict the rate of adsorption. This factor is essential and useful in predicting the adsorption mechanism (Divband *et al.*, 2016). The dynamics of the MB adsorption process by laterite soil were evaluated by the pseudo-first-order (equation 4; Lagergren, 1898) and pseudo-second-order (equation 5; Ho & McKay, 1999) kinetic models. The non-linear forms of these models are given below:

$$q_t = q_e (1 - e^{-k_1 t}) \quad \dots(4)$$

$$q_t = \frac{q_e^2 k_2 t}{1 + q_e k_2 t} \quad \dots(5)$$

where q_t and q_e are the amounts of MB adsorbed on the adsorbent (mg g^{-1}) at time t and equilibrium time, respectively; k_1 is the rate constant of the pseudo-first-order kinetics (min^{-1}), and k_2 is the rate constant of the pseudo-second-order kinetics ($\text{g mg}^{-1} \text{min}^{-1}$).

Adsorption isotherm studies

Adsorption isotherm experiments were conducted using a series of solutions with initial MB concentrations of 10–50 mg/L with an optimum solution pH and optimum adsorbent at room temperature. The MB mixtures were shaken at 120 rpm and analyzed after equilibration to determine the residual MB concentration. Equilibrium data are essential requirements for the successful modeling of adsorption systems. Different theoretical and empirical relationships exist for modeling the adsorption process (Divband *et al.*, 2016). In this study, Langmuir, Freundlich, and Temkin models were applied to describe the adsorption process, and the equations are given below (Freundlich, 1909; Langmuir, 1916; Kinniburgh, 1986). The best-fit isotherm can be chosen using linear regression analysis of these models and comparing their correction coefficient (R^2).

A linear form of the Langmuir isotherm is expressed as follows:

$$\frac{1}{q_e} = \frac{1}{q_{max} \times b C_e} + \frac{1}{q_{max}} \quad \dots(6)$$

where C_e = the equilibrium concentration of adsorbate (mg/L), q_e = the amount of solute adsorbed per gram of the adsorbent at equilibrium (mg/g), q_{max} = maximum monolayer coverage capacity (mg/g), b = adsorption equilibrium constant (L/mg).

A linear form of the Freundlich isotherm is expressed as follows:

$$\log q_e = \log K + \frac{1}{n} \log C_e \quad \dots(7)$$

Constants K and n indicate the adsorption capacity and adsorption intensity, respectively.

A linear form of the Temkin isotherm is expressed as follows:

$$q_e = B \ln K_t + B \ln C_e \quad \dots(8)$$

where $B = (RT/b)$. T is the absolute temperature in K , and R is the universal gas constant in (J/mol-K). In this model, K_t is the binding constant which represents the maximum binding energy, and the constant B is related to the heat of adsorption.

Desorption study

The laterite samples were loaded with 100 mL of 30 mg/L methylene blue dye solution, and the mixture was shaken for 60 min at 120 rpm at room temperature. The MB-loaded laterite samples were separated from the mixture by centrifuging at 4000 rpm for 10 min. The collected samples for the experiment were washed with distilled water and oven-dried at 50 °C for 24 hours and later used for desorption studies. This laterite powder was dispersed in 100 mL solutions of dichloromethane (DCM) and 9:1 DCM : methanol solutions, which contained 1 g of MB dye-loaded laterite powder. The mixtures were stirred at 120 rpm at room temperature for 60 min. Laterite was separated from the mixture by centrifuging at 4000 rpm for 10 min. The MB dye desorption capacity ($q_{e, \text{desorption}}$, mg/g) was calculated using equation (9),

$$q_{e, \text{desorption}} = \frac{V C_f}{M} \quad \dots(9)$$

where, $q_{e, \text{desorption}}$ is the amount of dye desorbed from the dye saturated sorbent per gram of sorbent, at equilibrium (mg/g), C_f is the MB dye concentration in the desorbing solution (mg/L), V is the eluent solution volume (L), and M is the dye saturated laterite weight (g).

The desorption efficiency (%) of MB dye was calculated using equation (10),

$$D\% = \frac{q_{e, \text{desorption}}}{q_{e, \text{adsorption}}} \times 100 \quad \dots(10)$$

where, $D\%$ is MB dye desorption efficiency (%) and $q_{e, \text{desorption}}$, and $q_{e, \text{sorption}}$ are the MB dye desorption and sorption capacities (mg/g), respectively. All the experiments were performed in replicate.

RESULTS AND DISCUSSION

Characterization of laterite

The XRD analyses showed the presence of goethite, gibbsite, quartz, kaolinite, and haematite as significant constituents of laterite (Figure 1). Studies by Nayanthika *et al.* (2018) and Dissanayake (1980) have obtained similar results. According to the BET analysis results, the specific surface area of laterite soil was $72.52 \text{ m}^2 \text{ g}^{-1}$ (Table 1). This is considerably higher than previous studies related to laterite soil (Vithanage *et al.*, 2012). According to the IUPAC classification, the isotherms (Figure 2) obtained are Type IV (Thommes *et al.*, 2015).

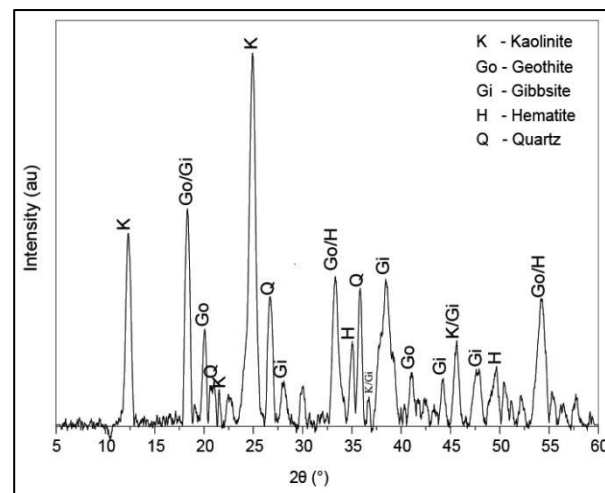


Figure 1: XRD study of raw laterite

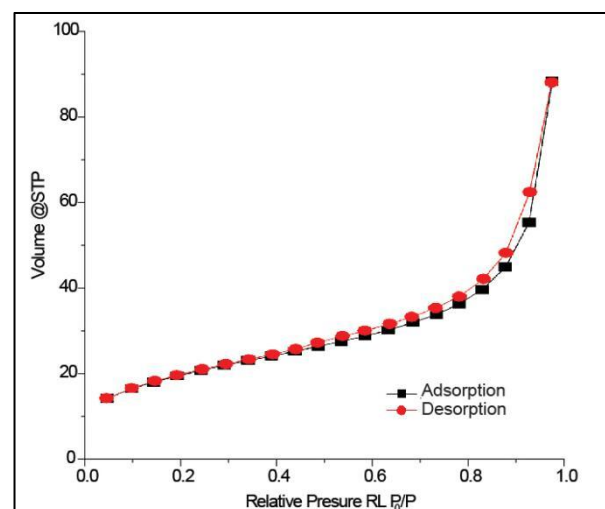


Figure 2: Low temperature nitrogen adsorption and desorption isotherms for raw laterite

Mesoporous adsorbents give Type IV isotherms. The recorded average pore radius of laterite was 3.81 nm, confirming the mesopore pore size. Mesoporous materials typically favour adsorbents due to their narrow pore size distributions, high surface area, simple functionalization strategies with organics, biocompatibility, and low toxicity (Wu & Zhao, 2011). Therefore, it confirms the applicability of laterite soil for the study.

The cation exchange capacity (CEC) for the soil sample was obtained as 9.22 cmol(+)/kg (Table 1). Cationic dyes such as MB are absorbed by clay minerals mainly by cation exchange. Therefore, MB adsorption depends on exchangeable cations of laterite soil (Kahr & Madsen, 1995). The irregular and porous surface of raw laterite could be observed in the SEM images of raw laterite shown in Figure 3(a). The EDX analysis shown in Figure 3(b) further investigated the laterite soil surface. EDX results demonstrate that elements such as Fe (6.4%), Al (12.1%), Si (14.7%), O (66.2%), and Ca (1.71%) are present in raw laterite samples. The results are analogous to previous studies by Vithanage *et al.* (2012).

Table 1: Physico-chemical properties of raw laterite

Parameter	Values
Moisture content (%)	18.9
pH	4.7
ORP (mV)	88
EC (us/cm)	34.2
TOC (%)	7.8
OM (%)	0.74
LOI (%)	15.23
BET specific surface area (m ² /g)	72.52
Average pore diameter (nm)	3.81
pH _{ZPC}	6.6
CEC (cmol(+)/kg)	9.22

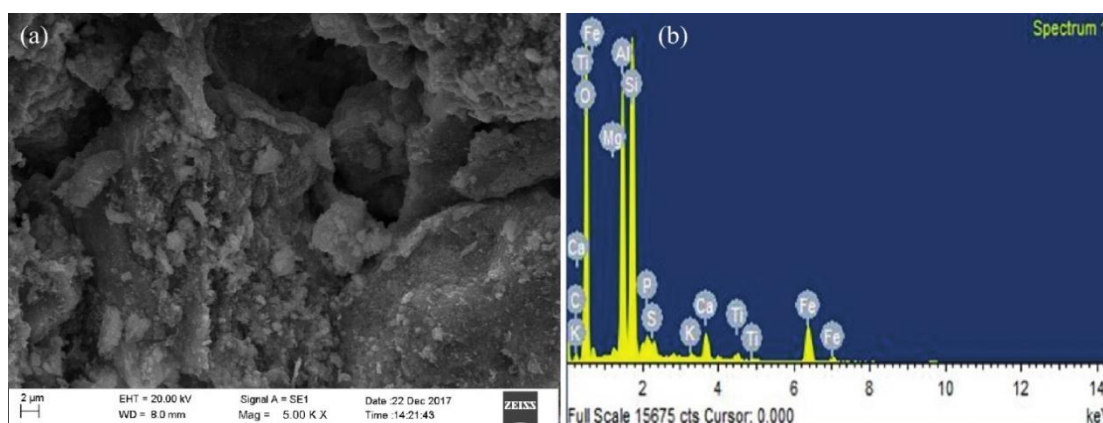


Figure 3: (a) SEM; (b) SEM-EDX spectra of raw laterite

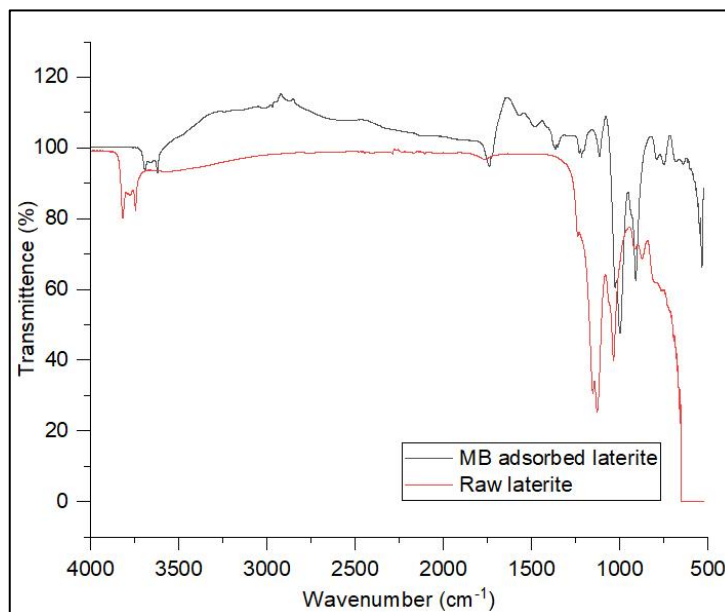


Figure 4: FTIR spectra of laterite before and after MB adsorption

The FTIR spectra indicate six absorption bands in the OH stretching vibration region (Figure 4) at 3818, 3799, 3792, 3779, 3773, and 3745 cm^{-1} (Vithanage *et al.*, 2012). These correspond to the OH stretching vibrations of the surface and inner Al-OH groups of the gibbsite. In the region of 1200–900 cm^{-1} , the bands in the region observed are 1154, 1128, 1036, and 913 cm^{-1} . These can be attributed to the stretching vibrations of the Si-O-Si of free quartz and kaolinite in laterite kaolinite (Mouni *et al.*, 2018). The FTIR spectra of laterite soil after MB adsorption showed considerable changes. The broadening of the OH stretch features around 3500 cm^{-1} indicates increased hydrogen bonding. Most of the IR bands that correspond to metal-oxygen bonds (M-O) and metal hydroxide bonds (M-OH), show small wavenumber shifts after MB adsorption (Vithanage *et al.*, 2012). New absorption bands were observed at 1738, 1478, 1365, 1230, and 1216 cm^{-1} after MB dye was adsorbed. These bands could be assigned to -C-N-, -C=N-, and -C=C- stretching in heterocyclic poly rings of MB (Sakin Omer *et al.*, 2018). Thus, it was evident that MB adsorption had occurred onto the surface of laterite soil.

The pH_{zpc} of laterite, according to previous studies, has been calculated as 3.98 (Sarkar *et al.*, 2006), 7.40 (Pham *et al.*, 2017) and 8.72 (Vithanage *et al.*, 2012). The pH_{zpc} varies with the composition of the laterite sample (Zhang *et al.*, 2016). In this study, it was found to be 6.60.

Effect of contact time

The effect of contact time on the MB adsorption capacity of laterite soil was determined with the initial MB concentration of 30 mg/L at different adsorbent dosages, from 0.1 g to 1.0 g per 100 mL of MB solution. (Figure 5). It was found that the MB adsorption capacity of laterite was rapid at the beginning stages of contact time. After 20 minutes, the adsorption rate decreases with time, and the adsorption process reaches equilibrium within 60 minutes. This process might be due to a higher number of binding sites and free pores available on laterite for the adsorption of MB during the initial stages. However, the free binding sites and pores were used as time passed, and the rate slowed down due to binding sites and pores getting exhausted. After this point, adsorption was controlled only by the rate at which MB molecules were transported from the exterior to the interior sites of the adsorbent (Shooto *et al.*, 2020). Similar results were also reported by other researchers where the MB adsorption was found to increase with the increase in contact time, but after reaching equilibrium, adsorption remained constant (Hameed & Ahmad, 2009; Mouni *et al.*, 2018; Shooto *et al.*, 2020). Therefore, according to the obtained results, a contact time of 60 minutes was chosen for further experiments.

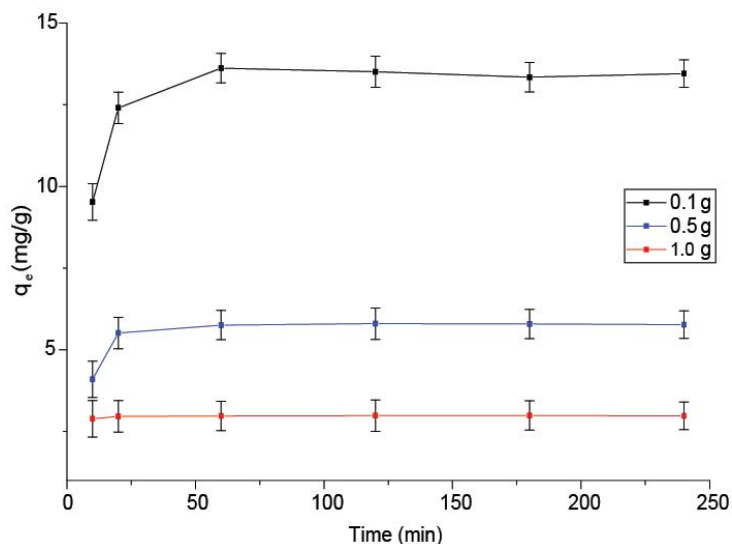


Figure 5: Effect of contact time on the MB removal efficiency of raw laterite, $C_0 = 30$ mg/L, Volume of MB solution = 100 mL

Effect of dosage

Adsorbent dosage is another important factor in determining the optimum adsorbent dose required to remove a definite amount of pollutants from the solution. In general, an increase in adsorbent dosage increases the adsorption of adsorbate from the solution due to the availability of more active sites and increases in surface area at higher dosages (Divband *et al.*, 2016). It was evident that with the increase in adsorbent dosage from 0.1 to 4.0 g, the MB adsorption capacity decreased (Figure 6a), and the removal efficiency of laterite increased (Figure 6b). This could be related to the use of the surface area in an unsaturated form. According to the findings of this study, increasing the laterite dosage from 0.5 to 4.0 g reduced the q_e (mg/g) from 39.40 to 2.49 mg/g (Figure 6). This means that, while an adsorbent's mass increase can give a large accessible surface area, the pollutant's unsaturated adsorption pattern causes the adsorbent to be used in an undesirable way (Ong *et al.*, 2007). This concept is particularly relevant in the development of cost-effective and large-scale industrial dye removal systems.

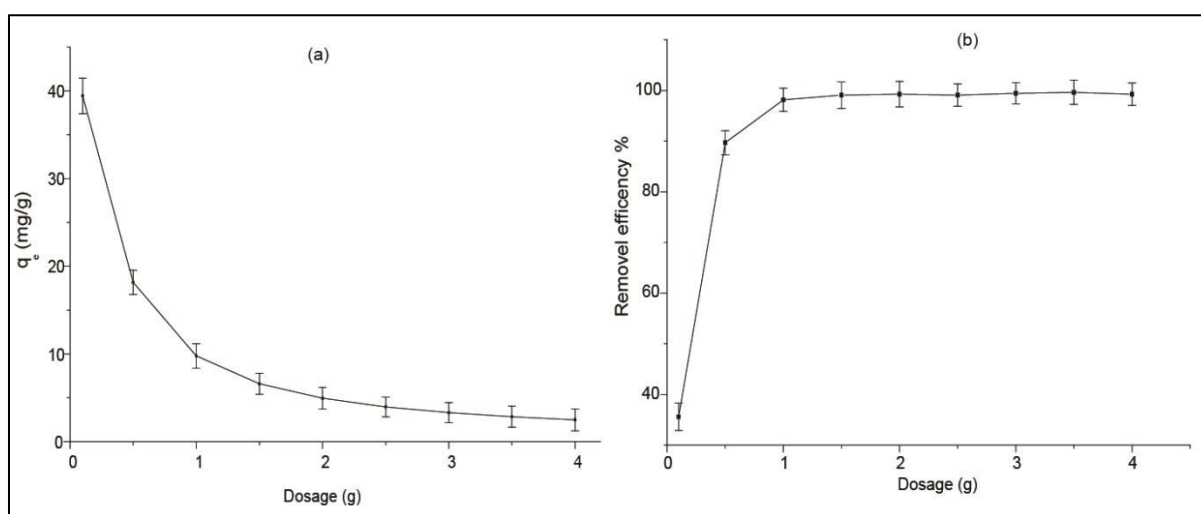


Figure 6: (a) Effect of adsorbent dosage on MB adsorption capacity (q_e) of raw laterite in 100 mL of MB; (b) effect of adsorbent dosage on the MB removal efficiency of raw laterite, $C_0 = 30$ mg/L, $t = 60$ min, Volume of MB solution = 100 mL

Further increase in adsorbent dosage beyond 1.0 g did not significantly affect the MB removal efficiency. Similar results were reported by other researchers where MB removal efficiency from aqueous solutions increased up to the optimum dosage, and with further increase in adsorbent dose, the removal efficiency remained constant (Franca *et al.*, 2009; Mouni *et al.*, 2018). Therefore, based on the results of this study, an adsorbent dosage of 1.0 g was selected for further experiments.

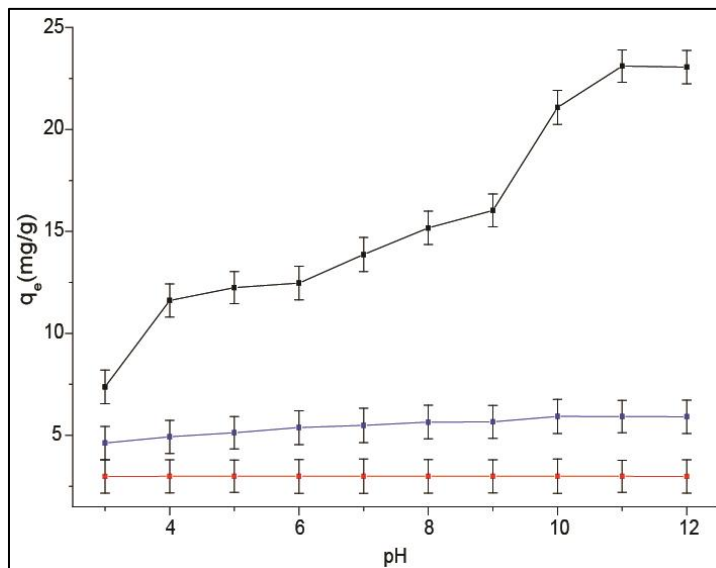


Figure 7: Effect of pH on MB adsorption on the raw laterite at 25 °C, $C_0 = 30$ mg/L, $m = 1.0$ g, $t = 60$ min, Volume of MB solution = 100 mL

Effect of pH

The pH of the dye solution plays a vital role in adsorption capacity (Hameed & Ahmad, 2009). The removal efficiency increased with increasing pH at lower adsorbent dosages (Figure 7). Lower adsorption at acid pH can be explained by the fact that the surface of the adsorbent was protonated. This would attract anions, and the excess of H^+ ions would compete with the dye cations for adsorption sites (Shooto *et al.*, 2020). At higher pH values (6–12) the dye adsorption was almost constant when the adsorbent dosage was high. The presence of excess adsorption sites can explain this. In the range of pH 3–12, the effect of pH on the removal efficiency of a dosage of 1.0 g adsorbent in 100 mL MB dye solution was almost constant. Consequently, the effect of pH on this MB adsorption is evident.

As the pH_{ZPC} of laterite soil is approximately 6.6, when the pH of the solution is higher than 6.70, the surface of laterite would be negatively charged. As a result, cationic MB dye ions are attracted to laterite in aqueous solution by electrostatic forces of attraction (Hameed & Ahmad, 2009; Mouni *et al.*, 2018). Similar results have been obtained in previous studies of MB adsorption onto garlic peel (Hameed & Ahmad, 2009), kaolin (Mouni *et al.*, 2018), Agar/ κ -carrageenan composite hydrogel (Duman *et al.*, 2018), and mucuna beans (Shooto *et al.*, 2020).

Effect of ionic strength

The effect of ionic strength on the dye uptake was studied by measuring q_e in the presence of the different salts NaCl, KCl, $MgCl_2$, and $CaCl_2$. Results indicated that an increase in the salt concentration decreased the dye's absorption into the laterite soil. KCl and $MgCl_2$ showed similar effects on MB adsorption (Figure 8). Previous studies show that the presence of salt in the aqueous medium of the MB dye shields the electrostatic forces of opposite charges between the dye molecule and the adsorbent material, like laterite soil (Mouni *et al.*, 2018).

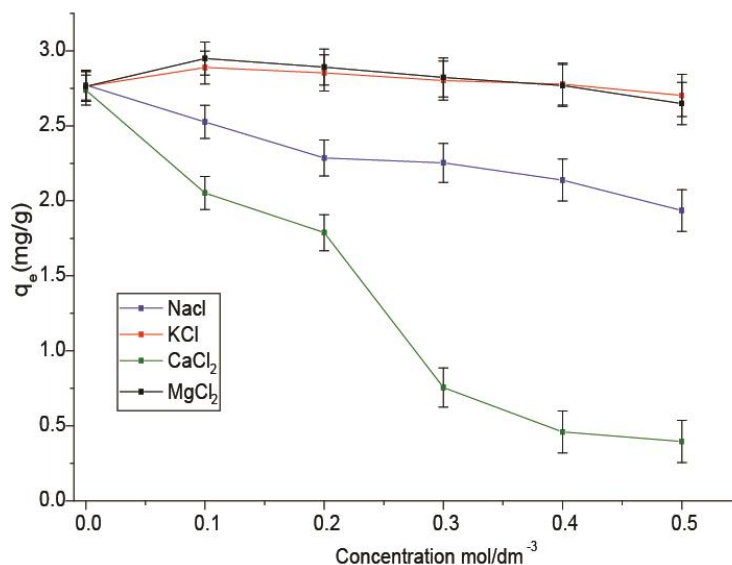


Figure 8: The effect of ionic strength on the MB removal efficiency, $C_0 = 30$ mg/L, $m = 1.0$ g, $t = 60$ min. Volume of MB solution = 100 mL

Adsorption kinetic studies

Kinetic models for the adsorption of MB on laterite clay provide useful pieces of evidence for efficiency and feasibility (Limousin *et al.*, 2007; Mouni *et al.*, 2018). In this study, the pseudo-first-order and pseudo-second-order rate equations were used. The pseudo-second-order equation provided an excellent fit, with a regression coefficient $R^2 = 0.99$ (Figure 9). Moreover, the experimental q_e value (2.930 mg/g) was comparatively close to the calculated q_e value (2.974 mg/g) in the pseudo-second-order model, which further suggests the superiority of the said model over the pseudo-first-order kinetic models (Table 2). The kinetics of MB sorption on the raw laterite sorbent thus follows the pseudo-second-order rate expression. A good fit of experimental data with the pseudo-second-order model would indicate that chemical adsorption is the rate-controlling mechanism. This suggests that the rate-limiting step may involve valency forces through the sharing or exchange of electrons between sorbent and sorbate (Ho & McKay, 1999). Similar results have also been reported by other researchers where the pseudo-second-order kinetic model has shown good agreement with the experimental data for adsorption of MB dye (Franca *et al.*, 2009; Mouni *et al.*, 2018; Shooto *et al.*, 2020).

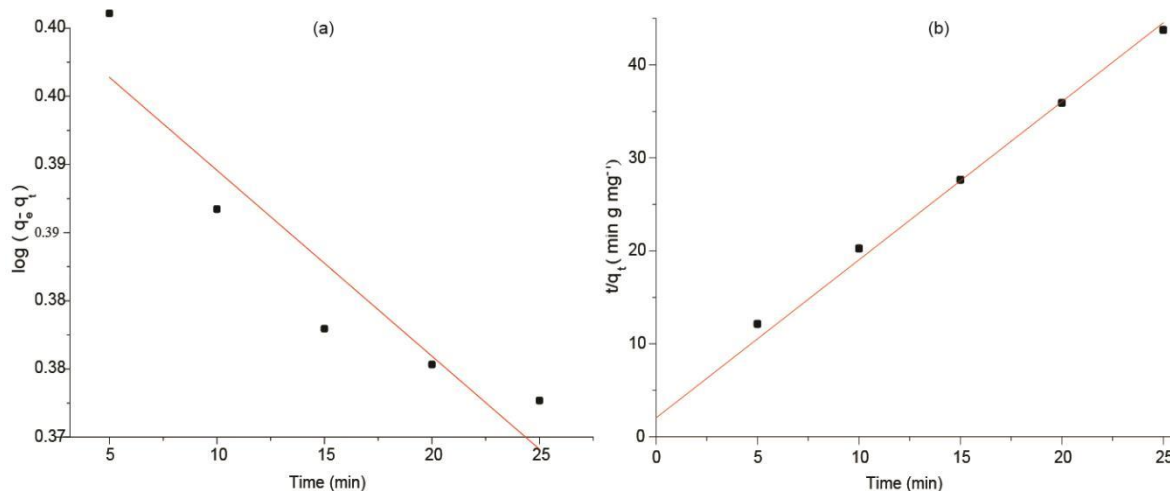


Figure 9: (a). Pseudo first order and (b). pseudo second-order kinetics of MB adsorption onto raw laterite

Table 2: Kinetic parameters for the removal of MB by raw laterite

C_0	Pseudo first order kinetics				Pseudo second order kinetics			
	k_1 (min^{-1})	q_{exp} (mg/g)	q_{cal} (mg/g)	R^2	k_2 ($\text{g mg}^{-1} \text{min}^{-1}$)	q_{exp} (mg/g)	q_{cal} (mg/g)	R^2
30 (mg/L)	-5.44×10^{-5}	2.930	1.497	0.87	0.0558	2.930	2.974	0.99

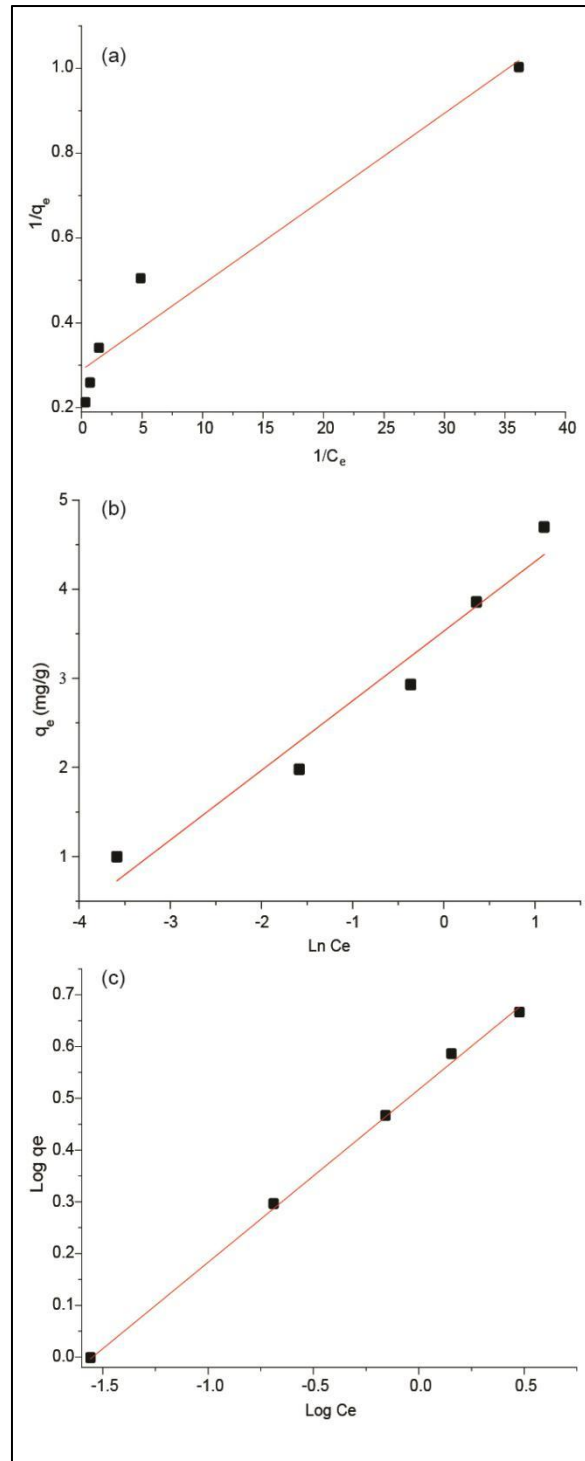


Figure 10: (a) Langmuir, (b) Temkin and (c) Freundlich isotherm for the sorption of MB dye on to raw laterite

Adsorption isotherms

The adsorption characteristic equilibrium studies of laterite for MB removal from aqueous solutions were investigated. The experimental data fitted the Freundlich adsorption isotherm (Figure 10) with an R^2 of 0.99, which means multilayer adsorption played a dominant role. The K_f value of the Freundlich isotherm model is 3.33 L g^{-1} . In addition, the experimental adsorption capacity (q_e) is 2.930 mg/g , which is similar to the calculated adsorption capacity (2.949 mg/g) using the Freundlich isotherm model. The n value in the Freundlich model is 2.994 (between 1 and 10), indicating favourable MB adsorption by the laterite (Divband *et al.*, 2016). Similar results have been seen in studies carried out to remove MB (Shooto *et al.*, 2020). When the Langmuir isotherm model was considered, the data fitted with an R^2 of 0.94. According to this model, the maximum monolayer adsorption capacity was calculated as 3.46 mg/g . The Temkin isotherm fitted with an $R^2 = 0.96$ with a K_t value of 91.73 (mg/g) (Table 3). Furthermore, the experimental adsorption capacity data curve (C_e versus q_e) was compared to the estimated adsorption capacities of the Langmuir, Freundlich, and Temkin isotherm models (Figure 11). These results indicate that the Freundlich isotherm model best fits the experimental adsorption capacity data, when compared with the Langmuir and Temkin isotherm models.

Table 3: Isotherm parameters for MB adsorption on to raw laterite

Model	Parameters	Value
Langmuir	$b \text{ (L mg}^{-1}\text{)}$	14.31
	$q_{\max} \text{ (mg/g)}$	3.46
	R^2	0.94
Freundlich	$K_f \text{ (L g}^{-1}\text{)}$	3.33
	N	2.99
	R^2	0.99
Temkin	$K_t \text{ (L mg}^{-1}\text{)}$	91.73
	$B \text{ (J mol}^{-1}\text{)}$	0.78
	R^2	0.96

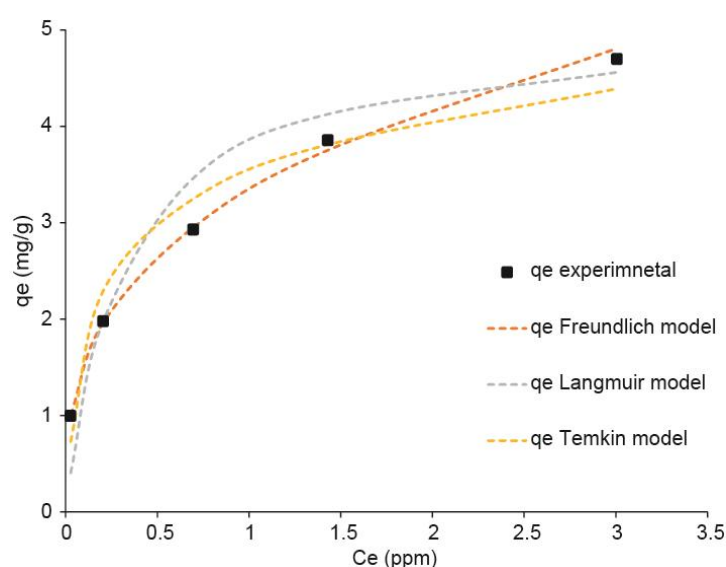


Figure 11: Variation of experimental adsorption capacity curve and isotherm model adsorption capacity curves

Desorption study

When considering the results of the desorption study, all solvents showed low desorption efficiencies (Figure 12). DCM resulted in the highest desorption efficiency of 33.89 %, whereas the lowest, 2.98%, was reported when acetone was used. Therefore, it can be said that laterite retains MB successfully after its adsorption from aqueous solutions. Regeneration is only efficient if the cost of regeneration is lower than the cost of production of the adsorbent (Ahmed *et al.*, 2016). In this case, as very small amounts of MB desorb from laterite in the case of all solvents, regeneration would not be efficient.

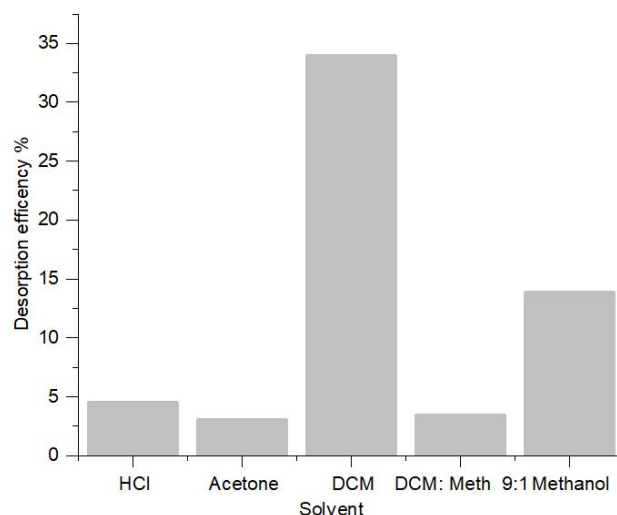


Figure 12: Effect of different solvents on the desorption of dye from MB loaded laterite soil

CONCLUSION

This study suggests that the laterite is an effective adsorbent for MB adsorption from an aqueous solution. The effect of pH for the removal efficiency of adsorbent dosage of 1.0 g was almost constant in the range of pH 3–12. As a result, the effect of pH on this MB adsorption can be justifiable. The removal of MB was initially rapid, and after 20 min, the rate of adsorption decreased. The optimum contact time and optimum dosage for removing MB from 100 mL of 30 mg/L dye solutions were obtained as 60 minutes and 1.0 g, respectively. The experimental data fitted well with the pseudo-second-order kinetic model, which suggests that chemical adsorption is the rate-controlling mechanism. The data also fitted the Freundlich isotherm model, which indicates that multilayer adsorption played a dominant role. Finally, our studies revealed that raw laterite is a cost-effective alternative for commercially available, expensive adsorbent material to remove methylene blue from aqueous solutions with an adsorption capacity of 2.930 mg/g.

When the adsorption capacities of the adsorbents used for MB removal are considered, raw laterite has a adsorption capacity of 2.930 mg/g, whereas bone charcoal has an adsorption capacity of 5 mg/g and fly ash has adsorption capacity of 5.718 mg/g (Kumar *et al.*, 2005). However, in the study, raw laterite was used to remove MB without any processing, demonstrating that this commonly available environmentally friendly material has the potential to remove MB from aqueous solutions.

Acknowledgement

This study was conducted under the AHEAD ICE grant. The authors would like to thank the Central Instrument Centre, Faculty of Applied Sciences, University of Sri Jayewardenepura, the Nano-composite Research Group of the University of Sri Jayewardenepura for its support in conducting the BET analysis. We acknowledge the support of the Department of Forestry and Environmental Sciences and the Research Council of the University of Sri Jayewardenepura.

Availability of data and material

The authors declare that all necessary data supporting the findings of this study are available within the article. If additional data supporting this study's findings are required, they can be made available from the corresponding author upon reasonable request.

REFERENCES

- Ahmed M.B., Zhou J.L., Ngo H.H. & Guo W. (2016). Insight into biochar properties and its cost analysis. *Biomass and Bioenergy* **84**: 76–86.
DOI: <https://doi.org/10.1016/j.biombioe.2015.11.002>
- Awomeso J.A., Taiwo A.M., Gbadebo A.M. & Adenowo J.A. (2010). Studies on the pollution of water body by textile industry effluents in Lagos, Nigeria. *Journal of Applied Sciences in Environmental Sanitation* **5**: 353–359.
- Dissanayake C.B. (1980). Mineralogy and chemical composition of laterites of Sri Lanka. *Geoderma* **23**: 147–155.
- Divband L., Hooshmand A., Ali A., Soltani A., Abbasi F. & Bhatnagar A. (2016). Removal of nitrate from aqueous solution by modified sugarcane bagasse biochar. *Ecological Engineering* **95**: 101–111.
DOI: <https://doi.org/10.1016/j.ecoleng.2016.06.035>
- Duman O., Polat T.G., Diker C.Ö. & Tunç S. (2018). Agar/κ-carrageenan composite hydrogel adsorbent for the removal of Methylene Blue from Water. *International Journal of Biological Macromolecules* **135**: 577.
DOI: <https://doi.org/10.1016/j.ijbiomac.2020.05.191>
- Franca A.S., Oliveira L.S. & Ferreira M.E. (2009). Kinetics and equilibrium studies of methylene blue adsorption by spent coffee grounds. *Desalination* **249**: 267–272.
DOI: <https://doi.org/10.1016/j.desal.2008.11.017>
- Freundlich H.M.F. (1906). Over the adsorption in solution. *Journal of Physical Chemistry* **57**: 385–471.
- Ghanizadeh G. & Asgari G. (2010). Adsorption kinetics and isotherm of methylene blue and its removal from aqueous solution using bone charcoal. *Reaction Kinetics, Mechanisms and Catalysis* **102**(1): 127–142.
DOI: <https://doi.org/10.1007/s11144-010-0247-2>
- Ghosh D. & Bhattacharyya K.G. (2002). Adsorption of methylene blue on kaolinite. *Applied Clay Science* **20**: 295–300.
DOI: <https://doi.org/10.1080/01932699908943843>
- Gillman G.P. & Sumpter E.A. (1986). Modification to the compulsive exchange method for measuring exchange characteristics of soils. *Australian Journal of Soil Research* **24**: 61–66.
DOI: <https://doi.org/10.1071/SR9860061>
- Hameed B.H. & Ahmad A.A. (2009). Batch adsorption of methylene blue from aqueous solution by garlic peel, an agricultural waste biomass. *Journal of Hazardous Materials* **164**: 870–875.
DOI: <https://doi.org/10.1016/j.jhazmat.2008.08.084>
- Hameed B.H., Din A.T.M. & Ahmad A.L. (2007). Adsorption of methylene blue onto bamboo-based activated carbon: Kinetics and equilibrium studies. *Journal of Hazardous Materials* **141**: 819–825.
DOI: <https://doi.org/10.1016/j.jhazmat.2006.07.049>
- Hao O.J., Kim H. & Chiang P.C. (2000). Decolorization of wastewater. *Critical Reviews in Environmental Science and Technology* **30**: 449–505.
DOI: <https://doi.org/10.1080/10643380091184237>
- Ho Y. & McKay G. (1999). Pseudo-second order model for sorption processes. *Process Biochemistry* **34**: 451–465.
DOI: <https://doi.org/10.1021/acs.oprd.7b00090>
- Hong S., Wen C., He J., Gan F. & Ho Y.S. (2009). Adsorption thermodynamics of methylene blue onto bentonite. *Journal of Hazardous Materials* **167**: 630–633.
DOI: <https://doi.org/10.1016/j.jhazmat.2009.01.014>
- Houas A., Lachheb H., Ksibi M., Elaloui E., Guillard C. & Herrmann J.M. (2001). Photocatalytic degradation pathway of methylene blue in water. *Applied Catalysis B: Environmental* **31**: 145–157.
DOI: [https://doi.org/10.1016/S0926-3373\(00\)00276-9](https://doi.org/10.1016/S0926-3373(00)00276-9)
- Kahr G. & Madsen F.T. (1995). Determination of the cation exchange capacity and the surface area of bentonite, illite and kaolinite by methylene blue adsorption. *Applied Clay Science* **9**: 327–336.
- Kinniburgh D.G. (1986). General purpose adsorption isotherms. *Environmental Science and Technology* **20**: 895–904.
DOI: <https://doi.org/10.1021/es00151a008>
- Kumar K., Ramamurthi V. & Sivanesan S. (2005). Modeling the mechanism involved during the sorption of methylene blue onto fly ash. *Journal of Colloid and Interface Science* **284**(1): 14–21.
DOI: <https://doi.org/10.1016/j.jcis.2004.09.063>
- Lagergren (1898). About the theory of so-called adsorption of soluble substances. *Kungliga Svenska Vetenskapsakademiens Handlingar* **24**: 1–39.
- Langmuir I. (1916). The constitution and fundamental properties of solid and liquids. Part I. Solids. *Journal of the American Chemical Society* **38**: 2221–2295.

- Maiti A., Kumar B., Kumar J., & De S. (2013). Comparison of treated laterite as arsenic adsorbent from different locations and performance of best filter under field conditions. *Journal of Hazardous Materials* **262**: 1176–1186.
DOI: <https://doi.org/10.1016/j.jhazmat.2012.06.036>
- Mitra S., Thakur L.S. & Rathore V.K. (2015). Removal of Pb (II) and Cr (VI) by laterite soil from synthetic waste water : single and bi-component adsorption approach. *Desalination and Water Treatment* **57**(39): 18406–18416.
DOI: <https://doi.org/10.1080/19443994.2015.1088806>
- Mohammed M., Shitu A. & Ibrahim A. (2014). Removal of methylene blue using low-cost adsorbent: a review. *Research Journal of Chemical Sciences* **4**(1): 91–102.
- Mouni L., Belkhir L., Bollinger J.C., Bouzaza A., Assadi A., Tirri A., Dahmoune F., Madani K. & Remini H. (2018). Removal of methylene blue from aqueous solutions by adsorption on kaolin: kinetic and equilibrium studies. *Applied Clay Science* **153**: 38–45.
DOI: <https://doi.org/10.1016/j.clay.2017.11.034>
- Nayanthika I.V.K., Jayawardana D.T., Bandara N.J.G.J., Manage P.M. & Madushanka R.M.T.D. (2018). Effective use of iron-aluminum rich laterite based soil mixture for treatment of landfill leachate. *Waste Management* **74**: 347–361.
DOI: <https://doi.org/10.1016/j.wasman.2018.01.013>
- Ong S., Lee C. & Zainal Z. (2007). Removal of basic and reactive dyes using ethylenediamine modified rice hull. *Bioresource Technology* **98**(15): 2792–2799.
- Pham T.D. *et al.* (11 authors) (2017). Adsorptive removal of copper by using surfactant modified laterite soil. *Journal of Chemistry* **2017**: 1986071.
- Pollard S.J.T., Fowler G.D., Sollars C.J. & Perry R. (1992). Low - cost adsorbents for waste and wastewater treatment: a review. *Science of the Total Environment* **116**: 31–52.
- Rafatullah M., Sulaiman O., Hashim R. & Ahmad A. (2010). Adsorption of methylene blue on low-cost adsorbents: A review. *Journal of Hazardous Materials* **177**: 70–80.
DOI: <https://doi.org/10.1016/j.jhazmat.2009.12.047>
- Ranasinghe R.M.S.C., Werellagama D.R.I.B. & Weerasooriya R. (2014). Arsenite removal from drinking water using naturally available laterite in sri lanka. *Engineer: Journal of the Institution of Engineers, Sri Lanka* **47**(2): 23–31.
DOI: <http://doi.org/10.4038/engineer.v47i2.6865>
- Rezaei Kalantary R., Dehghanifard E., Mohseni-Bandpi A., Rezaei L., Esrafil A., Kakavandi B. & Azari A. (2015). Nitrate adsorption by synthetic activated carbon magnetic nanoparticles: kinetics, isotherms and thermodynamic studies. *Desalination and Water Treatment* **57**: 1–11.
DOI: <https://doi.org/10.1080/19443994.2015.1079251>
- Sakin Omer O., Hussein M.A., Hussein B.H.M. & Mgaidi A. (2018). Adsorption thermodynamics of cationic dyes (methylene blue and crystal violet) to a natural clay mineral from aqueous solution between 293.15 and 323.15 K. *Arabian Journal of Chemistry* **11**: 615–623.
DOI: <https://doi.org/10.1016/j.arabjc.2017.10.007>
- Sarkar M., Banerjee A., Pramanick P.P. & Sarkar A.R. (2006). Use of laterite for the removal of fluoride from contaminated drinking water **302**: 432–441.
DOI: <https://doi.org/10.1016/j.jcis.2006.07.001>
- Shoote N.D., Nkutha C.S., Guilande N.R. & Naidoo E.B. (2020). Pristine and modified mucuna beans adsorptive studies of toxic lead ions and methylene blue dye from aqueous solution. *South African Journal of Chemical Engineering* **31**: 33–43.
DOI: <https://doi.org/10.1016/j.sajce.2019.12.001>
- Thommes M., Kaneko K., Neimark A.V., Olivier J.P., Rodriguez-Reinoso F., Rouquerol J. & Sing K.S.W. (2015). Physisorption of gases, with special reference to the evaluation of surface area and pore size distribution (IUPAC Technical Report). *Pure and Applied Chemistry* **87**: 1051–1069.
DOI: <https://doi.org/10.1515/pac-2014-1117>
- Vithanage M., Jayarathna L., Upamali A., Dissanayake C.B., Bootharaju M.S. & Pradeep T. (2012). Modeling sorption of fluoride on to iron rich laterite. *Colloids Surfaces A: Physicochemical and Engineering Aspects* **398**: 69–75.
DOI: <https://doi.org/10.1016/j.colsurfa.2012.02.011>
- Wu Z. & Zhao D. (2011). Ordered mesoporous materials as adsorbents. *Chemical Communications* **47** 3332–3338.
DOI: <https://doi.org/10.1039/c0cc04909c>
- Zhang L., Hong S., He J., Gan F. & Ho Y. (2011). Adsorption characteristic studies of phosphorus onto laterite. *Desalination and Water Treatment* **25**: 98–105.
DOI: <https://doi.org/10.5004/dwt.2011.1871>
- Zhang M., Bolan N.S., Chen S.S., Rajapaksha A.U., Tsang D.C.W., Gao B., Vithanage M., Ok Y.S. & Mandal S. (2016). Engineered/designer biochar for contaminant removal/immobilization from soil and water: Potential and implication of biochar modification. *Chemosphere* **148**: 276–291.
DOI: <https://doi.org/10.1016/j.chemosphere.2016.01.043>

RESEARCH ARTICLE

Food Technology

Comparison of physicochemical and sensory properties of African butter seed (*Pentadesma butyracea*) and cocoa fats for potential use in future food applications

NPS Jayathissa^{1*}, ABG Silva², WMT Madhujith¹, PGSM De Silva², R Jayatissa²

¹Department of Food Science and Technology, Faculty of Agriculture, University of Peradeniya, Peradeniya, Sri Lanka.

²Medical Research Institute, Dr. Danister De Silva Mawatha, Colombo 08, Sri Lanka.

Submitted: 02 March 2022; Revised: 09 July 2022; Accepted: 26 August 2022


Abstract: African butter (*Pentadesma butyracea*) seeds are rich in edible fat, while cocoa butter is an expensive product obtained from fermented and dried cocoa beans. The aim of our study was to analyze the physicochemical and sensory properties of African butter seed fat and cocoa fat while determining their potential food applications. Chemically extracted fat was utilized for determination of physicochemical properties according to AOCS guidelines. Physically extracted fat was utilized for preparation of cookies and determination of sensory properties. Acid value, free fatty acid value and iodine value of African butter seed fat and cocoa fat were 1.05 ± 0.17 vs. 2.06 ± 0.14 mg KOH/g, $0.53 \pm 0.09\%$ vs. $1.14 \pm 0.07\%$ and 48.65 ± 3.03 vs. 34.31 ± 0.97 g I₂/100g respectively. Saponification values of African butter seed fat and cocoa fat were 177.0 ± 0.6 mg KOH/g and 194.2 ± 1.1 mg KOH/g respectively. Between 25 and 30 °C, the solid fat content ranged from $31.8 \pm 0.05\%$ to $6.85 \pm 0.07\%$ for African butter seed fat and $36.14 \pm 0.87\%$ to $11.15 \pm 0.11\%$ for cocoa fat. The contents of stearic and oleic acids which are abundant in African butter seed fat were $39.05 \pm 0.16\%$ and $56.97 \pm 0.27\%$ respectively while those of in cocoa fat were $37.75 \pm 0.06\%$ and $34.12 \pm 0.14\%$. Results of hedonic test performed for cookies prepared by incorporating the two kinds of fats highlighted that there was a significant difference relative to the preference ($p < 0.05$) for colour, while there was no significant difference with respect to the preference for flavour, texture and overall acceptability ($p > 0.05$). There is a high potential to develop African butter seed fat as a fat spread, a cocoa butter alternative and in preparation of cookies.

Keywords: African butter seed fat, cocoa fat, cookies, fatty acid profile, physicochemical properties, sensory properties.

INTRODUCTION

African butter trees (*Pentadesma butyracea*) are naturally found in Africa from Guinea Bissau to the western regions of the Republic of Congo. In Sri Lanka, several plants are grown at the Royal Botanical Garden, Peradeniya and also, a small plantation could be seen in Hunuwala estate, Kahawatta. ‘Tallow tree’ and ‘butter tree’ are commonly used English names for *Pentadesma butyracea* plants (Ayegnon *et al.*, 2015). These plants belong to the family of *Clusiaceae* and they can grow up to a height of about 20 m (Tchobo *et al.*, 2007). Butter tree kernels are found to be rich in edible fat and fresh kernels are consumed like kola in African regions (Ayegnon *et al.*, 2015). Different communities of the northern regions of Benin use tallow seed fat for edible purposes, mainly as a cooking oil rather than therapeutic and cosmetic applications. They employ various traditional processing techniques in preparation of butter from tallow seeds. Various pretreatment steps like boiling of fresh kernels followed by different drying techniques such as solar drying, direct sun drying, and smoking are employed, prior to the extraction which is associated with steps such as heating, crushing, milling, and churning (Badoussi, 2014).

Cocoa butter is a valuable product obtained from the cocoa bean processing industry. It is manufactured by pressing cocoa liquor obtained from grinding cocoa nibs separated from mature, fermented, and dried cocoa

* Corresponding author (jayathissasandaru@gmail.com;  <https://orcid.org/0000-0002-4369-217X>)



This article is published under the Creative Commons CC-BY-ND License (<http://creativecommons.org/licenses/by-nd/4.0/>). This license permits use, distribution and reproduction, commercial and non-commercial, provided that the original work is properly cited and is not changed in anyway.

beans (Beckett, 2009). Blending of cocoa butter in chocolates and confectionery products yields numerous unique physicochemical and sensory properties, such as melting characteristics in mouth with typical mouth feel. Because of the prevailing gap between the supply and demand with respect to cocoa butter, the industry is switching to focus on cocoa butter alternatives at present. Shea butter is used as a cocoa butter alternative in the manufacturing of chocolate and confectionery items in Europe (Naik & Kumar, 2014). Palmitic, stearic, and oleic are the three major fatty acids common to African butter seed fat and shea butter (Adomako, 1977). Therefore, there is a potential to develop African butter seed fat as a cocoa butter alternative.

In the manufacture of a fat spread, different vegetable oils including palm, corn, cottonseed, soy, safflower, and sunflower oils are used. In order to obtain the semi solid nature of the fat spread either partial hydrogenation or blending of oils having different solid fat contents is required. Artificial colourants are also added to obtain a desirable yellow colour in some types of fat spread (Marcus, 2013). Because of the semi solid nature at room temperature and the unique bright yellow colour of African butter seed fat, hydrogenation and addition of colourants are not required. Therefore, the objectives of this study were to determine the applicability of African butter seed fat as a cocoa butter alternative, a type of fat spread, and its suitability in the preparation of cookies via determination of physicochemical properties of African butter seed fat and cocoa fat. Furthermore, a cookie product has been developed by incorporating African butter seed fat and cocoa fat separately and their sensory properties have been compared in order to evaluate their applicability in bakery products such as cookies.

MATERIALS AND METHODS

Materials and chemicals

Seeds of the African butter tree (*Pentadesma butyracea*) were obtained from the Royal Botanical Garden, Peradeniya, Sri Lanka. Ripened cocoa pods were obtained from the Export Agriculture Department, Matale, Sri Lanka.

Absolute ethanol, hydrochloric acid, potassium hydroxide, phenolphthalein, glacial acetic acid, potassium iodide solution, sodium thiosulphate, starch, Wijs solution, cyclohexane, n-hexane, sodium hydroxide, methanol, and concentrated sulphuric acid were purchased from Sigma Aldrich, USA. In addition, authentic standard for gas chromatography (SUPELCO 37 component FAME Mix, 1 x1 mL varied conc, in dichloromethane) and single standards were used for fatty acid profile analysis, with a column capillary gas chromatograph (Agilent HP-88; 100m length, 0.25mm ID).

Pretreatments and pre-preparation techniques

African butter seeds were obtained by removing the mesocarp of fallen fruits and subjected to washing and cleaning, followed by sun drying for 3 ds with 6 h of exposure to sunlight on each day. Then the seeds were cracked by using a hammer (4340 alloy steel) and the cracked pieces were sun dried on raised white polythene mats for 5 ds with 3 h of exposure to the sunlight per day. Cocoa beans were separated from pods and were fermented for 5 ds. Fermented seeds were sun dried on raised white polythene mats for 5 ds with 6 h of exposure to the sunlight. At the end of each hour, African butter seed pieces and cocoa beans were turned and mixed with hands covered with gloves.

A portion of each dried source (African butter seeds and cocoa beans) was ground into a fine powder by using a grinder (Jaipan, Model No.1000). Seed powder was stored in air tight plastic containers to be used in solvent extraction. The remainder of each type, were kept in non-ground form, to be used in physical extraction. The moisture content of the ground seed samples of African butter seeds and cocoa beans was determined (AACC 44-15A) prior to the chemical extraction of fat.

Extraction of fat

Fat was extracted by physical and chemical methods (Physical extraction was employed to avoid the contamination of fat samples with non food grade chemicals, since the cookies are evaluated by the panelists). Physical extraction was conducted using an industrial mini expeller (screw press, single barrel, alloy: steel and

cast iron). Extraction of oil was performed by feeding cracked seed parts, 2-3 cm in average size, to the expeller in small batches. A single extraction was performed for 5 min and the expeller was kept switched off for 10 min under ventilation via an electric fan. This process of extraction was continued with intervals of 10 min. Initially, fat was collected to aluminium vessels and such collected fats were filtered via a muslin cloth into glass containers and stored in freezing conditions (minimum level -2 °C) in a refrigerator until they were used for preparation of cookies.

Chemical extraction was performed using hexane in a Soxhlet apparatus. The extraction was carried out for 6 h. After the extraction procedure hexane was evaporated off using a rotary evaporator (Heidolph 2000) at 65 °C. Extracted fats were stored in labelled air tight glass containers under refrigerated conditions (4-6 °C) until they were taken for physicochemical tests. Oil yield from chemical extraction was determined before subjecting the extracted fats to physicochemical tests.

Determination of physicochemical properties

Slip melting point (Cc 3-25, AOCS 1998), smoke point (Cc 9a -48, AOCS 1998) and chemical properties such as acid value and free fatty acid content (Cc 5a-40, AOCS 1998) and iodine value (Cd Id-92 AOCS 1998), saponification value (Cd 3-25 AOCS 1998) were determined. In addition, colour was determined by using colorimeter (CHN Spec, CS-10) and expressed as L*, a*, b* values. All the measurements were taken for three replicates and the values were expressed as mean ± sd.

Solid fat content was measured at 10 different selected temperatures from 0-45 °C by using a Bruker NMR analyzer (ISO, 2008). Fat sample was initially melted at 80-100 °C for 15 min. A residue free well mixed sample was selected and filled in to 10 mm diameter sample tubes to a height of 4 cm. The sample tubes were maintained at 60 °C for 5 min and then at 0 °C for 60 min. Then the sample was transferred to the temperature at which the particular measurement is needed and maintained at that temperature for 30 min. The samples were measured in triplicates at each selected temperature, 0 °C, 5 °C, 10 °C, 15 °C, 20 °C, 25 °C, 30 °C, 35 °C, 40 °C, and 45 °C. Each sample was inserted into the pulsed NMR spectrometer for a 6 s analysis and a curve was created representing free induction decay (FID) vs. time while displaying the reading of SFC percentage on the monitor at the particular temperature concerned was read off the display on the monitor.

The fatty acid composition of each type of fat was analysed according to the method described by O'Fallon *et al.* (2007) with some modifications. The internal standard C17:0 (10.3 mg dissolved in 1 mL of dichloromethane) was added into a screw capped pyrex culture tube. This was dried under a stream of N₂ gas. Then, 40 µL of the oil sample was added to the culture tube and weighed. Then 0.7 mL of 10 N KOH and 5.3 mL of methanol were added to culture tube and vortexed for 30 seconds. The tubes were incubated in a water bath set at 55 °C for 1.5 h with vigorous shaking for every 20 min. The tubes were allowed to cool in cold tap water to bring to room temperature. Then, 0.58 mL of 24 N H₂SO₄ was added to each tube, the mixture was vortexed well and incubated at 55 °C for 1.5 h with vigorous shaking every 20 min. After completion of the incubation, each tube was cooled in tap water. Following that, about 3 mL of n-hexane was added, and the tube vortexed for 3 min and centrifuged for 5 min at 2000 rpm. The hexane layer was collected into a 5 mL test tube containing 0.1 g of Na₂SO₄. Then it was decanted, vortexed for 10 s, allowed to settle, dried under stream of N₂ and 1.5 mL of dichloromethane added. The tube was vortexed for 10 s and kept for 5 min. After that, the dichloromethane layer was transferred into a GC autosampler vial, and it was dried under N₂ gas. Finally, the volume was made up with 0.5 mL Suprasolv dichloromethane and the sample analyzed using GC-FID.

The weight (in g) of each individual fatty acid (W_X) in 100 g of test sample is expressed as

$$W_X = \frac{A_X \times W_{IS} \times 1.0047 \times R_X \times F_{FAX} \times 100}{A_{IS} \times W_{TS}} \quad \dots(1)$$

where,

- A_X - Peak area counts for FAME_X in test sample
- W_{IS} - Weight of C17:0 TAG internal standard (in g) added to the test sample

1.0047	- Conversion of C17:0 TAG internal standard from TAG to FAME
R_X	- Theoretical flame ionization detector response factor (TCF) for FAMEs relative to 17:0 FAME internal standard
F_{FAX}	- Conversion factor for conversation of FAME _X in the test sample to its corresponding fatty acid
A_{IS}	- Peak area counts of the C17:0 FAME internal standard added to the test sample as 17:0 TAG
W_{TS}	- Weight of test sample in g

GC-parameters:

Injection port temperature: 250 °C; detector temperature: 250 °C; oven temperature: isothermal at 180 °C (32 min), ramped at 20 °C/min to 215 °C (hold 31.25 min); carrier gas: Helium; column head pressure 286 kPa, flow rate 1.0 mL/min, linear velocity 19 cm/s, split ratio 100:1. As the capillary column, Agilent HP-88 (100m length, 0.25mm ID, stationary phase of 88%-Cyanopropyl 12% -aryl-polysiloxane) was used.

Preparation of cookies

This procedure was followed for both African butter seed fat and cocoa fat. Initially, 40 g of fat was allowed to melt. Then 35 g of finely ground and sieved sugar was added in to the melted butter and it was followed by the addition of 80 g of wheat flour. After that, half of an egg yolk and 1 mL of vanilla essence were added and mixed. Then round shapes were made using a mold and baking was done using an oven at 150 °C for 15 min.

Determination of sensory properties of cookies prepared by incorporating the two fats separately

Similar to the acceptance test as described by Choi (2013), a set of 30 subjects were selected randomly for the study as panelists. Those subjects were within the age range of 20-60 years, belonging to both genders, and residing in the Polgahawela city area, North Western province, Sri Lanka. Subjects met following criteria; freedom from any oral disease, freedom from systemic diseases, non smoking, non-alcoholic, not chewing betel, and not under medication as described by Mabbithasri *et al.* (2020). All the panelists were informed in detail about the study after obtaining their consent to participate. A single cookie of weight 5-6 g made by incorporating each type of fat was offered on a white-coloured ceramic dish to every randomly selected panelist to get sensory properties (colour, flavour, texture and overall acceptability) evaluated based on their preference. Fifteen randomly selected subjects were presented with African butter seed fat incorporated cookies initially and then cookies incorporated with cocoa fat while it was done vice versa for the other 15 subjects in order ensure the randomness of presenting the samples. They were advised to cleanse their mouth with warm water (60 °C) before and after evaluating flavour of each sample. The main tool used in collecting data was a ballot paper comprised of 05-point hedonic scale based on consumer preference from like very much to dislike very much as described by Choi (2013). The collected responses were analyzed via Wilcoxon signed rank test by using SPSS (version 25).

RESULTS AND DISCUSSION

The moisture contents of the ground seed powder of African butter seeds and cocoa beans were determined to be 5.82% and 6.24% respectively. Employing a proper drying technique is essential to remove moisture, to facilitate the removal of oil from tissues during extraction and to inactivate some enzymes such as lipase. Oil yields of African butter seeds and cocoa beans via chemical extraction were 38.94% and 44.23% respectively. Tchobo *et al.* (2007) have shown that the oil yield of African butter seeds obtained from 10 different regions of Benin varies from 39.1 to 47.3%. The oil yield obtained for cocoa beans in the present study is lower than the value revealed by Adomako (1976), which was determined to be 53.4%. The oil yield might have been influenced by some factors such as geographical location, climate, and variety.

Physicochemical properties of African butter seed fat and cocoa fat

Table 1 shows physicochemical properties of African butter seed fat and cocoa fat. Slip melting point of African butter seed fat is closer to the value of 37.5 - 38.2 °C as reported by Adomako (1976). The slip melting point of cocoa butter also falls in the melting point range of 29 - 40 °C as reported by Naik and Kumar (2014). As shown by Tchobo *et al.* (2013), the average L* (lightness), a* (redness) and b* (yellowness) values obtained for African butter seed fat that was extracted using the traditional method (grinding and then churning with hot water until fat is separated) are L = 63 ± 20, a = -2.06 ± 1.64 and b = 24.73 ± 1.11. L* a* b* values of African butter seed fat that was extracted mechanically by using a screw expeller in the current study, also show closer values to the fat extracted by traditional means. Colour gets affected mainly due to different postharvest handling practices of the seeds such as drying. A dark-coloured fat is obtained when the seeds are not dried properly and during rainy seasons, as described by Ayegnon *et al.* (2015). The temperature during the expulsion of oil also might influence the colour of the extracted fat. Since the colour values determined in the present study are closer to the previous study, it can be assumed that approximately similar conditions had been employed during postharvest handling of seeds and extraction of fat. Higher L* and b* values correspond to the unique bright yellow colour inherited by African butter seed fat. Because of this natural yellow colour, it is not required to add artificial colourants as in conventional margarine or fat spread production.

Table 1: Physicochemical properties of African butter seed fat and cocoa fat

Property	African butter seed fat	Cocoa butter
Slip melting point	37 °C	35.5 °C
Smoke point	225 °C	238 °C
Colour	L*: 60.47 ± 0.37, a*: -2.84 ± 0.6, b*: 24.14 ± 0.16	L*: 47.05 ± 0.68, a*: 2.74 ± 0.55 b*: 12.36 ± 0.16
Acid value	1.05 ± 0.17 mg KOH/g	2.06 ± 0.21 mg KOH/g
Free fatty acids value	0.53 ± 0.09%	1.04 ± 0.06%
Iodine value	48.65 ± 3.03 g I ₂ /100g	34.31±0.97 g I ₂ /100g
Saponification value	177.0 ± 0.6 mg KOH/g	194.2 ± 1.1 mg KOH/g

Smoke point of African butter seed fat is slightly lower than that of in cocoa fat. In cocoa fat, because of the higher content of saturated fatty acids such as palmitic (C16:0) and stearic (C18:0) acid, the smoke point has a slightly higher value when compared with African butter seed fat. But both values are above 200 °C which is a basic characteristic of oils that are suitable for frying. Smoke point, flash point and fire point are the three specific temperatures that are determined, in order to investigate the thermal stability of fats. Smoke point is the temperature at which a continuous smoke begins to evolve from the sample. With the degradation of sample above the smoke point, volatiles are produced and the rate of evolving those volatiles determines the flash point and fire point. Flash point is the temperature at which the evolved volatiles produce a temporary ignition when a flame is applied, while the fire point is defined as the temperature at which a continuous combustion can be sustained with the application of a flame. Therefore, in this study the smoke point has been determined, since it can be considered that temperatures below that point are in the safe zone for application of fats in food products that are subjected to baking and frying. Further research is required to determine the frying stability of African butter seed fat.

The acid value of African butter seed fat is 1.05 ± 0.17 mg KOH/g while its free fatty acid content (expressed as oleic %) is in compliance with the range of 0.5 ± 0.1% to 2.36 ± 0.1% shown by Tchobo *et al.* (2007) from analyzing fats extracted from *Pentadesma butyracea* kernels collected from 10 different areas in Northern Benin. The acid value of cocoa fat is 2.06 ± 0.21 mg KOH/g and its fatty acid content (expressed as stearic %) is 1.04 ± 0.06%. The acid value obtained for cocoa butter is slightly above the corresponding value reported by Adomako (1976) which was reported as 1.8 mg KOH/g. With that, the free fatty acids content (expressed as stearic %) also has a slight increase when compared with the value of 0.9%, reported by Adomako (1976). But still the free fatty acid content value obtained in the present study is lower than the critical value of 1.75% for cocoa fat as shown by Guehi *et al.* (2010). As revealed by Essien and Tettey (2016), the free fatty acid content is directly proportional to the storage time of cocoa beans and there is an interaction of the

fermentation period with the storage time finally affecting the FFA %. In the present study, the mean acid value of African butter seed fat is lower when compared with the mean acid value of cocoa fat, highlighting the fact that the quality of African butter seed fat is higher and refining steps can be applied effectively.

The iodine value of African butter seed fat is closer to the value of 47.3 g I₂/100g reported by Adomako (1976). In cocoa fat, the iodine value is within the range of 32 - 35 g I₂/100g reported by Naik and Kumar (2014). The iodine value is an index of the degree of unsaturation of fatty acids in a particular oil or a fat. When comparing the iodine values of the two types of fats, African butter seed fat has shown a higher iodine value than that of cocoa fat, indicating a higher level of unsaturated fatty acids in African butter seed fat in comparison to cocoa fat. The saponification value of African butter seed fat is lower when compared with cocoa fat. Saponification value gives an idea about mean molecular weight of the triacylglycerols in the fat sample. Therefore, the relatively lower saponification value of African butter seed fat can be related to its fatty acid composition and their high mean molecular weight.

Solid fat content

Table 2 shows solid fat content values obtained for African butter seed fat and cocoa fat separately at selected temperatures from 0 to 45 °C. SFC curve derived for African butter seed fat (Figure 1), depicts its hardness at temperatures below 20 °C, since the slope of the curve is very low. As depicted in the table 2, SFC percentages obtained for African butter seed fat are higher than 60%, which indicate its characteristic hardness. Within the temperature range 20-25 °C, the initiation of a slope in the curve shows the resistance of African butter seed fat to heat supplied or the resistance to melting. In the range 25-35 °C the curve depicts intensive melting of the African butter seed fat sample. Within this range, the solid fat content has been drastically reduced from 31.80 ± 0.05% to 2.11 ± 0.03%.

The SFC content varies from 31.80 ± 0.05% to 6.85 ± 0.07% within the temperature range of 25 - 30 °C which can be defined as working or utilization temperature range. Devi and Khatkar (2016) reveal that an SFC range of 15-20% at utilization temperature is appropriate for cookie preparation. The SFC content of African butter seed fat from 25 °C to 30 °C approximately fits the SFC range of 15-20%. According to Devi and Khatkar (2016), the liquid fraction of fat at this temperature is responsible for the lubricating effect which can improve the mixing process, whereas the solid fraction is involved in incorporation of air during mixing. The combination of the functionality of these solid and liquid fractions of fat at the utilization temperature results in improving the ultimate functional performance and textural nature of raw fat, as well as foods prepared by incorporating such fats. Since there is a relationship between SFC and characteristics of baked goods, as revealed by Lai and Lin (2006), African butter seed fat can be suggested as a favourable type of fat in preparing bakery items such as cookies.

In addition to that, the SFC profile of African butter seed fat can be compared with SFC curves of different margarine types such as soft margarine, brick margarine, and shelf stable and pastry margarines described by Sahri and Dian (2011), in order to determine the potential in developing it as a type of a margarine. The SFC value of African butter seed fat which is 60.84% at 20 °C is much closer to the SFC range of 65-70% at 20 °C which is the characteristic SFC range of pastry margarine type at that temperature. In addition to that, at 30 °C, African butter seed fat has exhibited a SFC value of 6.85% which is much closer to the SFC range of 8-10% in shelf stable margarine type at the same temperature. Therefore, it can be claimed that African butter seed fat shows an intermediate SFC profile, showing characteristics of both pastry margarine and shelf stable margarine within that particular temperature range of 20-30 °C. Similar to shelf stable margarine, African butter seed fat also exhibits nearly a complete melt down at temperatures above 35 °C, highlighting its convenience in spreading, working at room temperature, and favourable melting behaviour during consumption.

When focusing on cocoa butter (Table 2), higher SFC values at temperatures below 15 °C highlight its hard nature, while the temperature range from 15-25 °C shows its resistance to heating, with the initiation of the slope in the curve as shown in Figure 1. Within the temperature range of 25-35 °C, an intensive melting behaviour is depicted in the SFC curve of cocoa fat. The SFC content at 20 °C and 25 °C are 54.97 ± 0.24% and 36.18 ± 0.87% respectively and those values are lower when compared with the SFC values of cocoa butter in

some previous studies. Ribeiro *et al.* (2012) have depicted the SFC ranges at 20 °C and 25 °C as 60 - 70% and 50 - 60%, respectively. In addition to that, Shukla (2006) has indicated the SFC value of cocoa butter at 25°C as 53.3% for Brazilian cocoa butter. According to Ribeiro *et al.* (2012), there is a correlation between the solid fat content value and the triacyl glycerol (TAG) profile of cocoa butter. Disaturated-monounsaturated triacyl glycerols (TAGs composed of two saturated fatty acids and one monounsaturated fatty acid) are the predominant type of TAG class present in cocoa butter and SFC values vary depending on the content. When the disaturated-monounsaturated TAG level gets reduced in the cocoa butter sample, its solid fat content value decreases more than the expected level. Geographical factors and cocoa variety might be having an influence on this and it has been revealed by Shukla (2006) that SFC values range from 74.8 - 83.7% at 25 °C in cocoa butter available in countries like Ghana, Nigeria, and Malaysia. When considering the application of cocoa fat, its utilization in the preparation of cookies is minimal mainly because of its high cost and lesser availability in the market to purchase in retail amounts. But there is a potential to apply cocoa butter in manufacturing cookies, since there is an extensive melting shown from 25 - 35 °C, which highlights the cooling and creaminess sensation within the mouth during consumption. In addition, the presence of SFC values from $36.14 \pm 0.87\%$ to $11.15 \pm 0.11\%$ in cocoa fat within the utilization temperature range (25-30 °C) is an indication of its suitability to be used in cookie preparation since the ideal SFC in a fat that can be used for cookie preparation is 15 - 20% according to the study conducted by Devi and Khatkar (2016).

Table 2: Solid fat contents of African butter seed fat and cocoa fat measured by NMR (direct)

Temperature (°C)	Solid fat content (%)	
	African butter seed fat	Cocoa fat
0	81.57 ± 0.03	93.15 ± 0.84
5	82.17 ± 0.08	93.31 ± 0.68
10	79.36 ± 0.02	91.27 ± 0.69
15	72.91 ± 0.04	81.06 ± 0.86
20	60.84 ± 0.03	54.97 ± 0.24
25	31.80 ± 0.05	36.14 ± 0.87
30	6.85 ± 0.07	11.15 ± 0.11
35	2.11 ± 0.03	1.64 ± 0.03
40	1.75 ± 0.03	1.93 ± 0.08
45	1.83 ± 0.04	1.97 ± 0.05

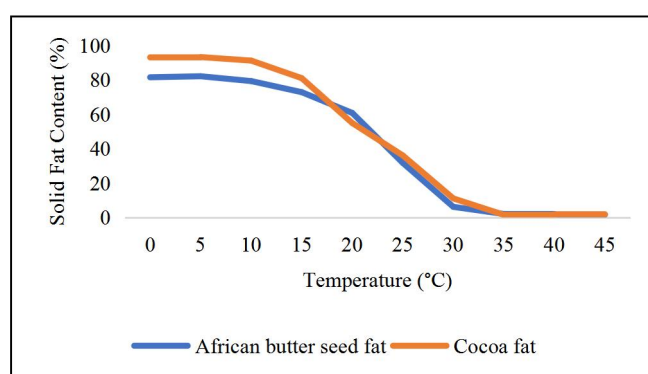


Figure 1: SFC curves for African butter seed fat and cocoa fat

When comparing the two SFC curves of African butter seed fat and cocoa fat, it is clear that there is a slight gap in the curves drawn relative to the SFC values at the same temperature range (Figure 1). A noticeable difference is shown in SFC values within 0 -15 °C while there is a smaller difference within 25 -35 °C among these two types of fats. These contrasts between the two curves can be merged by altering triacyl glycerol composition via

enzymatic transesterification to produce cocoa butter equivalents as highlighted by Naik and Kumar (2014). In addition to that blending of different compatible oils can also be done in order to alter the SFC values at selected temperatures as revealed by Sahri and Dian (2011).

Fatty acid composition of African butter seed fat and cocoa fat

GC chromatograms obtained for the fatty acid composition of African butter seed fat and cocoa fat are shown in the supplementary figures 1 and 2 respectively. Table 3 depicts percentages (by weight) of major fatty acids present in African butter seed fat and cocoa fat. In African butter seed fat, stearic and oleic are the two fatty acids present in abundance with respect to saturated and monounsaturated fatty acid types, respectively. The percentage of stearic acid is in the range 38.4 - 47% in African butter seed fat collected from 10 different regions of Benin, as reported by Tchobo *et al.* (2007). The fatty acid available in the highest percentage is oleic acid, and this value is close to 53.72% with respect to oleic acid in African butter seed fat, as revealed by Ayegnon *et al.* (2014). Linoleic and linolenic acids are the two major poly unsaturated fatty acids present in African butter seed fat, with percentage values of $0.82 \pm 0.00\%$ and $0.20 \pm 0.00\%$ respectively. In addition to that, there are no *trans* fatty acids detected in the analyzed sample of African butter seed fat.

When concerned about the fatty acid composition of cocoa fat, there are three fatty acids present in higher percentages, namely palmitic, stearic and oleic acids. Palmitic and stearic are the two major saturated fatty acid types and their percentage weights were found to be in the ranges of 24.5 - 33.7%, 33.7 - 40.2% respectively, as reviewed by Naik and Kumar (2014). Oleic acid is the major monounsaturated fatty acid present in cocoa fat which amounts to $34.12 \pm 0.14\%$, and that value is close to 36.1% as reported by Adomako (1976). Also, that value fits in to the range of 26.3 - 35% as revealed by Naik and Kumar (2014). With regard to the major types of poly unsaturated fatty acids, linoleic acid content is $2.53 \pm 0.00\%$ while linolenic acid content is $1.23 \pm 0.00\%$ in cocoa fat. There are no *trans* fats detected in the analyzed sample of cocoa fat.

Table 3: Fatty acid composition of African butter seed fat and cocoa fat

Fatty acid	African butter seed fat weight (%)	Cocoa fat weight (%)
Palmitic (C16:0)	2.78 ± 0.11	24.14 ± 0.07
Stearic (C18:0)	39.05 ± 0.16	37.75 ± 0.06
Oleic (C18:1)	56.97 ± 0.27	34.12 ± 0.14
Linoleic (C18:2)	0.82 ± 0.00	2.53 ± 0.00
Linolenic (C18:3)	0.20 ± 0.00	1.23 ± 0.00

When comparing the two fatty acid profiles of African butter seed fat and cocoa fat, they can be considered as approximately similar. However, the content of palmitic acid is significantly higher in cocoa fat than in African butter seed fat. This has resulted in an increase of total saturated fatty acid content in cocoa fat compared to African butter seed fat. The fatty acid profile is directly linked with the triacyl-glycerol (TAG) composition. Most abundant TAGs present in the African butter seed fat are 1(3)-stearoyl-2-oleoyl-3(1)-stearoyl-sn-glycerol (SOS) and 1(3)-stearoyl-2-oleoyl-3(1)-oleoyl-sn-glycerol (SOO) as revealed by Aissi *et al.* (2018). This has led to the presence of a higher content of stearic and oleic acids in African butter seed fat. According to the findings of Adomako (1976), major triacyl glycerols present in cocoa fat are 1(3)-palmitoyl-2-oleoyl-3(1)-stearoyl-sn-glycerol (POS), 1(3)-stearoyl-2-oleoyl-3(1)-stearoyl-sn-glycerol (SOS), and 1(3)-palmitoyl-2-oleoyl-3(1)-palmitoyl-sn-glycerol (POP). This has resulted in increasing the content of the fatty acids, stearic, oleic, and palmitic acids, in cocoa fat. There is a potential to convert selected abundant TAGs of African butter seed fat, namely SOO and SOS, to POS which is the most abundant TAG type in cocoa fat in order to develop African butter seed fat as a cocoa butter alternative. Transesterification, which is performed by using either chemicals or enzymes, can be cited as a method to equalize the TAG composition of African butter seed fat to cocoa fat.

According to Tchobo *et al.* (2013), the major antinutritional constituents found in African butter seeds are phytates and oxalate, which have been quantified as 0.42% and 1.04% respectively. Phytate is present in many food items such as nuts, legumes, cereal germ or bran, beans, carrots, broccoli, potatoes, and wheat. Based on

the findings of Schiemmer *et al.* (2009), the phytic acid contents of oil seeds such as soybeans, linseed, sesame seed, and rape seed are 1.0 - 2.22%, 2.15 - 3.69%, 1.44 - 5.36% and 2.50% respectively. Therefore, the phytate content in African butter seeds can be considered as much lower when compared with these oil seeds. As described by Schiemmer *et al.* (2009), phytates are known to be partially degraded in the human stomach and intestine. And also, those can be degraded by employing different processing conditions at temperatures above 110 °C, which requires further research with respect to African butter seeds. Oxalates are also present in many foods such as spinach, almonds, cashews, beet, and potatoes. Since oxalates and phytates are water soluble, boiling of African butter seeds in water is recommended as a possible pretreatment method, which is already followed in traditional processing of African butter seed fat.

Apart from naturally occurring antinutritional compounds, there is a tendency towards forming some process induced toxins such as polycyclic aromatic hydrocarbons (PAH), due to exposure of oils to a high temperature above 400 °C. Pyrolysis of oil starts at temperatures above 200 °C according to Shahidi *et al.* (1997). Even though such very high temperatures are not achieved during the present study, necessary precautions were implemented to avoid generation of high temperature during the drying process and extraction of fat using an oil screw expeller. Use of non-heating surfaces when drying, limiting the time of exposure to sun light, performing oil extraction in a discontinuous manner allowing to cool down the interior of the machine and collecting oils initially into the aluminium containers are some of the precautionary measures taken.

Sensory evaluation of cookies prepared by incorporating the two fats

Cookies prepared by incorporating the two types of fats separately were presented to the selected panelists. Preference levels for sensory attributes of colour, flavour, texture and overall acceptability for cookies prepared by incorporating the two fats are shown in Supplementary Figure 3. Phrases with scores from 5 to 1, which correspond to different degrees of preference, from 'like very much' (corresponding score = 5) to 'dislike very much' (corresponding score = 1) have been used. In addition, Table 4 shows a summary of Wilcoxon signed rank test results which were obtained by analyzing sensory data collected for the two cookie types. There is a significant statistical difference between the preferences for colour of cookies prepared by incorporating the two kinds of fats ($p < 0.05$). The preference of the panelists for colour of cookies prepared from African butter seed fat is higher than that for cookies prepared from cocoa butter. There is no significant statistical difference with respect to the preference shown towards flavour of the two types of cookies ($p > 0.05$). Where the subjects' preference for texture is concerned, there is no significant statistical difference with respect to the two cookie types ($p > 0.05$). With regard to the preference for overall acceptability, there is no significant statistical difference in relation to two types of cookies ($p > 0.05$).

Table 4: Wilcoxon Signed ranks for the preference for cookies made by incorporating African Butter fat and cocoa fat

Sensory attributes of cookie samples	Ranks	N	Significance (p)
Colour, AFBF ₁ - Colour, CF ₁	Negative ranks	4	0.018
	Positive ranks	14	
	Ties	12	
	Total	30	
Flavour, AFBF ₁ - Flavour, CF ₁	Negative ranks	6	0.193
	Positive ranks	11	
	Ties	13	
	Total	30	
Texture, AFBF ₁ - Texture, CF ₁	Negative ranks	9	0.617
	Positive ranks	7	
	Ties	14	
	Total	30	
Overall acceptability, AFBF ₁ - Overall acceptability, CF ₁	Negative ranks	2	0.132
	Positive ranks	6	
	Ties	22	
	Total	30	

AFBF₁: Cookies prepared by incorporating African butter seed fat, CF₁: Cookies prepared by incorporating cocoa fat.

CONCLUSION

The physicochemical properties of African butter seed fat determined in this study reflect the potential of using this fat as an edible fat that can be utilized even under different processing conditions. Fatty acid profiles of the two fat types are approximately similar and there is a good potential to develop African butter seed fat as a cocoa butter alternative. The SFC profile of African butter seed fat, specially within the temperature range of 25-30 °C indicates the applicability of this fat in bakery items such as cookies. There is no significant difference with respect to the preference for flavour, texture, and overall acceptability among panelists for the two cookie types developed by incorporating African butter fat and cocoa fat ($p > 0.05$), while there is a significant difference for colour ($p < 0.05$).

REFERENCES

- Adomako D. (1977). Fatty acid composition and characteristics of *Pentadesma butyracea* fat extracted from Ghana seeds. *Journal of the Science of Food and Agriculture* **28**: 384–386.
DOI: <https://doi.org/10.1002/jsfa.2740280411>
- AACC (2000). *Approved Methods of the AACC: Method 44-15A*, 10th edition. Cereals and Grains Association, St. Paul, MN, USA.
- AOCS (1998). *Official Methods and Recommended Practices: Method Cc 3-25*, 5th edition. American Oil Chemists' Society, Urbana, Illinois, USA.
- AOCS (1998). *Official Methods and Recommended Practices: Method Cc 5a-40*, 5th edition. American Oil Chemists' Society, Urbana, Illinois, USA.
- AOCS (1998). *Official Methods and Recommended Practices: Method Cc 9a-48*, 5th edition. American Oil Chemists' Society, Urbana, Illinois, USA.
- AOCS (1998). *Official Methods and Recommended Practices: Method Cd 3-25*, 5th edition. American Oil Chemists' Society, Urbana, Illinois, USA.
- AOCS (1998). *Official Methods and Recommended Practices: Method Cd Id-92*, 5th edition. American Oil Chemists' Society, Urbana, Illinois, USA.
- Aissi M.V., Tchobo F.P. & Soumanou M.M. (2018). Chemical composition of traditionally processed *Pentadesma butyracea* sabine seeds and butter. *Journal of Microbiology, Biotechnology and Food Sciences* **7**(6): 576–579.
DOI: <https://doi.org/10.15414/jmbfs.2018.7.6.576-579>
- Ayegnon B. P., Kayode P.A.P., Tchobo F.P., Asokpota P., Soumanou M.M. & Hounhouigan D.J. (2014). Profiling the quality characteristics of the butter of *Pentadesma butyracea* with reference to shea butter. *Journal of the Science of Food and Agriculture* **95**(15): 3137–3143.
DOI: <https://doi.org/10.1002/jsfa.7052>
- Ayegnon B. P., Kayode P.A.P., Gnanvi G., Madode Y., Balbine F.A., Azokpota P., Soumanou M.M. & Hounhouigan D.J. (2015). Screening of the kernels of *Pentadesma butyracea* from various growing sites of Benin and evaluation of their antioxidant pigments content. *African Journal of Biotechnology* **14**(37): 2724–2733.
DOI: <https://doi.org/10.5897/AJB2015.14833>
- Badoussi E., Azokpata P., Madode Y.E., Kayode P.A.P., Dossou A., Soumanou M. & Hounhouigan D.J. (2014). Variations in the traditional processing methods of *Pentadesma butyracea* butter in northern Benin. *Food Chain* **4**(3): 261–274.
DOI: <https://doi.org/10.3362/2046-1887.2014.026>
- Beckett S.T. (2009). Traditional chocolate making. In: *Industrial Chocolate Manufacture and Use*, pp. 1-9. Wiley-Blackwell, West Sussex, UK.
- Belitz H.-D., Grosch W. & Schieberle P. (2009). Lipids. In: *Food Chemistry*, pp 158-245. Springer-Verlag Berlin, Germany.
- Bernolde P., Kayode A.P.P., Nassia I., Barea B., Tchobo F.P. & Hounhouigan D.J. (2015). Effects of storage conditions on the fatty acid composition of the butter of tallow tree (*Pentadesma butyracea*). *Journal of Applied Biosciences* **92**(1): 8630–8638.
DOI: <https://doi.org/10.4314/jab.v92i1.7>
- Choi S.E. (2013) Sensory evaluation. In: *Food Science: An Ecological Approach* (eds. S. Edelman), pp. 84–111. Jones & Bartlett Learning LLC, Burlington, Massachusetts, USA.
- Devi A. & Khatkar B.S. (2016). Physicochemical, rheological and functional properties of fats and oils in relation to cookie quality: A review. *Journal of Food Science and Technology* **53**(10): 3633–3641.
DOI: <https://doi.org/10.1007/s13197-016-2355-0>
- Dhaka V., Gulia N., Ahlawat K.S. & Khatkar B.S. (2011). Trans fats-sources, health risks and alternative approach: A review. *Journal of Food Science and Technology* **48**(5): 534–541.
DOI: <https://doi.org/10.1007/s13197-010-0225-8>
- Essien W.A.J. & Tetley E. (2016). Fat content and free fatty acid level of cocoa beans (*Theobroma cocoa*) relative to

- fermentation and storage periods. *Proceedings of the 10th International Conference on Controlled Atmosphere and Fumigation in Stored Products (CAF2016)*, 6-11 November. New Delhi, India, pp. 58–61.
- Guehi T., Danide A.T., Dabonne S. & Kedjebo, K.B.D. (2010). Performance of different fermentation methods and the effect of their duration on the quality of raw cocoa beans. *International Journal of Food Science and Technology* **45**(12): 2508–2514.
DOI: <https://doi.org/10.1111/j.1365-2621.2010.02424.x>
- ISO (2008). *ISO 8292-1:2008-Animal and Vegetable Fats and Oils - Determination of Solid Fat Content by Pulsed NMR*, 1st edition. International Organization for Standardization, Geneva, Switzerland.
- Lai H.M. & Lin T.C. (2006). Bakery products: science and technology. In: *Bakery Products: Science and Technology*. (eds. Y.H. Hui, H.H. Corke & H.I. De Leyn), pp 3–65. Nip WK, Cross N Blackwell Publishing, Hoboken, New Jersey, USA.
DOI: <https://doi.org/10.1002/9780470277553.ch1>
- Mabbithasri A, Jayaraj G. & Dev R.G. (2020). Effect of age on taste perception- A review. *European Journal of Molecular and Clinical Medicine* **07**(01): 2941–2948.
- Marcus J.B. (2013). Chapter 6-Lipids basics: Fats and oils in foods and health: Healthy lipid choices, roles and applications in nutrition, food science and the culinary arts. In: *Culinary Nutrition* (eds. J.B. Marcus), pp 231-277. Academic Press, USA.
DOI: <https://doi.org/10.1016/B978-0-12-391882-6.00006-6>
- Naik B. & Kumar V. (2014). Cocoa Butter and Its alternatives: A review. *Journal of Bioresource Engineering and Technology* **1**: 7–17
- O’Fallon J.V., Busboom J.R., Nelson M.L & Gaskins C.T. (2007). A direct method for fatty acid methyl ester synthesis: Application to wet meat tissues, oil and feed stuffs, *Journal of Animal Science* **85**(06): 1511–1521.
DOI: <https://doi.org/10.2527/jas.2006-491>
- Ribeiro A.P.B., Silva R.C., Gioielli L.A., Goncalves M.I.A., Grimaldi R., Goncalves L.A.G. & Keickbusch T.G. (2012). Physico-chemical properties of Brazilian cocoa butter and industrial blends Part I - Chemical composition, solid fat content and consistency. *Grasas y Aceites* **63**(01): 89–99.
DOI: <https://doi.org/10.3989/gya.069111>
- Sahri M.M. & Dian N.L.H.M. (2011). Formulation of trans-free and low saturated margarine. *Journal of Oil Palm Research* **23**: 958–967.
- Schlemmer U., Frolich W., Prieto R.M. & Grases F. (2009). Phytate in foods and significance for humans: Food sources, intake, processing, bioavailability, protective role and analysis. *Molecular Nutrition and Food Research* **53**: 330–375.
DOI: <https://doi.org/10.1002/mnfr.200900099>
- Shahidi F., Wanasundara P.K.J.P.D. & Wanasundara U.N. (1997). Changes in edible fats and oils during processing. *Journal of Food Lipids* **4**: 199–231.
DOI: <https://doi.org/10.1111/j.1745-4522.1997.tb00093.x>
- Shukla V.K.S. (2006). Cocoa butter, and cocoa butter equivalents cocoa butter substitutes. In: *Handbook of Functional Lipids*. (eds. C.C. Akoh). pp. 279–307. CRC Press, Boca Raton, Florida, USA.
- Tchobo F.P., Alitanou G., Laguerre M. & Natta R. (2013). Evaluation of the chemical composition of *Pentadesma butyracea* butter and defatted kernels. *International Journal of Biosciences* **3**(1): 101–108.
- Tchobo F.P., Natta A.K., Barea B., Barouh N., Piombo G., Pina M., Villeneuve P., Soumanou M.M. & Sohounhloue D.C.K. (2007). Characterization of *pentadesma butyracea sabine* butters of different production regions in Benin. *Journal of American Oil Chemists’ Society* **84**(8): 755–760.
DOI: <https://doi.org/10.1007/s11746-007-1102-0>
- Tchobo F.P., Piombo G., Pina M., Soumanou M.M., Villeneuve P. & Sohounhloue D.C.K. (2009). Enzymatic synthesis of cocoa butter equivalent through transesterification of *Pentadesma butyracea* butter. *Journal of Food Lipids* **16**(4): 605–617.
DOI: <https://doi.org/10.1111/j.1745-4522.2009.01169.x>
- Wilczek M.M., Olszewski R. & Krupienicz A. (2017). Trans-Fatty Acids and cardiovascular disease: Urgent need for legislation. *Cardiology* **138**(4): 254–258.
DOI: <https://doi.org/10.1159/000479956>

Link to download supplementary data:

<https://jnsfsl.sjoi.info/articles/10.4038/jnsfsr.v51i1.10982/galley/7263/download/>

RESEARCH ARTICLE

Germplasm Characterization

Assessment of submergence stress responses and mining allelic variations of submergence tolerance gene *Sub1A* in Sri Lankan rice germplasm¹.

T Kariyawasam¹, D Nanayakkara¹, A Sumanarathna¹, D Weerasinghe², L Suriyagoda³ and D Jayatilake^{1*}

¹Department of Agricultural Biology, Faculty of Agriculture, University of Peradeniya Peradeniya, Sri Lanka.

²Regional Rice Research and Development Centre, Bombuwala, Sri Lanka.

³Department of Crop Science, Faculty of Agriculture, University of Peradeniya, Peradeniya, Sri Lanka.

Submitted: 14 March 2022; Revised: 16 July 2022; Accepted: 26 August 2022

Abstract: The development of submergence tolerant (ST) rice cultivars is a priority in rice breeding programmes globally, as floods significantly curtail rice production. *Sub1A* is the major known gene conveying submergence tolerance in rice, carrying two variants; *Sub1A-1* (tolerance allele) and *Sub1A-2* (susceptible allele). Sri Lanka hosts genetically diverse rice germplasm; however, the allelic diversity of the *Sub1A* gene among the Sri Lankan rice germplasm remains unknown. Hence, the current study focuses on the assessment of submergence stress responses and identification of the allelic diversity of the *Sub1A* gene in a panel of 64 Sri Lankan rice varieties/accessions. Submergence stress responses of the rice panel were evaluated and *Sub1A* allelic variations were assessed using a modified gel-based marker, *ABUOP0003*. A Bayesian approach was used to assess the genetic structure of the rice panel and its association with the *Sub1A* alleles was explored. Thirteen rice accessions/varieties showed significantly similar ($p > 0.05$) survival percentages (SP - 77 to 93%) as ST reference FR13A. The *ABUOP0003* marker assay revealed that 13 rice accessions/varieties carry *Sub1A-1*. The rice accessions *Godaheenati*, *Heenkarayal*, *Goda wee* and *Dik wee* carried the *Sub1A-1* allele, as well as expressing a tolerance response to submergence stress. No significant association ($p < 0.05$) was observed between the *Sub1A* alleles and submergence stress responses indicating additional genes at play. The deduced genetic structure of the rice panel revealed two genetically isolated gene pools, and the *Sub1A* alleles did not associate with any specific gene pool, indicating that the allele divergence pre-dates germplasm introductions and varietal development attempts in Sri Lanka.

Keywords: Marker *ABUOP0003*, rice, Sri Lankan rice germplasm, *Sub1A-1* allele, submergence tolerance.

INTRODUCTION

Among the widely cultivated crops, rice (*Oryza sativa* L.), despite its semi-aquatic habit, is one of the most flood-prone crops. During rainy seasons paddy fields are subjected to frequent flooding due to poor drainage, which results in partial or complete inundation for prolonged periods. This limits the supply of oxygen and sunlight to rice plants, hindering photosynthesis and leading to a shortage of overall cellular energy (Loreti *et al.*, 2016). It is reported that more than 15% of the global paddy fields are affected by floods annually, causing significant harvest losses (Bailey-Serres & Voisenek, 2008).

Rice can be subjected to submergence stress at any growth stage. Complete submergence at the germination stage could result in poor germination, developmental delays, and seedling death due to anoxia or hypoxia stress conditions (Ismail *et al.*, 2009; Loreti *et al.*, 2016). However, rice plants carrying genetic tolerance could germinate even under such conditions, due to adaptations such as rapid coleoptile elongation and delayed radicle development (Ismail *et al.*, 2009; Magneschi & Perata, 2009; Hattori *et al.*, 2011). During the vegetative phase (seedling stage or tillering stage), submergence tolerant plants can withstand inundation in

¹Nanayakkara N.H.L.D.L.D. & Jayatilake D.V. (2020). Marker ABUOP0003: A Modified Molecular Marker for Gel-based Genotyping of Submergence Tolerance Gene *Sub1A* in Rice. In: Proceedings of the 9th YSF symposium, 13 November. pp. 207.

* Corresponding author (djayatilake@agri.pdn.ac.lk;  <https://orcid.org/0000-0002-9909-1437>)



This article is published under the Creative Commons CC-BY-ND License (<http://creativecommons.org/licenses/by-nd/4.0/>). This license permits use, distribution and reproduction, commercial and non-commercial, provided that the original work is properly cited and is not changed in anyway.

flood waters for 10-14 days. As an adaptation to withstand submergence stress the tolerant plants either maintain a suppressed growth (up to an inundation period of 2 weeks; Bailey-Serres *et al.*, 2010) or increase their height (up to an inundation period of 4 weeks; Hattori *et al.*, 2011). Even though most tolerant rice plants will resume their growth with the receding flood waters, some plants will eventually die due to lodging and exhaustion of energy reserves (Winkel *et al.*, 2013).

Tolerance to submergence is genetically controlled by quantitative trait loci (QTL). Among them, *Sub1* is the major QTL involved with submergence tolerance in rice, and it is mapped to the rice chromosome 9 (Xu & Mackill, 1996). The *Sub1* is the main QTL conveying submergence tolerance and it accounts for 69% of the phenotypic variance in rice submergence tolerance (Xu & Mackill, 1996). The *Sub1* consists of three main genes, *Sub1A*, *Sub1B*, and *Sub1C* (Xu *et al.*, 2006). Of the three genes, *Sub1A* is the major contributor towards submergence tolerance. The *Sub1A* gene is known to be bi-allelic (*Sub1A-1* and *Sub1A-2*), where *Sub1A-1* is known to convey a tolerance response and *Sub1A-2* a susceptible response to submergence stress (Xu *et al.*, 2006). According to Xu *et al.* (2006), the *Sub1A* gene is absent in *japonica* rice varieties and the two alleles of *Sub1A* are reported in some *indica* rice varieties. Identification of rice accessions/varieties carrying the tolerance *Sub1A-1* allele will give the rice breeders the ultimate advantage of incorporating the best genetic background against submergence stress in released rice varieties. In previous studies, Sri Lankan traditional rice accessions *Kurkaruppan*, *Godaheenati*, and *Thavalu* have been identified to carry the *Sub1A-1* tolerance allele (Vergara & Mazaredo, 1975; Xu & Mackill, 1996; Xu *et al.*, 2006; Bailey-Serres *et al.*, 2010; Panda *et al.*, 2021). However, the *Sub1A* alleles carried by most Sri Lankan rice accessions/varieties remain unknown. The availability of this vital genomic information is beneficial for rice breeders to make informed decisions in rice breeding programmes. Therefore, in the current study, submergence tolerance responses of 64 Sri Lankan rice accessions/varieties, along with two known submergence stress response references FR13A for tolerance and *Swarna* for susceptibility to submergence (Xu *et al.*, 2006; Neeraja *et al.*, 2007; Singh *et al.*, 2010; Emerick & Ronald, 2019; Baksh *et al.*, 2021) were assessed in a replicated field trial in artificial screening tanks. Further, the *Sub1A* alleles carried by the respective rice accession/variety were identified using a modified gel-based molecular marker, to identify and recommend potential donors carrying *Sub1A-1* mediated genetic tolerance to submergence for the use in rice breeding programmes.

MATERIALS AND METHODS

Plant material

For the current study, a panel of 66 rice accessions consisting of 40 Sri Lankan newly improved rice varieties (SLNIV), 24 Sri Lankan traditional rice accessions (SLTA), and two references (submergence tolerant reference line FR13A and submergence susceptible reference variety *Swarna*) were used (Supplementary file S1). Rice seeds were sourced from the Plant Genetic Resources Centre, Gannoruwa, Sri Lanka and the Regional Rice Research and Development Centre, Bombuwala, Sri Lanka. DNA extraction of these rice accessions/varieties was carried out using a modified CTAB method (Doyle & Doyle, 1987).

Genetic structure and diversity analysis

Sixty-four rice accessions consisting of SLNIVs and SLTAs were subjected to PCR amplification using 12 unlinked molecular markers representing all rice chromosomes (Supplementary file S2). A PCR amplification was carried out in a thermal cycler (CT1000, Bio-Rad, USA) using a 15 µL final PCR reaction volume with 150 ng DNA template, 1× Gotaq® Green Master Mix (Promega Corporation, Madison, Wisconsin, USA), 0.33 µM forward and reverse primers each, volumed up with nuclease free water (Promega Corporation, Madison, Wisconsin, USA). The PCR amplicons were resolved and visualized on a 3% (w/v) Agarose gel (Sigma Aldrich, Merck group, Germany) pre-stained with 5% (v/v) ethidium bromide (Sigma Aldrich, Merck group, Germany) using a gel documentation system (UVCI-1100, Major Science, USA). The rice accessions/varieties were genotyped based on the resulting band sizes defined based on a 100 bp DNA ladder (Promega Corporation, Madison, Wisconsin, USA).

Bayesian structure analysis was performed using an admixture model in Structure v2.3.4 (Pritchard *et al.*, 2000). To resolve the optimum most probable number of ancestral clusters (K), the score matrix was analyzed

assuming $K = 1$ to $K = 10$ clusters with repetitive ten runs for each K , 500,000 Markov Chain Monte Carlo iterations (MCMC), and a burn-in period of 200,000 iterations. The optimum K was derived based on log-likelihood values in Structure Harvester v0.6.93 (Earl & vonHoldt, 2012) based on the delta- K against K Evanno plot. The optimum K value was used with 700,000 MCMC iterations and a burn-in period of 300,000 iterations for the final run in Structure v2.3.4. The resulting outcome was modified using Structure Plot v2.0 (<http://omicsspeaks.com/strplot2/>) and the resulting plot and the probability values were examined to deduce the possible historical genetic admixtures present within the rice panel considered.

Allelic characterization of rice panel for *Sub1A* using *ABUOP0003* marker

The *Sub1A-1* genomic sequences of the rice breeding line IR40931 (a descendant of the submergence tolerant breeding line FR13A) were retrieved from the National Centre for Biotechnology Information (NCBI) repository (GenBank accession number: DQ011598; Xu *et al.*, 2006), and *Sub1A-2* genomic sequence of the Cultivar 93-11 (a submergence susceptible cultivar) was retrieved from the Gramene Database (Gene ID: BGIOGA038325; Ganie *et al.*, 2020). The sequences were aligned using the ClustalW feature (Thompson *et al.*, 2003) in Geneious v7.1.3 (Kearse *et al.*, 2012), and the MAPK (mitogen-activated protein kinases) site carrying the T/C SNP assayed by the previously published dominant sequence tagged site (STS) marker *AEX1* (Septiningsih *et al.*, 2009) was annotated. Based on Septiningsih *et al.* (2009), the sequences of the *AEX1* forward (*AEXF*; common primer hereinafter named as *ABUOP0003F*; 5'-AGGCGGAGCTACGAGTACCA-3' sequence) and allele specific primer (*AEX1R*; T allele specific primer at MAPK site hereinafter named as *ABUOP0003R1*; 5'-GCAGAGCGGCTGCGA-3' sequence) were retrieved and annotated on to the *Sub1A* sequence alignment of IR40931 and Cultivar 93-11. To convert the dominant *AEX* marker to a co-dominant state, a second allele specific primer was designed targeting the alternative allele at the MAPK site (C allele specific primer referred hereinafter as *ABUOP0003R2*; 5'-GCAGAGCGGCTGCGG-3' sequence) using the Primer3 (Untergasser *et al.*, 2012) feature in Geneious v7.1.3 (Kearse *et al.*, 2012).

The two primer pairs *ABUOP0003F/R1* and *ABUOP0003F/R2* were separately assayed on three rice accessions (FR13A, known to carry *Sub1A-1*; Cultivar 93-11, known to carry *Sub1A-2*; and *Swarna*, known not to carry the *Sub1A* gene) and an artificial heterozygote (created by mixing equal quantities of DNA of FR13A and Cultivar 93-11). The PCR amplification of *ABUOP0003* was carried out for the DNA samples using a 15 μ L final PCR reaction volume containing 150 ng template DNA, 1 \times of GoTaq[®] Green Master Mix (Promega, USA), 0.33 μ M concentration of the primer combination *ABUOP0003F/R1* and 0.26 μ M of *ABUOP0003F/R2* in a thermal cycler (CT1000, Bio-Rad, USA) with 1 mg/mL Bovine Serum Albumin. For the non-template control sample, template DNA was replaced by nuclease-free water (Promega, USA). The touchdown PCR programme consisted of the following steps: an initial denaturation step at 95 °C for 5 min followed by 10 cycles of PCR amplification with 30 s denaturation step at 95 °C, 30 s primer annealing touchdown step at 65 °C with a drop of 0.5 °C per each cycle and 45 s primer extension step at 72 °C. This was followed by 30 cycles of 30 s denaturation step at 95 °C, 30 s primer annealing at 60 °C and 45 s primer extension step at 72 °C and a final primer extension step for 5 min at 72 °C. The amplified products were resolved and visualized on a pre-stained 3% (w/v) agarose gel with 5% (v/v) ethidium bromide. In order to resolve the same sized allele-specific products resulted from the separate-tube PCR (carried out with primer combinations of *ABUOP0003R1/F* and *ABUOP0003R2/F*) as a co-dominant assay, the resultant PCR products of the same DNA samples were loaded sequentially with a 10 min interval apart. The gel image was captured using a gel documentation system (UVCI-1100, Major Science, USA) and the *Sub1A* alleles were scored as *Sub1A-1* 'tolerant allele', *Sub1A-2* 'susceptible allele' or as heterozygous in the tested rice panel. In the event of repeated no amplification, the reason was thought of as absence of the *Sub1A* gene or a PCR failure. The *ABUOP0003* assay was repeated for the remaining accessions/varieties of the core rice panel and the respective alleles carried by them were determined.

Field evaluation for submergence stress responses

Field evaluation of the 66 rice accessions/varieties for submergence stress responses was conducted at the Regional Rice Research and Development Centre, Bombuwala, Sri Lanka, following methods described by Singh *et al.* (2010) and Emerick & Ronald (2019) in artificial screening tanks. Healthy rice seeds from each rice accession/variety were sown onto paddy soil-filled troughs, following a completely randomized design layout in

three replicates. After 2 wks, in each replicate, the additional seedlings were thinned out leaving ten healthy seedlings with similar physical appearance. On the 14th day after sowing, the number of surviving seedlings was counted and the seedling troughs intended for submergence stress treatment were placed in concrete tanks filled with irrigated water to a 1 m depth for a duration of 2 wks. The troughs intended to serve as the control experiment were maintained in a separate tank without submerging and were kept well-watered. At the 14th day after submergence, the seedling troughs in the submergence stress treatment were de-submerged for a period of 14 ds and the survival percentage of each rice accession/variety was calculated based on the number of surviving seedlings. The survival rates of the control experiment were used to check for germination and general survival of seedlings during the experimentation period, where above 80% survival at the end of 21 ds after sowing was considered as the acceptable standard. For the treatment experiment, the estimated median of the survival percentage for each accession/variety was calculated using the Friedman test in Minitab 17 (Minitab, Inc.; www.minitab.com). Based on the estimated median scores, the rice accessions/varieties, which showed no significant difference ($p > 0.05$) to FR13A, the known submergence tolerant line, were grouped as ‘tolerant’. Further, the rice accessions/varieties which showed no significant difference ($p > 0.05$) to *Swarna*, the known submergence susceptible variety, were grouped as ‘susceptible’ and the rice accessions/varieties, which are significantly more susceptible ($p > 0.05$) than *Swarna*, were grouped as ‘highly susceptible’. The accessions/varieties categorized in-between were considered as the ‘intermediate’ group. A pairwise comparison was carried out using the Mann-Whitney U test, and a Box and Whiskers plot was constructed in Minitab 17 (Minitab, Inc.; www.minitab.com) to visualize the survival percentage of the accessions/varieties carrying *Sub1A-1* and *Sub1A-2* under submergence stress.

RESULTS AND DISCUSSION

Changes in the global climate have made rainfall patterns unpredictable leading to frequent inundation of lowland rain fed paddy fields for prolonged periods causing submergence stress in rice plants. This has led to a significant decrease in the productivity of these lands and the situation is worsening as most rice varieties in cultivation are not suitable for such flood-prone areas. Therefore, with limited options to prevent flooding from devastating the croplands, exploration of genetic potential in rice to survive prolonged submergence and recovery is an important aspect that has caught the attention of the rice breeders globally. Sri Lanka is host to many rice accessions, where the genetic potential of some Sri Lankan rice germplasm (SLNIVs and SLTAs) in terms of tolerance to submergence has been reported in several studies (Ranawake *et al.*, 2013; Ranawake *et al.*, 2014) and in varietal descriptors. However, the submergence response of many other accessions, especially some of the SLTAs remain unknown.

Submergence tolerance in rice is controlled by the *Sub1* gene cluster, with major tolerance conveyed via *Sub1A* gene. However, the alleles of *Sub1A* carried by most Sri Lankan rice accessions/varieties remain unknown to date. In the current study, FR13A (the tolerance reference) and *Swarna* (the susceptible reference) were used to identify submergence tolerant and susceptible rice accessions/varieties from a core rice panel consisting of 64 rice accessions/varieties (40 SLNIVs and 24 SLTAs) in a replicated field trial conducted in artificial screening tanks and *Sub1A* alleles carried by these rice accessions/varieties were identified using a modified gel-based DNA marker for the use in rice breeding programmes.

Genetic structure and diversity analysis of the core rice panel

To understand the genetic structure of the core rice panel used in the current study, a Bayesian genetic assessment analysis was conducted. Based on the Structure Harvester Evanno plot, the optimum most probable number of ancestral clusters (K; Figure 1A) for the study panel was set at K = 2 (Figure 1B - Group 1 (green) and Group 2 (brown)). Group 1 consisted of 39 assigned genotypes, all belonging to SLNIVs, and Group 2 consisted of 18 assigned genotypes belonging to SLTAs ($\geq 95\%$ assignment probability). The remaining seven accessions/varieties were grouped as carrying historical genetic admixtures, with *Murungakayan*, *Maa wee* and Bw 272-6b resembling mostly Group 1 (with an assignment probability 64-77%), and *Pachchaperumal*, *Pokkali*, *Dahanala* and *Dik wee* resembling mostly Group 2 (with an assignment probability of 88-94%). Further, in the core rice panel, 97.5% of the SLNIVs were assigned to Group 1 and 75% of the SLTAs were assigned to Group 2. Hence in general SLNIVs and SLTAs are representing genetically isolated gene pools at a $\geq 95\%$ assignment probability.

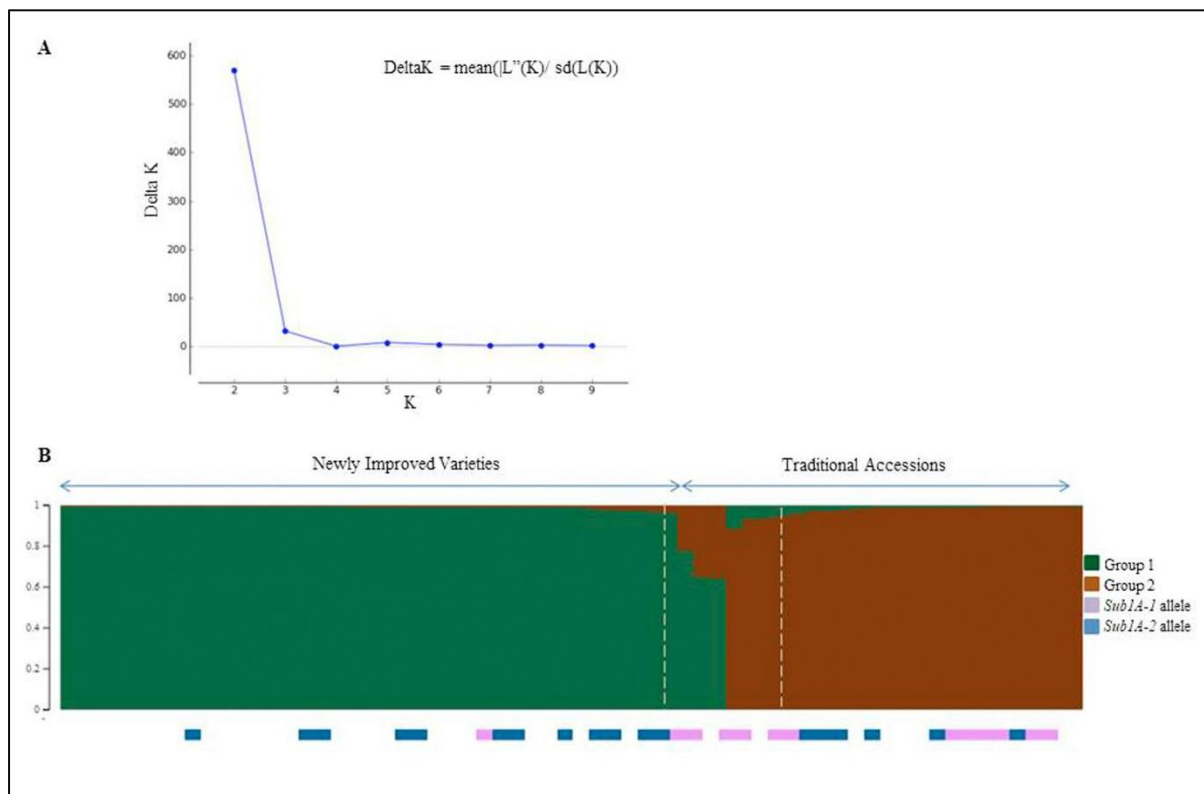


Figure 1: Illustration of (A) Structure Harvester Evanno plot with optimal K and (B) genetic structure of 64 Sri Lankan rice accessions/variety based 12 genome-wide unlinked DNA markers and the variation of *Sub1A* alleles based on the *ABUOP0003* marker

Characterization of rice accessions for *Sub1A* alleles with *ABUOP0003*

The major gene conveying submergence tolerance in rice is *Sub1A*, and of its two allele forms (*Sub1A-1* and *Sub1A-2*) only *Sub1A-1* conveys tolerance to submergence stress (Xu *et al.*, 2006). Therefore, the identification of rice accessions/variety that carry the tolerance allele *Sub1A-1* is important to make informed decisions at critical decision making junctions in rice breeding programmes. To track the *Sub1A* alleles, the marker *AEX*, which interrogates an SNP at the MAPK site in the *Sub1A* gene, is commonly used. According to Xu *et al.* (2006) and Septiningsih *et al.* (2009), *AEX* is a dominant STS marker designed to amplify the *Sub1A-1* tolerance allele (T of codon TCG; resulting in a serine at the 186 amino acid position in the SUB1A amino acid sequence), but not the *Sub1A-2* susceptible allele (C of codon CCG; resulting a proline at the same amino acid position). However, due to its dominant nature, the marker *AEX* was unable to differentiate heterozygotes and the *Sub1A-2* allele from an absent *Sub1A* gene or a failed PCR reaction. As a result, a secondary site in the *Sub1A* gene was targeted using the cleaved amplified polymorphic sequence (CAPs) marker *GnS2* (Neeraja *et al.*, 2007), where the tolerant allele (A) and the susceptible allele (G) could be differentiated with a subsequent restriction enzyme digestion with *AluI/PvuII* enzymes. Though *GnS2* is a codominant marker, the need to use restriction enzyme digestion makes it expensive and time inefficient. As a result, Moon *et al.* (2019) designed a Kompetitive allele-specific polymorphism (KASP) marker covering both sites targeted by *AEX* and *GnS2* for rapid codominant detection of the *Sub1A* alleles. However, the use of KASP markers is restricted in technology-limited countries and hence, in the current study, a modification to the *AEX* marker assay was introduced to amplify the MAPK site polymorphism as a gel-based codominant marker. The modified gel-based marker is hereinafter presented as *ABUOP0003*. The *ABUOP0003* marker assay comprises of three primers (Figure 2A); forward primer of the marker *AEX* as the common forward primer (*ABUOP0003F*), the tolerance allele specific *AEX* reverse primer (*ABUOP0003R1*) and a newly designed susceptible allele specific primer (*ABUOP0003R2*).

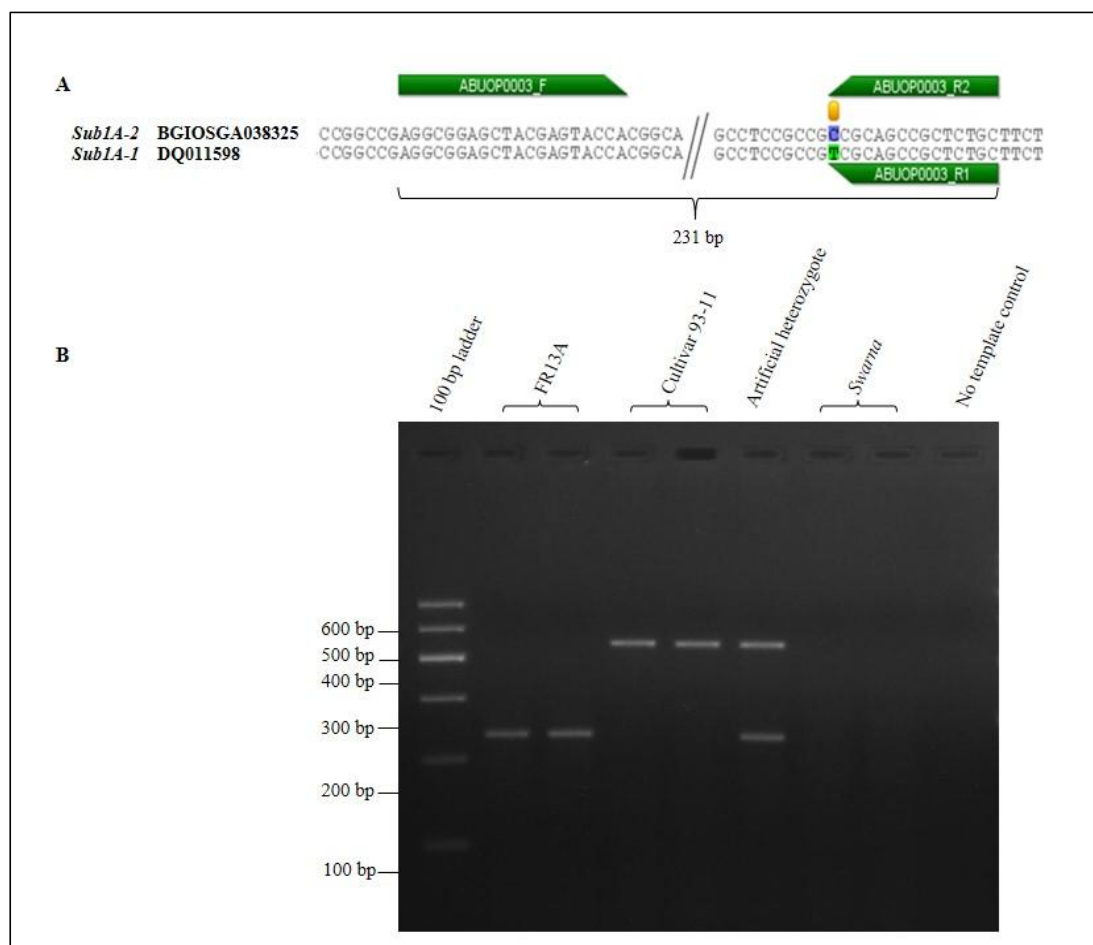


Figure 2: Illustration of the (A) single nucleotide polymorphism and the anchored position of *ABUOP0003* and (B) visualization of the PCR amplicons of *ABUOP0003* for rice accessions *FR13A*, *Cultivar 93-11*, and *Swarna* and an artificial heterozygote.

The primer pairs *ABUOP0003F/R1* and *ABUOP0003F/R2* both amplified a fragment of 231 bp in a separate-tube PCR assay. The primer combination *ABUOP0003F/R1* amplified a fragment only from the submergence tolerant reference *FR13A* carrying the *Sub1A-1*, and *ABUOP0003F/R2* amplified a fragment only from the susceptible reference *Cultivar 93-11* carrying *Sub1A-2* (Figure 2B). Both *ABUOP0003F/R1* and *ABUOP0003F/R2* assays resulted in amplification for the artificial heterozygote. When the PCR products of *ABUOP0003F/R1* and *ABUOP0003F/R2* were loaded onto the same well leading with a 10 min interval on a 1.5 % Agarose gel, the expected polymorphism could be visualized in a co-dominant state (Figure 2B). Further, the marker assay was validated for specificity with the rice accession *Swarna*, known to be without the *Sub1A* gene, where no amplification for marker *ABUOP0003* was observed (Figure 2B). Therefore, the modified gel-based marker *ABUOP0003* was diagnostic to confidently differentiate the alleles *Sub1A-1* from *Sub1A-2*. Therefore, we recommend the modified marker *ABUOP0003*, over the previously used dominant *AEX* STS marker, KASP marker and CAPS marker, as a gel-based, codominant and economical assay, especially targeting technology-limited setups. However, with respect to the absence of a PCR product in *ABUOP0003* assay, it is difficult to confidently rule out a PCR failure from an absence of the *Sub1A* gene. Therefore, it is recommended to assay such accessions/varieties multiple times alongside a positive control.

Out of the panel of 66 rice accessions/varieties, the *ABUOP0003* marker identified 14 rice accessions/varieties as carrying the tolerance allele *Sub1A-1* (*FR13A*; SLNIVs At 354 and Bw 272-6b; and SLTAs *Maa wee*, *Heen Karayal*, *Godaheenati*, *Dik wee*, *Mada el*, *Dewareddiri*, *Pokkali*, *Pachchaperumal*, *Kahata wee*, *Podihatatha* and *Sudugoda wee*). Of these only the accession *Godaheenati* has been previously characterized as carrying the *Sub1A-1* tolerance allele (Xu *et al.*, 2006; Singh *et al.*, 2010). Interestingly, there is no apparent pedigree overlap with respect to these varieties/ accessions (Supplementary file S1). From the tested

rice panel 19 accessions/varieties were identified as carrying susceptible *Sub1A-2* allele, of which 13 were SLNIVs and six were SLTAs (Supplementary file S3). Despite repeated attempts conducted alongside positive controls, the remaining 32 rice accessions (*Swarna*, 25 SLNIVs and seven SLTAs) did not result in PCR amplification for the marker *ABUOP0003* (Supplementary file S3). While there is a possibility that these 32 rice varieties/accessions do not carry the *Sub1A* gene, like in variety *Swarna*, a definitive conclusion could not be drawn despite the repeated attempts to rule out a possible PCR failure. Out of the 64 rice accessions in the core rice panel, 20% carried the *Sub1A-1* tolerance allele and 30% carried the *Sub1A-2* susceptible allele (Supplementary file S3).

The genetic structure and the diversity analysis of the core rice panel indicated minimal evidence of gene flow between the SLNIVs and SLTAs (Figure 1B). According to Pucciariello and Perata (2013), the wild rice accessions from Sri Lanka revealed no evidence of carrying *Sub1A* gene, and they reported several landraces that carried *Sub1A-1* and *Sub1A-2* alleles, indicating the possibility of early settlers bringing in seeds containing *Sub1A* gene from the Indian basin or later introduction of germplasm carrying *Sub1A* through exotic lines used in breeding programmes. The current study further strengthens the theory presented in Pucciariello and Perata (2013), where *Sub1A* alleles were identified from both SLNIVs (*i.e.*, newly developed mainly through introductions) and SLTAs (*i.e.*, including landraces and heirloom accessions) even under the proposed limited gene flow scenario (Figure 1B).

Field evaluation for identification of submergence tolerant rice accessions/varieties

In the current study, phenotypic assessment of submergence responses was assessed in order to deduce the associations of the submergence responses with the allele carried at the *Sub1A* gene. Furthermore, it was intended to identify tolerant rice accessions/varieties that should be recommended as tolerance donors for the development of bi-parental/multi-parental mapping populations for QTL identification and varietal development programs (*i.e.*, through backcross breeding and gene pyramiding). In the current study, the seedling stage submergence responses were assessed based on the survival percentage after submerging 14 day old seedlings for a period of 14 days followed by a de-submerged recovery period of 14 days. The survival percentage ranged between 6 - 97% in the rice panel (Figure 3; Supplementary file S3). Out of the 64 Sri Lankan rice accessions/varieties evaluated for submergence stress responses, 13 rice accessions/varieties showed no significant difference ($p > 0.05$; Figure 3) to FR13A (the submergence tolerance reference), and hence, was grouped as ‘tolerant’ to submergence stress (survival percentage 77 – 93%). Among the 13 rice accessions/varieties in the ‘tolerant’ group, eight SLNIVs (At 362, Bg 310, Bw 363, At 303, Bg 359, Bg 369, At 308 and Bg 352) and five SLTAs (*Maa wee*, *Heenkarayal*, *Godaheenati*, *Batapola el*, and *Dik wee*) were identified.

Among the submergence susceptible group, 13 rice accessions/varieties were reported as having similar responses to *Swarna*, the susceptible reference cultivar ($p > 0.05$; SLNIVs Bg 250, Bw 14-509, Bw 272-6b, Bw 12-574, Bg 94-1, Bw 400, At 307, Bg 300, Bw 351, Ld 368 and Bw 11-3403; and SLTAs *Podihatatha*, and *Sudugoda wee*; Figure 3). Further, 12 rice accessions/varieties were reported as prone to submergence even more than *Swarna* (SLNIVs Bg 251, Bg 302, At 373, Bw 451, Ld 253, Bw 367, Bg 360, Ld 365, Ld 371 and At 311; and SLTAs *Dahanala* and *Kuru wee*; Figure 3). Hence, altogether 25 rice accessions/varieties were reported as ‘susceptible’ (survival percentage 6 - 57%; Supplementary file S3). The remaining 26 rice accessions/varieties (11 SLNIVs and 15 SLTAs) are grouped as “intermediate” in their submergence response as they were neither as tolerant as FR13A, nor as susceptible as *Swarna*, the tolerant and susceptible reference cultivars, respectively (Figure 3; Supplementary file S3).

Out of the SLTAs *Godaheenati* has been previously reported as tolerant to submergence (Xu & Mackill, 1996; Xu *et al.*, 2006; Bailey-Serres *et al.*, 2010; Panda *et al.*, 2021) and hence is in agreement with the current study. Though Ranawake *et al.* (2014a) reported evaluation of several SLNIVs for submergence tolerance, the survival rates of the said experiment were extremely low compared to the current study; therefore, the two studies could not be compared meaningfully. Moreover, given that submergence stress tolerance is a quantitative trait, it is noteworthy that variations in submergence stress responses can be expected in varieties/accessions across experiments due to the differences in experimental and environmental conditions (Ranawake *et al.* 2014b; Rathnayake *et al.* 2012; Rupasinghe *et al.* 2016).

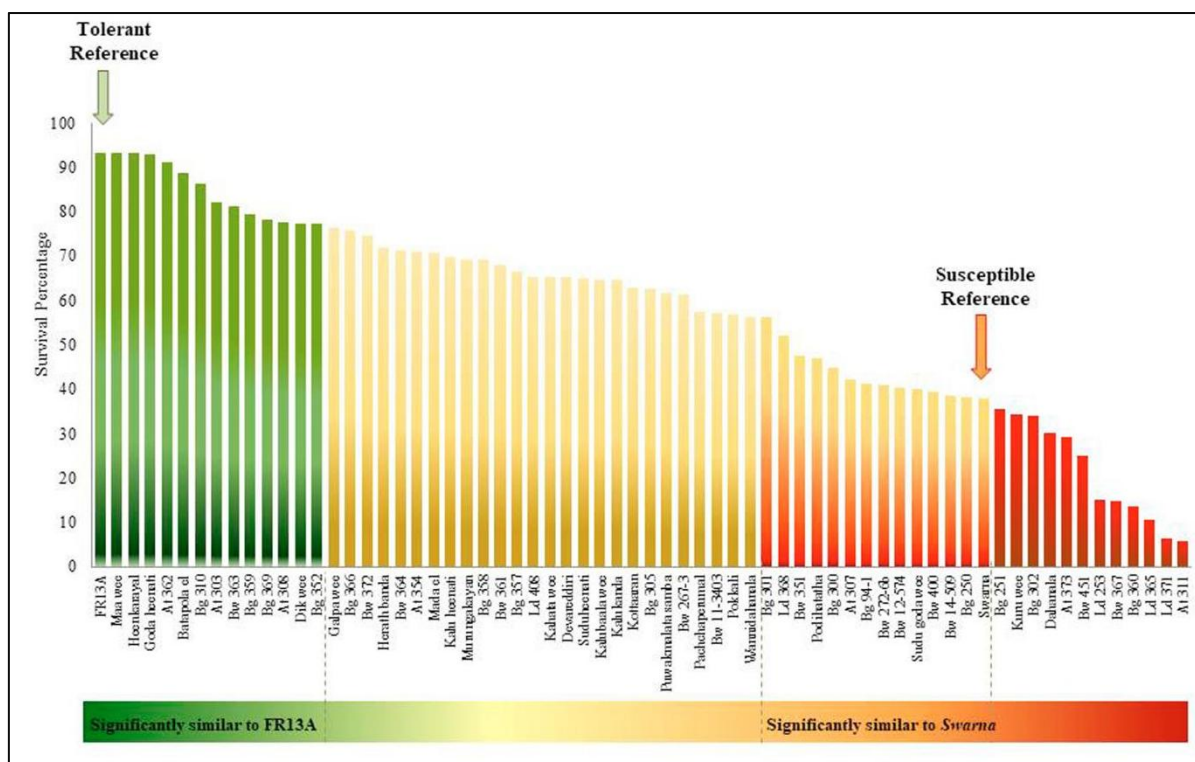


Figure 3: Illustration of submergence stress responses of 64 rice accessions/varieties based on their estimated median scores

Association of *Sub1A* alleles with submergence stress responses

Among the rice accession/varieties confirmed to be carrying *Sub1A* alleles (13 with *Sub1A-1* and 19 with *Sub1A-2*) no significant association ($p < 0.05$) could be found with respect to their submergence stress response in the field trial (Figure 4). Of the 13 rice accessions/varieties reported as tolerant to submergence in the current field study, only *Maa wee*, *Heenkarayal*, *Godaaheenati* and *Dik wee* were confirmed to carry *Sub1A-1*. The tolerant accessions/varieties *Batapola el*, *At 362*, *Bg 359*, *Bg 369*, and *Bg 352* carried *Sub1A-2*. Further, the *Sub1A* allele status of the varieties *Bg 310*, *At 303*, *At 308*, and *Bw 363* remain unconfirmed (as the possibility that some of them are not carrying the *Sub1A* gene could not be definitively ruled out; Supplementary file S3). These rice accessions/varieties, which do not carry the *Sub1A-1* allele, yet express a tolerant response to submergence, could be carrying other known tolerant alleles such as *Sub1C-1* (which could mask the susceptible response of *Sub1A-2* (Xu *et al.*, 2006) or novel QTL/genes unique to the Sri Lankan rice germplasm. Therefore, it is recommended to study the genetic background of such accessions/varieties to further understand the underlying genetic control of submergence stress responses through QTL mapping/gene discovery.

Of the 25 rice accessions which reported a submergence susceptible response similar to or more severe than *Swarna*, three (*Bw 272-6b*, *Sudugoda wee* and *Podihatatha*) reported the presence of *Sub1A-1* allele and five (*At 307*, *Bw 400*, *Bg 94-1*, *Bg 250* and *Kuru wee*) reported the presence of *Sub1A-2* allele. The allele calls of the remaining 17 rice accessions/varieties (Supplementary file S3) could not be confidently confirmed as the absence of *Sub1A* gene or a PCR failure. The reported susceptibility to submergence stress in the three rice accessions carrying the *Sub1A-1* allele indicates that there could be other genetic factors governing submergence tolerance than the impact of *Sub1A* locus alone (*i.e.*, susceptibility factors). Therefore, further investigations on the genetic mechanism underlying the susceptibility expressed by the three rice accessions *Bw 272-6b*, *Sudugoda wee* and *Podihatatha* will be beneficial.

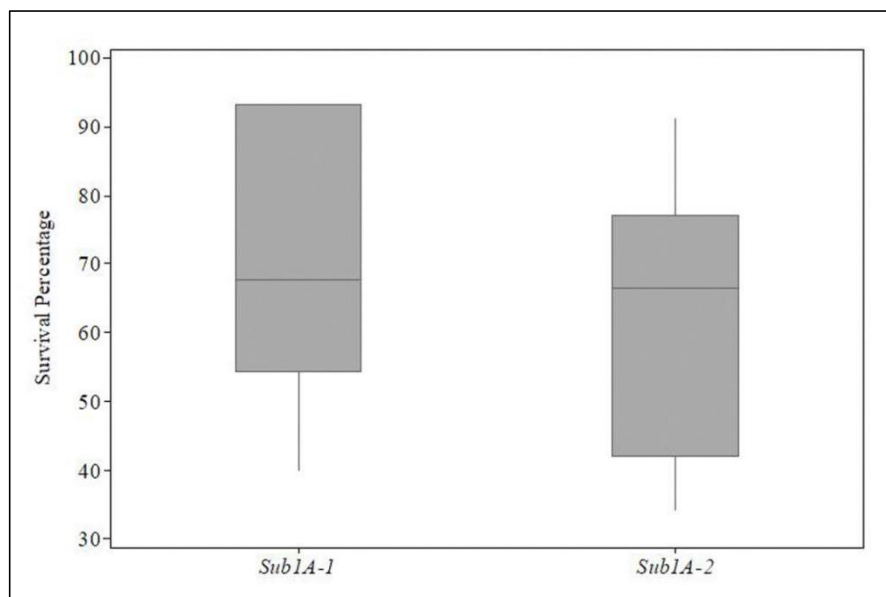


Figure 4: Box and Whiskers plot illustrating the submergence stress response of rice varieties/accessions carrying the *Sub1A-1* and *Sub1A-2* alleles.

CONCLUSION

Allele characterization using the modified gel-based marker *ABUOP0003* revealed the presence of the *Sub1A-1* tolerance allele in the SLNIVs At 354 and Bw 272-6b, and the SLTAs; *Maa wee*, *Heen Karayal*, *Godaheenati*, *Dik wee*, *Mada el*, *Dewareddiri*, *Pokkali*, *Pachchaperumal*, *Kahata wee*, *Podihatatha*, *Sudugoda wee*. Further, nineteen accessions/varieties carried the susceptible *Sub1A-2* allele, and the allele call of the remaining 32 rice accessions/variety could not be confidently verified as absence of *SubA* gene or a PCR failure. The Bayesian genetic structure analysis revealed that the rice panel consisted of two genetically isolated gene pools, in which the occurrence of the *Sub1A* alleles did not show a strong association to the proposed genetic structure grouping. This indicates an allelic divergence of the *Sub1A* gene, which pre-dates germplasm introductions and varietal development attempts in Sri Lanka. In a field trial, the SLNIVs; At 362, Bg 310, Bw 363, At 303, Bg 359, Bg 369, At 308 and Bg 352 and SLTAs; *Maa wee*, *Heenkarayal*, *Godaheenati*, *Batapola el* and *Dik wee* were identified with similar submergence tolerance responses as with the submergence tolerant reference FR13A. Of the remaining rice varieties/accessions, 25 were reported as submergence susceptible, while 26 were reported with intermediate responses to submergence stress. No significant association of the presence of the *Sub1A* allele (*Sub1A-1* and *Sub1A-2*) could be deduced with their respective submergence stress responses. However, given that the SLTAs *Maa wee*, *Heenkarayal*, *Godaheenati* and *Dikwee* carried the *SubA-1* tolerance allele and produced a submergence tolerant stress response, these could be recommended as suitable genetic donors for rice breeding programmes.

Acknowledgement

The authors acknowledge that this work was carried out with a grant from UNESCO and the International Development Research Centre (IDRC), Ottawa, Canada. The views expressed herein do not necessarily represent those of UNESCO, IDRC or its Board of Governors. The authors also acknowledge Dr. Kanishka Ukuwela, Faculty of Applied Sciences, Rajarata University of Sri Lanka, Mihinthale for the support given in genetic structure analysis.

REFERENCES

- Bailey-Serres J., Fukao T., Ronald P., Ismail A., Heuer S. & Mackill D. (2010). Submergence tolerant rice: *SUB1*'s journey from landrace to modern cultivar. *Rice* **3**(2): 138–147.
DOI: <https://doi.org/10.1007/s12284-010-9048-5>
- Bailey-Serres J. & Voesenek L. (2008). Flooding stress: acclimations and genetic diversity. *Annual Review of Plant Biology* **59**: 313–339.
DOI: <https://doi.org/10.1146/annurev.arplant.59.032607.092752>
- Baksh S.K., Donde R., Kumar J., Mukherjee M., Meher J., Behera L. & Dash S. K. (2021). Genetic relationship, population structure analysis and pheno-molecular characterization of rice (*Oryza sativa* L.) cultivars for bacterial leaf blight resistance and submergence tolerance using trait specific STS markers. *Physiology and Molecular Biology of Plants* **27**(3): 543–562.
DOI: <https://doi.org/10.1007/s12298-021-00951-1>
- Doyle J.J. & Doyle J.L. (1987). A rapid DNA isolation procedure for small quantities of fresh leaf tissue. *Phytochemical Bulletin* **19**:11–15.
- Earl D. A. & vonHoldt B. M. (2012). STRUCTURE HARVESTER: A website and program for visualizing STRUCTURE output and implementing the Evanno method. *Conservation Genetics Resources* **4**(2): 359–361.
DOI: <https://doi.org/10.1007/s12686-011-9548-7>
- Emerick K. & Ronald P. C. (2019). *Sub1* rice: Engineering rice for climate change. *Cold Spring Harbor Perspectives in Biology* **11**(12): a034637.
DOI: <https://doi.org/10.1101/cshperspect.a034637>
- Ganie S.A., Ahammed G.J. & Wani S.H. (2020). Vascular plant one zinc-finger (VOZ) transcription factors: novel regulators of abiotic stress tolerance in rice (*Oryza sativa* L.). *Genetic Resources and Crop Evolution* **67**(4): 799–807.
DOI: <https://doi.org/10.1007/s10722-020-00904-9>
- Hattori Y., Nagai K. & Ashikari M. (2011). Rice growth adapting to deepwater. *Current Opinion in Plant Biology* **14**(1): 100–105.
DOI: <https://doi.org/10.1016/j.pbi.2010.09.008>
- Ismail A.M., Ella E.S., Vergara G.V. & Mackill D.J. (2009). Mechanisms associated with tolerance to flooding during germination and early seedling growth in rice (*Oryza sativa*). *Annals of Botany* **103**(2):197–209.
DOI: <https://doi.org/10.1093/aob/mcn211>
- Kearse M. et al. (14 authors) (2012). Geneious Basic: an integrated and extendable desktop software platform for the organization and analysis of sequence data. *Bioinformatics* **28**(12):1647–1649.
DOI: <https://doi.org/10.1093/bioinformatics/bts199>
- Loreti E., van Veen H. & Perata P. (2016). Plant responses to flooding stress. *Current Opinion in Plant Biology* **33**: 64–71.
DOI: <https://doi.org/10.1016/j.pbi.2016.06.005>
- Magneschi L. & Perata P. (2009). Rice germination and seedling growth in the absence of oxygen. *Annals of Botany* **103**(2):181–196.
DOI: <https://doi.org/10.1093/aob/mcn121>
- Moon J.H., Son D., Lee J.W. & Yoo S.C. (2019). Development of Kompetitive allele specific PCR markers for submergence tolerant gene *Sub1* in rice. *Plant Breeding and Biotechnology* **7**(1): 62–66.
DOI: <https://doi.org/10.9787/PBB.2019.7.1.62>
- Neeraja C.N. et al. (11 authors) (2007). A marker-assisted backcross approach for developing submergence-tolerant rice cultivars. *Theoretical and Applied Genetics* **115**(6): 767–776.
DOI: <https://doi.org/10.1007/s00122-007-0607-0>
- Panda D., Barik J. & Sarkar R.K. (2021). Recent advances of genetic resources, genes and genetic approaches for flooding tolerance in rice. *Current Genomics* **22**(1): 41–58.
DOI: <https://doi.org/10.2174/1389202922666210114104140>
- Pucciariello C. & Perata P. (2013). Quiescence in rice submergence tolerance: An evolutionary hypothesis. *Trends in Plant Science* **18**(7): 377–381.
DOI: <https://doi.org/10.1016/j.tplants.2013.04.007>

- Ranawake A., Amarasingha U. & Dahanayake N. (2014a). Agronomic characters of some traditional rice (*Oryza sativa* L.) cultivars in Sri Lanka. *Journal of the University of Ruhuna* **1**(1): 3–9.
DOI: <http://doi.org/10.4038/jur.v1i1.6150>
- Ranawake A.L., Amarasinghe U.G.S. & Senanayake S. (2014b). Submergence tolerance of some modern rice cultivars at seedling and vegetative stages. *Journal of Crop and Weed* **10**(2): 240–247.
- Rathnayake N., Bentota A., Dissanayake D., Perera K., Sooriyapathirana S. & Jayasekera G. (2013). DNA markers RM 464A and RM 219 haplotypes are effective in selecting *Sub-1* locus for the introgression of submergence tolerance into new rice varieties. *Ceylon Journal of Science (Biological Sciences)* **41**(2): 125–136.
DOI: <http://doi.org/10.4038/cjsbs.v41i2.5382>
- Rupasinghe M.G.N., Samarasinghe W.L.G. & De Silva K.M.S. (2016). Submergence tolerant rice line for flood prone areas in Sri Lanka. *Annals of the Sri Lanka Department of Agriculture* **18**: 233–236.
- Septiningsih E.M., Pamplona A.M., Sanchez D.L., Neeraja C.N., Vergara G.V., Heuer S., Ismail A.M. & Mackill D.J. (2009). Development of submergence-tolerant rice cultivars: the *Sub1* locus and beyond. *Annals of Botany* **103**(2):151–160.
DOI: <https://doi.org/10.1093/aob/mcn206>
- Singh N. *et al.* (12 authors) (2010). Molecular marker survey and expression analyses of the rice submergence-tolerance gene *SUB1A*. *Theoretical and Applied Genetics* **121**(8): 1441–1453.
DOI: <https://doi.org/10.1007/s00122-010-1400-z>
- Thompson J.D., Gibson T.J. & Higgins D.G. (2003). Multiple sequence alignment using ClustalW and ClustalX. *Current Protocols in Bioinformatics* **1**: 2–3.
DOI: <https://doi.org/10.1002/0471250953.bi0203s00>
- Untergasser A., Cutcutache I., Koressaar T., Ye J., Faircloth B.C., Remm M. & Rozen, S.G. (2012). Primer3—new capabilities and interfaces. *Nucleic Acids Research* **40**(15): e115–e115.
DOI: <https://doi.org/10.1093/nar/gks596>
- Vergara B.S & Mazaredo A. (1975). Screening for resistance to submergence under greenhouse conditions. In: *Proceedings of the International Seminar on Deepwater Rice*, 21-26 August. Bangladesh Rice Research Institute, Dacca, Bangladesh, pp. 67–70.
- Winkel A., Colmer T.D., Ismail A.M. & Pedersen, O. (2013). Internal aeration of paddy field rice (*Oryza sativa*) during complete submergence—importance of light and floodwater O₂. *New Phytologist* **197**(4):1193–1203.
DOI: <https://doi.org/10.1111/nph.12048>
- Xu K., Xu X., Fukao T., Canlas P., Maghirang-Rodriguez R., Heuer S., Ismail A.M., Bailey-Serres J., Ronald P.C. & Mackill, D.J. (2006). *Sub1A* is an ethylene-response-factor-like gene that confers submergence tolerance to rice. *Nature* **442**(7103): 705–708.
DOI: <https://doi.org/10.1038/nature04920>
- Xu K. & Mackill D. J. (1996). A major locus for submergence tolerance mapped on rice chromosome 9. *Molecular Breeding* **2**(3): 219–224.
DOI: <https://doi.org/10.1007/BF00564199>

Link to download supplementary data:

<https://jnsfsl.sljol.info/articles/10.4038/jnsfsl.v51i1.11121/galley/7267/download/>

RESEARCH ARTICLE

Statistical Modelling

A comparison of model parameter estimation methods for complex survey survival data

IT Jayamanne*, A Ramanayake and RV Jayatillake

Department of Statistics, Faculty of Science, University of Colombo, Colombo 03, Sri Lanka.

Submitted: 01 October 2021; Revised: 23 August 2022; Accepted: 23 September 2022

Abstract: When estimation of model parameters is the target in survey data, the inference on the model can be based on a pure model-based approach or a model-assisted approach which is a hybrid approach combining design-based and model-based methods. This study aims to compare these methods for survival data that are gathered from a stratified random sampling design. The Accelerated Failure Time (AFT) model was fitted to describe the relationship between the censored response variable and the explanatory variables. Resampling methods with different sample sizes and different sampling designs from a real dataset were considered in the study to generate samples. The AFT models were fitted to each of the samples using, firstly a pure model-based method ignoring the survey design and weights, secondly a model-based method with survey weights, and finally a model-assisted method considering both survey design and weights. Squared bias, variance, and mean squared error (MSE) were used to compare the three approaches. The AFT model, with all covariates and the best AFT model with the best set of covariates and distribution, were analyzed. Even though it was challenging to select the best method for all cases, the second and third approaches worked better for small samples than the first approach.

Keywords: Analytical studies, model-assisted, post-stratification, survey design, survival data.

INTRODUCTION

In analytical studies, groups of subjects are compared to estimate the magnitude of the association between exposures and outcomes. Statistical models play a vital role in identifying this association. In general, the primary focus of the statistical model is on estimating and evaluating the model and its associations. Thus, data analysts often neglect to consider the complex sampling design features, such as stratification, clustering, and unequal probability of selection when performing analytical studies. Data are frequently analyzed as if they are from a simple random sample, perhaps due to convenience or lack of proper guidance. The inference on the model can be performed based on a pure model-based approach or a model-assisted approach. The latter is a hybrid approach combining both design-based and model-based methods. While the model-based framework, relies only on modelling, particularly the model distributional assumptions, the model-assisted framework incorporates the random sampling mechanism (Opsomer, 2009; Sterba, 2009; Pfeffermann, 2011).

Survey design weights play a vital role in incorporating survey design features of the complex survey data into the model. In the model-assisted approach, the sampling weights are used to estimate the parameters, and besides the sample design is used to determine the variances of the estimates (Lohr, 2010). Complex survey designs namely, stratification, clustering, and multistage sampling lead to estimates having standard errors different from data obtained using simple random sampling (SRS). Besides, post-stratification and nonresponse adjustments also affect the variance. The design effects (deff) are used to quantify the effect of the design on the variance of the point estimates (Lumley, 2010; Lohr, 2010). Several methods for estimating variances for regression estimates for complex survey data were introduced, namely Taylor linearization and resampling methods as Balanced Repeated Replication, Jackknife, and Bootstrap. These methods were implemented in

* Corresponding author (imali@stat.cmb.ac.lk;  <https://orcid.org/0009-0002-0314-5021>)



This article is published under the Creative Commons CC-BY-ND License (<http://creativecommons.org/licenses/by-nd/4.0/>). This license permits use, distribution and reproduction, commercial and non-commercial, provided that the original work is properly cited and is not changed in anyway.

some software packages to correct the standard error in complex survey data. In the absence of the model-assisted method implementation in the statistical software, Lohr (2010) advised running the programs with design weights to acquire accurate parameter estimates. She further mentioned several reviews about the effect of survey weights on regression estimates. She recommends performing the analysis with and without design weights to perceive the difference in the model parameter estimates.

Quite a few theoretical pieces of evidence (Sarndal *et al.*, 2003; Binder & Roberts, 2009; Lohr, 2010; Lumley, 2010) explained the pros and cons of model-based and model-assisted inference on regression parameters. However, there is a lack of substantial evidence to evaluate the inference framework for analytical studies for complex surveys on survival data. Most of the simulation studies focused on generating hypothetical data and comparing the performances of linear or logistic regression models. A few authors (DuMouchel & Duncan, 1983; Binder *et al.*, 2005), have used real data to distinguish the differences. Even in these studies, only a few aspects of the model are evaluated and none of the studies was based on survival data. Hence, the main focus of this study is to reduce this gap by designing a study based on a real dataset to distinguish the inference methods for complex surveys of survival data.

Even though pure model-based approaches were well developed in almost all statistical packages many years ago, model-assisted inferences were only implemented recently in some statistical software. Different mechanisms were used to integrate the complex design structure of the data into different models during the model estimation procedure. The focus of this research solely will be on the Accelerated Failure Time (AFT) model. The AFT model is a popular model used to explain the relationship between a survival response (time to an event) and other explanatory variables. A typical feature of the survival response is that the time to an event is not always observed, and observations are subject to censoring. The AFT model relates the logarithm of the survival time linearly to covariates. Specific parametric error distribution for the AFT model is assumed and hence a particular survival distribution. If the survival data is from a simple random sampling, the pure model-based inferences can be used to estimate the model parameters. In the presence of complex survey data, one can either follow a pure model-based approach or a model-assisted approach. However, most of the pure model-based software packages allow the user to include survey weight for the analysis. Thus, one can perform a study based on these three approaches. Though selecting the best approach prior to analysis is a dilemma, after analyzing data using these three approaches, the analyst may be able to select the best model based on the Akaike information criterion (AIC) or the Bayesian information criterion (BIC) and the validation of model assumption. However, it would be beneficial if proper guidelines can be given to the analyst prior to the analysis to select the best approach on available data. Furthermore, it is also necessary to assess the impact of the survey design on the conclusion from the analysis.

In consequence, this study aims to compare the three approaches mentioned above for survival data that are gathered from a complex survey design with proportionate and disproportionate stratified random samples. It will describe the strengths and weaknesses of the three approaches via a simulation study. The difference in the model performances for the full model, the best fitted model (best set of covariates), changes in the distribution will also be investigated. Besides, the effect of post-stratification on model parameters will also be studied.

MATERIALS AND METHODS

As discussed in the introduction, a simulation study was carried out to achieve the objective of the study. First, a real dataset was obtained to generate data for the simulation study. Then the theoretical difference between the three methods of estimation is described in section 2.2. Next, the simulation framework was designed to achieve the objectives of the study.

Data for the simulation study

A survey was conducted in the year 2016 on a stratified random sample of all Arts graduates from Sri Lankan universities who had graduated in 2012 to identify the changes in their employment over time. The waiting time for the first employment is the response variable, and the qualitative explanatory variables considered are

university, gender, ethnicity, area lived, type of school attended, parent’s highest education, civil status at the time of employment (civilStatusAtFE), English grade at GCE O/L, English grade at GCE A/L (ALEnglish), the class received (Class) and the type of degree (DegreeType). There were 386 complete records that consisted of 15 interval-censored and 10 right-censored data (Jayamanne & Ramanayake, 2018). Almost all the past studies on finding factors associated with the waiting time for the first employment had followed a model-based approach (Grilli *et al.*, 2001; Moore, 2006; Salas-Velasco, 2007). The log-logistic AFT model was chosen as the best fitted model to explain the relationship between the time to first employment and the explanatory variables (Jayamanne & Ramanayake, 2017). The best set of covariates and their coefficient were estimated using the survival package in R following the stepwise backward selection method having the lowest AIC and BIC. Only the Class, ALEnglish, Gender, civilStatusAtFE, DegreeType, and Ethnicity variables were significant, and these values are depicted in Table 1. Since all the variables are qualitative, coefficient values are depicted with respect to the reference level.

Table 1: Parameters of the AFT model

	Variable	Coefficient	Parameter value
1		(Intercept)	1.5312
2		General	0.6166
3	Class	Second Lower	0.5183
4		Second Upper	0.511
5		Absent	1.0476
6	ALEnglish	B	0.8313
7		C	1.1059
8		F/W	1.0021
9		S	1.2355
10	Gender	Male	0.3529
11	civilStatusAtFE	Single	-0.2416
12	DegreeType	Special	-0.2487
13	Ethnicity	Sinhala	-0.6972
14		Tamil	-0.0792
15		Log(scale)	-0.7545

To compare the estimation methods precisely, the parameters of the population AFT model are required. But since population survival data are unavailable, the dataset itself was considered to be the population data. Hence the above model coefficients were assumed to be regression parameters.

The theoretical concepts

In AFT models, the direct effect of the explanatory variables on the survival time is measured. Assume survival data are the realization of n random variables T_1, \dots, T_n , depending on the covariate vector, $X_i = (X_{i1}, \dots, X_{ip})'$. The AFT model is denoted as,

$$\log T_i = X_i' \beta + \varepsilon \quad \dots(1)$$

where $\beta = (\beta_1, \dots, \beta_p)$ represents unknown regression parameters and $\varepsilon = (\varepsilon_1, \dots, \varepsilon_n)$ are independent and identically distributed with density $g(e)$. Under the parametric approach, error density consists of μ , the location parameter (intercept) and σ , the scale parameter.

Hence the equation can be rewritten as,

$$\log T_i = \mu + X_i' \beta + \sigma \varepsilon^* \quad \dots (2)$$

where ε^* is the standardized error term with a particular survival time distribution. The most commonly used survival distributions for AFT are exponential, Weibull, log-logistic, lognormal, and generalized gamma.

The maximum likelihood estimation method can be used to estimate $p+2$ parameters in the pure model-based approach using the likelihood L . When $L_i(\theta)$ corresponds to the parametric model for independent observations with density $f_i(t; \theta)$ and survival function $S_i(t; \theta)$,

$$L = \prod_{i=1}^n [L_i(\theta)] = \prod_{i=1}^n [f_i(t_i; \theta)]^{\delta_i} [S_i(t_i; \theta)]^{1-\delta_i} \quad \dots(3)$$

where δ_i is the event indicator. $\delta_i = 1$, if the i^{th} observation is an event and $\delta_i = 0$, if the i^{th} observation is censored.

When the AFT model is extended to complex survey data, the first fundamental difference in the likelihood function is to incorporate sampling weight w_i for $i = 1, \dots, n$ as follows. This likelihood is called pseudo-likelihood

$$PL = \prod_{i=1}^n [L_i(\theta)]^{w_i} . \quad \dots(4)$$

Hence, both model-based with sampling weight and model-assisted approaches use sampling weights to estimate $p+2$ parameters with the use of pseudo-likelihood. Parameter estimations are obtained using the Newton Raphson method.

The standard errors of the model-assisted parameter estimates were obtained using Taylor series linearization (Lohr, 2010; Lumley, 2020). This is the corrected standard error which incorporates both sampling weight and design. In the model-based with sampling weight approach, only sampling weights are incorporated to get the corrected standard deviation. It uses robust variance estimation.

A simulation study was carried out to achieve the objectives of this study as follows.

The Framework of the simulation study

The extensive simulation study is discussed in three steps;

- Step 1: Generating data
- Step 2: Fitting AFT Models under the three approaches described earlier
- Step 3: Comparing the estimates

Step 1: Generating data

Considering the survey data as the population ($N = 386$), 1000 samples were drawn by resampling with replacements (bootstrap replicates) for each different sample size and survey design.

Sample sizes: 50, 100, 200

Sampling design:

- Stratified sampling with equal weights by taking the gender as strata
(e.g., when $n = 100$, *Female* = 78 and *Male* = 23)
- Stratified sampling with unequal weights by considering the gender as strata
 - Higher weights for females (when $n = 100$, *Female* = 50 and *Male* = 50)
 - Higher weights for males (when $n = 100$, *Female* = 85 and *Male* = 15)
- Stratified sampling with equal weights by choosing the degree as strata
- Stratified sampling with unequal weights by taking the degree as strata
 - Higher weights for general degree holders
 - Higher weights for special degree holders

Altogether 18 (= 3 inferences × 6 different designs) different cases with each having 1,000 stratified random sample data were considered in this study.

Step 2: Fitting AFT models:

- AFT models were fitted for each dataset using three approaches namely
- Pure model-based approach
 - Model-based with sampling weights
 - Model-assisted approach

The parameter estimates of the full model with all covariates were obtained under the three inference approaches. However, the best fitted model for the sample data may be different from the population model. Hence it would be improper to consider an insignificant explanatory variable in the AFT model. Thus, the best fitted model with only significant covariates (variables in Table 1) was considered for the model comparisons under the three approaches, by following the stepwise backward selection method having the lowest AIC and BIC with the best fitted distribution suited for the sample data. The best fitted distribution was selected by selecting the model which gives minimum AIC values out of the models fitting all available distributions. Furthermore, the best fitted model parameter estimates with post-stratified weights were also compared.

These models were fitted using the Survival package in R to perform pure model-based and model-based with survey weights approaches, while the Survey package is used to perform a model-assisted method considering design features such as stratification and survey design weights (Bogaerts *et al*, 2017; Lumley, 2020).

Step 3: Compare estimates

A variety of measures such as bias, variance and Mean Square Error (*MSE*) were considered for comparing the different approaches. The parameter β_{ij} represents the j^{th} coefficient of i^{th} sample.

$$\text{Average parameter estimates of } \beta_j = \sum_{i=1}^{1000} \frac{\widehat{\beta}_{ij}}{1000} \text{ for } j = 1, \dots, p \quad \dots(5)$$

where p is the number of coefficients present in the best fitted model, and $\widehat{\beta}_{ij}$ is the estimate of parameter β_{ij} .

Individual parameter estimates

$$\text{Relative bias of } \beta_{ij} = \text{relB}(\widehat{\beta}_{ij}) = \frac{(\widehat{\beta}_{ij} - \beta_j)}{\beta_j} \quad \dots(6)$$

$$\text{Squared bias of } \beta_{ij} = \text{SB}(\widehat{\beta}_{ij}) = (\widehat{\beta}_{ij} - \beta_j)^2 \quad \dots(7)$$

$$\text{MSE of } \widehat{\beta}_{ij} = \text{MSE}(\widehat{\beta}_{ij}) = \text{SB}(\widehat{\beta}_{ij}) + \text{var}(\widehat{\beta}_{ij}) \quad \dots(8)$$

Total parameter estimates for full model

$$\text{Total squared bias} = \text{TSB}(\widehat{\beta}_i) = \sum_{j=1}^p (\widehat{\beta}_{ij} - \beta_j)^2 \quad \dots(9)$$

$$\text{Total variance} = \text{Tvar}(\widehat{\beta}_i) = \sum_{j=1}^p \text{var}(\widehat{\beta}_{ij}) \quad \dots(10)$$

$$\text{Total MSE} = \text{TMSE}(\widehat{\beta}_i) = \sum_{j=1}^p \text{MSE}(\widehat{\beta}_{ij}) \quad \dots(11)$$

Average parameter estimates for the best model

$$\text{Let } \alpha_{ij} = \begin{cases} 1 & \text{if } \widehat{\beta}_{ij} \text{ is in the best fitted model} \\ 0 & \text{otherwise} \end{cases}$$

$$\text{Average squared bias} = \text{ASB}(\widehat{\beta}_i) = \frac{\sum_{j=1}^p \alpha_{ij} * (\widehat{\beta}_{ij} - \beta_j)^2}{\sum_{j=1}^p \alpha_{ij}} \quad \dots(12)$$

$$\text{Average variance} = AVar(\hat{\beta}_i) = \frac{\sum_{j=1}^p \alpha_{ij} * \text{var}(\hat{\beta}_{ij})}{\sum_{j=1}^p \alpha_{ij}} \quad \dots(13)$$

$$\text{Average MSE} = AMSE(\hat{\beta}_i) = \frac{\sum_{j=1}^p \alpha_{ij} * \text{MSE}(\hat{\beta}_{ij})}{\sum_{j=1}^p \alpha_{ij}} \quad \dots(14)$$

RESULTS AND DISCUSSION

The core findings of the simulation study are depicted in this section using the statistics described in the methodology.

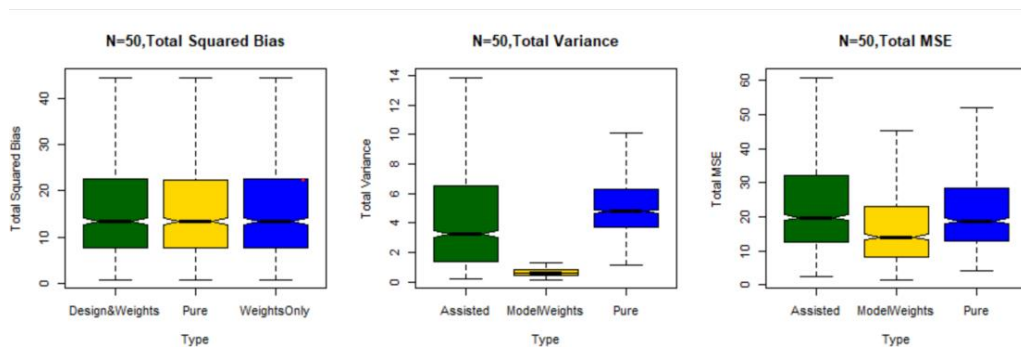


Figure 1: Total parameter estimates of the full model

Full model

Figure 1 depicts the total parameter estimates of the full model under three inference approaches for the 1000 sample data. Even though the overall relative bias is quite similar for the three methods, total variance and MSE are quite varied for the three approaches. The total variance is lowest for the model-based method with weight (yellow). Even though the variability of the total variance of the model-assisted method (green) is higher than that of the pure model-based approach (blue), the median value is lesser for the model-assisted method. A similar trend is shown by total MSE as well. The model-based approach with weight does not give the correct variance estimates as it only takes weights but not the design into consideration when estimating variance.

It is essential to explore the individual differences of the beta coefficient estimates under the three approaches. For almost all cases, there is not a considerable difference in the squared bias among the three methods. However, as illustrated in Figure 1, the estimated variance varied significantly. Regardless of the approach used, variances are higher for the intercept, ALEnglish and class coefficients. For almost all the coefficients, the variance is the highest for pure model-based (green) followed by model-based with weights. This indicates that the model-assisted approach has given rise to parameter estimates with smaller variance by incorporating both the design features such as stratification as well as unequal weights. Similar trends are shown for the other 17 cases and the MSE as well.

The best fitted model

As seen in Figure 2, the main reason for the higher variances for A/L English is the insignificance of the coefficients in the full model in the simulated data. Therefore, it is essential to consider only the explanatory variables that are significant in the model in order to select the best fitted AFT model for each sample. At first, the best fitted distribution of the AFT model was selected among a set of distributions using minimum AIC value, and then the best fitted collection of covariates was also chosen using minimum AIC values. It was noticed that the best fitted distribution for the AFT model is the same for all three approaches for all cases. It may be because the best fitted distribution is selected first for the waiting time variable, and it is not affected by

the parameter estimation approaches. Thus, the variation in the best fitted distribution is depicted in Figure 3 by the sample size. It can be seen that with the increase in sample size, sample data attain population distribution.

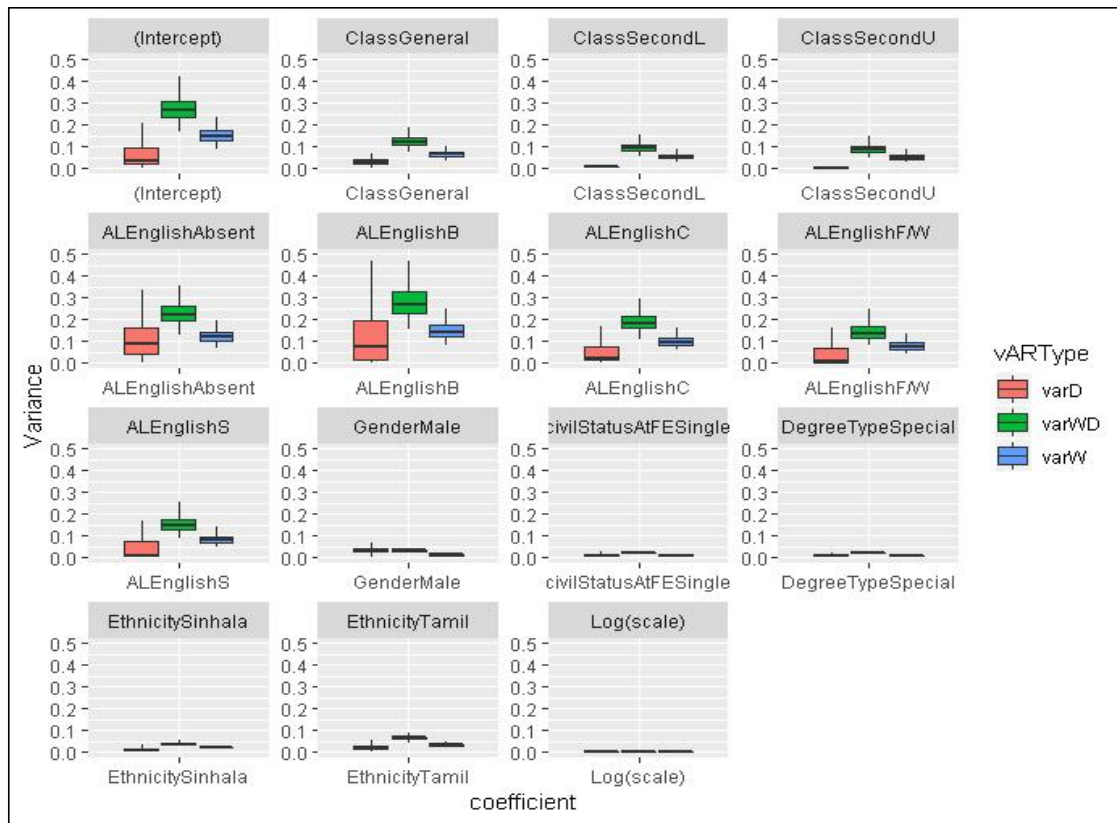


Figure 2: Estimated variances in beta coefficients by inference approach (n = 200, unequal weights, gender)

(Note: varD - variance from Model-assisted approach; varWD - variance from Pure Model-based approach; and varW - variance from Model-based with weights approach.)

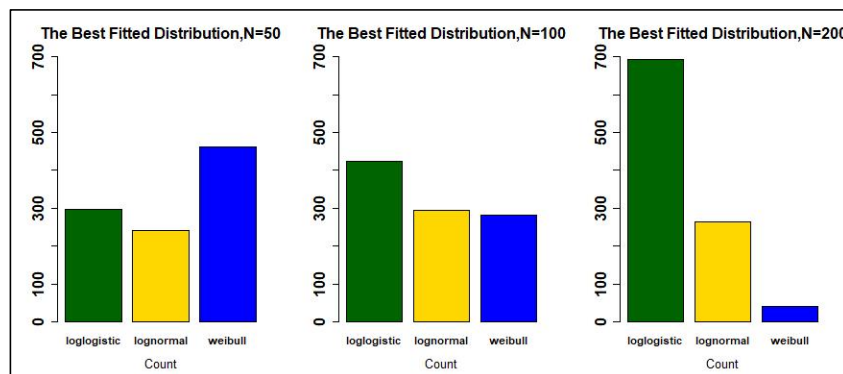


Figure 3: The best fitted distribution of the AFT model

Figure 4 depicts the summary of the significant covariates selected in the best fitted AFT model for 1000 samples for each different sample size. As the significance of the covariates depend on the selected data for the model, for some covariates the percentages tend to increase and decrease non-monotonically with sample size. However, it can be seen that with the increase in the sample size, ethnicity and gender variables are almost certainly included in the best fitted model for all three approaches.

As seen in Figure 4, a majority of the covariates are included in the best fitted model for all the sample sizes when the estimates are based on the model-based with weights approach compared to the other two approaches.

	N=50, equal weights			N=100, equal weights			N=200, equal weights				
	Model Assited	Model with weights	Pure model	Covariate	Model Assited	Model with weights	Pure model	Model Assited	Model with weights	Pure model	
Class	59%	93%	59%	Class	55%	89%	55%	Class	47%	77%	50%
ALEnglish	73%	99%	61%	ALEnglish	65%	97%	73%	ALEnglish	76%	94%	77%
Gender	85%	85%	89%	Gender	92%	90%	91%	Gender	98%	98%	98%
CivilStatus	86%	81%	89%	CivilStatus	88%	78%	84%	CivilStatus	89%	87%	88%
Degree	86%	82%	89%	Degree	88%	80%	87%	Degree	91%	88%	90%
Ethnicity	91%	98%	94%	Ethnicity	99%	100%	98%	Ethnicity	100%	100%	100%

Figure 4: Percentages of the covariates present in 1,000 sample by sample sizes

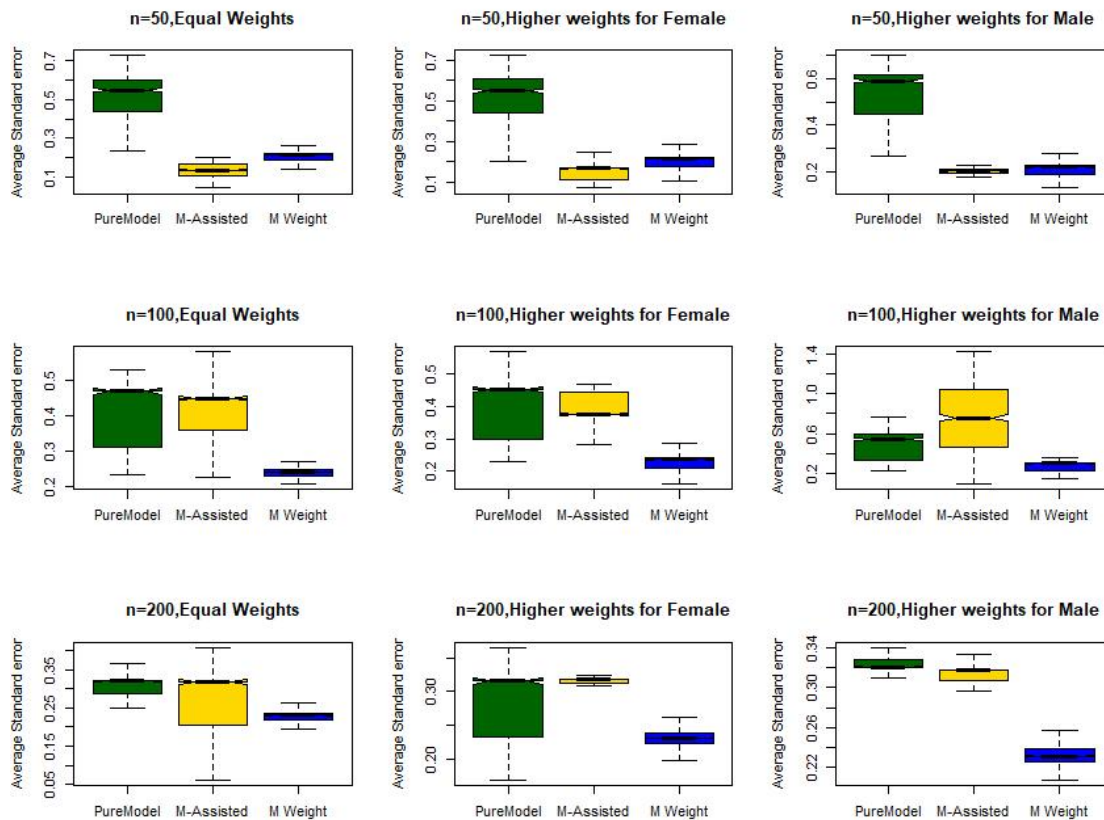


Figure 5: Average Squared Bias of the best fitted model with the best fitted distribution

It is essential to compare the estimations of the three methods for the best AFT model with the best fitted distribution. As stated in the methodology, the average squared bias, average standard error, and average MSE were considered instead of the total due to the absence of insignificant coefficients in some of the best fitted models using equations 12 to 14. The distributions of these statistics for 1000 observations are depicted in Figures 5 to 7. It is clear that the standard bias, standard error, and MSE are reduced with the increase of sample size.

As illustrated in Figure 5, when the sample sizes are proportionate to the population (sampling is ignorable), the three approaches end up having a similar average squared bias. However, when the sample sizes are disproportionate to the population sizes of the strata, the model-based approach with weights performed well when a fewer number of people are taken from small samples. Furthermore, it seems that the model-assisted and model-based with weight approaches perform well when sample sizes are small. For larger sample sizes, the model-assisted approach outperforms other approaches in terms of average squared bias.

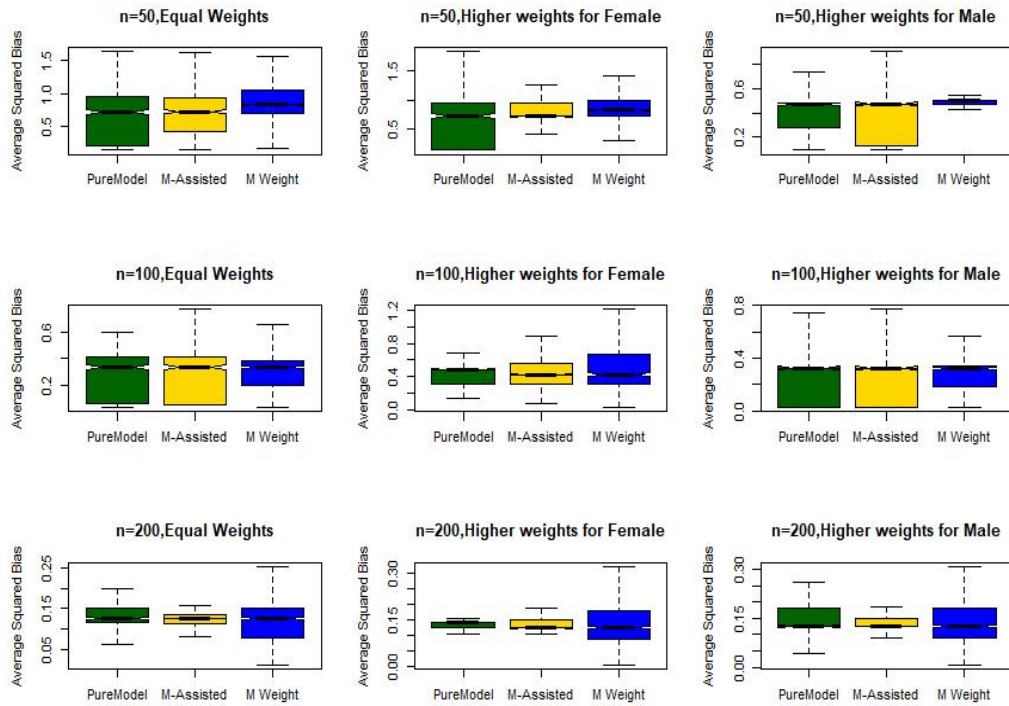


Figure 6: Average Standard Errors of the best fitted model with the best fitted distribution

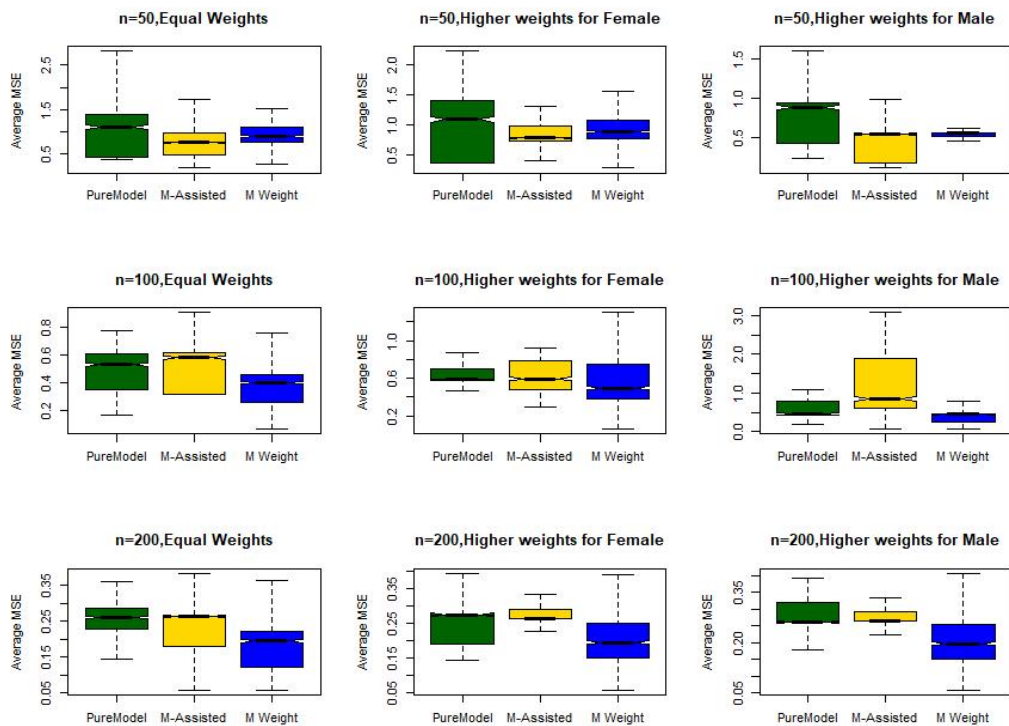


Figure 7: Average MSE of the best fitted model with the best fitted distribution

According to Figure 6, average standard errors are less for both model-assisted and model-based with weights approaches compared to the pure model-based approach for small sample size. Even though the model-based with weights approach outperforms the other two approaches for all cases, standard errors are not adjusted for the design.

The average MSE also depicted similar results, suggesting that the model-assisted or model-based with weights approaches are suitable for AFT model parameter estimation for small sample fractions (Figure7). Also the model-based with weights approach outperform the other approaches in all cases.

Effect of stratification and post-stratification

Even though all the above analysis considers gender as the stratification variable, the degree variable was also used to generate stratified random samples and most of the results are quite similar to those obtained when stratified by the gender variable.

Post-stratification is a method used for adjusting the sampling weights to account for underrepresented groups in the population. It is vital to investigate post-stratification on AFT model parameter estimations. Each stratified random sample is post-stratified by different variables such as ethnicity, class, and civil status to adjust weights to signify under representations. The best fitted AFT models with the best set of covariates were fitted for the post-stratified data using the three approaches. Even though there are only slight differences in the parameter estimation for the full model among the three strategies for post-stratified data, the differences are quite noteworthy for the best fitted model. Figures 8 and 9 show the average squared bias and standard error when $n = 100$, with disproportionate weights when gender was considered as the stratum variable. The top left most figure gives the estimates without a post-stratification and the rest are the estimates after post-stratifications.

As seen in Figure 8, model-based with weights and model-assisted estimations tend to be less biased after adjusting for post-stratification, except only when post-stratification is done by the class. Though it is difficult to identify the best post-stratification variable, ethnicity and civil status work better than other variables for both model-assisted and model-based with weights approaches.

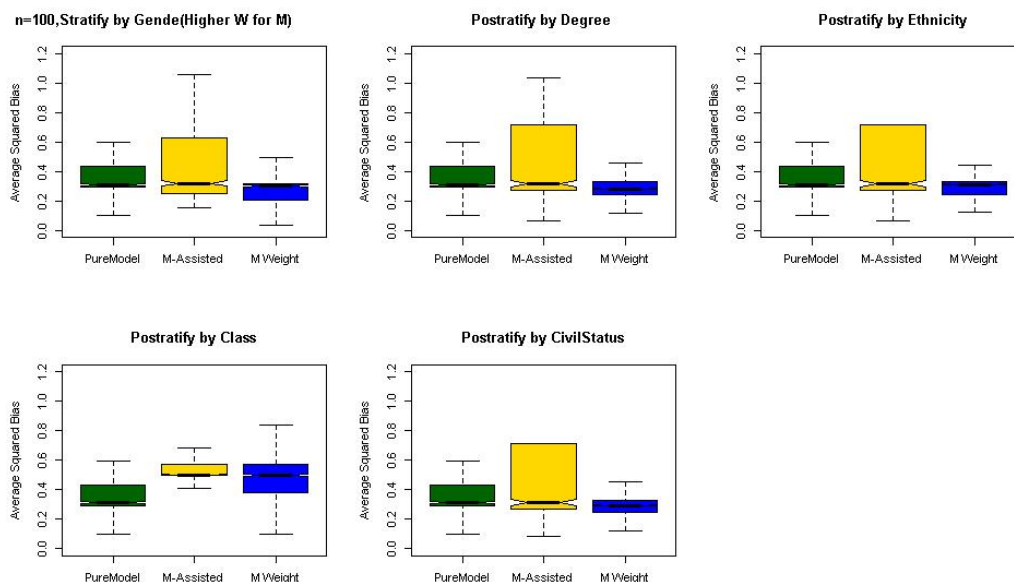


Figure 8: Average squared bias of the best fitted model for post-stratified samples

As depicted in Figure 9, the average standard error of the estimates of the model-based with weights and model-assisted approaches decreased after post-stratification comparatively, except when post-stratified by class for the

model-assisted method. The average MSE follows a similar trend as in Figure 9, suggesting post-stratification by civil status, which produced a smaller MSE for both model-assisted and model-based with weights methods. Hence, both are comparatively better than pure model-based estimates.

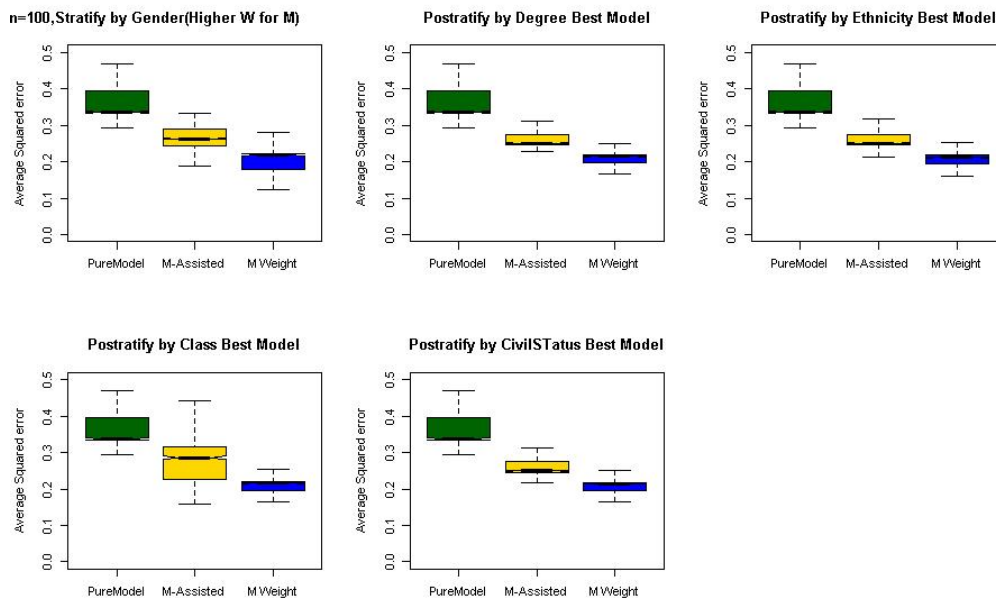


Figure 9: Average squared error of the best fitted model for post-stratified samples

As this study is based on a real dataset that contains data for waiting time to first employment of Arts graduates in Sri Lanka and explanatory variables, it is also important to highlight the findings of the AFT model. The AFT model revealed that gender, GCE Advanced level English grade, civil status, the class received, degree type, and ethnicity were the significant factors associated with the waiting time for the first employment of Arts graduates in Sri Lanka. Though the final model fitted to waiting time in this study was different from the past studies (Grilli, *et al.*, 2001; Moore, 2006; Salas-Velasco, 2007), gender and degree type are the common factors associated with the waiting time to first employment in all studies.

CONCLUSION

This section highlights some of the substantive findings of the study by comparing the pure model-based, model-based with weights, and model-assisted methods of estimating model parameters of the Accelerated Failure Time model for complex survey data. It is commonly believed that the sampling weights and stratification will have a significant effect on these three ways of estimations. To explore these differences, a simulation study was conducted on a real dataset by resampling.

When all the covariates of the population model were considered for the sample data, the insignificant covariates deviate quite a lot from the true parameter values. Even though it was challenging to select the best approach for the full model based on squared bias, it was noticed that the model-based with weights and model-assisted methods outperform pure model-based methods in terms of standard error and MSE of estimates. However, as it is not appropriate to include insignificant variables in the model, the best set of covariates was identified for each sample based on the minimum AIC values for the AFT model with the best fitted distribution. It was discovered that most of the covariates of the model-based with weights method were significant compared to the other two. In general, model-assisted and model-based with weight approaches considerably improve with a decrease in sample sizes or an increase in the complexity of the sampling design. However, it is noted that the model-assisted approach was not the best across all measures used in this simulation study. Often the sampling weights are adjusted to compensate for the coverage errors and non-responses using post-stratification, raking, and calibration. Therefore, the effects of the adjusted weights on model parameter estimations were also evaluated by post-stratified weights. It was noticed that the standard bias, variance, and

the MSE of the model parameters were further reduced in model-based with weights and model-assisted methods depending on the used post-stratification variable. Hence, it is suggested to use post-stratified weights for the model-based approach and model-assisted methods to estimate AFT model parameters when the data are from a stratified random sample. However, one should be careful in selecting the post-stratification variable as it may sometimes worsen the bias of an estimate.

It is recommended to use the model-assisted approach or model-based with weights when the data is from a complex survey design when the software is available, since there is an impact for the conclusions of the analytical studies.

Acknowledgements

The authors would like to thank the University of Colombo for funding this research under its Research Grant 2016 and also the National Centre for Advanced Study in Humanities and Social Sciences (NCAS) for postgraduate research grant 2016. Further, the authors are grateful to all the Arts graduates who responded to this survey.

REFERENCES

- Binder D. & Roberts G. (2009). Design- and model-based inference for model parameters. In: *Handbook of Statistics* (ed. C.R. Rao), volume 29B, pp. 33–54. Elsevier, Netherlands.
DOI: [https://doi.org/10.1016/S0169-7161\(09\)00224-7](https://doi.org/10.1016/S0169-7161(09)00224-7)
- Binder D., Kovacevic S. & Roberts G. (2005). How important is the informativeness of the sample design? . *Proceedings of the Survey Methods Section, SSC Annual Meeting*. Statistical Society of Canada, Ottawa, Canada, pp. 1–11.
- Bogaerts K., Komarek A. & Lesaffre E. (2017). *Survival Analysis with Interval; Censored Data: A Practical Approach with Examples in R, SAS, and BUGS*, 1st edition. Chapman & Hall/ CRC Press, New York, USA.
DOI: <https://doi.org/10.1201/9781315116945>
- DuMouchel W. & Duncan G. (1983). Using sample survey weights in multiple regression analyses of stratified samples. *Journal of the American Statistical Association* **78**(383): 535–543.
DOI: <https://doi.org/10.1080/01621459.1983.10478006>
- Grilli L., Biggeri L. & Bini M. (2001). The transition from university to work: a multilevel approach to the analysis of the time to obtain the first job. *Journal of the Royal Statistical Society Series A* **164**(2): 293–305.
DOI: <https://doi.org/10.1111/1467-985X.00203>
- Jayamanne I. & Ramanayake K. (2017). A study on the waiting time for the first employment of arts graduates in Sri Lanka. *Proceedings of 19th International Conference on Machine Learning and Data Analysis*, 1-2 August. Sydney, Australia.
- Jayamanne I. & Ramanayake K. (2018). Population mean estimation using weight adjustment for unit nonresponses. *Proceedings of 4th ISM International Statistical Conference*, Sunway University, Malaysia, p. 19.
- Lohr S.L. (2010). *Sampling Design and Analysis*, 3rd edition. Chapman and Hall/CRC Press, New York, USA.
DOI: <https://doi.org/10.1201/9780429298899>
- Lumley T. (2010). *Complex Surveys: A Guide to Analysis Using R*. John Wiley & Sons, New Jersey, USA.
DOI: <https://doi.org/10.1002/9780470580066>
- Lumley T. (2020). *Survey: Analysis of Complex Survey Samples (Version 3.33-2)*. Available at <http://r-survey.r-forge.r-project.org/survey/>, Accessed, 15 July 202.
- Moore T. (2006). Survival analysis of transitions from benefit to work using administrative data. *Labour, Employment and Work in New Zealand* **2006**: 91–98.
DOI: <https://doi.org/10.26686/lew.v0i0.1323>
- Opsomer J.D. (2009). *Handbook of Statistics*, volume 29B: *Sample Surveys, Inference and Analysis* (eds. D. Pfeffermann & C.R. Rao). North Holland Publishing Co., Netherlands.
- Pfeffermann D. (2011). Modelling of complex survey data: Why model? why is it a problem? how can we approach it? *Survey Methodology* **37**(2): 115–136.
- Salas-Velasco M. (2007). The transition from higher education to employment in Europe: the analysis of the time to obtain the first job. *Higher Education* **54**(3): 333–360
DOI: <https://doi.org/10.1007/s10734-006-9000-1>
- Sarndal C.E., Swensson B. & Wretman J. (2003). *Model Assisted Survey Sampling*. Springer, New York, USA.
- Sterba S. (2009). Alternative model-based and design-based frameworks for inference from samples to populations: From polarization to integration. *Multivariate Behavioral Research* **44**(6): 711–740.
DOI: <https://doi.org/10.1080/00273170903333574>

RESEARCH ARTICLE

Materials Science

Mechanically exfoliated graphene from Sri Lankan vein graphite for field effect transistor application

M Thanihaichelvan*, M Joy Karunya and U Sutharsini

Department of Physics, University of Jaffna, Jaffna 40000, Sri Lanka.

Submitted: 22 October 2021; Revised: 16 September 2022; Accepted: 23 September 2022


Abstract: In this work, a single layer of graphene was exfoliated from Sri Lankan vein graphite obtained from the Kahatagaha graphite mines, and field effect transistors (FETs) were fabricated to study their electronic properties. Graphite pieces were carefully examined, and a small piece of graphite was separated with possible large graphene sheets. A simple Scotch tape technique was used to transfer graphene from the selected graphite pieces onto a 300 nm SiO₂ coated Si (SiO₂/Si) substrate for FET fabrication. The thickness and the uniformity of the graphene layers were tested using atomic force microscopy (AFM). The thickness of the transferred single layer graphene was confirmed to be 0.4 nm. The AFM images also confirmed the presence of double layer graphene with thickness of 0.9 nm. FETs were fabricated by creating electrical contacts using successive thermal evaporation of chrome and gold on the transferred graphene layers with a channel length of 5 μm. Results showed that the graphene FETs showed an ambipolar current response with a positive Dirac voltage. The calculated average electron and hole mobility in the graphene channel were 252 (±57) and 592 (±125) cm²V⁻¹s⁻¹ respectively. The positive Dirac voltage could be attributed to the sulphur content in the graphite obtained from Kahatagaha graphite mines. Our studies suggests that the Sri Lankan graphite can be used as a raw material for graphene exfoliation and device application.

Keywords: Field effect transistor, graphene, graphite, Kahatagaha graphite mine, mobility, Sri Lanka.

INTRODUCTION

Graphene is a single atomic layer of graphite and, consists of carbon atoms which are arranged in a two-dimensional honeycomb lattice (Geim & Novoselov, 2007). Graphene has unique mechanical and electronic properties, by having σ bonds of 1.46 Å and a 2.46 Å lattice parameter. It shows zero gap semiconductor properties with charge carrier mobility greater than 2×10^5 cm²/V s and thermal conductivity greater than 3000 W/m K (Li *et al.*, 2014). The field effect transistor (FET) plays a leading role in different electronic applications. The graphene FET consists of single or multiple layers of graphene or a thin film made up of graphene flakes as a channel (Novoselov *et al.*, 2004; Geim & Novoselov, 2007; Schedin *et al.*, 2007). Due to the zero bandgap of graphene, typical graphene FETs exhibit ambipolar behavior (Reddy *et al.*, 2011). A graphene based FET has a high reactivity to electrical perturbation and high carrier mobility. Due to these properties, graphene FET devices have been used in various applications including biosensors (Murugathas *et al.*, 2020).

Graphene was first identified and recognized in 2004, by Geim and Novoselov (Novoselov *et al.*, 2004). A small amount of graphene were obtained by peeling the layers apart from the highly oriented pyrolytic graphite (HOPG) crystals using Scotch tape. In 2010 Geim and Novosolv won the Nobel prize for the discovery and characterization of graphene sheets (Novoselov *et al.*, 2004). Thereafter, several techniques have been established for graphene synthesis. They are mechanical exfoliation, chemical exfoliation, chemical synthesis, and thermal chemical vapour deposition (CVD). Mechanical exfoliation is the first observed method of graphene synthesis (Bhuyan *et al.*, 2016). Graphene sheets which are produced using this method showed high quality, in comparison with other methods, with lateral sizes up to 100 μm (Booth *et al.*, 2008).

* Corresponding author (thanihai@univ.jfn.ac.lk;  <https://orcid.org/0000-0002-0481-3194>)



This article is published under the Creative Commons CC-BY-ND License (<http://creativecommons.org/licenses/by-nd/4.0/>). This license permits use, distribution and reproduction, commercial and non-commercial, provided that the original work is properly cited and is not changed in anyway.

Graphite is a naturally occurring mineral containing millions of single layers of graphene flakes stacked by weak Van der Waals forces, to form the rocks (Bhuyan *et al.*, 2016). Graphite forms when carbon experiences heat and pressure from the Earth's crust and upper mantle. Even though several countries all over the world mine graphite, Sri Lankan graphite is known as the best graphite, with some of the deposits having carbon content up to 100% (Dissanayake, 1981; Handl, 2021). Unlike the other graphite deposits in the world, the graphite deposits in Sri Lanka are formed as a result of cooling and reduction of atmospheric CO₂ (Touret *et al.*, 2019; Handl, 2021). Kahatagaha, Kolongaha, and Bogala are the main graphite mines found in Sri Lanka. Graphite occur in various morphologies, with different physical and structural characteristics like plate, flake, and fibrous graphite (Wevitavidana *et al.*, 2012). However, Sri Lanka is still exporting bulk graphite as a raw material. Recently, Sri Lankan scientists started working on value addition to graphite and exploring the potential applications of Sri Lankan graphite. Somaweera *et al.* (2021) reported the mechanical and thermal properties of Sri Lankan vein graphite powder. Manaratne *et al.* (2017), have studied the structural and optical properties of graphene oxide fabricated from high purity Sri Lankan vein graphite. The Sri Lankan graphite can be used for solar energy generation and storage (Gao *et al.*, 2017; Manaratne *et al.*, 2017; Amaraweera *et al.*, 2018; Gunasekara, 2021) and water purification applications. Jayamaha *et al.* (2017), demonstrated an electrochemical double layer capacitor made with PEO and Sri Lankan natural graphite. However, there were no attempts made to study the electrical characteristics of Sri Lankan graphite.

In this work, the methods to make graphene FETs were explored, using commercial grade Sri Lankan graphite obtained from Kahatagaha mines with a purity of 97% as the graphene source. A single layer of graphene sheets was successfully separated, followed by transferring the substrate and demonstrating the application for FETs. The electronic properties including electron and hole mobility were also studied.

MATERIALS AND METHODS

Large chunks of commercial grade graphite (purity 97%) from Kahatagaha mines, Sri Lanka, were used for our study. A piece of graphite was selected with highly oriented graphite layers as shown in Figure 1(a). From the large piece, a small piece of graphite was selected carefully to obtain exfoliated graphene with larger area. The selected piece of graphite is shiny and smooth, which is an indication of the presence of large pieces of graphene flakes as illustrated in Figure 1(a). Then graphene was exfoliated from the selected piece of graphite using the Scotch tape method, as described in Figure 1.

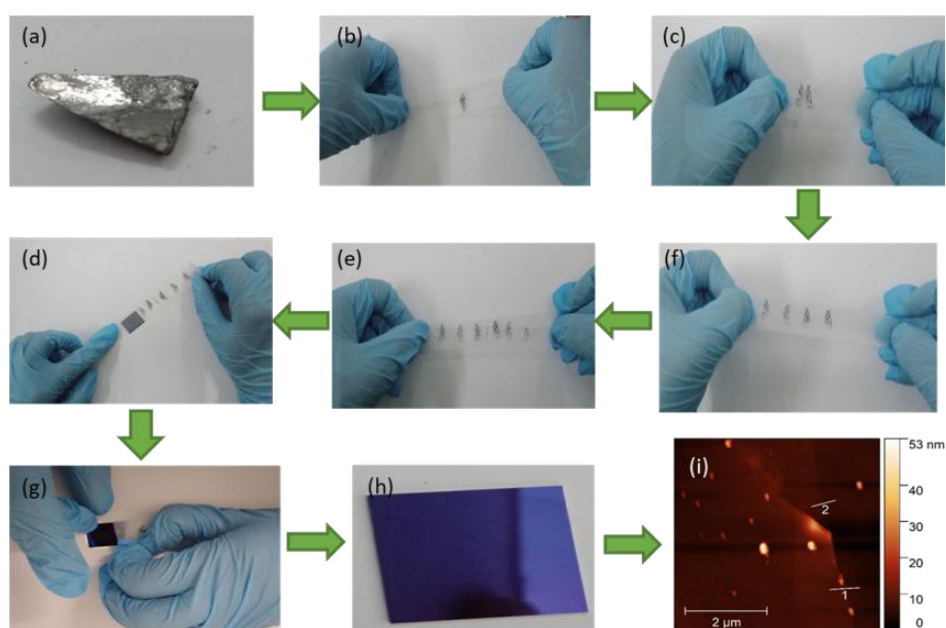


Figure 1: Photographs showing (a) selected piece of graphite for graphene extraction; (b) to (f) successive scotch tape peeling method of graphene layer and (g) graphene transferred on to SiO₂/Si substrate; (h) graphene transferred SiO₂/Si substrate and (i) AFM image of the transferred graphene layer

As shown in the Figure 1(b) to 1(f), graphene was repeatedly peeled off several times using Scotch tape. This procedure was repeated until all possible single graphene layers were obtained. Subsequently the graphene layer was transferred to the silicon wafer chip as shown in Figure 1(g). After that, the important features of the graphene layers were examined using an optical microscope and atomic force microscopy (AFM). The AFM images were used to measure the thickness of graphene layers. Back-gated graphene FETs were fabricated using mechanically exfoliated monolayer graphene. Fabrication of graphene FET using the silicon substrate as a back gate is an enchanting method. In this study, Scotch tape was used to peel off graphene layers from large graphite chunks.

The graphene FET was fabricated by depositing source and drain electrodes on the graphene sheet using thermal evaporation under vacuum (Thanihaichelvan *et al.*, 2018, 2019; Murugathas *et al.*, 2019). A shadow mask with a channel length of 5 μm and width of 1 mm was used to define the source and drain electrodes. The effective channel width was measured by using an optical microscope. These graphene FETs were then electrically characterized by using a computer interfaced source measuring unit (Keithley 4200) at room temperature (Thanihaichelvan *et al.*, 2022). The circuit connections used for measurements, along with the schematic of the fabricated FET, are illustrated in Figure 2. The transfer curves of the fabricated FETs were measured by sweeping the gate voltage from -40 V to 40 V with a supply voltage of 10 mV.

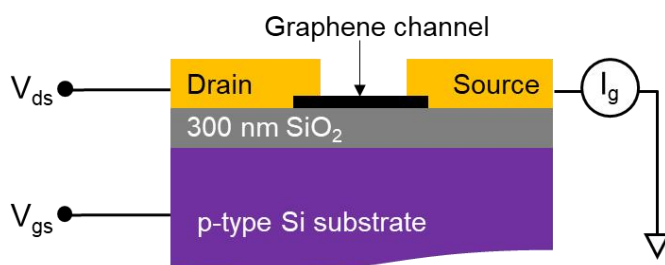


Figure 2: Schematic diagram of graphene FET with circuit connections to study the electronic properties of the FET

RESULTS AND DISCUSSION

The graphene-transferred SiO_2/Si substrate was examined under an optical microscope, and the image captured using a charge-coupled device (CCD) camera is shown in Figure 3(c). The bright yellow area in the middle represents multiple layers of graphene. Layers of graphene in circled areas marked X and Y were tested with AFM for thickness calculations.

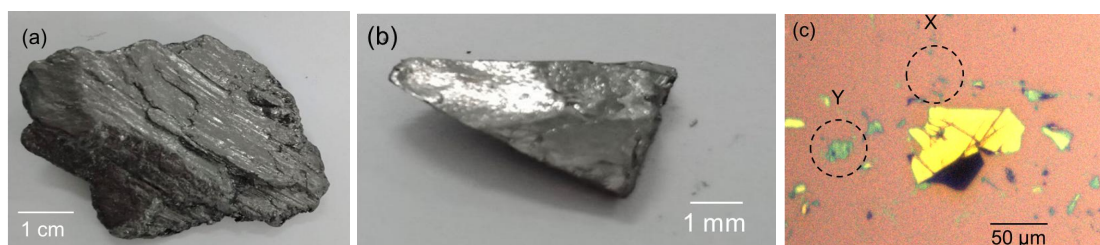


Figure 3: Photograph of (a) a large piece of graphite received from Kahatagaha mine; (b) a selected small piece of graphite for graphene exfoliation, and (c) the optical microscope image of the transferred graphene sheets on the SiO_2/Si substrate.

Structural properties of graphene layers

AFM images were used to measure the thickness of the deposited graphene layers. The thickness of graphene sheets arranged between the source and the drain contacts were identified by line scanning across the possible graphene-substrate interface from the AFM images taken on the graphene sheets. The AFM images and their line profiles are depicted in Figure 4, and the thickness of the graphene layers in the channel was determined. As in Figure 4(a) two different contrasts can be seen and this indicates the presence of two different layers one stacked on another. Three-line profiling across both surfaces was done, and is shown in Figure 4(b). From Figure 4(b) it was possible to determine, across the line 1, that the thickness is about 0.9 nm and across the line 2, the thickness is about 0.4 nm. Theoretically, the thickness of a single layer graphene is about 0.335 nm. So, it can be confirmed that the thickness across the line 2 is approximately equal to the thickness of monolayer graphene and the line profiling across line 1 corresponds to two layers of graphene.

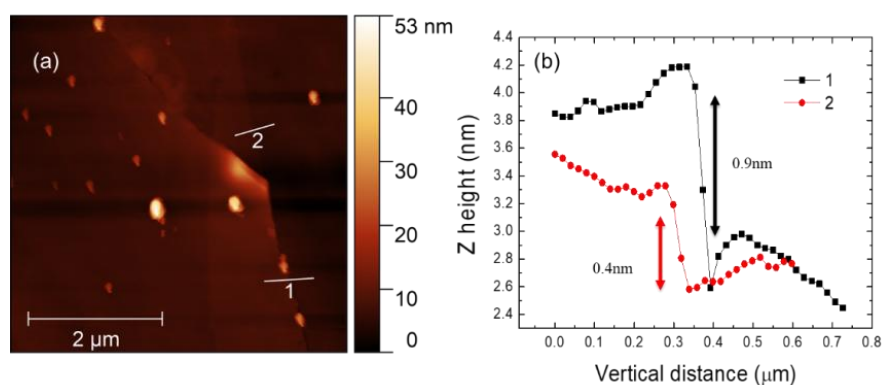


Figure 4: (a) AFM image with two different layers of graphene transferred onto the SiO₂/Si substrate; (b) line scanning data taken across lines named 1 and 2 in the AFM image.

Again, the AFM images were taken on the transferred graphene marked in circle Y as indicated in Figure 3(c), and are shown in Figure 5(a). Figure 5(a) shows the graphene-substrate interface. After the AFM test the line profiling was done and all three lines confirm that the thickness of graphene layer is about 0.4 nm, which is consistent with the thickness of monolayer graphene. The AFM studies on the transferred layer confirmed the presence of single layer graphene on the substrate.

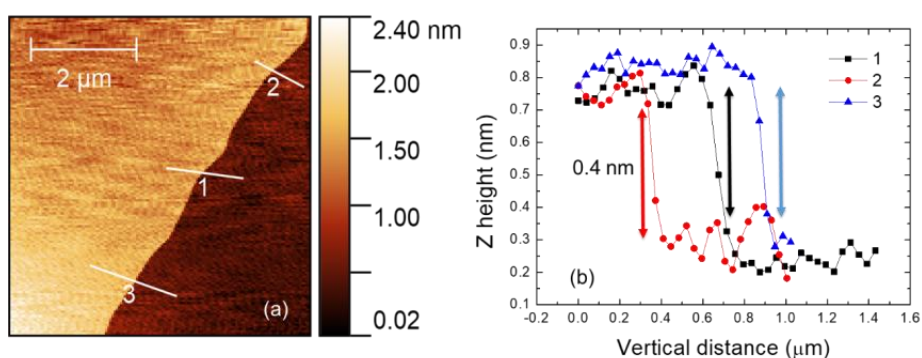


Figure 5: (a) AFM image with a monolayer of graphene; (b) the line scanning profile for the monolayer of graphene across the lines named 1, 2, and 3 in the AFM image.

Electronic properties of graphene FET

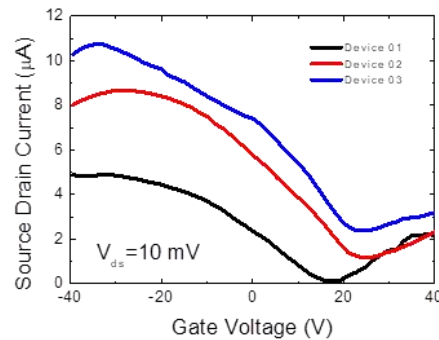


Figure 6: Transfer characteristic curves of three graphene FETs made from graphene

Transfer characteristics can be determined by observing the source-drain current with variation of gate-source voltage. The FET were made by depositing the source and drain electrodes using thermal evaporation. A total of 24 devices were fabricated and 3 of them showed field dependent conductance. Figure 6 shows the transfer characteristic graph of three of the tested graphene FET devices and the electrical properties of all three graphene FETs were summarized in Table 1.

Table 1: Electronic parameters of tested graphene FETs

	On-current (μA)	On-off ratio	Dirac voltage (V)
Device 01	4.8	44	17
Device 02	8.0	7.5	24
Device 03	10.2	4.53	22

The transfer curves show ambipolar behaviour with an on-current of 4.8 to 10.2 μA for a relatively lower source-drain voltage of 10 mV. It is well known that graphene is an ambipolar material and the graphene FET can have a minimum conductance (Dirac point), with varying gate voltage. Theoretically, the Dirac point of an intrinsic graphene FET must be zero volts as the band gap of graphene is zero (Geim & Novoselov, 2007; Reddy *et al.*, 2011). However, the Dirac voltage of a graphene FET can be shifted positively or negatively due to the dopants and charged molecules on the graphene surface (Ohno *et al.*, 2015; Andronescu & Schuhmann, 2017; Lee *et al.*, 2018). As shown in Figure 6 and Table 1, for all three fabricated FETs, the Dirac voltage is found to be positive (+17.0, +22.0 and +24.0 respectively), which indicates that the graphene layer is p-type doped (Murugathas *et al.*, 2020). This positive Dirac point shows the hole dominated conductance of the fabricated graphene flakes at zero gate voltages. This can be attributed to the presence of oxygen species in the graphene surface (Ohno *et al.*, 2015). Sri Lankan graphene also contains sulphur as a common impurity, which can also produce a positive Dirac voltage (Murugathas *et al.*, 2020). The on-off ratio of the fabricated FETs was found to be 44, 7.5 and 4.53. The relatively lower on-off ratio is also a common observation for graphene FETs with channel widths of more than 1 μm (Yang & Murali, 2010; Reddy *et al.*, 2011; Crosser *et al.*, 2015). A high on-off ratio of 44 was observed for device 1. This could be due to the narrow channel width and edge effects during the charge transport.

The mobility of the carriers is an important variable to understand the performance of graphene-based devices. The direct transconductance method was used to calculate the mobility of fabricated FETs. The transconductance (g_m) value was calculated from transfer characteristics.

The field effect hole and electron mobility values were calculated using the following equation:

$$\mu = \frac{g_m L}{W C V_{ds}}$$

where L is length of the channel, W is width of the channel, and C is the specific capacitance of gate oxide (300 nm thickness of SiO_2). The transconductance $g_m = \left(\frac{\partial I_{ds}}{\partial V_{gs}}\right)$ was calculated from the linear region of the transfer curves. The electron mobility was found from the right side of the curve and the hole mobility from the left side of the curve. The calculated mobility values are given in Table 2 for all three tested FET devices.

Table 2: Electron and hole mobility values of fabricated graphene FETs

	Electron mobility ($\text{cm}^2\text{V}^{-1}\text{s}^{-1}$)	Hole mobility ($\text{cm}^2\text{V}^{-1}\text{s}^{-1}$)
Device 01	282.2	592.2
Device 02	287.1	717.5
Device 03	186.0	465.8

The mobility values found in this work appears to be low, which could be due to the scattering contribution from the SiO_2 substrate or the graphene layer. It was also noted that commercial grade graphite with a purity of 97% was used for FET fabrication. It was also noted that the hole mobility was relatively higher than the electron mobility in all three tested devices. This indicates that the electrons in the Sri Lankan graphene have relatively higher effective mass when compared to the holes. The mobility asymmetry and higher hole mobility has also been observed and reported in many other graphene FET studies (Lu *et al.*, 2012; Liang *et al.*, 2015; Urban *et al.*, 2020).

CONCLUSION

In summary, graphene sheets were successfully exfoliated from Sri Lankan graphite using the Scotch tape method and graphene FETs with a global back gate geometry were fabricated. AFM images were used to confirm the existence of single layer graphene in the substrate. It was found that the fabricated graphene FETs showed an ambipolar current response with a positive Dirac voltage. The mobility values varied from device to device, and it was noted that the electron mobility of the FETs was smaller than the hole mobility, indicating the increased effective mass of electrons in Sri Lankan graphene.

REFERENCES

- Amaraweera T.H.N.G., Balasooriya N.W.B., Wijayasinghe H.W.M.A.C., Attanayake A.N.B., Mellander B.E. & Dissanayake M.A.K.L. (2018). Surface modification of natural vein graphite for the anode application in Li-ion rechargeable batteries. *Ionics* **24**: 3423–3429.
DOI: <https://doi.org/10.1007/S11581-018-2523-5>
- Andronescu C. & Schuhmann W. (2017). Graphene-based field effect transistors as biosensors. *Current Opinion in Electrochemistry* **3**(1): 11–17.
DOI: <https://doi.org/10.1016/j.coelec.2017.03.002>
- Bhuyan M.S.A., Uddin M.N., Islam M.M., Bipasha F.A. & Hossain S.S. (2016). Synthesis of graphene. *International Nano Letters* **6**: 65–83.
DOI: <https://doi.org/10.1007/s40089-015-0176-1>
- Booth *et al.* (11 authors) (2008). Macroscopic graphene membranes and their extraordinary stiffness. *Nano Letters* **8**(8): 2442–2446.
DOI: <https://doi.org/10.1021/nl801412y>
- Crosser M.S., Brown M.A., McEuen P.L. & Minot E.D. (2015). Determination of the thermal noise limit of graphene biotransistors. *Nano Letters* **15**(8): 5404–5407.
DOI: <https://doi.org/10.1021/acs.nanolett.5b01788>
- Dissanayake C.B. (1981). The origin of graphite of Sri Lanka. *Organic Geochemistry* **3**(1-2): 1–7.
DOI: [https://doi.org/10.1016/0146-6380\(81\)90006-1](https://doi.org/10.1016/0146-6380(81)90006-1)

- Gao X., Zhan C., Yu X., Liang Q., Lv R., Gai G., Shen W., Kang F. & Huang Z.H. (2017). A High performance lithium-ion capacitor with both electrodes prepared from Sri Lanka graphite Ore. *Materials* **10**(4): 414.
DOI: <https://doi.org/10.3390/MA10040414>
- Geim A.K. & Novoselov K.S. (2007). The rise of graphene. *Nature Materials* **6**: 183–191.
DOI: <https://doi.org/10.1038/nmat1849>
- Gunasekara B.P., Perera K.S., Vidanapathirana K.P. & Vignarooban. K. (2021). Optimization and application of a gel polymer electrolyte in solid state super capacitors with graphite electrodes. *Advances in Materials Research* **10**(2): 137–147.
DOI: <https://doi.org/10.12989/AMR.2021.10.2.137>
- Handl W. (2021). Natural graphite, In: *Industrial Carbon and Graphite Materials* (eds. H. Jäger & W. Frohs) pp. 165–171. John Wiley and Sons Ltd, New York, USA.
DOI: https://doi.org/10.1002/9783527674046.CH6_1_4
- Jayamaha B., Dissanayake M.A.K.L., Vignarooban K., Vidanapathirana K.P. & Perera K.S. (2017). Electrochemical double layer capacitors with PEO and Sri Lankan natural graphite. *Advances in Energy Research* **5**(3): 219–226
DOI: <https://doi.org/10.12989/ERI.2018.5.3.219>
- Lee S., Nathan A., Alexander-Webber J., Braeuninger-Weimer P., Sagade A.A., Lu H., Hasko D., Robertson J. & Hofmann S. (2018). Dirac-point shift by carrier injection barrier in graphene field-effect transistor operation at room temperature. *ACS Applied Materials and Interfaces* **10**(13): 10618–10621.
DOI: <https://doi.org/10.1021/acsami.8b02294>
- Li Q., Mahmood N., Zhu J., Hou Y. & Sun S. (2014). Graphene and its composites with nanoparticles for electrochemical energy applications. *Nano Today* **9**: 668–683
DOI: <https://doi.org/10.1016/j.nantod.2014.09.002>
- Liang Y., Liang X., Zhang Z., Li W., Huo X. & Peng L. (2015). High mobility flexible graphene field-effect transistors and ambipolar radio-frequency circuits. *Nanoscale* **7**: 10954–10962.
DOI: <https://doi.org/10.1039/C5NR02292D>
- Lu C.C., Lin Y.C., Yeh C.H., Huang J.C. & Chiu P.W. (2012). High mobility flexible graphene field-effect transistors with self-healing gate dielectrics. *ACS Nano* **6**(5): 4469–4474.
DOI: <https://doi.org/10.1021/NN301199J>
- Manorathe C.H., Rosa S.R.D. & Kottegoda I.R.M. (2017). XRD-HTA, UV Visible, FTIR and SEM interpretation of reduced graphene oxide synthesized from high purity vein graphite. *Material Science Research India* **14**(1): 19–30.
DOI: <https://doi.org/10.13005/msri/140104>
- Murugathas T., Hamiaux C., Colbert D., Kralicek A.V., Plank N.O.V. & Carraher C. (2020). Evaluating insect odorant receptor display formats for biosensing using graphene field effect transistors. *ACS Applied Electronic Materials* **2**(11): 3610–3617.
DOI: <https://doi.org/10.1021/acsaelm.0c00677>
- Murugathas T., Zheng H.Y., Colbert D., Kralicek A. V., Carraher C. & Plank N.O.V. (2019). Biosensing with insect odorant receptor nanodiscs and carbon nanotube field-effect transistors. *ACS Applied Materials and Interfaces* **11** (9), 9530–9538.
DOI: <https://doi.org/10.1021/acsami.8b19433>
- Novoselov K.S., Geim A.K., Morozov S.V., Jiang D., Zhang Y., Dubonos S.V., Grigorieva I.V. & Firsov A.A. (2004). Electric field in atomically thin carbon films. *Science* **306**(5696): 666–669.
DOI: <https://doi.org/10.1126/science.1102896>
- Ohno Y., Maehashi K. & Matsumoto K. (2015). Graphene biosensor. In: *Frontiers of Graphene and Carbon Nanotubes* (eds. K. Matsumoto), pp. 91–104. Springer, Tokyo, Japan.
DOI: https://doi.org/10.1007/978-4-431-55372-4_7
- Reddy D., Register L.F., Carpenter G.D. & Banerjee S.K. (2011). Graphene field-effect transistors. *Journal of Physics D: Applied Physics* **44**(31): 3001.
DOI: <https://doi.org/10.1088/0022-3727/44/31/313001>
- Schedin F., Geim A.K., Morozov S.V., Hill E.W., Blake P., Katsnelson M.I. & Novoselov K.S. (2007). Detection of individual gas molecules adsorbed on graphene. *Nature Materials* **6**: 652–655.
DOI: <https://doi.org/10.1038/nmat1967>
- Somaweera D., Abeygunawardane G.A., Weragoda S. & Vigneswaran S. (2021). Mechanical and thermal characterization of Sri Lankan vein graphite powder. *Proceedings of the 2021 Moratuwa Engineering Research Conference (MERCon)*, 27-29 July. Institute of Electrical and Electronics Engineers (IEEE), pp. 664–669.
DOI: <https://doi.org/10.1109/MERCON52712.2021.9525803>
- Thanihaichelvan M., Browning L.A., Dierkes M.P., Reyes R.M., Kralicek A.V., Carraher C., Marlow C.A. & Plank N.O.V. (2018). Data on liquid gated CNT network FETs on flexible substrates. *Data in Brief* **21**: 276–283.
DOI: <https://doi.org/10.1016/j.dib.2018.09.093>
- Thanihaichelvan M., Browning L.A., Dierkes M.P., Reyes R.M., Kralicek A.V., Carrahe C., Marlow C.A. & Plank N.O.V. (2019). Metallic-semiconducting junctions create sensing hot-spots in carbon nanotube FET aptasensors near percolation. *Biosensors and Bioelectronics* **130**: 408–413.
DOI: <https://doi.org/10.1016/j.bios.2018.09.021>

- Thanahaichelvan M., Surendran S.N., Kumanan T., Sutharsini U., Ravirajan P., Valluvan R. & Tharsika T. (2022). Selective and electronic detection of COVID-19 (Coronavirus) using carbon nanotube field effect transistor-based biosensor: A proof-of-concept study. *Materials Today Proceedings* **49**: 2546–2549
DOI: <https://doi.org/10.1016/j.matpr.2021.05.011>
- Touret J.L.R., Huizenga J.M., Kehelpannala K.V.W. & Piccoli F. (2019). Vein-type graphite deposits in Sri Lanka: The ultimate fate of granulite fluids. *Chemical Geology* **508**: 167–181.
DOI: <https://doi.org/10.1016/J.CHEMGEO.2018.03.001>
- Urban F., Lupina G., Grillo A., Martucciello N. & Bartolomeo A.D. (2020). Contact resistance and mobility in back-gate graphene transistors. *Nano Express* **1**(1): 010001.
DOI: <https://doi.org/10.1088/2632-959X/AB7055>
- Wevitavidana W.V.R.T., Amaraweera T.H.N.G. & Balasooriya N.W.B. (2012). Structural characteristics of natural graphite and synthetic graphite. *Proceedings of the Research Symposium of Uva Wellassa University*, 22-23 November. Uva Wellassa University, Badulla, Sri Lanka, pp 425–427.
- Yang Y. & Murali R. (2010). Impact of size effect on graphene nanoribbon transport. *IEEE Electron Device Letters* **31**(3): 237–239.
DOI: <https://doi.org/10.1109/LED.2009.2039915>

Thermal Engineering

Assessment of transverse thermal conductivity of coir fibre using experimental, analytical, and numerical methods

LG Chamath^{1,3}, LKT Srimal^{2*} and GA Sewvandi¹

¹ Department of Materials Science and Engineering, Faculty of Engineering, University of Moratuwa, Moratuwa, Sri Lanka.

² Department of Mechanical and Manufacturing Engineering, Faculty of Engineering, University of Ruhuna, Hapugala, Galle, Sri Lanka.

³ Division of Mechanical Engineering Technology, Institute of Technology, University of Moratuwa, Diyagama, Homagama, Sri Lanka.

Submitted: 31 December 2021; Revised: 30 August 2022; Accepted: 23 September 2022

Abstract: Researchers aim to produce sustainable insulation materials using lignocellulose fibres (natural plant fibres). Lignocellulose fibres are readily available, biodegradable, and low-cost materials for insulation. However, these materials are formulated as composites and not as fibres alone. Thus, the thermal properties of these composites depend on the volume fraction of each phase. The evaluation of thermal conductivity can be followed by experimental, analytical, and numerical methods. Numerical and analytical methods are convenient investigational methods; they are more cost-effective, have a higher degree of flexibility in design enhancement, and are faster methods of analysing results than the experimental method. The thermal conductivity value of each phase should be used to analyse the thermal properties of composite materials. However, there is no specific method to determine the thermal conductivity of natural fibres. Therefore, this work suggests a new method to find the thermal conductivity of coir fibres. The method follows the inverse calculation of the analytical methods to find the thermal conductivity of coir fibres, and the substitution values for the equations will be determined by an experimental method. The two-phase composite was fabricated by coir fibres and epoxy with different volume fractions. Next, the thermal conductivity was measured for the fabricated composite and epoxy using the hot disk method. Finally, the transverse thermal conductivity of the fibre was calculated using available analytical models namely, the Rule of mixture, Maxwell's model, Rayleigh's model, and the Lewis-Nielsen model. The thermal conductivity value determined was 0.3058 W/mK. The results were validated through numerical modelling. The thermal conductivity of fibres was determined using a binderless compacted fibre disk, and the obtained value was 0.2797 W/mK. This value was correlated with the results obtained with the analytical and numerical methods.

Keywords: Analytical, coir, FEM, fibres, insulations, thermal conductivity.

INTRODUCTION

Energy consumption in a building is a critical factor since one-third of global energy is required for various activities in the building sector, such as cooking, lighting, air conditioning, and others (Asdrubali *et al.*, 2015; Muzathik, 2016). Hence it is responsible for one-third of Green House Gas (GHG) emissions (Aditya *et al.*, 2017; Kumar *et al.*, 2020). Air conditioning the building to maintain indoor thermal comfort requires high energy (Katili *et al.*, 2015). Therefore, reducing the cooling load for air conditioning will reduce the energy needed (Muzathik, 2003; Gunawardhana *et al.*, 2016; 2017). The cooling load of the indoor atmosphere depends on the heat transfer through the building envelope (Straube, 2011). Therefore, using insulation materials will control the heat transfer through the building envelope (Aditya *et al.*, 2017; Kumar *et al.*, 2020).

Building insulation materials are primarily categorised as conventional materials, state-of-the-art materials, and sustainable materials (Azwa *et al.*, 2013). However, many research studies are currently performed to produce insulation materials using natural plant fibres (lignocellulose fibres) (Bozsaky, 2010; Santhosh & Hiremath, 2020). The reason is that these fibres are bio-degradable, readily available, require low embodied energy for manufacturing, and are non-toxic (Manohar, 2012; Aditya *et al.*, 2017; Hao *et al.*, 2018). Natural

* Corresponding author (srimal@mme.ruh.ac.lk;  <https://orcid.org/0000-0002-3285-3214>)



This article is published under the Creative Commons CC-BY-ND License (<http://creativecommons.org/licenses/by-nd/4.0/>). This license permits use, distribution and reproduction, commercial and non-commercial, provided that the original work is properly cited and is not changed in anyway.

fibres also show properties such as low thermal conductivity, low density, and better mechanical properties. Therefore, coir fibres, oil palm fibres, sugarcane fibres, cotton, flax, hemp, and pineapple fibres are used to fabricate sustainable insulation materials (Manohar, 2012; Asdrubali *et al.*, 2015; Volf *et al.*, 2015; Velichko *et al.*, 2017).

A binder material is necessary to adhere to these fibres without using fibre alone. Hence, these sustainable insulation materials are formulated as composite materials. The insulation properties of the composite material depend on the volume fraction of the fibres and the binder. Some research studies have investigated the effect of thermal conductivity (K_{eff}) of the composite on its fibre loading (Devireddy & Biswas, 2016; 2018; Sahu *et al.*, 2016). Here, epoxy was the commonly used binder material to fabricate the composite because of its high thermal and dimensional stability, better mechanical and chemical stability, and increased durability. It also shows negligible shrinkage after the curing period due to being 100% solid phase (Saba *et al.*, 2016; Yashas *et al.*, 2018).

The K_{eff} of the composites were mainly analysed through experimental, analytical, and numerical methods (Devireddy & Biswas, 2016; 2018; Sunil & Manavendra, 2017; Rashid *et al.*, 2019). However, analytical methods are more attractive in research as they are cheaper, faster, and more convenient than numerical and experimental methods (Sunil & Manavendra, 2017; Samarth, 2018).

Several analytical models were employed to predict the K_{eff} of the composites made from natural fibres and thermoset resins (Devireddy & Biswas, 2016; 2018; Sahu *et al.*, 2016). The Rule of mixture, Maxwell's model, Rayleigh's model, and Lewis-Nielsen model helped to analyse the composites' K_{eff} (Devireddy & Biswas, 2016; 2018; Sahu *et al.*, 2016). The K_{eff} of a composite can be basically calculated from the Rule of mixture. The Rule of mixture has two types of modes: parallel and series models. The parallel model can be used to determine the K_{eff} in the longitudinal direction and the series model can be used to determine the K_{eff} in the transverse direction. In the longitudinal direction, the direction of the heat flow is assumed to be parallel to the fibre orientation, and the transverse direction fibre orientation is perpendicular to the heat flow (Devireddy, 2016; Samarth, 2018). Maxwell's model is the first identified analytical model to evaluate the K_{eff} in a heterogeneous medium. Mainly it is applicable to a structure with well-distributed spherical particles in a matrix phase (Progelhof *et al.*, 1976; Pietrak & Wiśniewski, 2015). This model provides accurate results up to 0.25 of volume fraction (Pietrak & Wiśniewski, 2015). Rayleigh's model is a popular model that evaluates the K_{eff} of a composite with continuous fibres. It can also be applied to mixtures with a higher volume ratio than the Maxwell model (Pietrak & Wiśniewski, 2015). Among these models, Lewis-Nielsen model is an attractive model to determine K_{eff} in transverse and longitudinal directions (Progelhof *et al.*, 1976). This simple model is applicable to a wide range of filler shapes and orientations that gives higher accuracy, up to 0.4 volume fractions, without considering the interfacial thermal resistance (Pietrak & Wiśniewski, 2015).

Sahu *et al.* (2016) studied the K_{eff} for longitudinal direction in a composite made from short banana fibres and an epoxy matrix. Here, the Rule of mixture and Maxwell's and Bruggeman's models were used for analysing the results. The values obtained from the Rule of mixture show the highest deviation from the experimental results. Maxwell's and Bruggeman's results are very close to each other (Sahu *et al.*, 2016). However, Bruggeman's model was developed from different assumptions than Maxwell's model, but both models were developed to evaluate the thermal conductivity in spherical particles in a continuous phase (Progelhof *et al.*, 1976).

Devireddy *et al.* (2018) evaluated the K_{eff} in the longitudinal direction of a hybrid composite made from jute fibres, banana fibres, and epoxy resin. Here, the Rule of mixture, Geometric mean model, Halpin-Tsai, and Lewis-Nielsen models analytically evaluated the K_{eff} . The Geometric mean model shows the highest deviation from the experimental results. The values obtained from Halpin-Tsai and Lewis-Nielsen model show a closer relationship (Devireddy & Biswas, 2018). The Lewis-Nielsen model was obtained from the modification of the Halpin-Tsai model (Progelhof *et al.*, 1976). Hence the results may have a closer relationship.

Further, Devireddy *et al.* (2016) compared the K_{eff} in the transverse direction with K_{eff} in a longitudinal direction for the hybrid composite discussed above. Here, K_{eff} values in the transverse direction produce lower values than in the longitudinal direction (Devireddy & Biswas, 2016). The reason is that the heat flux is parallel

to the fibre orientation in the longitudinal arrangement, and it increases thermal conductivity (Devireddy & Biswas, 2016). Also, Mishra *et al.* (2011) evaluated the K_{eff} of the composites that contain hollow glass spheres in the epoxy matrix. Here, Maxwell's model, Russell's model, and Lewis-Nielsen model were used to evaluate K_{eff} analytically. Russell's model produced the highest deviation, and Maxwell's model offers the closest relationship with the experimental results (Mishra *et al.*, 2011).

These results led to the conclusion that the analytical models' results vary with filler shape, size, distribution through the matrix, the thermal conductivity of the constituent materials, and the bond between the filler and matrix. Therefore, it is better to analyse K_{eff} of the composites using a numerical method to confirm the accuracy of the results (Pietrak & Wiśniewski, 2015; Samarth, 2018).

The above findings indicate that the thermal conductivity of each phase should be applied when analysing the K_{eff} of the composite using analytical and numerical methods. However, thermal conductivity values for these substances were obtained from the literature (Devireddy & Biswas, 2016; 2018; Sahu *et al.*, 2016). The thermal conductivity of fibres has been found mainly from the binderless compacted fibre disks (Rodríguez *et al.*, 2011; Manohar, 2012; Asdrubali *et al.*, 2015), but the thermal conductivity value changed with the density of the fibre disk. Therefore, the thermal conductivity of a single fibre cannot be determined using this. Also, the thermal conductivity in transverse orientation is very important to design insulation materials, because the lowest thermal conductivity is given by that orientation. However, finding the transverse thermal conductivity of a single fibre is a difficult task. Therefore, this study suggests a novel method for measuring the thermal conductivity of fibres (Kumara *et al.*, 2016; Chamath *et al.*, 2022; Udayakumara *et al.*, 2022). In the previous studies (Mishra *et al.*, 2011; Devireddy & Biswas, 2016; 2018; Sahu *et al.*, 2016), the K_{eff} value of the composites has been evaluated from analytical methods by substituting the thermal conductivity of each phase. For this study, the inverse calculation method is used. Here, the K_{eff} of the composite and thermal conductivity of the matrix were determined, followed by analytically defining the thermal conductivity value of fibres. With that aim, a two-phase composite was formulated with different fibre volume fractions. Here, coir fibres were selected as the fibrous material due to their low thermal conductivity (Srimal *et al.*, 2014; 2015; Sathishkumar *et al.*, 2018; Rashid *et al.*, 2019), low density (Petroudy, 2017), and high moisture resistance (Ramamoorthy *et al.*, 2015; Petroudy, 2017). Then the K_{eff} of the composite was measured experimentally, and the thermal conductivity of the coir fibres was calculated using the Rule of mixture, Maxwell model, Rayleigh's model, and Lewis-Nielsen model. The results were validated by numerical analysis.

A binderless compacted coir fibre disk was prepared, and the thermal conductivity of the disk was measured experimentally. Then the thermal conductivity of coir fibres was calculated using Landauer's equation (Smith *et al.*, 2013). The results of this method helped to validate the results of the previous method.

MATERIALS AND METHODS

Density measurement of coir fibres

Fibres were treated using a 4% NaOH solution (Chamath *et al.*, 2020), and the density was measured before fabrication. The Archimedes method was used to measure the density of fibres. Here, 25 mL density bottles were used. Canola oil available in the market acted as the immersion liquid because it helps to coat the fibre well due to its low viscosity and surface tension (Truong *et al.*, 2009; Amiri *et al.*, 2017).

The density of fibres (ρ_{fibre}) was calculated using equation (1),

$$\rho_{\text{fibre}} = \frac{(m_2 - m_1)}{(m_4 - m_1) - (m_3 - m_2)} \times \frac{m_4 - m_1}{25} \quad \dots(1)$$

where, m_1 is the weight of the density bottle, m_2 is the weight of the density bottle with fibres, m_3 is the density bottle with canola oil and fibres, and m_4 is the weight of the density bottle with canola oil. All weighted values are given in grams (g).

Composite fabrication

The conventional hand lay-up method was used to fabricate the composite. This method is widely used in research activities due to its low cost (Elkington *et al.*, 2015). However, uniaxially oriented fibres should be used to get uniform distribution in the composite (Yashas *et al.*, 2018). According to Lewis-Nielsen model, if the fibre length is higher than 15 times the aspect ratio, it can be considered a uniaxially oriented fibre (Progelhof *et al.*, 1976; Devireddy & Biswas, 2018). Lengthy fibres show curliness and reduce the uniaxial distribution. Because of these factors, coir fibres were cut into 5 mm in length. Then the fibres were mixed with epoxy in different volume ratios as shown in Table 1. Here, epoxy was prepared with a binder and the hardener with a 2:1 ratio according to the manufacturer's instructions. The mixture was then poured into the wooden mould (100 mm × 50 mm × 10 mm).

Table 1. Composition of fabricated samples

Sample no.	Weight of fibres (g)	Volume of epoxy (mL)	Composition
1	1.150	49.0	Fibre (2 vol%) + Epoxy (98 vol%)
2	2.300	48.0	Fibre (4 vol%) + Epoxy (96 vol%)
3	2.875	47.5	Fibre (5 vol%) + Epoxy (95 vol%)
4	4.600	46.0	Fibre (8 vol%) + Epoxy (92 vol%)
5	5.750	45.0	Fibre (10 vol%) + Epoxy (90 vol%)

The mould was allowed 48 hours to complete the curing process, and the K_{eff} of the samples were measured using the hot wire disk (Yuksel, 2016; Zhao *et al.*, 2016). Each sample was cut into two separate pieces as per the instrument setup. Then the sensor of the hot wire disk was placed between the two separated samples, as shown in Figure 1. Here, the temperature of the sensor was maintained at 30 °C.



Figure 1: Measuring the thermal conductivity of the fabricated composite using the hot wire disk.

Evaluation of the thermal conductivity of fibres

The thermal conductivity of fibres was calculated from the Rule of mixture, and Maxwell's, Rayleigh's, and Lewis-Nielsen models, after measuring the K_{eff} from the hotwire disk.

Here, the fibre orientation is perpendicular to the heat flow. Therefore, a series model was necessary to analyse the K_{eff} in this orientation, as given by equation (2).

$$K_{eff} = \frac{1}{\frac{V_m}{K_m} + \frac{V_f}{K_f}} \quad \dots(2)$$

Where K_m is the thermal conductivity of the matrix, V_m is the volume fraction of the matrix, K_f is the thermal conductivity of fibre, and V_f is the volume fraction of fibre.

Equation (3) presents Maxwell’s model.

$$K_{eff} = K_m \frac{2K_m + K_f - V_f(K_m - K_f)}{2K_m + K_f + V_f(K_m - K_f)} \dots(3)$$

Equation (4) presents Rayleigh’s model,

$$\frac{K_{eff}}{K_m} = 1 + \frac{2V_f}{C_1 - V_f + C_2(0.30584V_f^4 + 0.013363V_f^8 + \dots)} \dots(4)$$

where $C_1 = \frac{K_f + K_m}{K_f - K_m}$ and $C_2 = \frac{K_f - K_m}{K_f + K_m}$.

Equation (5) presents Lewis-Nielsen model,

$$K_{eff} = K_m \left[\frac{1 + ABV_f}{1 - BV_f \Psi} \right] \dots(5)$$

where $B = \frac{\frac{K_f}{K_m} - 1}{\frac{K_f}{K_m} + A}$ and $\Psi = 1 + \left(\frac{1 - \phi_m}{\phi_m^2} \right) V_f$.

Table 2 presents the value of the constant ‘A’ in equation (5). The aspect ratio of fibre is above 15, and the direction of the heat flow is perpendicular to the direction of the fibre orientation. Therefore, 0.5 can be selected as the value for constant ‘A’, as per Table 2.

Table 2: The value of the constant ‘A’

Type of dispersed phase	Direction of heat flow	A
Cubes	Any	2.00
Spheres	Any	1.50
Aggregate of spheres	Any	2.50/φ ₀ - 1
Randomly oriented rods aspect ratio = 2	Any	1.58
Randomly oriented rods aspect ratio = 4	Any	2.08
Randomly oriented rods aspect ratio = 6	Any	2.80
Randomly oriented rods aspect ratio = 10	Any	4.93
Randomly oriented rods aspect ratio = 15	Any	8.38
Uniaxial oriented fibres	Parallel to fibres	2L/D
Uniaxial oriented fibres	Perpendicular to fibres	0.50

Table 3 provides the value of constant ‘φ_m’. The fibre distribution is uniaxial random. Therefore, the value of 0.8200 could be selected as the φ_m value.

Finite element method

It is better to validate the analytically evaluated thermal conductivity value using a numerical method. Normally, fibres are randomly distributed throughout the matrix in a composite; hence it is difficult to model the random arrangement in the numerical method. However, the main objective of the research is the evaluation of the transverse thermal conductivity of the fibres. Therefore, the heat flow should be applied perpendicular to the fibre direction. Also, some assumptions are considered during the computational analysis, such as, fibres and matrix are microscopically and homogeneously distributed throughout the composite, fibres have the same shape and size, fibre and matrix have a perfect bonding, thermal resistance between two phases is negligible, and the composite is void-free throughout (Rao *et al.*, 2015; 2018; Priya *et al.*, 2016; Devireddy & Biswas, 2018;

Rashid *et al.*, 2019). The Ansys software package was used for this study while considering the abovementioned assumptions (Sahu *et al.*, 2016; Sunil, 2017; Devireddy & Biswas, 2018; Rashid *et al.*, 2019).

Table 3: The value of constant ' φ_m '

Shape of particle	Type of packing	φ_m
Spheres	Hexagonal close	0.7405
Spheres	Face centred cubic	0.7405
Spheres	Body centred cubic	0.6000
Spheres	Simple cubic	0.5240
Spheres	Random close	0.6370
Spheres	Random close	0.6010
Rods of fibres	Uniaxial hexagonal close	0.9070
Rods of fibres	Uniaxial simple cubic	0.7850
Rods of fibres	Uniaxial random	0.8200
Rods of fibres	Three-dimensional random	0.5200

Also, it is important to identify the cross-section view of the coir fibre to decide the element for the numerical analysis. Therefore, scanning electron microscope (SEM) image analysis was done to obtain a cross-section view of the fibres. The fibres have an approximately circular cross-section, as shown in Figure 2. The circular cross-section provides an additional advantage for the analytical and numerical modelling of the composite.

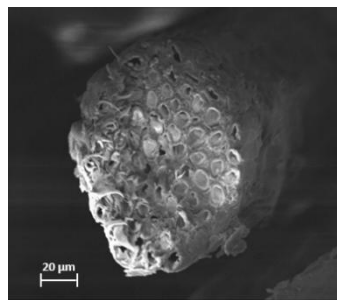


Figure 2: SEM image representing the cross-section of a coir fibre ($\times 1000$)

Then, the fibre distribution in the epoxy matrix could be assumed as a square pattern and hexagonal pattern, as shown in Figure 3 for the numerical analysis (Sihn & Roy, 2011; Rao *et al.*, 2015; Devireddy & Biswas, 2016).

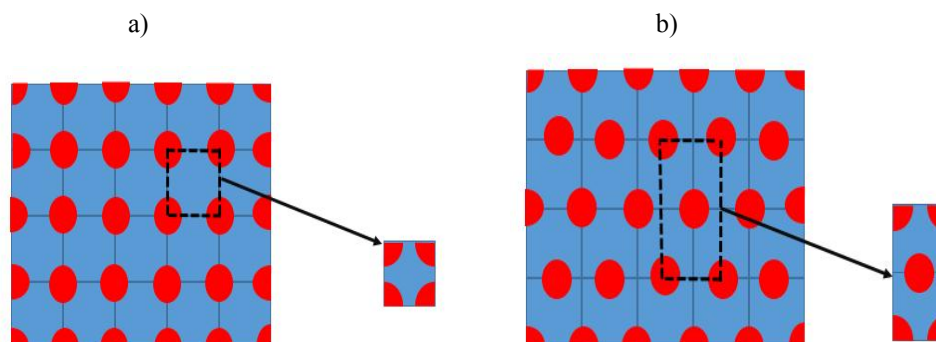


Figure 3: Schematic representation of the fibre distribution in a) square pattern, b) hexagonal pattern

Then, the fibre distribution can be simplified as an isolated unit cell that has a three-dimensional physical model with a periodic arrangement of cylindrical fibres in epoxy cubes. Figure 4 represents the isolated unit cell of the square array pattern (Sahu *et al.*, 2016; Devireddy & Biswas, 2018).

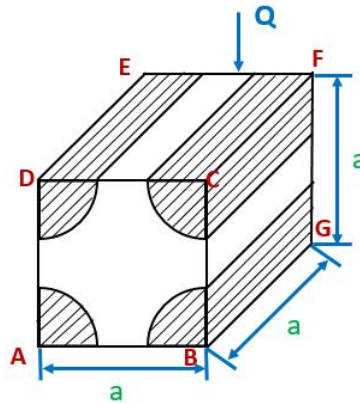


Figure 4: Isolated unit cell of the square array pattern

The above unit cells are simplified as a quarter unit cell, as shown in Figure 5, to reduce the complexity of geometry and computing time (Rao *et al.*, 2015). It is vital to use an orthogonal coordinate system that represents the fibre direction on the z-axis; the x-axis is the plane of the unit cell, which is perpendicular to the fibres, and the y-axis is perpendicular to the plane of the unit cell and perpendicular to the fibres. Here, the fibre diameter was measured using a primo star iLED microscope, and the average diameter was 201.6 μm , while the length of the unit cell was calculated corresponding to the volume ratio of 0% to 0.1%.

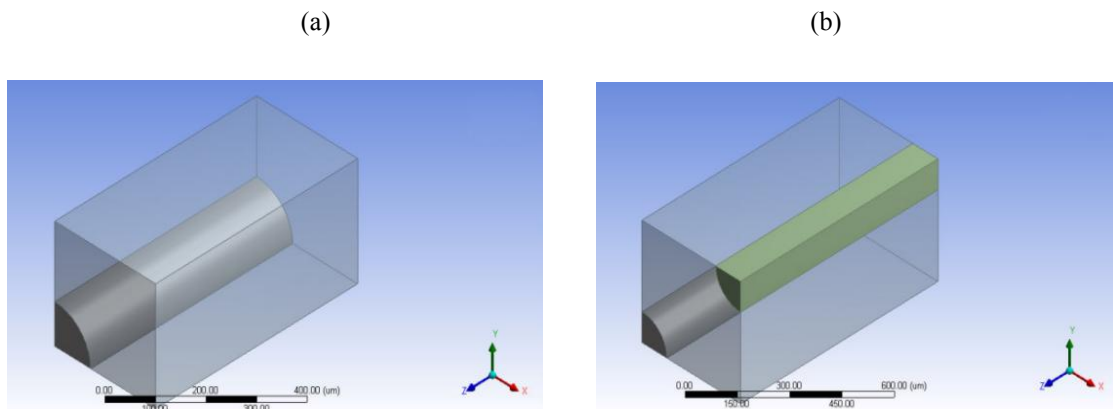


Figure 5: The developed quarter unit cell for the numerical analysis a) square array, b) hexagonal array

The boundary condition for FEM to analyse thermal conductivity

For finding the transverse thermal conductivity of the unit cell, the heat load was applied as a temperature for both plane face (30 °C) and opposite face (25 °C) to maintain a temperature difference of 5 °C. Other faces, parallel to the heat flow, are assumed to be adiabatic (Ilyas & Rejeesh, 2015; Priya *et al.*, 2016; Devireddy & Biswas, 2018; Rao, 2018). The heat distribution throughout the unit cell was analysed by Ansys software, and the thermal conductivity of the unit cell was calculated by Fourier’s law, as shown in equation (6),

$$Q_x = -K (dT/da) \dots(6)$$

where K is the thermal conductivity of the unit cell, dT/da is the temperature gradient in the x-direction, and Q_x is the heat flux along the x-direction.

Preparation of coir fibre specimen to measure thermal conductivity

A cylindrical-shaped specimen was prepared by compressing 5 mm coir fibres without using a binder (Rodríguez *et al.*, 2011). Here, a 20 Mpa pressure was applied on 6.61 g coir fibres with a mould diameter of 25 mm. The thermal conductivity reading was obtained from the hot wire disk after removing the specimen from the mould, as shown in Figure 6.

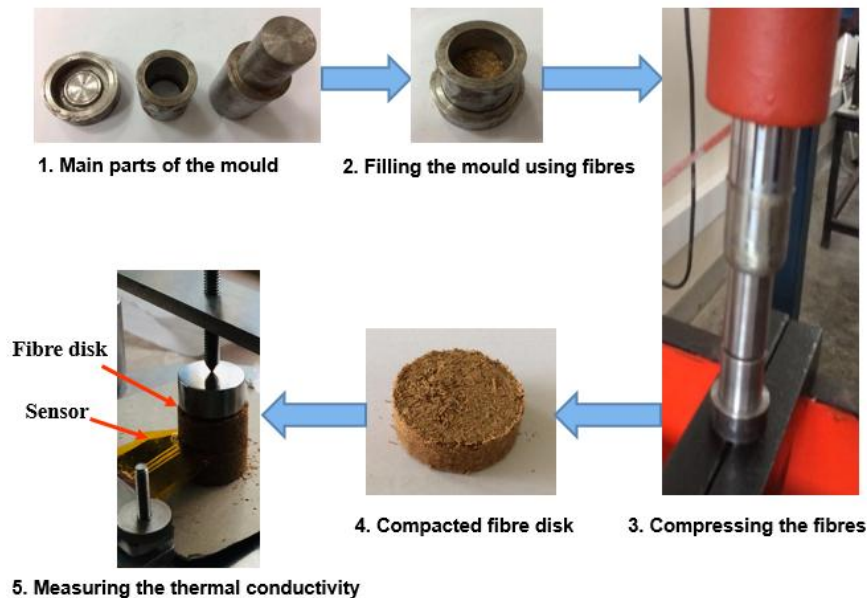


Figure 6: Illustration of the preparation method of binder-less compacted disk

Then the density of the compacted disk was calculated, and it was 0.936 gcm^{-3} . According to this density value, the compacted fibre disk contains a 0.2280 volume fraction of air. However, to predict the thermal conductivity of coir fibres, Landauer's equation was used to calculate the thermal conductivity of coir fibres because the structure is open porous when the volume fraction is in the range of $0.15 < V_p < 0.65$ (Smith *et al.*, 2013). Equation (7) provides the Landauer's equation.

$$K_{eff} = \frac{1}{4} \left[K_p(3V_p - 1) + K_m(2 - 3V_p) + \left\{ [K_p(3V_p - 1) + K_s(2 - 3V_p)]^2 + 8K_mK_p \right\}^{1/2} \right] \dots (7)$$

Where K_p is the thermal conductivity of air at 25 °C, and V_p is the volume fraction of air.

RESULTS AND DISCUSSION

Thermal conductivity of the fabricated composite

A significant influence is noted in the effective thermal conductivity of the composite after adding fibres. The K_{eff} of the composites increases with fibre loading. It was concluded that the thermal conductivity of fibre is higher than the thermal conductivity of pure epoxy.

The transverse K_{eff} of the composite for each fibre loading and the thermal conductivity value of epoxy were substituted to the Rule of mixture, and Maxwell's, Rayleigh's, and Lewis Nielsen's models, to find the fibre thermal conductivity. Table 4 summarises the calculated thermal conductivity values of fibres for each loading.

Figure 7 illustrates the measured K_{eff} of the composites with different fibre loadings of coir fibre in the transverse direction using the hot wire disk.

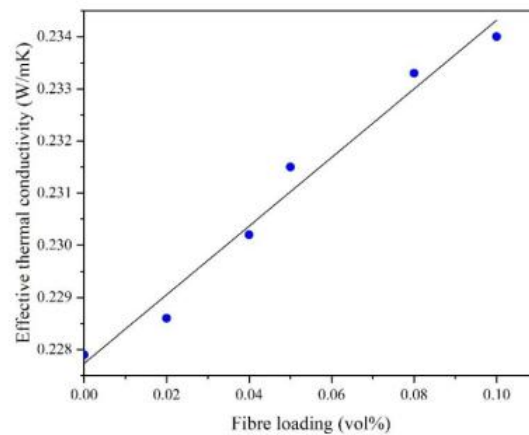


Figure 7: Effective thermal conductivity of the fabricated composites using the hot wire disk

Table 4: Calculation of thermal conductivity of coir fibre

Fibre loading	K_{eff} of the composite	K_f from Rule of mixture	K_f from Maxwell's model	K_f from Rayleigh's model	K_f from Lewis-Nielsen model
0.02	0.2286	0.2946	0.2815	0.2836	0.2825
0.04	0.2302	0.3172	0.2992	0.3029	0.3049
0.05	0.2315	0.3432	0.3140	0.3199	0.3249
0.08	0.2333	0.3209	0.2960	0.2999	0.3138
0.10	0.2340	0.3133	0.2976	0.3015	0.3028
Average K_f value		0.3192	0.2977	0.3016	0.3058

According to the above calculation, the average K_f values obtained from different models are 0.3192 W/mK, 0.2977 W/mK, 0.3016 W/mK, and 0.3058 W/mK.

Selecting the most suitable value is challenging. Hence, each value is separately substituted to the Rule of mixture, and Maxwell's, Rayleigh, and Lewis Nielsen models. The behaviour of substituted values in the models was then compared with the experimental values to select the best value for the K_f . Figures 8 a), b), c) and d) present the comparisons of the substituted values into models with experimental values

The models show a variation with the regression line of the experimental values according to Figures 8a) – 8d). The reason is the difference in the assumption during the development of micromechanical models of the analytical models, such as fibre shape, distribution, and interfacial contact between the matrix and fibre material. Also, void formation in the composite and changes in the orientation of fibres may have caused this situation. Therefore, it is essential to calculate percentage errors associated with the respective experimental values with models to identify the best value for K_f .

Table 5 presents the percentage errors associated with the respective experimental values with the substituted K_f value of 0.3192 W/mK to the Rule of mixture and Maxwell's, Rayleigh's, and Lewis Nielsen's models in Figure 8a).

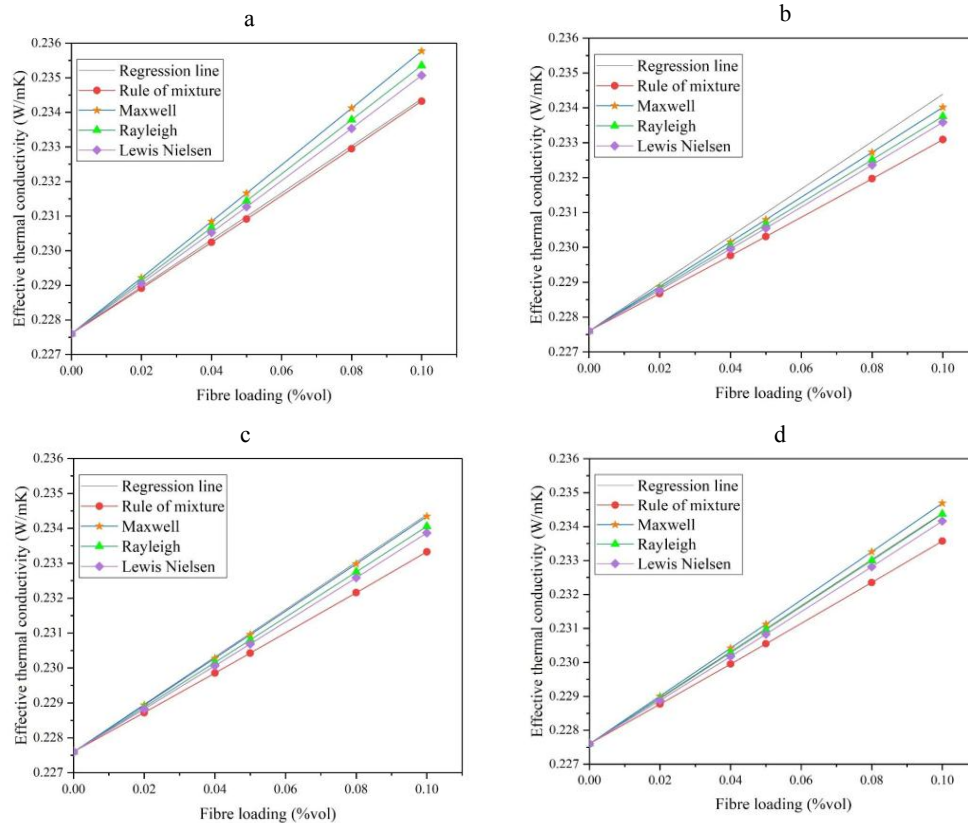


Figure 8: The behaviour of thermal conductivity of fibre with analytical models a) thermal conductivity value 0.3192 W/mK; b) thermal conductivity value 0.2977 W/mK; c) thermal conductivity value 0.3016; W/mK d) thermal conductivity value 0.3058 W/mK

Table 5: Percentage errors in Figure 8a) with the experimental values

Fibre Loading	Experimental K_{eff} (W/mK)	Percentage error			
		Rule of mixture	Maxwell	Rayleigh	Lewis Nielsen
0.02	0.2290	0.0218	0.1136	0.0742	0.0393
0.04	0.2303	0.0347	0.2301	0.1520	0.0912
0.05	0.2340	0.0390	0.2857	0.1905	0.1169
0.08	0.2330	0.0343	0.4678	0.3218	0.2189
0.10	0.2343	0.0299	0.5888	0.4138	0.2901
Average percentage error (E)		0.0319	0.3372	0.2305	0.1513
Mean value of E		0.1877			

The Rule of mixture and Maxwell’s, Rayleigh’s, and Lewis-Nielsen models give the average percentage errors (E) of 0.0319, 0.3372, 0.2305, and 0.1513, respectively. The mean value of E is 0.1877. The same calculations were made for Figures 8b) -8d), and the results are summarised in Table 6.

Table 6. Mean value of E in Figures 8a) – 8d)

Figure No.	Substituted K_f value (W/mK)	Mean value of E
8a)	0.3192	0.1877
8b)	0.2977	0.2029
8c)	0.3016	0.1321
8d)	0.3058	0.0923

The substitution of the K_f value of 0.3058 W/mK produced a minimum percentage error of 0.0923. Therefore, the thermal conductivity of coir fibre can be taken as 0.3058 W/mK. It is important to validate this value using a numerical method, and the next section discusses the numerical analysis for the validation.

Numerically validating the thermal conductivity of fibres

The value of 0.3058 W/mK was validated from the numerical methods using square array pattern and hexagonal array pattern. Figure 9 provides the temperature distribution in square and hexagonal array patterns for the 0.1 fibre ratio.

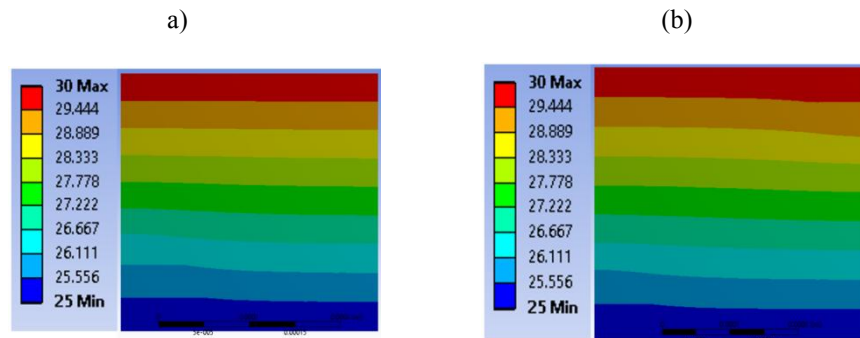


Figure 9: The temperature distribution in quarter unit cell: a) square array pattern, b) hexagonal array pattern

The temperature distribution is uniform in the upper region of Figure 9a). However, it shows an uneven distribution around the bottom region of the quarter unit cell due to the presence of fibre. Also, the temperature distribution is uneven in the top and bottom regions of Figure 9b) due to the presence of fibres. But it will show a uniform distribution in the middle region of the quarter unit cell.

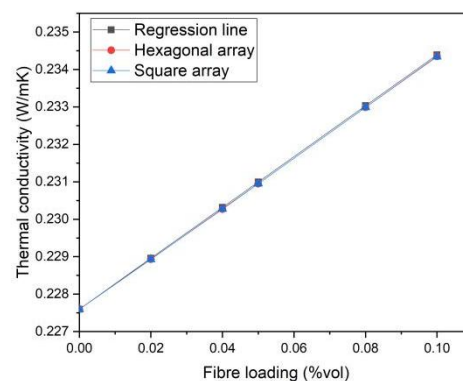


Figure 10: Comparison of the thermal conductivity values from the experimental and numerical methods

According to Figure 10, the values obtained from the numerical method overlap with the regression line of the experimental values. Hence, the transverse thermal conductivity of the coir fibres can be accepted as 0.3058 W/mK according to the results of experimental, analytical, and numerical methods.

Thermal conductivity of compacted coir fibres

According to the cross-section view of the SEM image analysis in Figure 2, fibres show a porous structure. However, the thermal conductivity of the fibre is given by the combination of the porous and cellulose parts, because the porous structure is not continuous from one end to another end of the fibre. This porous structure is given by the lumen of the fibre cell structure. Therefore, it can be assumed as a close porous structure. In the composite fabrication method, the fibre surface was fully covered by epoxy. Therefore, in the binderless compacted disk method Landauer's method should be applied to the whole structure of the fibre, with a combination of porous and cellulose parts due to the close porosity of the fibre.

According to Landauer's method in equation (7), the calculated value of the thermal conductivity of coir fibres is 0.2797 W/mK. The results obtained from the compacted fibre disk are close to the value of 0.3058 W/mK. However, the variation in the results may be due to the interfacial thermal resistance in the structure (Ahmadi *et al.*, 2019).

CONCLUSION

In this study, a composite material was fabricated using epoxy and coir fibres for different fibre loadings. Then the effective thermal conductivity (K_{eff}) of the composites was measured. Here, the K_{eff} of the composite was higher than the thermal conductivity of pure epoxy, and the K_{eff} was increased with the increasing fibre loading in the composite. Hence, it may be due to the higher thermal conductivity of coir fibres than epoxy. Then the experimentally measured K_{eff} values can be used to calculate the thermal conductivity of coir fibres analytically. Therefore, the analytical models are a practical approach to finding the thermal conductivity in coir fibres due to the close relation with the experimental values. The transverse thermal conductivity of the fibre could be taken as 0.3058 W/mK by the comparison of the results obtained from the analytical models. Additionally, validation of the transverse thermal conductivity value of 0.3058 W/mK using the numerical method will add value to this research work. Here, the numerical results and experimental results overlapped with each other and it proved that 0.3058 W/mK could be taken as the thermal conductivity of the fibre. Further, a binderless compacted fibre disk was prepared and the thermal conductivity of the disk was measured to validate the results obtained from the previous method. Here, the void content of the disk was 22.8%, which shows an open porous structure. Therefore, the thermal conductivity of fibre was calculated using Landauer's equation and the value was 0.2797 W/mK. However, this method could be used to validate the value of 0.3058 W/mK, despite the difference between the two values.

Acknowledgement

The authors wish to thank the Department of Physics, The Open University Sri Lanka and Department of the Mechanical Engineering, University of Moratuwa, Sri Lanka for providing valuable support in the resource arrangements of this study.

REFERENCES

- Aditya L., Mahlia T.M.I., Rismanchi B., Ng H.M., Hasan M.H., Metselaar H.S.C., Muraza O. & Aditya H.B. (2017). A review on insulation materials for energy conservation in buildings. *Renewable and Sustainable Energy Reviews* **73**: 1352–1365.
DOI: <https://doi.org/10.1016/j.rser.2017.02.034>
- Ahmadi M., Ansari R. & Hassanzadeh-Aghdam M.K. (2019). Finite element analysis of thermal conductivities of unidirectional multiphase composites. *Composite Interfaces* **26**(12): 1035–1055.
DOI: <https://doi.org/10.1080/09276440.2019.1578588>
- Amiri A., Triplett Z., Moreira A., Brezinka N., Alcock M. & Ulven C.A. (2017). Standard density measurement method development for flax fiber. *Industrial Crops and Products* **96**: 196–202.
DOI: <https://doi.org/10.1016/j.indcrop.2016.11.060>
- Asdrubali F., D'Alessandro F. & Schiavoni S. (2015). A review of unconventional sustainable building insulation materials. *Sustainable Materials and Technologies* **4**: 1–17.
DOI: <https://doi.org/10.1016/j.susmat.2015.05.002>
- Azwa Z.N., Yousif B.F., Manalo A.C. & Karunasena W. (2013). A review on the degradability of polymeric composites based on natural fibres. *Materials and Design* **47**: 424–442.
DOI: <https://doi.org/10.1016/j.matdes.2012.11.025>
- Bozsaky D. (2010). The historical development of thermal insulation materials. *Periodica Polytechnica Architecture* **41**(2): 49–56.
DOI: <https://doi.org/10.3311/pp.ar.2010-2.02>
- Chamath L.G., Srimal L.K.T. & Sewvandi G.A. (2020). Effect of alkaline concentration on the surface properties of coir fibers. *Proceeding of the National Engineering Research Symposium*, volume 1, 10 December. NERDC, Ja Ela, Sri Lanka, pp. 7–12.
DOI: 10.13140/RG.2.2.36167.37283
- Chamath L.G., Srimal L.K.T. & Sewvandi G.A. (2022). Evaluating the thermal conductivity of three-phase insulation

- composite using analytical and numerical methods. *2022 Moratuwa Engineering Research Conference (MERCon)*, 27–29 July. University of Moratuwa, Sri Lanka.
DOI: 10.1109/MERCon55799.2022.9906166
- Devireddy S.B.R. & Biswas S. (2016). Physical and thermal properties of unidirectional banana-jute hybrid fiber-reinforced epoxy composites. *Journal of Reinforced Plastics and Composites* **35**(15): 1157–1172.
DOI: <https://doi.org/10.1177/0731684416642877>
- Devireddy S.B.R. (2016). Mechanical, thermal and physical properties of hybrid banana-jute fibers reinforced epoxy and polyester composites : modeling and experiments mechanical, thermal and physical properties of hybrid banana-jute fibers reinforced epoxy and polyester. *PhD Thesis*, National Institute of Technology, Rourkela, India.
- Devireddy S.B.R. & Biswas S. (2018). Thermo-physical properties of short banana-jute fiber-reinforced epoxy-based hybrid composites. *Proceedings of the Institution of Mechanical Engineers, Part L: Journal of Materials: Design and Applications* **232**(11): 939–951.
DOI: <https://doi.org/10.1177/1464420716656883>
- Elkington M., Bloom D., Ward C., Chatzimichali A. & Potter K. (2015). Hand layup: understanding the manual process. *Advanced Manufacturing: Polymer and Composites Science* **1**(3): 138–151.
DOI: <https://doi.org/10.1080/20550340.2015.1114801>
- Gunawardhana H.P.B., Chamath L.G. & Sewvandi G. A. (2016). A methodology to control the interior temperature of vehicles parked under the sun. *Proceeding of the 2016 Manufacturing and Industrial Engineering Symposium (MIES)*, 22–22 October. Waters Edge, Battaramulla, Sri Lanka, pp. 1–5.
DOI: <https://doi.org/10.1109/MIES.2016.7779990>
- Gunawardhana H.P.B., Chamath L.G. & Sewvandi G.A. (2017). Solar powered mini air conditioner for automobiles. *Proceeding of the Materials Engineering Symposium on Innovations for Industry*, Department of Materials Science and Engineering, University of Moratuwa, Sri Lanka. Available at <http://dl.lib.uom.lk/handle/123/17361>, Accessed 27 August 2022.
- Hao L.C., Sapuan S.M., Hassan M.R. & Sheltami R.M. (2018). Natural fiber reinforced vinyl polymer composites. In: *Natural Fibre Reinforced Vinyl Ester and Vinyl Polymer Composites*, pp 27–70. Woodhead Publishing, Sawston, UK.
DOI: <https://doi.org/10.1016/b978-0-08-102160-6.00002-0>
- Ilyas N.P. & Rejeesh C.R. (2015). Modelling and thermal analysis of medium density coir composite boards. *International Journal of Engineering Research and Technology* **4**(08): 557–559.
DOI: <https://doi.org/10.17577/IJERTV4IS080554>
- Katili A.R., Boukhanouf R. & Wilson R. (2015). Space cooling in buildings in hot and humid climates - a review of the effect of humidity on the applicability of existing cooling techniques. *Proceedings of 14th International Conference on Sustainable Energy Technologies (SET)*, 25–27 August, Nottingham, UK.
DOI: <https://doi.org/10.13140/RG.2.1.3011.5287>
- Kumar D., Alam M., Zou P.X.W., Sanjayan J.G. & Memon R.A. (2020). Comparative analysis of building insulation material properties and performance. *Renewable and Sustainable Energy Reviews* **131**: 110038.
DOI: <https://doi.org/10.1016/j.rser.2020.110038>
- Kumara P.D.C., Viraj M.P.S., Jayaweera H.H.E., Muzathik A.M. & Ariyaratne T.R. (2016). Experimental investigation of the temperature dependency of the thermal conductivity of glass wool used in a steam generator. *Proceedings of the Annual Research Symposium 2016*, 11–22 October. University of Colombo, Sri Lanka, p. 275.
- Manohar K. (2012). Experimental investigation of building thermal insulation from agricultural by-products. *British Journal of Applied Science and Technology* **2**(3): 227–239.
DOI: <https://doi.org/10.9734/bjast/2012/1528>
- Mishra D., Satapathy A. & Patnaik A. (2011). Processing and thermal conductivity characterization of solid glass microspheres filled polymer composites. *Proceeding of 14th International Conference on Advanced Materials and Processing Technologies*, Istanbul, Turkey.
- Muzathik A.M. (2003). Economic potential of energy conservation in a five star hotel. *M.Eng. thesis*, University of Moratuwa, Sri Lanka. Available at <http://dl.lib.mrt.ac.lk/theses/handle/123/401>, Accessed 27 August 2022.
- Muzathik A.M. (2016). Green Sri Lanka through energy conservation: commercial building as a case study. The Official e-newsletter of the Institution of Engineers Sri Lanka. Available at <http://ioes18.wildapricot.org/Green-Sri-Lanka-through-energy-conservation>, Accessed 27 August 2022.
- Petroudy S.R.D (2017). Physical and mechanical properties of natural fibers. In: *Advanced High Strength Natural Fibre Composites in Construction*, pp. 59–83. Woodhead Publishing, Sawston, UK.
DOI: <https://doi.org/10.1016/B978-0-08-100411-1.00003-0>
- Pietrak K. & Wiśniewski T. (2015). A review of models for effective thermal conductivity of composite materials. *Journal of Power of Technologies* **95**(1): 1424.
- Priya K.B., Abid A.M. & Sai R.N.G. (2016). Design and analysis of square model unit cell for the prediction of thermal conductivity of fibre reinforced composites. *International Journal of Applied Engineering Research* **11**(10): 7166–7170.
- Progelhof R.C., Throne J.L. & Ruetsch R.R. (1976). Methods for predicting the thermal conductivity of composite systems:

- A review. *Polymer Engineering and Science* **16**(9): 615–625.
DOI: <https://doi.org/10.1002/pen.760160905>
- Rao B.R., Raju V.R. & Rao K.M. (2015). Effect of fibre shape on transverse thermal conductivity of unidirectional composites. *Sadhana - Academy Proceedings in Engineering Sciences* **40**(2): 503–513.
DOI: <https://doi.org/10.1007/s12046-014-0323-9>
- Ramamoorthy S.K., Skrifvars M. & Persson A. (2015). A review of natural fibers used in biocomposites: Plant, animal and regenerated cellulose fibers. *Polymer Reviews* **55**(1): 107–162.
DOI: <https://doi.org/10.1080/15583724.2014.971124>
- Rao T.S., Rao B.R. & Murthy V.B. (2018). Transverse thermal conductivity of hollow fiber composites. *International Journal of Engineering Technology Science and Research* **5**(5): 389–394.
- Rashid K., Haq E.U., Kamran M.S., Munir N., Shahid A. & Hanif I. (2019). Experimental and finite element analysis on thermal conductivity of burnt clay bricks reinforced with fibers. *Construction and Building Materials* **221**: 190–199.
DOI: <https://doi.org/10.1016/j.conbuildmat.2019.06.055>
- Rodríguez N.J., Yáñez-Limón M., Gutiérrez-Miceli F.A., Gomez-Guzman O., Matadamas-Ortiz T.P., Lagunez-Rivera L. & Feijoo J.A.V. (2011). Assessment of coconut fibre insulation characteristics and its use to modulate temperatures in concrete slabs with the aid of a finite element methodology. *Energy and Buildings* **43**(6): 1264–1272.
DOI: <https://doi.org/10.1016/j.enbuild.2011.01.005>
- Saba N., Jawaid M., Alothman O.Y., Paridah M.T. & Hassan A. (2016). Recent advances in epoxy resin, natural fiber-reinforced epoxy composites and their applications. *Journal of Reinforced Plastics and Composites* **35**(6): 447–470.
DOI: <https://doi.org/10.1177/0731684415618459>
- Sahu Y.K., Agrawal A. & Satapathy A. (2016). Heat conduction behavior of short fiber reinforced polymer composites. *International Journal of Advanced Technology in Engineering Science* **4**(1): 215–226.
- Samarth S. (2018). Effective thermal conductivity of polymer composites: a review of analytical methods. *International Journal of Ambient Energy* **42**(8): 961–972.
DOI: <https://doi.org/10.1080/01430750.2018.1557544>
- Santhosh S.K. & Hiremath S.S. (2020). Natural fiber reinforced composites in the context of biodegradability: A review. *Encyclopedia of Renewable and Sustainable Materials* **5**(2020): 160–178.
DOI: <https://doi.org/10.1016/b978-0-12-803581-8.11418-3>
- Sathishkumar S., Naveen T.K., Jeevarathinam A., Karthik V. & Dhandapani N.V. (2018). Thermal conductivity of natural fiber reinforced plastics. *International Journal of Pure and Applied Mathematics* **118**(20): 43–51.
- Sihn S. & Roy A.K. (2011). Micromechanical analysis for transverse thermal conductivity of composites. *Journal of Composite Materials* **45**(11): 1245–1255.
DOI: <https://doi.org/10.1177/0021998310382311>
- Smith D.S., Alzina A., Bourret J., Nait-Ali B., Pennec F., Tessier-Doyen N., Otsu K., Matsubara H., Elser P. & Gonzenbach U.T. (2013). Thermal conductivity of porous materials. *Journal of Materials Research* **28**(17): 2260–2272.
DOI: <https://doi.org/10.1557/jmr.2013.179>
- Srimal L.K.T., Fernando M.A.R.V. & Sumith B. (2014). Value addition for coir fiber as low temperature insulation material. *MSc Thesis*. University of Moratuwa, Sri Lanka. Available at <http://dl.lib.uom.lk/handle/123/10957>, Accessed 27 August 2022.
- Srimal L.K.T. & Sumith B. (2015). Value addition for coir fiber as low temperature insulation material. *Proceeding of the 12th Academic Sessions 2015*, 4 March. University of Ruhuna, Matara, Sri Lanka.
- Straube J. (2011) Thermal controls in building, *Building Science Corporation*. Available at www.buildingscience.com/documents/digests/bsd-011-thermal-control-in-buildings, Accessed 27 August 2022.
- Sunil E.M. & Manavendra G. (2017). Experimental investigation on thermal properties of bagasse fly ash reinforced epoxy composite. *International Research Journal of Engineering and Technology* **4**(4): 124–128.
DOI: <https://doi.org/10.13140/RG.2.2.25891.32808>
- Truong M., Zhong W., Boyko S. & Alcock M. (2009). A comparative study on natural fibre density measurement. *Journal of the Textile Institute* **100**(6): 525–529.
DOI: <https://doi.org/10.1080/00405000801997595>
- Udayakumara D.G.G.V., De Silva I.R., Chamath L.G., Srimal L.K.T. & Gallage R. (2022). Design and fabrication of a system to measure thermal conductivity of compressible materials. *Proceeding of the 19th Academic Sessions 2022, University of Ruhuna, Matara, Sri Lanka*. Available at <http://ir.lib.ruh.ac.lk/xmlui/handle/iruor/5788>, Accessed 27 August 2022.
- Velichko E., Tskhovrebov E. & Shevchenko A. (2017). Environmental safety providing during heat insulation works and using thermal insulation materials. *MATEC Web of Conferences* **106**: 03009.
DOI: <https://doi.org/10.1051/mateconf/201710603009>
- Volf M., Diviš J. & Havlík F. (2015). Thermal, moisture and biological behaviour of natural insulating materials. *Energy Procedia* **78**: 1599–1604.
DOI: <https://doi.org/10.1016/j.egypro.2015.11.219>
- Yashas G.T.G., Sanjay M.R., Subrahmanya B.K., Madhu P., Senthamaraiannan P. & Yogesha B. (2018). Polymer matrix-natural fiber composites: an overview. *Cogent Engineering* **5**(1): 1446667.

DOI: <https://doi.org/10.1080/23311916.2018.1446667>

Yuksel N. (2016). The review of some commonly used methods and techniques to measure the thermal conductivity of insulation materials. In: *Insulation Materials in Context of Sustainability*, pp. 113–140. IntechOpen, London, UK,

Zhao D., Qian X., Gu X., Jajja S.A. & Yang R. (2016). Measurement techniques for thermal conductivity and interfacial thermal conductance of bulk and thin film materials. *Journal of Electronic Packaging, Transactions of the ASME* **138**(4): 1–64.

DOI: <https://doi.org/10.1115/1.4034605>

RESEARCH ARTICLE

Geotechnical Engineering

Estimation of soil liquefaction potential in Colombo Port City (Sri Lanka) using several design earthquakes

IACC Ilangakoon* and AMRG Athapaththu

Department of Civil Engineering, Faculty of Engineering, University of Peradeniya, Peradeniya, Sri Lanka.

Submitted: 10 November 2021; Revised: 23 September 2022; Accepted: 28 October 2022


Abstract: Considering the limited land area in the Colombo Business District, the development of reclaimed land in the Colombo coastline was initiated. Colombo Port City is the first-ever mega-reclaimed land project in Sri Lanka. Land reclamations in coastal areas very often have liquefaction-related issues. Liquefaction is a process which occurs mainly due to natural seismic events. Even though Sri Lanka is located in an earthquake-free geological region, events like the 2004 Tsunami and recent studies confirmed that seismic events cannot be ignored and should be considered in the design stages of structures. Therefore, the determination of the effects of seismic events on the port city project is of prime importance. The primary purpose of this paper is to present the assessment of liquefaction triggering potential and the post-liquefaction vertical settlement. Seismic soil liquefaction was evaluated for the port city in terms of the Factor of Safety against liquefaction along with the depth of the soil profiles under the seismic demand of five earthquake scenarios that could be anticipated. The analysis process was done for 142 locations using a Cone Penetration Test-based simplified empirical procedure. The results showed that the Factor of Safety against liquefaction resistance decreases with the depth, and post-liquefaction vertical settlement is considerably high in Phase 2 land plots at the site. An earthquake with a magnitude of 6.0 and a peak ground acceleration of 0.2 has been identified as the most critical combination among the selected design seismic scenarios.

Keywords: Colombo Port City, cone penetration test, earthquake, liquefaction, simplified empirical procedure.

INTRODUCTION

Liquefaction can be identified as a serious issue in coastal reclamation projects during the event of an earthquake. The most common reason for liquefaction is natural seismic events. During an event of a natural earthquake, rapid loading is generated on saturated soil layers. Due to this rapid loading, the granular structure of the soil is distorted and causes loosely packed particle groups to collapse. Because of these collapsing mechanisms and due to the insufficient time for dissipation of excess pore-water pressure through natural drainage, a liquefaction incident occurs. Due to that, the soil no longer acts as inactive grid particles, and owing to this, the strength, stiffness, and volume of the soil particles in the liquefied areas significantly decrease. During an event of liquefaction, various types of ground failure can occur. These include loss of bearing strength, lateral spreading, vertical settlement, and flow failure.

There are some spectacular examples of liquefaction failures during earthquakes. The Niigata earthquake (Seed & Idriss, 1967), which occurred in old, reclaimed land in Japan with a magnitude of either 7.5 or 7.6, is one of the worst incidents. It took the attention of the science world, and researchers started investigations right after that event. The Hyogoken-Nambu earthquake in 1995 (Tokimatsu & Asaka, 1998), the great east Japan earthquake in the year

* Corresponding author (charith.ilangakoon@gmail.com;  <https://orcid.org/0009-0008-4264-4775>)



This article is published under the Creative Commons CC-BY-ND License (<http://creativecommons.org/licenses/by-nd/4.0/>). This license permits use, distribution and reproduction, commercial and non-commercial, provided that the original work is properly cited and is not changed in anyway.

of 2011 (Yasuda *et al.*, 2012), and the series of earthquakes faced by New Zealand between 2010 and 2011 (Cubrinovski *et al.*, 2010) can be named major liquefaction incidents in history. The important factor is that all these mentioned failures were recorded due to the cyclic softening liquefaction.

There are several methods to evaluate the liquefaction potential. To represent the results obtained through those methods, four different main criteria can be named. Those are, in terms of a Factor of Safety (FOS), in terms of probability, in terms of liquefaction potential index (LPI) value, and in terms of the liquefaction-induced settlement. In this study, liquefaction potential was evaluated using the Factor of Safety method.

Evaluation of liquefaction potential in terms of factor of safety (FOS) is the most common approach, which is practised around the world. To calculate the FOS, various methodologies have been developed by scientists around the world. The two most commonly applied methods for the evaluation of factors of safety are the use of empirical correlations and the 'Simplified Procedure', which was proposed by Seed and Idriss (1971).

The theory behind the application of empirical correlation is based on the comparison of the grain size distribution (or any other *in situ* characteristic) of the site to the grain size envelope of sites that have liquefied in the past. When the grain size distribution of the target site falls within the envelope of grain sizes that have liquefied in history, then there is a chance of triggering liquefaction occurring at the targeted site (Shibata & Teeparaska, 1988).

A simply applicable empirical method was proposed by Iwasaki *et al.* (1981). It is based on the standard penetration test. The factor of safety of a specific layer can be calculated by a very simple equation (R/L) which consists only of *in situ* resistance (R) and the dynamic load induced in the soil element by a seismic motion (L). Lately, a lab-based method was presented by Hakam (2016). Inside a laboratory, artificial vibration, which is similar to an earthquake, is produced by a shaking table while measuring the acceleration and the settlement. Then by using those results, the relationship between grain size particles and the relative density associated with liquefaction resistance was determined for certain accelerations.

This study is based on the most convenient method, which is known as the simplified procedure developed by Seed and Idriss (1971). They considered a soil column as a rigid body, which is excited by the seismic loading at the base, and the shear wave propagates to the ground surface. Then the shear stress generated in the soil column was calculated by using the empirical equations proposed. The soil liquefaction mainly depends on the magnitude of the earthquake, intensity and duration of the ground motion, ground acceleration, density and effective confining pressure of the soil, thickness of the soil layer, fine content, the position of the groundwater table, and reduction of effective stress (Youd & Perkins, 1978). All these parameters can be reduced into two factors, namely, the intensity of seismic loading (cyclic stress ratio) that the soil will be subjected to, and characterization of the liquefaction resistance (cyclic resistance ratio) of the soil. By comparing cyclic stress ratio (CSR) and cyclic resistance ratio (CRR) with each other, it is possible to quantify the value of the occurrence of liquefaction at any particular depth at a site.

The general classification is that when $FOS > 1$, the ground is safe, and when $FOS < 1$, liquefaction is said to occur (Seed & Idriss, 1971). But in reality, the soil layer can be liquefied during an earthquake, even if the FOS is more than one (Juang & Jiang, 2000). As a solution, different studies introduced higher values for the FOS against liquefaction. Sonmez (2003) advised taking into account an FOS value of 1.2 at a specific depth for the layer to be deemed safe against liquefaction. Seed and Idriss (1971) considered soil layers with an FOS value within the range of 1.25 to 1.5 as non-liquefiable. Also, Ulusay and Kuru (2004) defined soil layers with an FOS value greater than 1.2 as non-liquefiable and soil layers with an FOS of 1.0 to 1.2 as marginally liquefiable. When comparing the past studies, 1.2 can be identified as a reasonable value for FOS against liquefaction failure (Sonmez, 2003).

Preliminary estimation of liquefaction-induced ground settlement is one of the best ways to visually represent the pre-assumed liquefaction damage to a liquefaction-prone site. For level ground conditions such as Colombo port city, the amount of settlement during earthquake shaking can be computed from the volumetric re-consolidation

strains induced as the excess pore water pressure dissipate. Based on the field experience during past earthquakes, Ishihara and Yoshimine (1992) identified that the amount of volumetric strain depends on penetration resistance and the CSR applied by the designed earthquake. Based on that, authors have established a family of curves by correlating relative density (D_r) and the conventional use of FOS against liquefaction with the volumetric strain resulting from the dissipation of pore-water pressures.

Many research studies have already been carried out related to the liquefaction potential of sea sand-filled land areas around the world. But this is the very first-ever mega land reclamation project in Sri Lanka. Therefore, a comprehensive study on liquefaction potential is required to identify possible hazards related to this project, as well as for future projects of a similar nature. In this part of the world, earthquakes or seismic waves are not a common event that happens regularly. Even though there are some methodologies available for monitoring seismic events of the countries located on tectonic plate boundaries, predicting earthquakes in the middle of the tectonic plates is almost impossible. As historical data or related evidence on liquefaction are rare on the island, this study was carried out to find the liquefaction potential in Colombo port city.

The main aim of this study is to find the liquefaction potential of Colombo port city by using a CPT-based simplified liquefaction assessment method for free-field level ground conditions. The key objectives achieved in the fulfilment of the aim can be set as the analysis of liquefaction triggering potential to find the liquefaction FOS variation with depth and to estimate the post-liquefaction vertical settlement to predict the potential of liquefaction to cause damage at the surface level of the Colombo port city. Five different and anticipatable earthquake magnitudes (M) were selected for the analysis process by considering the seismicity around the island. Key results are presented in the form of the FOS contours at several depths below the ground surface, along with the spatial distribution contours for post-liquefaction settlements at the ground surface.

This study was limited to studying only the geotechnical investigation data obtained through the cone penetration tests. Since only a section of the ground area of the Phase 02 land plots was improved as the first construction phase, the availability of the cone penetration test (CPT) results for those land plots is very low. Hence an assumption was made that the liquefaction behaviour of A-7, A2-3, and A2-2 land plots is unique to the available CPT locations of the respective land plots since ground improvement for those areas has not been carried out.

The study area

Colombo port city is the first and only mega coastal reclamation project in Sri Lanka to date. This project facilitates various purposes such as commercial, residential, hospitality and recreational. The reclaimed land of the Colombo port city is divided into two main construction phases based on the structures built in the area. Most of the high-rise buildings are planned to be constructed in Phase 1 land areas, and open spaces (parks and squares, waterfronts, and beach areas) with low-rise residential buildings in Phase 2 land areas. As the first construction phase of the project, construction activities will be initiated in the Phase 1 land plots. According to the master plan, construction work in Phase 2 will be commenced after a decade. Due to that, the entire Phase 1 and only a section of Phase 2 have been treated by using different improvement methods, and the rest of Phase 2 has not been improved since there is a possibility of natural compaction in those ground areas with time. Those two phases are further divided into 14 land plots based on the land requirement. Most of the CPT boreholes are densely clustered in the areas that will be used for the construction of high-rise buildings and roads. The records from CPT tests have been collected for 142 representative borehole locations in the Colombo port city to evaluate liquefaction potential. The depths of the CPT boreholes are in the range of 8 m to 23 m. Figure 1 shows an aerial view of Colombo port city, highlighting details of CPT locations and main construction phases.

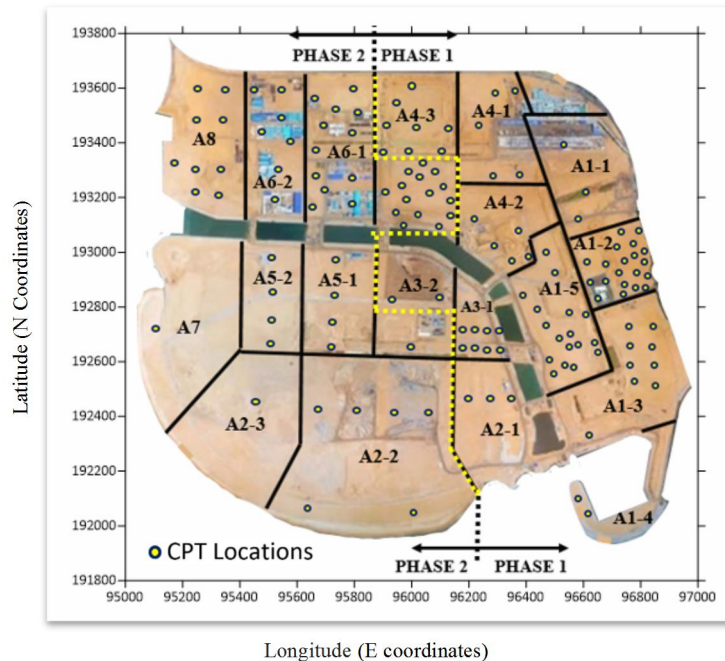


Figure 1: Aerial view of Colombo port city showing reclamation land plots, main construction phases, and locations of the 142 CPTs selected.

Earthquake ground motions

Sri Lanka lies away from the tectonic plate boundaries and the northwestern region of the Indo-Australian plate, which is known as a seismically inactive geological zone. Furthermore, intraplate seismic activities within Sri Lanka can be considered not significant (Seneviratne *et al.*, 2020). Owing to this, the effect of an earthquake is minimal and there are very few studies available related to earthquakes and seismic events around Sri Lanka. However, scientists and geologists are investigating the possibility of the emergence of a new plate boundary to the south of Sri Lanka (Dissanayake, 2005). Therefore, to select appropriate earthquake magnitudes and peak ground accelerations (PGA) for this analysis, a few recently completed studies were considered. Seneviratne *et al.* (2020) researched the historical records of earthquakes around Sri Lanka and identified the 1615 earthquake as the most significant earthquake that cost over 2000 people their lives. The authors have analyzed over 300 incidents and concluded that the Mannar rift zone and Comorin ridge constitute the critical zone of influence in Sri Lanka, which can generate an event of 6.9 magnitudes (475 years return period) at a depth of 10 to 15 km in the western ocean of the island. This study also highlighted that seismicity around Sri Lanka no longer can be ignored. Hence for design purposes, it must be considered. Weerasinghe *et al.* (2020) identified that cities in the Western Province, like Colombo, Negombo, and Gampaha, that are commercialized cities, can be exposed to a PGA of more than 0.1 g (where g is the gravitational acceleration), and for Colombo, the PGA was calculated to be 0.13 g. The authors have estimated seismic hazards for the island by using a relationship called deterministic seismic hazard assessment (DSHA) and two design earthquake magnitudes of $M = 6.0$ and $M = 6.9$. Uduweriya *et al.* (2020) estimated PGA values respective to the probable return period for several areas of the country by following the probabilistic seismic hazard assessment (PSHA) technique. The PSHA technique involves calculating how often a suite of specified levels of ground motion will be exceeded at the site. The authors have used the PSHA technique with a logic tree approach to minimize the effects of epidemic uncertainty. The study produced PGA values of 0.025, 0.107, and 0.207 for return periods of 50, 475, and 2500 years, respectively. By using a finite difference method, another study was carried out by Dananjaya *et al.* (2020) to investigate the seismicity around Sri Lanka. In both DSHA and PSHA techniques, the variation of bedrock level was not taken into consideration. Therefore, in this study, numerical

simulation was carried out to investigate the effect of variation of the bedrock profile on the seismic wave propagation through Sri Lanka. As the input data, acceleration time histories of seven real-time earthquake records were selected from the Pacific Earthquake Engineering (PEER). Then the analyzing process was done by simulating two-dimensional bedrock responses. As a result of the study carried out by Dananjaya *et al.* (2020), a PGA of 0.083 value for the Colombo district was obtained. By considering the whole island, Abayakoon (1996) showed the expected value of maximum ground acceleration in Sri Lanka could be 0.28 g. With the historical records of earthquakes triggered in the close vicinity of Sri Lanka, the above value is quite reasonable. Also, Kumarasiri and Abayakoon (2008) carried out soil liquefaction analysis for the coastal line of Sri Lanka and identified a few liquefiable sites in the country, and developed a map based on that. For this study authors used an earthquake magnitude of 6.0 and a PGA value of 0.2 g as the seismic combination by considering the recommendations presented by Abayakoon (1996).

Considering the seismic scenarios in and around the island as discussed in the above literature, five design earthquake combinations have been chosen for the liquefaction analysis as given in Table 1. The magnitude of 6.9 at a 475-year return period at an epicentral distance of 90 km (placed along the failed Mannar rift zone and Comorin ridge) earthquake was selected as the control (critical) earthquake. For the second one, $M = 6.0$ earthquake was selected with an epicentral distance of 15 km to investigate the effect of an earthquake of magnitude lower than critical but generating at a distance closer than the critical earthquake. To investigate the effects of an earthquake with a higher magnitude and generating at the same epicentral distance as critical, $M = 7.5$ was selected as the third design earthquake. The same combination used in Kumarasiri and Abayakoon (2008) was selected as the fourth design earthquake combination. By considering the highest values with possibilities concluded in the literature, $M = 6.9$ and $PGA = 0.2$ was used as the final combination.

Table 1: Design seismic combinations used for the study

Seismic combination	Earthquake magnitude	PGA Value
1	6.0	0.132
2	6.9	0.1
3	7.5	0.1
4	6.0	0.2
5	6.9	0.2

MATERIALS AND METHODS

The procedure for calculation of the factor of safety and liquefaction induced settlement can be summarized as follows.

Only the sand layers beneath the groundwater table were considered. Since soil type is uniform throughout the Port City premises (marine dredged sand), the soil type was independent from the consideration for the calculation process. The depth of the sand layers (CPT Depth), thicknesses of the sand layers below the groundwater table, and depth from the groundwater table to the sand layer were considered for the analysis. Cone resistance value, sleeve friction value, friction ratio, and pore pressure value were recorded, and computation was done for the total overburden pressure and effective overburden pressure by using the geotechnical properties of the site. Then the evaluation of CRR was carried out.

Testing an undisturbed soil sample under idealized field conditions is the best way of determining CRR. But for granular/sandy soils, it is almost impossible to collect undisturbed samples and simulate *in situ* stress conditions in the laboratory. Therefore, field tests can be considered the most appropriate approach, especially for granular soils. A standard penetration test (SPT), cone penetration test (CPT), and shear-wave velocity are the commonly used

methods for the evaluation of the liquefaction resistance of sandy soils. But CPT is the most preferred *in situ* test to assess the liquefaction potential of sandy soils. The main reason is that the nearly continuous soil profile that is provided by CPTs can be developed as a liquefaction resistance profile.

After the establishment of the simplified liquefaction analysis approach, many methods based on CPT have been developed for evaluating soil liquefaction resistance (Seed & Alba, 1986; Shibata & Teparaska, 1988; Stark & Olson, 1995; Olsen, 1997; Robertson & Wride, 1998; Schneider & Mayne, 2000; Juang *et al.*, 2003; Moss, 2006). Almost all of these methods follow the same format as in the simplified procedure, which judges whether the liquefaction of soil in a future seismic event will occur. But for calculating CRR in this study, the Robertson and Wride (1998) method (referred to herein as the Robertson method) was selected since it was recommended as a reliable and convenient method in a workshop organized by National Center for Earthquake Engineering Research (NCEER) in 1998 (Youd *et al.*, 2001). Also, to overcome the disadvantages of the other methods, the Robertson method developed an integrated approach, and for numerous studies, the Robertson method was adapted for the calculation of CRR (Juang *et al.*, 2003; Kumarasiri & Abayakoon, 2008). Major steps involved in the calculation of CRR by using the Robertson Method are shown below. Important parameters in the Robertson method are the soil behaviour type index (I_c), equivalent clean sand normalized CPT penetration resistance ($Q_{c1N,cs}$), the correction factor for the grain characteristics of the soil (K_c), normalized CPT penetration resistance (Q), and the normalized friction ratio (F), and finally, the CRR profile for an earthquake of magnitude (M) equal to 7.5, denoted as $CRR_{7.5}$.

Robertson and Wride method

1. Calculation of *in situ* stresses (Total vertical stress (σ_{v0}) and effective vertical stress (σ'_{v0})).
2. Calculation of normalized cone resistance (Q) and normalized friction ratio (F).
3. Calculation of soil behavior type index (I_c).
4. Calculation of cone penetration resistance which corrected for overburden stresses (Q_{c1N}).
5. Calculation of the correction factor (K_c) which is a function of the grain characteristics.
6. Calculation of the equivalent clean sand normalized penetration resistance [(Q_{c1N}) cs].
7. Determination of the CRR for earthquake magnitude of $M = 7.5$.

After the determination of CRR, an evaluation of the cyclic stress ratio (CSR) was carried out. CSR can be determined from the peak ground acceleration (PGA) that depends upon site-specific ground motion. The equation for CSR induced by earthquake ground motions formulated by Seed and Idriss (1971) is shown in equation (1),

$$CSR = 0.65 \left(\frac{\sigma_v}{\sigma'_v} \right) \left(\frac{a_{max}}{g} \right) r_d \quad \dots(1)$$

where,

- σ_v = Total vertical stress at the depth Z
- σ'_v = Effective vertical stress at the depth Z
- g = Acceleration of gravity
- a_{max} = Peak ground acceleration
- r_d = Shear stress reduction factor for depth Z given by equation (2).

$$r_d = \begin{cases} 1.0 - 0.00765 z, & z \leq 9.15m \\ 1.174 - 0.0267 z, & 9.15 < z \leq 23m \end{cases} \quad \dots(2)$$

In true conditions, the soil does not behave like a rigid body. Soil behaves more like a flexible body, and in the above equation (1), rigid body shear stress is reduced with a correction factor (r_d) or stress reduction factor to obtain the deformable body shear stress with depth (Seed & Idriss, 1971). The factor of 0.65 is to reduce the maximum shear stress. Therefore it is reasonably accurate to use for the calculation process. This originally developed

simplified equation can only be applied to earthquakes with a magnitude of 7.5. For different earthquake magnitudes, a factor called ‘magnitude scaling factor’ (MSF) should be used for the calculation process. In this research, MSF values proposed by Seed and Idriss (1982) were used for the calculation process. According to Seed and Idriss, the magnitude scaling factor is given by equation (3).

$$MSF = \left(\frac{M_w}{7.5}\right)^n; n = -2.56 \quad \dots(3)$$

PGA is the maximum ground acceleration that occurs during earthquake shaking at a particular location. It is not measured from the total energy that dissipates during an event. It is usually calculated by considering how hard the earth is shaking at that particular event. PGA is normally considered to be fixed for a specific region.

After all inclusions of factors, the final version of CSR used in this study was derived as equation (4):

$$CSR = 0.65 \left(\frac{\sigma_v}{\sigma'_v}\right) \left(\frac{a_{max}}{g}\right) \frac{r_d}{MSF} \quad \dots(4)$$

Finally, the computation of the factor of safety for the specific layer from the simplified method as shown in equation (5).

$$F.O.S. = \frac{CRR}{CSR} \quad \dots(5)$$

The same procedure was followed for the calculation of the factor of safety at the other CPT depths of the same soil profile. Determination of post-liquefaction site settlement values by using the FOS values generated by the Robertson and Wride (1998) method was carried out as the final step of the calculation process. The procedure involved in the calculation of FOS and vertical settlement is as follows.

Calculation of factor of safety and vertical settlement

Consider a borehole log ‘C-184’ of the ‘A4-3’ land lot in Phase 01 of the Colombo Port City premises. The selected sand layer is 17 m below the ground surface and 12.42 m below the groundwater table. The ground water table is located around 4.58 m below the ground surface.

CPT parameters at 17 m below the ground surface are,

- Cone resistance (qc) in MPa = 8.05
- Sleeve friction (fs) in MPa = 0.03
- Friction ratio (Rf) in % = 0.38

Table 2: Parameters of the selected CPT location C184

Parameter	Value
Water density (γ_w)	9.81 kN/m ³
Bulk unit weight of fill sand (γ_b)	18.00 kN/m ³
Water level (Z_w)	4.58 m
CPT level (Z)	17.00 m

1. Calculation of the in-situ stresses at 17 m below the ground surface by considering the unit weight of marine dredged sand used in the Colombo Port City as 18 kN/m³,

$$\begin{aligned}\sigma_{v0} &= (Z) (\gamma_b) \\ &= 17.00 \times 18.00 \\ &= 306.00 \text{ kPa}\end{aligned}$$

$$\begin{aligned}\sigma_{v0}' &= ((Z_w) (\gamma_b) + [(Z - Z_w) \times (\gamma_b - \gamma_w)]) \\ &= 4.58 \times 18.00 + [12.42 \times (18 - 9.81)] \\ &= 184.15 \text{ kPa}\end{aligned}$$

2. Evaluation of cyclic stress ratio (CSR)

a) Calculation of shear stress reduction factor (r_d) for depth Z from equation (2).

$$\begin{aligned}r_d &= 1.174 - 0.0267z \\ &= 1.174 - 0.0267(17) \\ &= 0.732\end{aligned}$$

b) Estimation of peak ground acceleration (PGA).

Table 3: Seismic combinations and the PGA values

Seismic combination	PGA value
1	0.132 g
2	0.1 g
3	0.1 g
4	0.2 g
5	0.2 g

c) Calculation of MSF from equation (3).

Table 4: Seismic combinations and the MSF values.

Seismic combination	Earthquake magnitude	MSF value
1	6.0	$\left(\frac{6.0}{7.5}\right)^{-2.56} = 1.77$
2	6.9	$\left(\frac{6.9}{7.5}\right)^{-2.56} = 1.23$
3	7.5	$\left(\frac{7.5}{7.5}\right)^{-2.56} = 1.00$
4	6.0	$\left(\frac{6.0}{7.5}\right)^{-2.56} = 1.77$
5	6.9	$\left(\frac{6.9}{7.5}\right)^{-2.56} = 1.23$

d) Determination of CSR from equation (1).

Table 5: Seismic combinations and the CSR values for C184 at 17 m depth.

Seismic combination	PGA value	CSR value
1	0.132 g	$0.65 \left(\frac{306}{184.15} \right) \left(\frac{0.132g}{g} \right) \frac{0.732}{1.77} = 0.059$
2	0.1 g	$0.65 \left(\frac{306}{184.15} \right) \left(\frac{0.1g}{g} \right) \frac{0.732}{1.23} = 0.064$
3	0.1 g	$0.65 \left(\frac{306}{184.15} \right) \left(\frac{0.1g}{g} \right) \frac{0.732}{1.00} = 0.079$
4	0.2 g	$0.65 \left(\frac{306}{184.15} \right) \left(\frac{0.2g}{g} \right) \frac{0.732}{1.77} = 0.089$
5	0.2 g	$0.65 \left(\frac{306}{184.15} \right) \left(\frac{0.2g}{g} \right) \frac{0.732}{1.23} = 0.13$

3. Evaluation of cyclic resistance ratio (CRR)

Robertson and Wride (1998) method

a) Calculation of normalized cone resistance (Q) and normalized friction (F) ratio.

$$\begin{aligned} Q &= (q_c - \sigma_{v0}) / \sigma_{v0}' \\ &= (8.05 - 0.306) / 0.184 \\ &= 42.08 \text{ MPa} \end{aligned}$$

$$\begin{aligned} F &= [f_s / (Q_c - \sigma_{v0})] * 100 \% \\ &= [0.031 / (8.05 - 0.306)] * 100 \% \\ &= 0.4 \end{aligned}$$

b) Calculation of soil behavior type index (Ic).

$$\begin{aligned} I_c &= [(3.47 - \log Q)^2 + (\log F + 1.22)^2]^{0.5} \\ &= [(3.47 - \log 42.08)^2 + (\log 0.4 + 1.22)^2]^{0.5} \\ &= 2.016 \end{aligned}$$

c) $I_c < 2.6$, so the calculation of cone penetration resistance corrected for overburden stresses (Qc1N).

$$\begin{aligned} Q_{c1N} &= \left(\frac{Q_c}{Pa^2} \right) \left(\frac{pa}{\sigma_{v0}'} \right)^{0.5} \\ &= \left(\frac{8.05}{0.1} \right) \left(\frac{0.1}{0.184} \right)^{0.5} \\ &= 59.34 \text{ MPa} \end{aligned}$$

- d) Calculation of corrected soil behavior type index (I_c).

$$\begin{aligned} I_c &= [(3.47 - \log Q_{c1N})^2 + (\log F + 1.22)^2]^{0.5} \\ &= [(3.47 - \log 59.34)^2 + (\log 0.4 + 1.22)^2]^{0.5} \\ &= 1.88 \end{aligned}$$

- e) Calculation of the correction factor (K_c) which is a function of the grain characteristics.

$$1.64 < I_c < 2.36 \text{ and } F < 0.5 \%,$$

Hence,

$$K_c = 1 \text{ (} 1.64 < I_c < 2.36 \text{ and } F < 0.5\%)$$

- f) Calculation of the equivalent clean sand normalized penetration resistance $[(Q_{c1N})_{cs}]$.

$$\begin{aligned} (Q_{c1N})_{cs} &= (K_c) (Q_{c1N}) \\ &= (1) (59.34) \\ &= 59.34 \text{ MPa} \end{aligned}$$

- g) Determination of the CRR for earthquake magnitude of $M = 7.5$.

$$\begin{aligned} CRR_{7.5} &= 0.833 \left(\frac{(Q_{c1N})_{cs}}{1000} \right) + 0.05 \\ &= 0.833 \left(\frac{59.34}{1000} \right) + 0.05 \\ &= 0.1 \end{aligned}$$

4. Computation of the factor of safety for the specific layer from equation 05

Layers with FOS values of lesser than 1.2 have been considered as locations that are susceptible to liquefaction. By repeating the same procedure, FOS values for all the soil layers located below the water table can be calculated.

Table 6: Calculated FOS values for C184 at 17 m depth.

Seismic Combination	CSR Value	Robertson Method	
		CRR Value	FOS
1	0.059	0.1	1.69
2	0.064	0.1	1.56
3	0.079	0.1	1.26
4	0.089	0.1	1.12
5	0.130	0.1	0.76

5. Determination of post-liquefaction site settlement values by using the FOS values generated by the Robertson method.

This method is essentially based on estimating the maximum cyclic shear strain of each layer during and after liquefaction which is estimated from the FOS against liquefaction and Relative Density of dredged sand (D_r), Where D_r can be correlated from CPT data based on the following equation (6) proposed by Tatsuoka and Asaka (1998).

Step 01: The factor of safety against liquefaction, FOS, has to be evaluated for each layer of sand deposits at a given location by any conventional method. For this study, FOS values obtained through the Robertson method were used.

Step 02: Calculation of Relative Density (D_r) value using equation No. 06.

$$\begin{aligned}
 D_r &= -85 + 76 \log(Qc1N) \\
 &= -85 + 76 \log(59.34) \\
 &= 49.77 \%
 \end{aligned}
 \tag{6}$$

Step 03: Calculation of maximum cyclic shear strain for post-liquefaction settlement by using the chart proposed by Zhang *et al.* (2004).

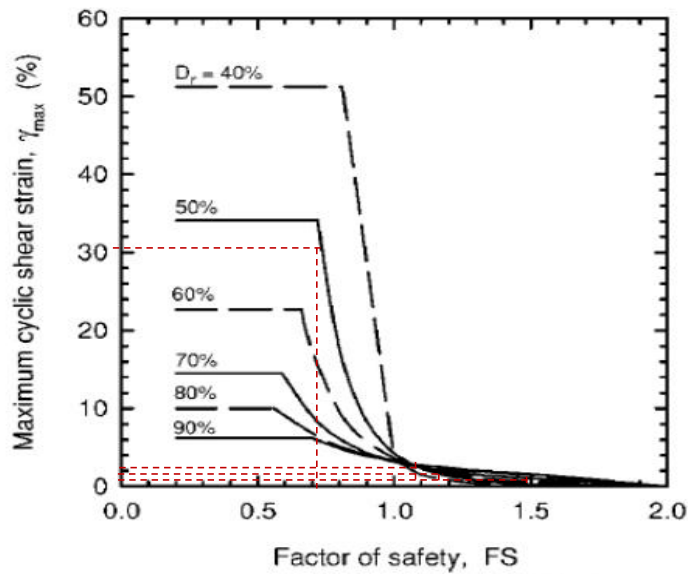


Figure 2: Maximum cyclic shear strain for post liquefaction lateral displacement proposed by Zhang *et al.* (2004).

Table 7: Calculated FOS values and maximum cyclic shear strain values for C184 at 17 m depth.

Seismic Combination	FOS Value	Maximum Cyclic Shear Strain (γ)
1	1.69	0.0
2	1.56	1.0
3	1.26	1.8
4	1.12	2.9
5	0.76	30.1

Step 04: Calculation of volumetric strain (ϵ) due to post-cyclic reconsolidation settlement by using the chart proposed by Ishihara and Yoshimi (1992).

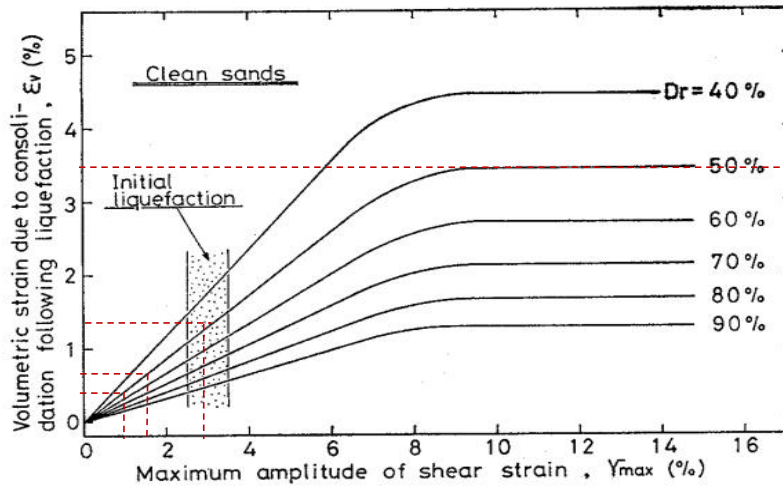


Figure 3: Recommended relationships for volumetric re-consolidation strains as a function of maximum shear strain and relative density (Ishihara & Yoshimi, 1992)

Table 8: Calculated maximum cyclic shear strain volumetric strain (γ) values and volumetric strain (ϵ) for C184 at 17m depth.

Seismic combination	Maximum cyclic shear strain (γ)	Volumetric strain (ϵ) %
1	0.0	0.00
2	1.0	0.35
3	1.8	0.70
4	2.9	1.40
5	30.1	3.30

Step 05: Settlement of the specific layer can be obtained by multiplying the volumetric Strain and the thickness of the layer as shown in equation No. 7.

$$\text{Settlement} = (\text{Volumetric strain}) (\text{Layer thickness})$$

$$S = (\epsilon)(\Delta Z) \tag{7}$$

Step 06: The determined volumetric strains can be multiplied by the respective layer thickness to obtain the settlement of the specific layer. Then by summing the settlement of the each layer, it is possible to determine the entire amount of ground settlement from using the equation 8.

$$S = \sum_{i=1}^j \epsilon_{vi} \Delta Z_i \tag{8}$$

- where,
- S = Liquefaction-induced ground settlement
 - ϵ_{vi} = Post-liquefaction volumetric strain for the soil sublayer i
 - ΔZ_i = Thickness of the sublayer i
 - j = Number of soil sublayers.

RESULTS AND DISCUSSION

Considering the high importance of the Colombo port city, this study attempts to evaluate the FOS against liquefaction and corresponding post-liquefaction settlement for the worst seismic scenarios for the port city, using the CPT-based simplified method. To illustrate the variation of the FOS of soils with depth, the result of the analysis for a representative profile from land plot A4-3 (C-184) in Colombo port city is shown in Figure 4.

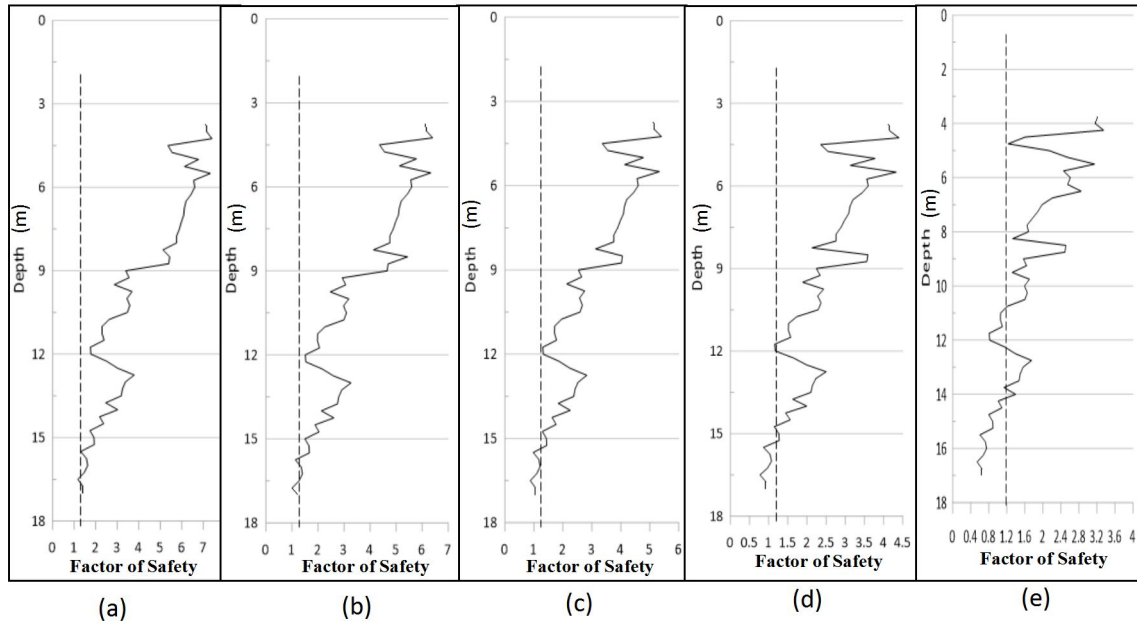


Figure 4: FOS values against liquefaction (a) combination 1; (b) combination 2; (c) combination 3; (d) combination 4; (e) combination 5.

The typical computation of FOS against liquefaction for earthquakes of different magnitudes is carried out at this representative borehole. It could be noted that the value of FOS is decreasing along with the depth of the selected borehole. Also, it is noted that the thickness of the liquefiable layers is increasing with the higher magnitudes of earthquakes.

Analysis was carried out by assuming five earthquake combinations, which may feasibly be triggered in and around Sri Lanka. Among the analyzed locations, some land plots in the Phase 02 section of the Colombo port city premises were found to be susceptible to soil liquefaction as per the simplified procedure.

The contour maps for the factor of safety values at 6 m, 12 m, and 18 m depths were mapped for the generation of liquefaction-susceptible zones. A remarkable reduction in the factor of safety values along the depth of the profiles was identified for almost all locations.

Figures 5 to 9 present the spatial distribution of the factor of safety values against liquefaction at 6.0 m, 12.0 m, and 17.0 m depths for five selected seismic combinations, respectively. It can be noted that the FOS values at a depth of 6 m are much higher than the values at 12 m and 17 m depths for all five earthquakes. Spatial distribution values for 17 m depth are pretty much similar to the 12 m depth values. But only for some locations, the value for 17 m depth is slightly lesser than that for 12 m depth.

It is obvious from the Figures 5 to 9 that the design earthquake combinations with $M = 6.9$ and $PGA = 0.2$ and, $M = 6.0$ and $PGA = 0.2$ have the lowest range of FOS spatial distribution values for all three depth ranges. The highest FOS values were recorded against $M = 6$ and $PGA = 0.132$ design earthquake. Values plotted for control earthquakes ($M = 6.9$ and $PGA = 0.1$) and earthquakes with a magnitude of 7.5 are varying within the same limits. From the contours of the FOS shown below, it is evident that for most of the locations, FOS values at all depths are higher than the established safe value of 1.2.

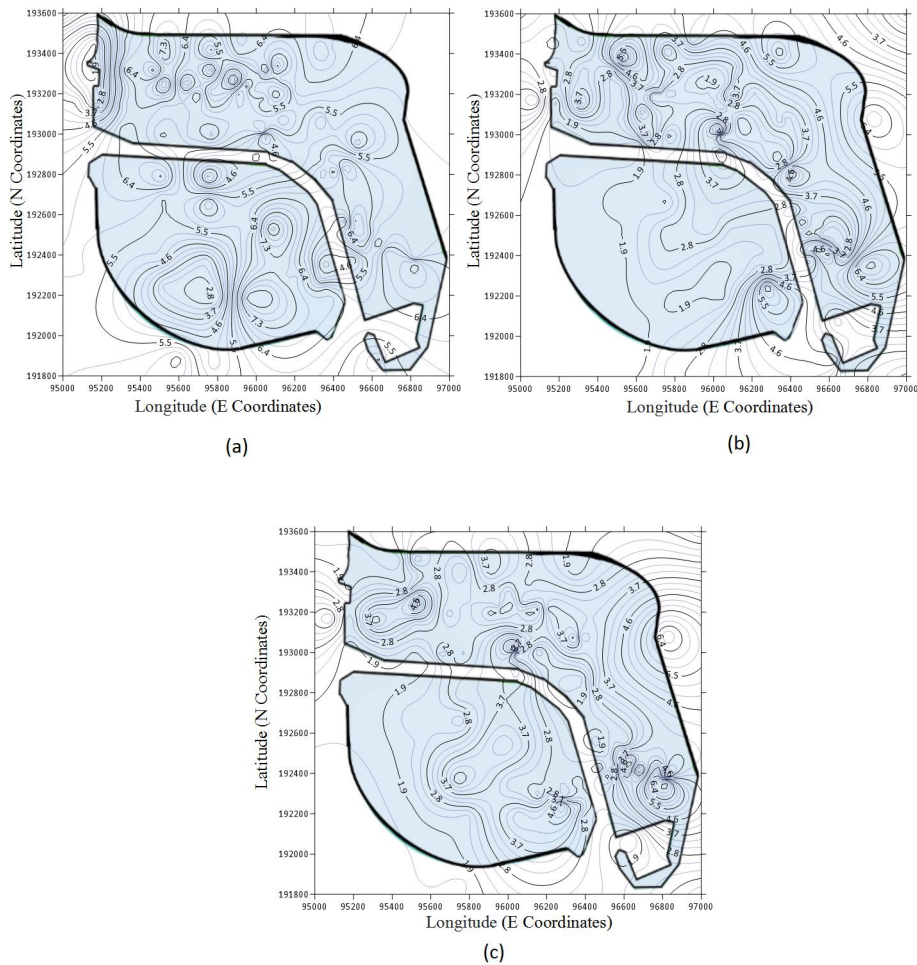


Figure 5: Contours of FOS against liquefaction potential for combination 1, (a) at a depth of 6 m; (b) at a depth of 12 m; (c) at a depth of 17 m, from the Robertson method.

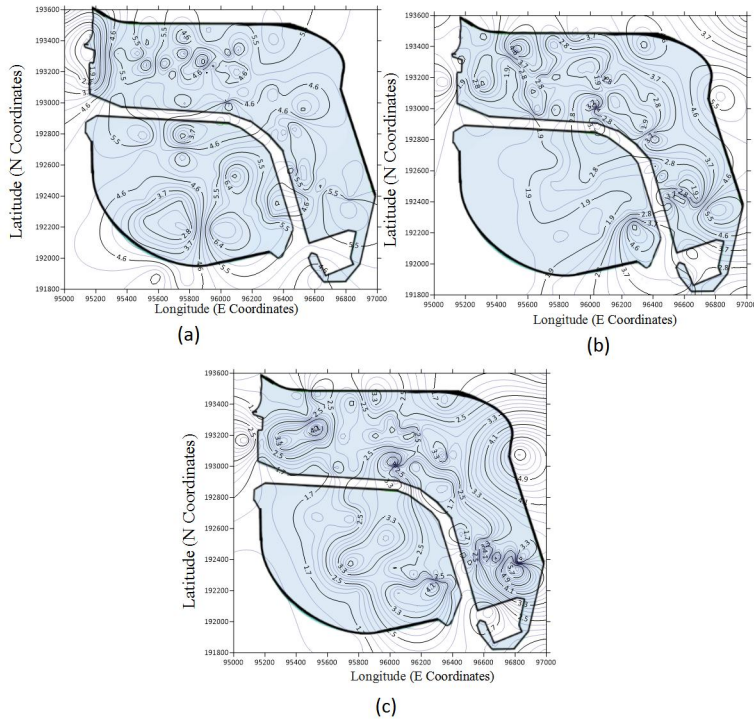


Figure 6: Contours of FOS against liquefaction potential for combination 2, (a) at a depth of 6 m; (b) at a depth of 12 m; (c) at a depth of 17 m, from the Robertson method.

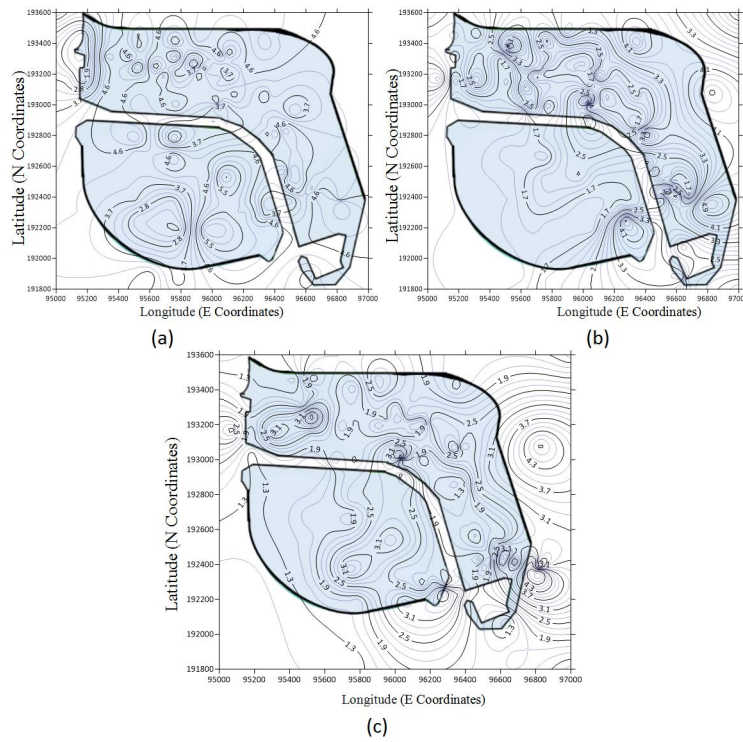


Figure 7: Contours of FOS against liquefaction potential for combination 3, (a) at a depth of 6 m; (b) at a depth of 12 m; (c) at a depth of 17 m, from the Robertson method.

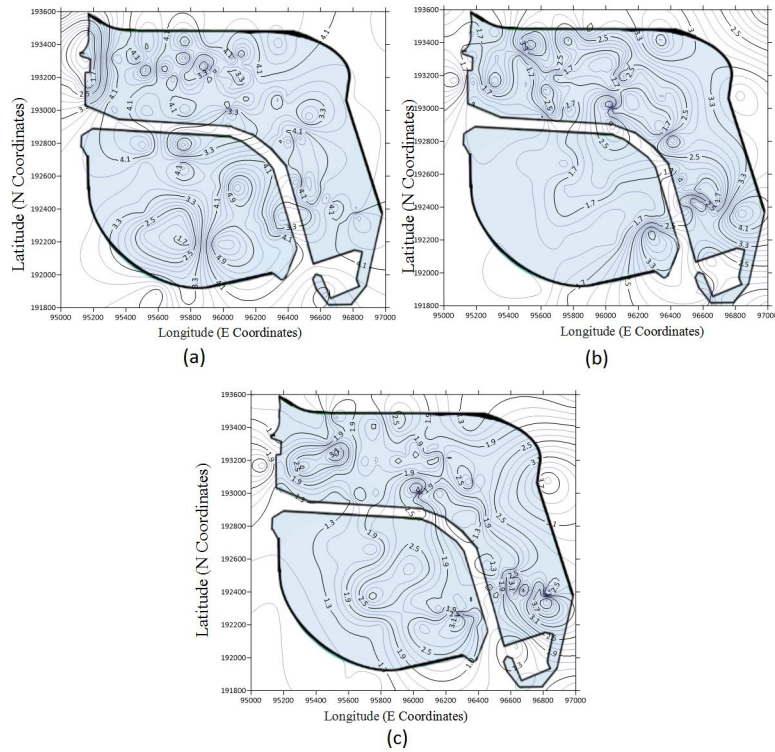


Figure 8: Contours of FOS against liquefaction potential for combination 4, (a) at a depth of 6 m; (b) at a depth of 12 m; (c) at a depth of 17 m, from the Robertson method.

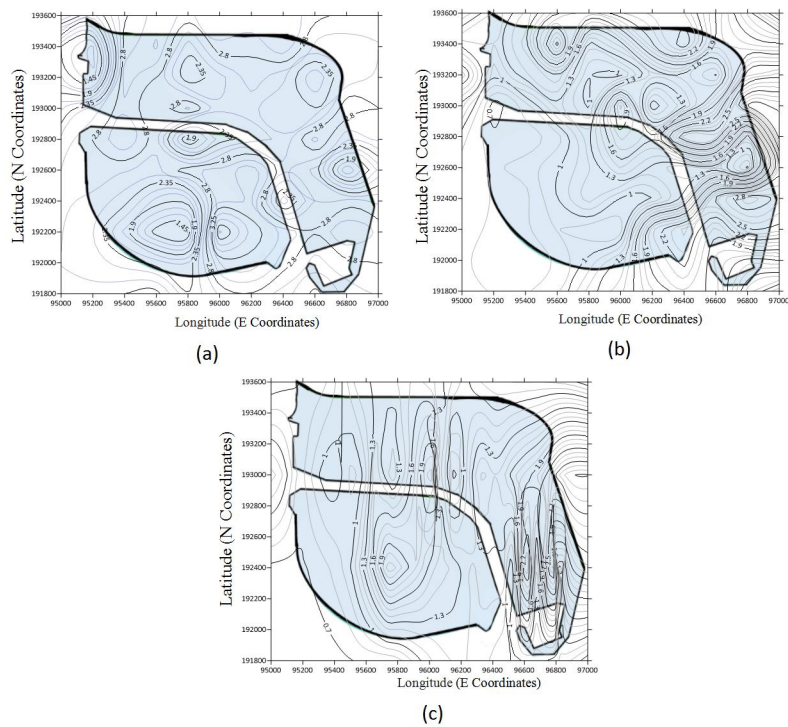


Figure 9: Contours of FOS against liquefaction potential for combination 5, (a) at a depth of 6 m; (b) at a depth of 12 m; (c) at a depth of 17 m, from the Robertson method.

These contours show the liquefaction vulnerability at different sites in the city. Liquefaction susceptibility for sites with FOS less than 1.2 can be identified as very high. Some of the land plots in the city, namely A8, A6-2, A6-1, A5-2, and A5-1 are highly vulnerable to severe liquefaction for earthquake combinations of 3, 4, and 5, according to the results generated.

To get a visual representation of analyzed boreholes, the results of the liquefaction triggering assessment of all 142 locations at the reclamation zone, under the control earthquake with seismic demand of the $M_w = 6.9$ and $PGA = 0.1$, are shown in Fig. 10 (a) in terms of the CSR (normalized for $M = 6.9$ and $\sigma'_v = 100$ kPa, denoted as $CSR_{6.9}$) as a function of the clean sand-equivalent corrected cone tip resistance (Q_{c1Ncs}).

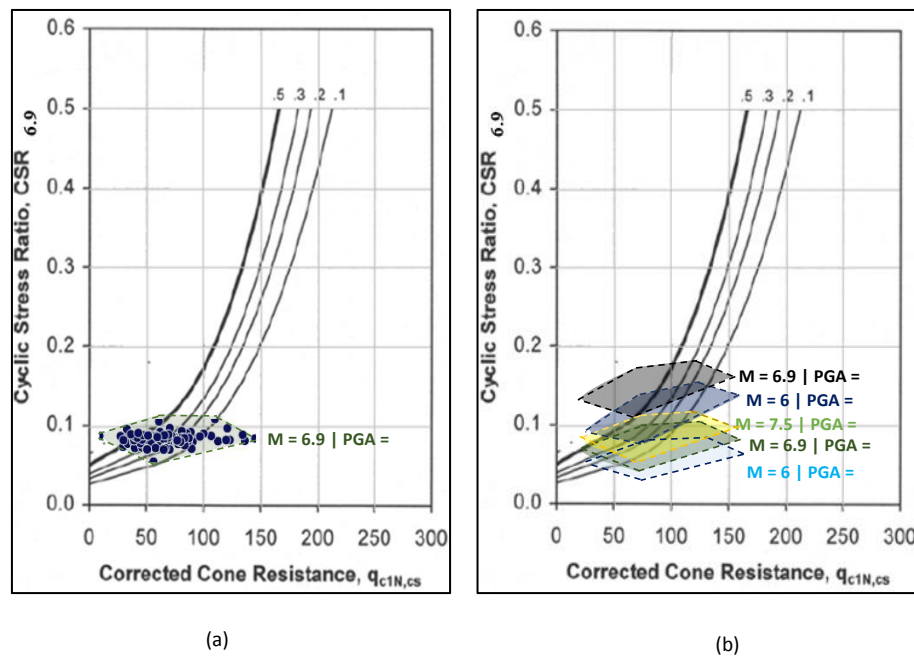


Figure 10: (a) Results of the simplified triggering analysis for CPT profiles for the control earthquake; (b) results of the simplified liquefaction triggering analysis for CPT profiles for the design earthquake combination 1, 3, 4 and 5 shown as general ranges of median CSR and Q_{c1Ncs} at each profile.

Each point represents the median Q_{c1Ncs} and CSR value in the critical layer for a single CPT location. CRR curves for the Probability of Liquefaction (PL) of 10%, 20%, 30%, and 40% given in the Robertson method are also plotted in the same graph for reference. It was noted that against the control earthquake of $M = 6.9$ and $PGA = 0.107$, most of the critical layers were plotted within the probability range of 30% to 50% and a few above the 50% line. Liquefaction triggering assessment under the seismic demands of the $M = 6.0 / PGA = 0.132$, $M = 7.5 / PGA = 0.1$, $M = 6.0 / PGA = 0.2$, and $M = 6.9 / PGA = 0.2$ earthquakes were also performed for the critical layers of all 142 CPT locations considered, and values are shown as box plots in Figure 10 (b), as general ranges of median CSR and Q_{c1Ncs} , concerning the control earthquake values. Results from this liquefaction triggering analysis show that all of the considered CPT locations can be identified as safe against the $M_w = 6.0 / PGA = 0.132$ earthquakes since respective CSR values, as plotted, appear below the 50% triggering curve. The earthquake combination with $M_w = 7.5$ and $PGA = 0.1$ has the same distribution of the results as the control earthquakes, with marginally higher CSR values. Against the earthquakes with $M_w = 6.0 / PGA = 0.2$ and $M_w = 6.9 / PGA = 0.2$, the most critical layers of

CPT profiles were plotted to appear above the 50% triggering curve. Hence special attention should be drawn to those locations with higher liquefaction triggering potential, which exceeds 50% against all four design earthquakes.

Figure 11 illustrates the spatial distribution of the estimated liquefaction-induced ground settlements for the Colombo port city, which was developed to predict the damage of liquefaction-induced settlement against the design earthquake combinations of magnitude $M_w = 6.9 / \text{PGA} = 0.1$, $M_w = 7.5 / \text{PGA} = 0.1$, $M_w = 6.0 / \text{PGA} = 0.2$ and, $M_w = 6.9 / \text{PGA} = 0.2$.

It was noted that vertical settlement against the earthquake combination 1, $M_w = 6.0 / \text{PGA} = 0.132$ is almost negligible, and the highest settlement values were estimated against the earthquake combination with $M_w = 6.9 / \text{PGA} = 0.2$, which was recorded around 600 mm (Figure 11) at Land Plot 8 which is located in Phase 2. Against the $M_w = 6.0 / \text{PGA} = 0.2$ and $M_w = 7.5 / \text{PGA} = 0.1$ earthquakes, post-liquefaction induced settlements were calculated as much higher compared to the control earthquake of $M_w = 6.9 / \text{PGA} = 0.1$. Also, the settlement values in Phase 2 land plots increase considerably with an increase in the magnitude of the earthquake.

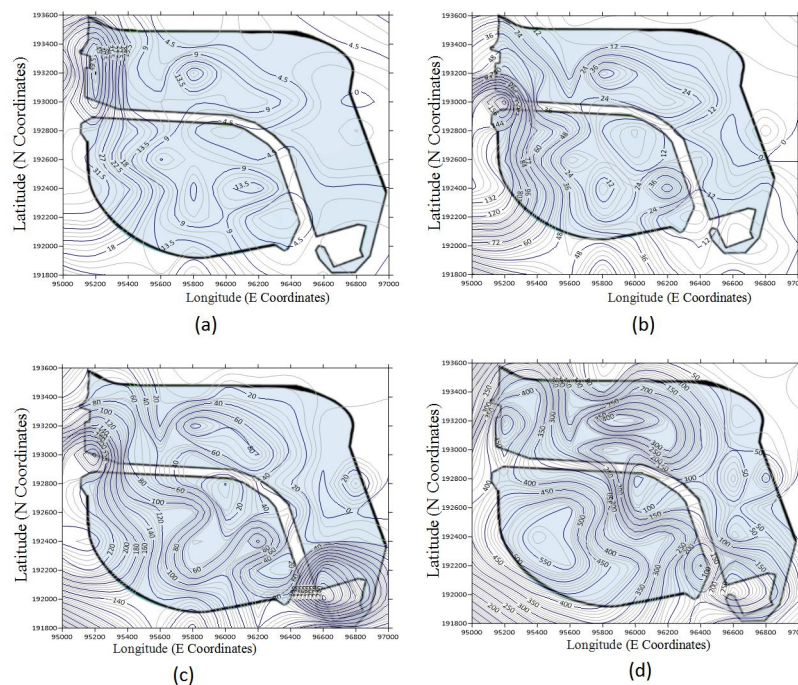


Figure 11: Contours of liquefaction-induced settlement values, (a) combination 2; (b) combination 3; (c) combination 4; (d) combination 5.

CONCLUSION

Under the present study, deterministic liquefaction triggering analysis was assessed by employing the CPT-based simplified method for free-field level ground conditions along with the post-liquefaction vertical settlement analysis.

The results revealed that the FOS values decrease along the depth under the seismic demand of considered design earthquakes. The effective depth of ground improvement, being only 6 m could be the reason for this observation. However, it is noted that critical layers in some CPT locations have a high possibility of liquefaction triggering with more than a 50% probability value. The probability of liquefaction triggering and liquefaction-induced ground settlement was considerably high in the Phase 2 ground plots, where limited improvements were carried out. Also, the maximum spatial distribution of settlements was calculated against the design earthquake

combinations with $M = 6.9 / PGA = 0.2$ and $M = 6.0 / PGA = 0.2$. According to the assumptions made due to the unavailability of CPT data in unimproved areas in Phase 2, it can be concluded that the actual FOS and settlement values are less than the values obtained from the contours since those values are based on available CPTs located in improved land areas in Phase 2.

Furthermore, out of five seismic design combinations, $M = 6.9 / PGA = 0.2$ and $M = 6.0 / PGA = 0.2$ have been identified as the most critical combinations in terms of post-liquefaction induced settlement and liquefaction triggering locations. Therefore, both earthquake combinations with $M = 6.9 / PGA = 0.2$ and $M = 6.0 / PGA = 0.2$ can be used for future assessment work and design work of Colombo port city or any other reclamation project located in Colombo.

Some of the land plots in Phase 2 of the city are highly vulnerable to severe liquefaction triggering and liquefaction-induced vertical settlement for the five earthquake combinations selected. These contour maps will help structural designers and city planners to check the vulnerability of the area against liquefaction. Also, these maps can be used effectively for future seismic safety plans and seismic hazard mitigation programs.

REFERENCES

- Abayakoon S.B.S. (1996). Seismic risk analysis of Sri Lanka. *Journal of the Geological Society of Sri Lanka* **6**: 65–72.
- Cubrinovski *et al.* (13 authors) (2010). Geotechnical reconnaissance of the 2010 Darfield (Canterbury) earthquake. *The Bulletin of the New Zealand Society for Earthquake Engineering* **43**(4): 243–320.
DOI: <https://doi.org/10.5459/bnzsee.43.4.243-320>
- Dissanayake C. (2005). A new plate boundary near Sri Lanka; Implications for future geo hazards. *Journal of the National Science Foundation of Sri Lanka* **33**(1): 5–8.
DOI: <https://doi.org/10.4038/jnsfr.v33i1.2361>
- Dananjaya R.M.S., Wijesundara K.K., Seneviratne H.N. & Dissanayake P.B.R. (2020). Determination of response spectra for Sri Lankan cities using finite difference method. *Engineer* **53**(3): 45–52.
DOI: <https://doi.org/10.4038/engineer.v53i3.7419>
- Hakam A. (2016). Laboratory liquefaction test of sand based on grain size and relative density. *Journal of the Engineering Technology Science* **48**(3): 334–344.
DOI: <https://doi.org/10.5614/j.eng.technol.sci.2016.48.3.7>
- Ishihara K. & Yoshimine M. (1992). Evaluation of settlements in sand deposits following liquefaction during earthquakes. *Soils and Foundations* **32**(1): 173–188.
DOI: <https://doi.org/10.3208/sandf1972.32.173>
- Iwasaki T., Tokida K. & Tatsuoka F. (1981). Soil liquefaction potential evaluation with use of the simplified procedure. *Proceeding of the International Conference on Recent Advance in Geotechnical Earthquake Engineering and Soil Dynamics*, 28 April. Missouri University of Science and Technology, St. Louis, USA, pp. 209–214.
- Juang C.H., Yuan H., Lee D.H. & Lin P.S. (2003). Simplified cone penetration test-based method for evaluating liquefaction resistance of soils. *Journal of the Geotechnical Geoenvironment Engineering* **129**(1): 66–80.
DOI: [https://doi.org/10.1061/\(ASCE\)1090-0241\(2003\)129:1\(66\)](https://doi.org/10.1061/(ASCE)1090-0241(2003)129:1(66))
- Juang C.H. & Jiang T. (2000). Assessing probabilistic methods for liquefaction potential evaluation. *Geotechnical Special Publication* **107**: 148–162.
DOI: [https://doi.org/10.1061/40520\(295\)10](https://doi.org/10.1061/40520(295)10)
- Kumarasiri H.C. & Abayakoon S.B.S. (2008). Potential of soil liquefaction in Sri Lanka- A dynamic approach to the mitigation of natural disasters. *Proceedings of Symposium of International Institute for Infrastructure Renewal and Reconstruction (IIIRR)*, April 2008. University of Calgary, Canada, pp. 10–12.
- Moss R.E.S. (2006). CPT-based probabilistic and deterministic assessment of in situ seismic soil liquefaction potential. *Journal of the Geotechnical Geoenvironment Engineering* **132**(8): 1032–1051.
DOI: [https://doi.org/10.1061/\(ASCE\)1090-0241\(2006\)132:8\(1032\)](https://doi.org/10.1061/(ASCE)1090-0241(2006)132:8(1032))
- Olsen R.S. (1997). Cyclic liquefaction based on the cone penetration test. *Proceeding of the NCEER Workshop on Evaluation of Liquefaction Resistance of Soils*. National Centre for Earthquake Engineering, State University of New York at Buffalo, New York, USA, pp. 225–276.

- Robertson P.K. & Wride C.E. (1998). Evaluating cyclic liquefaction potential using the cone penetration test. *Journal of the Geotechnical Engineering of Canada* **35**(3): 442–459.
DOI: <https://doi.org/10.1139/t98-017>
- Schneider J.A. & Mayne P.W. (2000). Liquefaction response of soil in Mid-America evaluated by seismic cone tests. *ASCE Geotechnical Special Publication* **97**: 1–16.
DOI: [https://doi.org/10.1061/40505\(285\)1](https://doi.org/10.1061/40505(285)1)
- Seed H.B. & de Alba P. (1986). Use of SPT and CPT tests for evaluating liquefaction resistance of sands. *Proceedings of the Special Conference on Use of in situ Testing in Geotechnical Engineering, Geotechnical Special Publication* **6**: 281–302.
- Seed H.B. & Idriss I.M. (1967). Analysis of soil liquefaction: Niigata earthquake. *Journal of the Soil Mechanics and Foundation Division* **93**(3): 83–108.
DOI: <https://doi.org/10.1061/JSFEAQ.0000981>
- Seed H.B. & Idriss I.M. (1971). Simplified procedure for evaluating soil liquefaction potential. *Journal of the Geotechnical Engineering Division* **97**(9): 1249–1273.
DOI: <https://doi.org/10.1061/JSFEAQ.0001662>
- Seed H.B. & Idriss I.M. (1982). Ground motions and soil liquefaction during earthquakes. In : *Earthquake Engineering Research Institute Monograph*. Earthquake Engineering Research Institute, Oakland, California, USA.
- Seneviratne H.N., Perera L.R.K., Wijesundara K.K., Dananjaya R.M.S. & de S. Jayawardena U. (2020). Seismicity around Sri Lanka from historical records and its engineering implications. *Engineer* **53**(2): 47–52.
DOI: <https://doi.org/10.4038/engineer.v53i2.7412>
- Shibata T. & Teparaska W. (1988). Evaluation of liquefaction potentials of soils using cone penetration tests. *Soils and Foundations* **28**(2): 49–60.
DOI: https://doi.org/10.3208/sandf1972.28.2_49
- Sonmez H. (2003). Modification of the liquefaction potential index and liquefaction susceptibility mapping for a liquefaction-prone area (Inegol, Turkey). *Environmental Geology* **44**: 862–871.
DOI: <https://doi.org/10.1007/s00254-003-0831-0>
- Stark T.D. & Olson S.M. (1995). Liquefaction resistance using CPT and field case histories. *Journal of the Geotechnical Engineering* **121**(12): 856–869.
DOI: [https://doi.org/10.1061/\(ASCE\)0733-9410\(1995\)121:12\(856\)](https://doi.org/10.1061/(ASCE)0733-9410(1995)121:12(856))
- Tokimatsu K. & Asaka A. (1998). Effects of liquefaction-induced ground displacements on pile performance in the 1995 Hyogoken Nambu earthquake. *Soils and Foundations* **2**(Sp): 163–178.
DOI: https://doi.org/10.3208/sandf.38.Special_163
- Uduweriya S.B., Wijesundara K.K., Dissanayake P.B.R., Susantha K.A.S. & Seneviratne H.N. (2020). Seismic response of Sri Lanka using PSHA technique. *Engineer* **53**(2): 39–45.
DOI: <https://doi.org/10.4038/engineer.v53i2.7411>
- Ulusay R. & Kuru T. (2004). 1998 Adana-Ceyhan (Turkey) earthquake and a preliminary microzonation based on liquefaction potential for Ceyhan Town. *Journal of the Natural Hazards* **32**: 59–88.
DOI: <https://doi.org/10.1023/B:NHAZ.0000026790.71304.32>
- Weerasinghe D.R., Seneviratne H.N., Kurukulasuriya L.C. & Wijesundara K.K. (2020). Seismic response of Sri Lanka using DSHA technique. *Engineer* **53**(2): 33–37.
DOI: <https://doi.org/10.4038/engineer.v53i2.7410>
- Yasuda S., Harada K., Ishikawa K. & Kanemaru Y. (2012). Characteristics of liquefaction in Tokyo Bay area by the 2011 Great East Japan Earthquake. *Soils and Foundations* **52**(5): 793–810.
DOI: <https://doi.org/10.1016/j.sandf.2012.11.004>
- Youd *et al.* (21 authors) (2001). Liquefaction resistance of soils - Summary report from the 1996 NCEER and 1998 NCEER/NSF workshops on evaluation of liquefaction resistance of soils. *Geotechnical and Geoenvironment Engineering* **127**(10): 817–833.
DOI: [https://doi.org/10.1061/\(ASCE\)1090-0241\(2001\)127:10\(817\)](https://doi.org/10.1061/(ASCE)1090-0241(2001)127:10(817))
- Youd T.L. & Perkins D.M. (1978). Mapping liquefaction-induced ground failure potential. *Journal of the Geotechnical Engineering Division* **104**: 443–446.
DOI: <https://doi.org/10.1061/AJGEB6.0000612>
- Zhang G., Robertson P.K. & Brachman R.W.I. (2004). Estimating liquefaction-induced lateral displacements using the standard penetration test or cone penetration test. *Geotechnical and Geoenvironment Engineering ASCE* **130**(8): 861–871.
DOI: [https://doi.org/10.1061/\(ASCE\)1090-0241\(2004\)130:8\(861\)](https://doi.org/10.1061/(ASCE)1090-0241(2004)130:8(861))

RESEARCH ARTICLE

Environmental Microbiology

Insights into the ecological roles of assembling genomes for stimulated methanogenic archaea *Methanoculleus* in coal seams

BJ Liu and Y Li *

State Key Laboratory of Mining Response and Disaster Prevention and Control in Deep Coal Mines, Anhui University of Science and Technology, Huainan City, Anhui Province, 232001, China.

Submitted: 08 November 2021; Revised: 23 August 2022; Accepted: 27 January 2023


Abstract: Biogenic coalbed methane is produced by biological processes mediated by the synergistic interaction of microbial complexes in coal seams. However, the comprehensive ecological role of methanogenic archaea in biogenic coalbed methane production remains poorly understood. Here, we study the metagenome assembled genomes (MAGs) of *Methanoculleus* from coal seams, which were stimulated by minimal salts plus yeast media in anaerobic conditions. The *Methanoculleus* genus accounted for the highest proportion of archaea ($80.4 \pm 2.8\%$) once the CH₄ concentration in the headspace increased to $15.0 \pm 2.6\%$ on the 50th day. The *Methanoculleus* MAGs were closely related to *M. thermophiles*; even so, 30 genes were detected in MAGs which were lacking in the genomes of *M. thermophiles* ATCC 33837. A deeper look at the metabolic pathway showed several metabolic pathways, including methanogenesis, glycolysis, urea cycle, TCA cycle and sulphur reduction. The CO₂ and acetate were the primary carbon sources of these cells for the methanogenesis pathway. Glycolysis and sulphate reduction processes were the main processes for providing acetate. In addition, the cells had a variety of other functions, including nitrogen fixation and hydrogen production. Overall, this study enabled a better understanding of the ecological roles of *Methanoculleus* for biogenic methane in coal seams by combining bioinformatic techniques.

Keywords: Metabolic pathway, metagenome assembly, methanogenesis, sulphate reduction.

INTRODUCTION

Coalbed methane (CBM) is an important medium for transforming global energy utilisation. The harm to the environment caused by this simple organic matter is much lower than that caused by the exploitation of fossil energy, including oil and coals (Ritter *et al.*, 2015; McLeish *et al.*, 2021). CBM mainly includes thermogenic and biogenic processes in its formation. A staggering proportion (20-40%, even higher under favourable biogeologic conditions) of global methane reserves are biogenic, being mediated by the synergistic interaction of microbial complexes (Thielemann *et al.*, 2004; Faiz & Hendry, 2006; Rathi *et al.*, 2019). Therefore, the biogenic coalbed methane formation mechanism and development have gradually attracted more attention.

To our knowledge, the formation of biogenic coalbed methane is a very complex process which involves a series of functional groups, including hydrolysing and fermenting bacteria, hydrogen and acetogen producing bacteria, and methane-producing archaea (Wang *et al.*, 2018; Vick *et al.*, 2019a). The researchers on coal seam microorganisms mainly focused on the abundance and activity of methanogenic archaea, besides microbial diversity (Szafranek-Nakonieczna *et al.*, 2018; Plyatsuk *et al.*, 2020), because these methanogenic groups are the drivers of the final step in the degradation of organic matter in coal seams into methane, converting CO₂, H₂, acetate, formate, or other simple compounds in the coal seams into methane (Vick *et al.*, 2019a).

* Corresponding author (liyong20130104@163.com;  <https://orcid.org/0000-0002-8946-3962>)



This article is published under the Creative Commons CC-BY-ND License (<http://creativecommons.org/licenses/by-nd/4.0/>). This license permits use, distribution and reproduction, commercial and non-commercial, provided that the original work is properly cited and is not changed in anyway.

The methanogens that exist in coal seams are characterised by a variety of metabolic strategies, including strict hydrogenotrophs (such as *Methanobacterium* and *Methanoregula*), acetotrophs (e.g., *Methanotherix*), and formate utilisers (e.g., *Methanoregula*). However, the methanogenic archaea that drive the secondary biogenic CBM are diverse in coals from different regions. *Methanosarcina* were dominant archaea in the pristine Pniówek coal due to their metabolic flexibility (Pytlak *et al.*, 2020). *Methanosaeta* and *Methanobacterium* were dominant groups in the coals from the Konin Basin (Bucha *et al.*, 2020). *Methanobacterium* and *Methanosarcina* were dominant in the southern Qinshui Basin (Li *et al.*, 2020). However, the understanding of these methanogens has been limited to what they are and how to stimulate them. The ecological function of these archaea has not been thoroughly explored, which helps understand the formation mechanism of biogenic CBM.

Several researchers have attempted to stimulate the production potential of biogenic coalbed methane through various methods, including nutrients (Jones *et al.*, 2010; In't Zandt *et al.*, 2018), exogenous strains (Wang *et al.*, 2016) and other chemical means (Beckmann *et al.*, 2019; Webster *et al.*, 2019). In this study, it was found out that some methanogens can be stimulated and enriched by nutrients. Furthermore, we successfully constructed the metagenome assembled genomes (MAGs) of the foremost methanogenic archaea, *Methanoculleus* sp., from the metagenome of microbial communities in coal seams, using bioinformatics methods. By inferring the metabolic remodelling of these organisms from high-quality MAGs, the potential ecological functions of these organisms in coal seams are further explored. This study greatly expands our current understanding of methanogenic archaea *Methanoculleus* sp. in coal seams.

MATERIALS AND METHODS

Sample collection, culturing, DNA extraction, and sequencing

Coal samples were collected from 1412A coal working face of Zhangji Coal Mine (116°29' E, 32°46' N) in Huainan Mining Industry Co., Ltd., China. The coal samples at a distance of 15 m from the coal wall were taken by a coring rig (ZYD-3200S, Φ 108 mm), with a length of about 80-100 mm. The coal samples were surface-stripped with a sterile knife, placed in sterilised vacuum bags, and transported to the laboratory using an ice cooler. The maceral group composition (vitrinite, inertinite and exinite) in coal was analyzed based on ISO 7404-3: 2009, methods for the petrographic analysis of coals – Part 3: Method of determining maceral group composition, MOD. The proximate analysis indicators, including air dried basis moisture (M_{ad}), air dried basis ash (A_d), and dry ash-free volatiles (V_{daf}), were measured by an industrial analyzer (SDTGA8000, Sande, Changsha, China). The air dried basis total sulphur ($S_{t,d}$) was analyzed by an automatic coal sulphur meter (TKCL-6000, Tianke, Hebi, China). The basic properties of the coal sample were as follows: vitrinite 63.50%, inertinite 25.40%, exinite 11.10%, M_{ad} 1.93%, A_d 10.77 %, V_{daf} 33.36 %, $S_{t,d}$ 0.61%.

To stimulate the methane producing capacity of the coal, the coal samples were cultured in anaerobic conditions in minimal salts plus yeast media (MSY) that consisted of NH_4Cl 0.1 g/L, $K_2HPO_4 \cdot 3H_2O$ 0.4 g/L, $MgCl_2 \cdot 6H_2O$ 0.1 g/L, yeast extract 1 g/L, and trace element solution 1.0 mL/L (Li *et al.*, 2008). The coal samples with medium were cultured using 500 mL sterile culture bottles at 37 °C, the headspace air in the sterile culture bottles was replaced with high purity nitrogen and sealed with butyronitrile plugs.

To continuously monitor the methane production of the coal samples, the CH_4 concentration in the headspace of the sterile culture bottles was measured with a gas chromatograph equipped with a thermal conductivity detector (TCD) and a TDX-01 packed column using N_2 as a carrier gas. The temperatures of the detector, injector, and oven were 100, 105, and 60°C, respectively. The methane content in the headspace air increases slowly after 40 days, thus we collected samples on the 50th day.

After culturing, total DNA was extracted with the FastDNA® SPIN Kit for soil (MP Biomedicals, Cleveland, OH, USA) according to the manufacturer's instructions, each of the coal samples was subjected to metagenomic sequencing. Metagenomic sequencing was conducted with an Illumina Hiseq4000 by LC-Bio Technology Co., Ltd. (Hangzhou, China).

Metagenomic assembly and genome binning

The adapters and duplicated sequences for the raw sequencing data were removed by Trimmomatic. In addition, low quality reads with length < 50 bp and/or average phred value < 20 in a 4 bp sliding window were trimmed at both ends. The high-quality reads were assembled using Metahit (v1.2.8) with the parameter “-k 21, 29, 39, 59, 79, 99, 119, 141”. All the high-quality reads were mapped onto assembled scaffolds by BMap with the parameters “minid = 0.97, local = t”. The coverage information of scaffolds was computed by the script jgi_summarize_bam_contig_depths, and these scaffolds were binned into metagenome assembled genomes (MAGs) by MetaBAT2 with the parameters “-m 1500”. In addition, the genome completeness, potential contamination and strain heterogeneity of each MAG was evaluated by CheckM.

Analyses of genome bins

The binned genome was submitted in RAST for annotation and classification. Taxonomic affiliations of MAGs were determined with GTDB-Tk (Chaumeil *et al.*, 2020). Besides, the IQ-TREE was used to create a phylogenomic maximum-likelihood tree with the alignment of concatenated protein sequences derived from single copy marker genes retrieved from GTDB-Tk. In addition, the phylogenetic tree of protein coding sequences of desulphoferrodox in FeS₄ iron-binding domain-containing protein, putative sulphite reductase, and archaeal distant homology with glucose-6-phosphate isomerase were obtained from the reconstructed genome. The tree was constructed using MEGA-X by neighbour-joining tree and bootstrap method based on multiple protein sequence alignment (MUSCLE). The reference protein sequences were downloaded from NCBI.

RESULTS AND DISCUSSION

Binning results and identification

Genomic reconstruction of metagenomes is of great significance for understanding functional microorganisms (Hua *et al.*, 2019) in coal seams. Methanogenic archaea genomes assembled from metagenomes are helpful in revealing the biogeochemistry (Anantharaman *et al.*, 2016) of coal seam and their importance to the formation of biogenic methane. In this study, it was not possible to obtain all functional microbes in coal seam through nutrient stimulation. But the implementation of nutrient addition is conducive to understanding the methanogens with enrichment potential in the study area, which plays an important role in directly applying microorganisms to production. In this study, the CH₄ concentration in the headspace were increased to 15.0 ± 2.6% at the 50th day, which showed that a certain amount of methane was generated by stimulating the microbial activity of coal seam with nutrients. The *Methanoculleus* genus accounted for the highest proportion of archaea (80.4 ± 2.8%). In addition, 3 high-quality *Methanoculleus* MAGs (completeness > 90%, contamination < 5%) were successfully reconstructed from metagenomes that were sequenced from coal samples, after binning from the metahit generated assembly file (Table 1). From the GTDB-Tk analysis and phylogenetic tree based on the single copy marker genes (Figure 1), these three bins were highly related to *Methanoculleus thermophilus* ATCC 33837 (GenBank GCA_001571405.1). The binned genomes showed 61.3% GC content, and MAGs were classified as high quality with sizes ranging from 2.18 to 2.39 Mbp. Both rRNAs and tRNAs are detectable in MAGs. The results indicated that such *Methanoculleus* sp. were the main methanogens that are easily stimulated by nutrients in the study area. Coal seams are important underground anaerobic habitats in the world. The main methanogenic archaea in such anaerobic habitats differ greatly due to the difference of coal forming age (Liu *et al.*, 2019), pre coal material (Wang *et al.*, 2018), sedimentary environment (Tanikawa *et al.*, 2018) and microbial sources (Vick *et al.*, 2019b; Li *et al.*, 2021). *Methanosarcina* were dominant archaea in the pristine Pniówek

Table 1: Summary statistics of the *Methanoculleus* bins reconstructed from coal samples.

	Comp. (%)	Cont. (%)	GC	Contig N50 (Kbp)	Bases (Mbp)	No. of contigs	No. of CDS	No. of features	No. of tRNA	No. of rRNA
NL_1.7	97.71	2.614	0.613	238.83	2.39	16	2490	2739	49	3
NL_2.6	97.71	2.614	0.613	240.94	2.39	16	2498	2742	49	3
NL_3.1	96.40	2.614	0.613	151.64	2.18	33	2303	2526	50	4

Note: Comp. - completeness, Cont. - contamination

coal due to their metabolic flexibility (Pytlak *et al.*, 2020). *Methanosaeta* and *Methanobacterium* were dominant groups in the coals from the Konin Basin (Bucha *et al.*, 2020). *Methanobacterium* and *Methanosarcina* were dominant in the southern Qinshui Basin (Li *et al.*, 2020).

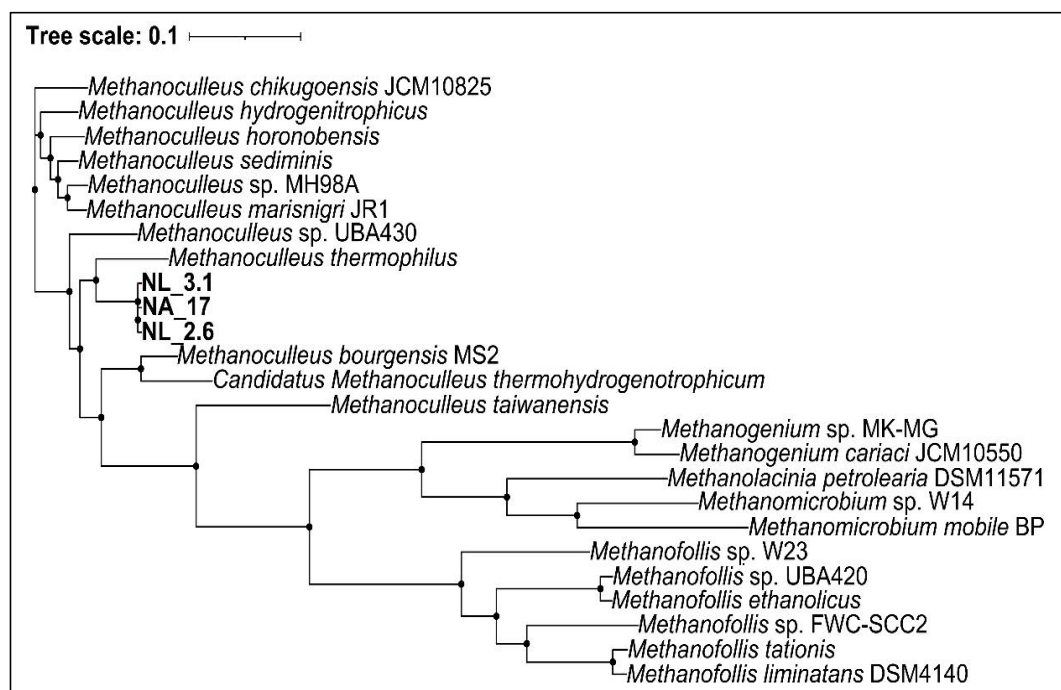


Figure 1: Phylogenetic tree of *Methanoculleus* MAGs. The phylogenetic tree was analyzed by GTDB-Tk (v1.3.0) based on their genome sequences and visualized by itol (<https://itol.embl.de/>).

Main metabolic pathway

From RAST annotation it was mined that the MAGs possessed the essential metabolic genes required for a normal archaeal cell to flourish in the anaerobic environments. The genome of MAGs showed the genes in the category of carbon, nitrogen and sulphur metabolism. The archaea showed transport and utilisation of multiple amino acid, tryptophan, biotin, carbohydrate, and inorganic acid (Supplementary Data 1-3). A deeper look at the metabolic pathway showed several metabolic pathways including methanogenesis, glycolysis, urea cycle, TCA cycle, and sulphur reduction (Figure 2). The CO₂ was the main carbon source for the methanogenesis pathway in these cells. Besides, acetate could also be utilised to produce CH₄ via serine metabolism.

In the special coal seam environment of this study area, *Methanoculleus* sp. could use CO₂ and acetate as the main metabolic substrates for methanogenesis. Among the metabolites of methanogenesis, CO₂ and acetate were the main precursors in coal seams. Beckmann *et al.* (2019) found that acetate is the primary energy carrier in the Sydney Basin coal reservoir. In addition, most biogenic CBM reservoirs are produced by CO₂ reduction (Zhang & Liang, 2017). In this study, the glycolysis pathway was still the main energy source of these methanogens in coal seams under anaerobic conditions. This pathway was an important process for *Methanoculleus* sp. to obtain acetate. In the process of glycolysis or the modified version, glucose-6-phosphate isomerase plays a central role in sugar metabolism of all the cells (Hansen *et al.*, 2001). And the archaeal distant homologue of glucose-6-phosphate isomerase was deemed as the first characterised archaeal member of the glucose-6-phosphate isomerase superfamily (Rudolph *et al.*, 2004), showing its importance in the archaeal metabolism. In addition, Rudolph *et al.* (2004) suggested that such genes might also be obtained from bacteria.

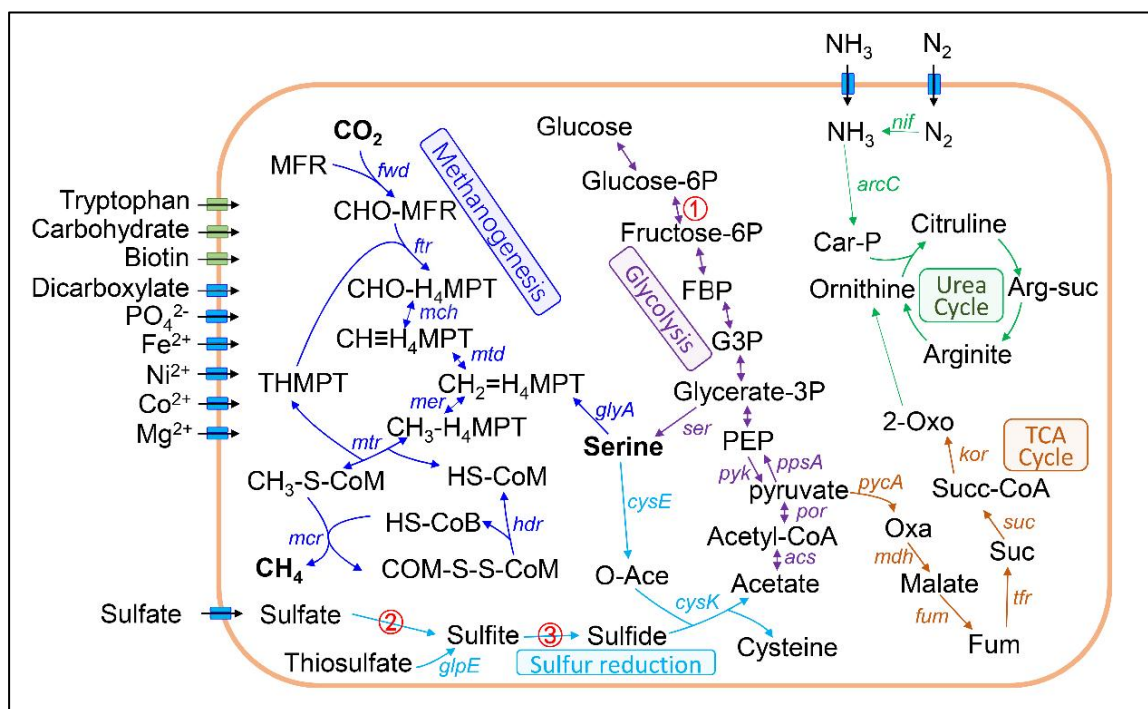


Figure 2: Overview of metabolic potentials in *Methanoculleus* MAGs. The significant major pathways related to metabolisms of carbon, nitrogen and sulphur, flagellar and motor protein, and various transporters in MAG groupings. Detailed gene information associated with above mentioned pathways was recorded in Supplementary Data 1-3. MFR: methanofuran; FBP: fructose-1,6-bisphosphatase; G3P: glyceraldehyde-3P; PEP: phosphoenolpyruvate; O-Ace: O-acetyl-L-serine; Car-P: carbamoyl-P; Arg-suc: arginosuccinate; 2-Oxo: 2-oxoglutarate; Succ-CoA: succinyl-CoA; Suc: succinate; Fum: fumarate; Oxa: oxaloacetate.

In these cells, methanogenesis was also associated with some important metabolic pathways including glycolysis and sulphur reduction. Glycerate-3P, the intermediate product of glycolysis, could also have produced serine through serine biosynthesis and eventually converted to CH₄. Sulphate could be reduced to sulphide, which could be forming acetate with O-acetyl-L-serine by cysteine synthase. In addition, several enzymes for reactions in these two processes were different from those for the general reactions in Kyoto encyclopaedia of genes and genomes (KEGG), such as archaeal distant homology with glucose-6-phosphate isomerase (D-glucose-6-phosphate \rightleftharpoons D-fructose-6-phosphate), desulphoferrodoxin FeS₄ iron-binding domain-containing protein (sulphate \Rightarrow sulphite) and putative sulphite reductase (sulphite \Rightarrow sulphide). The amino acid sequences in these enzymes were widely distributed in the *Methanoculleus* genus (Figure 3).

In this study, *cys* gene was the main sulphate reduction gene in MAG. Li *et al.* (2022) showed that sulphur reduction genes are mainly dominated by the *cys* genes, and also showed the core linking of the network co-occurrence of the C-N-S genes in coal seams. Besides, sulphates and other substances participate in reactions that convert organic substances into acetate (Matsuura *et al.*, 2021). The existence of these desulphurising *Methanoculleus* sp. may also favour coal degradation (Midgley *et al.*, 2010), because many desulphurizers could provide electron donors for the coal seam organic decomposition (Zhang *et al.*, 2015). Beckmann *et al.* (2019) considered that high sulphate concentrations did not prevent the growth of methanogenic archaea, but the sulphate-reducing bacteria had limited energy and competed with the methanogenic archaea. In this study, sulphate was also utilised by archaea through the certain sulphate reduction pathway. Several *cys* enzymes were used to synthesize sulphites and convert sulphates into sulphides; the existence of sulphate utilisation enhanced the archaeal ability to produce amino acids, such as cysteine and methionine (Tikariha & Purohit, 2019). This can also provide a small amount of acetate in the coal seams. The MAGs also had their specific genes for sulphate reduction including desulphoferrodoxin FeS₄ iron-binding domain-containing protein and putative sulphite reductase. Desulphoferrodoxin was first reported by Moura *et al.* (1990) in *Desulfovibrio desulphuricans* (ATCC 27774) and *Desulfovibrio vulgaris* (strain Hildenborough), suggesting its special sulphate reduction capacity.

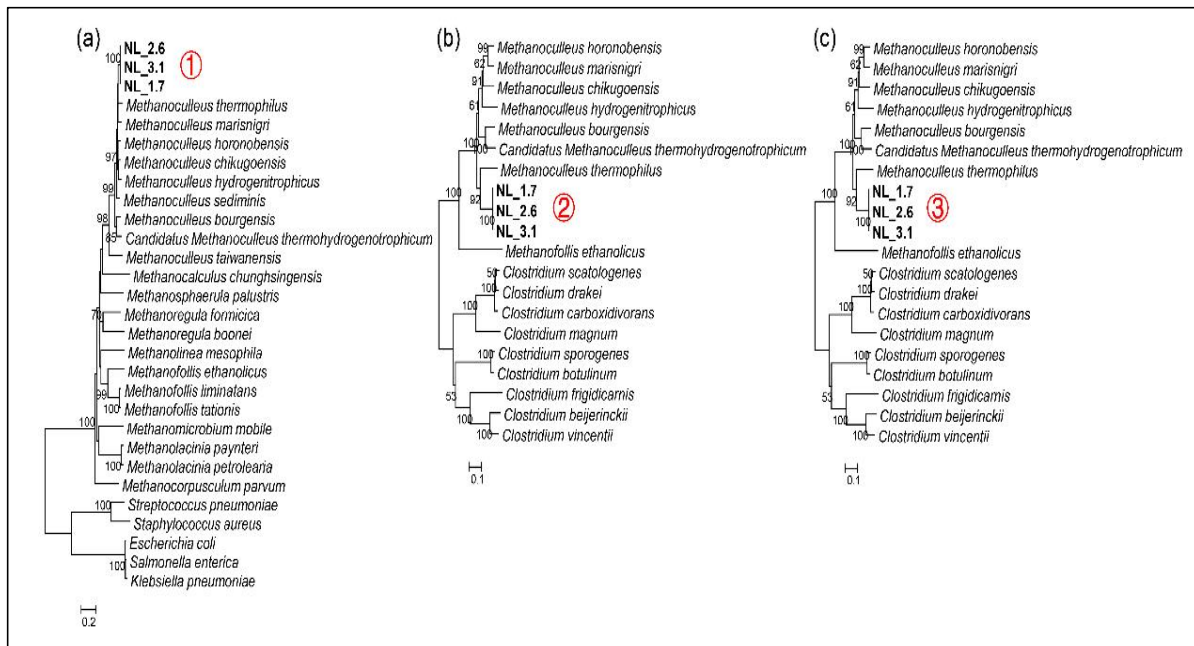


Figure 3: Phylogenetic analysis of protein coding sequences of desulfoferrodox in archaeal distant homology with glucose-6-phosphate isomerase (a), FeS₄ iron-binding domain-containing protein (b) and putative sulfite reductase (c) from reconstructed genome. Bootstrap values were based on 1000 replicates, and only bootstrap values higher than 50% are shown.

In addition, the cells had a variety of other functions including nitrogen fixation and hydrogen production. Therein, [NiFe] hydrogenase nickel incorporation protein (*hypA*), [NiFe] hydrogenase nickel incorporation-associated protein (*hypB*) and [NiFe] hydrogenase metallocentre assembly protein (*hypCDE*) were found in MAGs. Ammonia could be used by archaea to synthesise glutamate, other amino acids and nucleotides (Tikariha & Purohit, 2019). Thus the presence of a well-regulated mechanism such as nitrogen fixation by the bacteria makes them suitable candidates for methanogenesis with low nitrogen availability. *Methanoculleus* MAGs could also provide sufficient metabolic substrates for methane production in coal seams by producing hydrogen. In this study, it was surprising to simultaneously detect the *hypABCDE* genes. These genes are encoding [NiFe] hydrogenase nickel incorporation proteins or metallocentre assembly proteins, which are essential for hydrogen production (Quemeneur *et al.*, 2011; Rai *et al.*, 2019). This also provides energy for other hydrogen-trophic methanogens.

Compare metabolic reconstruction

Comparing to the genomic data of *M. thermophilus* ATCC 33837 (GenBank GCA_001571405.1), 30 genes were detected in all the three MAGs but not in the comparison genomes (Table 2). These genes mainly associated with a variety of metabolisms (amino acids and derivatives, carbohydrates, fatty acids, lipids, isoprenoids, and protein metabolism) and environmental response (cell wall and capsule, stress response, and virulence, disease, and defense). Among them, most genes were homologous with *Methanoculleus* spp. (not *M. thermophilus*) and those homologies ranged from 67% to 95%. A portion of genes were homologous with other methanogens, such as the alcohol dehydrogenase (EC 1.1.1.1) homology with *Methanospirillum* sp. (homology 77%), type III restriction-modification system methylation subunit (EC 2.1.1.72) homology with *Methanocorpusculum labreanum* (homology 55%), and circadian clock protein KaiC homology with *Candidatus Methanoperedens* sp. BLZ2 (homology 64%). In addition, a few genes were homologous with some bacteria, such as arginase (EC 3.5.3.1) homology with *Phyllobacterium zundukense* (homology 74%) and N-acetylneuraminate synthase (EC 2.5.1.56) homology with *Tautonia sociabilis* (homology 74%).

Table 2: Genes in the all the three MAGs but not detected in standard strain *Methanoculleus thermophilus* ATCC 33837.

Category	Gene	Homology with	% Homology
Amino acids and derivatives	Arginase (EC 3.5.3.1)	<i>Phyllobacterium zundukense</i>	74
	Delta-1-pyrroline-5-carboxylate dehydrogenase (EC 1.2.1.88)	<i>Methanomicrobiales archaeon 53_19</i>	86
Carbohydrates	Alpha-amylase (EC 3.2.1.1)	<i>Methanoculleus horonobensis</i>	85
	Glucoamylase (EC 3.2.1.3)	<i>Methanoculleus chikugoensis</i>	87
	1,4-alpha-glucan (glycogen) branching enzyme, GH-13-type (EC 2.4.1.18)	<i>Methanoculleus marisnigri</i>	91
Cell wall and capsule	N-acetylneuraminate synthase (EC 2.5.1.56)	<i>Tautonia sociabilis</i>	74
	Glucose-1-phosphate thymidyltransferase (EC 2.7.7.24)	<i>Methanoculleus bourgensis</i>	89
	dTDP-glucose 4,6-dehydratase (EC 4.2.1.46)	<i>Methanoculleus bourgensis</i>	84
	putative glycosyltransferase	<i>Methanoculleus bourgensis</i>	68
Clustering-based subsystems	Xanthosine/inosine triphosphate pyrophosphatase	<i>Methanoculleus bourgensis</i>	88
Cofactors, vitamins, Prosthetic Groups,	Alcohol dehydrogenase (EC 1.1.1.1)	<i>Methanospirillum</i> sp.	77
DNA metabolism	ATP-dependent DNA ligase (EC 6.5.1.1) LigC	<i>Candidatus Methanoculleus</i>	80
	Type III restriction-modification system methylation subunit (EC 2.1.1.72)	<i>Methanocorpusculum labreanum</i>	55
Fatty acids, lipids, and isoprenoids	(2E,6E)-farnesyl diphosphate synthase (EC 2.5.1.10)	<i>Methanoculleus marisnigri</i>	75
	Lycopene elongase (EC 2.5.1.-)	<i>Methanoculleus horonobensis</i>	89
	Phytoene dehydrogenase (EC 1.14.99.-)	<i>Methanoculleus hydrogenitrophicus</i>	94
	Phytoene synthase (EC 2.5.1.32)	<i>Methanoculleus sediminis</i>	86
	Dimethylallyltransferase (EC 2.5.1.1)	<i>Methanoculleus marisnigri</i>	75
	Octaprenyl diphosphate synthase (EC 2.5.1.90)	<i>Methanoculleus marisnigri</i>	75
Miscellaneous	DedA protein	<i>Methanoculleus</i> sp.	67
	Tungsten-containing aldehyde:ferredoxin oxidoreductase (EC 1.2.7.5)	<i>Methanoculleus</i> sp. MH98A	88
Nucleosides and Nucleotides	Xanthine permease	<i>Methanoculleus bourgensis</i>	75
Protein metabolism	Circadian clock protein KaiC	<i>Candidatus Methanoperedens</i> sp.	64
	DNA polymerase III alpha subunit (EC 2.7.7.7)	<i>Methanoculleus</i> sp.	71
	UDP-glucose 6-dehydrogenase (EC 1.1.1.22)	<i>Methanoculleus taiwanensis</i>	81
RNA metabolism	DNA-directed RNA polymerase subunit P (EC 2.7.7.6)	<i>Methanoculleus bourgensis</i>	95
stress response	Glycine betaine transporter OpuD	<i>Methanoculleus marisnigri</i>	92
	Superoxide dismutase [Mn/Fe] (EC 1.15.1.1)	<i>Methanoculleus marisnigri</i>	90
Virulence, disease and defense	Transcriptional regulator, MerR family	<i>Methanoculleus chikugoensis</i>	81
	Multi antimicrobial extrusion protein	<i>Methanoculleus marisnigri</i>	87

CONCLUSION

Together these results showed the stimulated methanogenic archaea *Methanoculleus* and further expanded the ecological function of the functional groups in coal seams. The MAGs might be assigned to *M. thermophilus*, although their functions were somewhat different from that of the standard strain. *Methanoculleus* sp. could use CO₂ and acetate as the main metabolic substrate for methanogenesis. Glycolysis and sulphate reduction processes were the main processes for providing acetate, both of which differ from other general species. Overall, this study enabled a better understanding of the ecological roles of *Methanoculleus* for biogenic methane production, using a combination of bioinformatic techniques.

Acknowledgement

This study was funded by the Independent Research Fund of the State Key Laboratory of Mining Response and Disaster Prevention and Control in Deep Coal Mines in Anhui University of Science and Technology (SKLMRDPC20ZZ09), the Key Research and Development Projects in Anhui Province (202004a07020054), and the Natural Science Foundation of the Anhui Province Education Department (KJ2020A0322).

REFERENCES

- Anantharaman K. *et al.* (14 authors) (2016). Thousands of microbial genomes shed light on interconnected biogeochemical processes in an aquifer system. *Nature Communications* **7**: e13219.
DOI: <https://doi.org/10.1038/ncomms13219>
- Beckmann S., Luk A.W.S., Gutierrez-Zamora M.L., Chong N.H.H., Thomas T., Lee M. & Manefield M. (2019). Long-term succession in a coal seam microbiome during in situ biostimulation of coalbed-methane generation. *The ISME Journal* **13**(3): 632–650.
DOI: <https://doi.org/10.1038/s41396-018-0296-5>
- Bucha M. *et al.* (11 authors) (2020). Microbial methane formation from different lithotypes of Miocene lignites from the Konin Basin, Poland: Geochemistry of the gases and composition of the microbial communities. *International Journal of Coal Geology* **229**: e103558.
DOI: <https://doi.org/10.1016/j.coal.2020.103558>
- Chaumeil P.A., Mussig A.J., Hugenholtz P. & Parks D.H. (2020). GTDB-Tk: A toolkit to classify genomes with the Genome Taxonomy Database. *Bioinformatics* **36**(6): 1925–1927.
DOI: <https://doi.org/10.1093/bioinformatics/btz848>
- Faiz M. & Hendry P. (2006). Significance of microbial activity in Australian coal bed methane reservoirs - A review. *Bulletin of Canadian Petroleum Geology* **54**: 261–272.
DOI: <https://doi.org/10.2113/gsepbull.54.3.261>
- Hansen T., Oehlmann M. & Schönheit P. (2001). Novel type of glucose-6-phosphate isomerase in the hyperthermophilic archaeon *Pyrococcus furiosus*. *Journal of Bacteriology* **183**(11): 3428–3435.
DOI: <https://doi.org/10.1128/JB.183.11.3428-3435.2001>
- Hua Z.S. *et al.* (18 authors) (2019). Insights into the ecological roles and evolution of methyl-coenzyme M reductase-containing hot spring Archaea. *Nature Communications* **10**: e4574.
DOI: <https://doi.org/10.1038/s41467-019-12574-y>
- In't Zandt M.H., Beckmann S., Rijkers R., Jetten M.S.M., Manefield M. & Welte C.U. (2018). Nutrient and acetate amendment leads to acetoclastic methane production and microbial community change in a non-producing Australian coal well. *Microbial Biotechnology* **11**(4): 626–638.
DOI: <https://doi.org/10.1111/1751-7915.12853>
- Jones E.J.P., Voytek M.A., Corum M.D. & Orem W.H. (2010). Stimulation of methane generation from nonproductive coal by addition of nutrients or a microbial consortium. *Applied and Environmental Microbiology* **76**(21): 7013–7022.
DOI: <https://doi.org/10.1128/aem.00728-10>
- Li D.M., Hendry P. & Faiz M. (2008). A survey of the microbial populations in some Australian coalbed methane reservoirs. *International Journal of Coal Geology* **76**(1-2): 14–24.
DOI: <https://doi.org/10.1016/j.coal.2008.04.007>
- Li Y., Liu B., Chen J. & Yue X. (2022). Carbon–nitrogen–sulfur-related microbial taxa and genes maintained the stability of microbial communities in coals. *ACS Omega* **7**(26): 22671–22681.
DOI: <https://doi.org/10.1021/acsomega.2c02126>
- Li Y., Liu B., Yuan L., Xue S., Liu X., Wu Z. & Chen J. (2021). Subsurface microbial invasion affects the microbial community of coal seams. *Energy and Fuels* **35**(9): 8023–8032.
DOI: <https://doi.org/10.1021/acs.energyfuels.1c00197>
- Li Y., Tang S.H., Zhang S.H. & Xi Z.D. (2020). In situ analysis of methanogenic pathways and biogeochemical features of CBM co-produced water from the Shizhuangnan block in the southern Qinshui Basin, China. *Energy and Fuels* **34**(5): 5466–5475.
DOI: <https://doi.org/10.1021/acs.energyfuels.9b04351>
- Liu B., Yuan L., Shi X., Li Y., Jiang C., Ren B. & Sun Q. (2019). Variations in microbiota communities with the ranks of coals from three permian mining areas. *Energy and Fuels* **33**(6): 5243–5252.
DOI: <https://doi.org/10.1021/acs.energyfuels.8b04413>
- Matsuura N., Masakke Y., Karthikeyan S., Kanazawa S., Honda R., Yamamoto-Ikemoto R. & Konstantinidis K.T. (2021). Metagenomic insights into the effect of sulfate on enhanced biological phosphorus removal. *Applied Microbiology and Biotechnology* **105**(5): 2181–2193.
DOI: <https://doi.org/10.1007/s00253-021-11113-4>

- McLeish A.G., Vick S.H.W., Grigore M., Pinetown K.L., Midgley D.J. & Paulsen I.T. (2021). Adherent microbes in coal seam environments prefer mineral-rich and crack-associated microhabitats. *International Journal of Coal Geology* **234**: e103652.
DOI: <https://doi.org/10.1016/j.coal.2020.103652>
- Midgley D.J., Hendry P., Pinetown K.L., Fuentes D., Gong S., Mitchell D.L. & Faiz M. (2010). Characterisation of a microbial community associated with a deep, coal seam methane reservoir in the Gippsland Basin, Australia. *International Journal of Coal Geology* **82**(3-4): 232–239.
DOI: <https://doi.org/10.1016/j.coal.2010.01.009>
- Moura I., Tavares P., Moura J.J., Ravi N., Huynh B.H., Liu M.Y. & LeGall J. (1990). Purification and characterization of desulfoferrodoxin. A novel protein from *Desulfovibrio desulfuricans* (ATCC 27774) and from *Desulfovibrio vulgaris* (strain Hildenborough) that contains a distorted rubredoxin center and a mononuclear ferrous center. *Journal of Biological Chemistry* **265**(35): 21596–21602.
DOI: [https://doi.org/10.1016/S0021-9258\(18\)45782-1](https://doi.org/10.1016/S0021-9258(18)45782-1)
- Plyatsuk L., Chernysh Y., Ablicieva I., Bataltsev Y., Vaskin R., Roy I., Yakhnenko E. & Roubik H. (2020). Modelling and development of technological processes for low rank coal bio-utilization on the example of brown coal. *Fuel* **267**: e117298.
DOI: <https://doi.org/10.1016/j.fuel.2020.117298>
- Pytlak A. et al. (13 authors) (2020). Stimulation of methanogenesis in bituminous coal from the upper Silesian coal basin. *International Journal of Coal Geology* **231**: e103609.
DOI: <https://doi.org/10.1016/j.coal.2020.103609>
- Quemeneur M., Hamelin J., Latrille E., Steyer J.P. & Trably E. (2011). Functional versus phylogenetic fingerprint analyses for monitoring hydrogen-producing bacterial populations in dark fermentation cultures. *International Journal of Hydrogen Energy* **36**(6): 3870–3879.
DOI: <https://doi.org/10.1016/j.ijhydene.2010.12.100>
- Rai P., Pandey A. & Pandey A. (2019). In-silico-mining of small sequence repeats in hydrogenase maturation subunits of *E. coli*, *clostridium*, and *Rhodobacter*. *International Journal of Hydrogen Energy* **44**(33): 17813–17822.
DOI: <https://doi.org/10.1016/j.ijhydene.2019.05.057>
- Rathi R., Lavania M., Singh N., Sarma P.M., Kishore P., Hajra P. & Lal B. (2019). Evaluating indigenous diversity and its potential for microbial methane generation from thermogenic coal bed methane reservoir. *Fuel* **250**: 362–372.
DOI: <https://doi.org/10.1016/j.fuel.2019.03.125>
- Ritter D., Vinson D., Barnhart E., Akob D.M., Fields M.W., Cunningham A.B., Orem W. & McIntosh J.C. (2015). Enhanced microbial coalbed methane generation: A review of research, commercial activity, and remaining challenges. *International Journal of Coal Geology* **146**: 28–41.
DOI: <https://doi.org/10.1016/j.coal.2015.04.013>
- Rudolph B., Hansen T. & Schönheit P. (2004). Glucose-6-phosphate isomerase from the hyperthermophilic archaeon *Methanococcus jannaschii*: characterization of the first archaeal member of the phosphoglucose isomerase superfamily. *Archives of Microbiology* **181**(1): 82–87.
DOI: <https://doi.org/10.1007/s00203-003-0626-4>
- Szafranek-Nakonieczna A., Zheng Y., Słowakiewicz M., Pytlak A., Polakowski C., Kubaczyński A., Bieganowski A., Banach A., Woliński A. & Stępniewska Z. (2018). Methanogenic potential of lignites in Poland. *International Journal of Coal Geology* **196**: 201–210.
DOI: <https://doi.org/10.1016/j.coal.2018.07.010>
- Tanikawa W., Tadaï O., Morono Y., Hinrichs K.U. & Inagaki F. (2018). Geophysical constraints on microbial biomass in subseafloor sediments and coal seams down to 2.5 km off Shimokita Peninsula, Japan. *Progress in Earth and Planetary Science* **5**(2018):58.
DOI: <https://doi.org/10.1186/s40645-018-0217-2>
- Thielemann T., Cramer B. & Schippers A. (2004). Coalbed methane in the Ruhr Basin, Germany: A renewable energy resource? *Organic Geochemistry* **35**(11): 1537–1549.
DOI: <https://doi.org/10.1016/j.orggeochem.2004.05.004>
- Tikariha H. & Purohit H.J. (2019). Assembling a genome for novel nitrogen-fixing bacteria with capabilities for utilization of aromatic hydrocarbons. *Genomics* **111**(6): 1824–1830.
DOI: <https://doi.org/10.1016/j.ygeno.2018.12.005>
- Vick S.H.W., Gong S., Sestak S., Vergara T.J., Pinetown K.L., Li Z., Greenfield P., Tetu S.G., Midgley D.J. & Paulsen I.T. (2019a). Who eats what? Unravelling microbial conversion of coal to methane. *Fems Microbiology Ecology* **95**(7): fiz093.
DOI: <https://doi.org/10.1093/femsec/fiz093>
- Vick S.H.W., Greenfield P., Pinetown K.L., Sherwood N., Gong S., Tetu S.G., Midgley D.J. & Paulsen I.T. (2019b). Succession patterns and physical niche partitioning in microbial communities from subsurface coal seams. *Iscience* **12**: 152–167.
DOI: <https://doi.org/10.1016/j.isci.2019.01.011>

- Wang A., Shao P., Lan F. & Jin H. (2018). Organic chemicals in coal available to microbes to produce biogenic coalbed methane: A review of current knowledge. *Journal of Natural Gas Science and Engineering* **60**: 40–48.
DOI: <https://doi.org/10.1016/j.jngse.2018.09.025>
- Wang H., Lin H., Rosewarne C.P., Li D.M., Gong S., Hendry P., Greenfield P., Sherwood N. & Midgley D.J. (2016). Enhancing biogenic methane generation from a brown coal by combining different microbial communities. *International Journal of Coal Geology* **154**: 107–110.
DOI: <https://doi.org/10.1016/j.coal.2015.12.006>
- Webster J., Lee M., Gurba L.W., Manefield M. & Thomas T. (2019). The effect of oxidative treatment on soluble compounds from Australian coal. *Fuel* **257**: e116071.
DOI: <https://doi.org/10.1016/j.fuel.2019.116071>
- Zhang J. & Liang Y.N. (2017). Evaluating approaches for sustaining methane production from coal through biogasification. *Fuel* **202**: 233–240.
DOI: <https://doi.org/10.1016/j.fuel.2017.04.037>
- Zhang J., Liang Y.N., Pandey R. & Harpalani S. (2015). Characterizing microbial communities dedicated for conversion of coal to methane in situ and ex situ. *International Journal of Coal Geology* **146**: 145–154.
DOI: <https://doi.org/10.1016/j.coal.2015.05.001>

Link to download supplementary data:

<https://jnsfsl.sljol.info/articles/10.4038/jnsfsr.v51i1.10779/galley/7265/download/>

RESEARCH ARTICLE

Mathematical Modelling

Analyzing the effects of quarantine, isolation, and vaccination on the spread of COVID-19 via a mathematical model

LW Somathilake

Department of Mathematics, Faculty of Science, University of Ruhuna, Matara, Sri Lanka.

Submitted: 09 September 2021; Revised: 25 July 2022; Accepted: 26 August 2022

Abstract: The main COVID-19 control strategies presently practiced are maintaining social distancing, quarantining suspected exposures, and isolating infectious people. In this paper, a deterministic compartmental mathematical model is proposed considering these three control strategies. Based on the proposed model the effect of vaccination on the suppression of the disease is discussed. Critical vaccination rate and vaccinated population size relevant to disease suppression are determined based on the proposed mathematical model. Different forms of the most used key term in infectious disease modelling, reproduction number, are determined relevant to the proposed model. Sensitivity analysis of the reproduction numbers is done to identify model parameters mostly affecting the spread of the disease. Based on the reproduction number of the model disease controlling parameter regions are determined and graphical representations of those parameter regions are presented. Based on the results of the proposed mathematical model, it is observed that earlier implementation of the vaccination process is helpful to better control the disease. However, it takes considerable time to invent successful vaccinations for newly out-breaking diseases like COVID-19. Therefore, it took considerable time to start the vaccination process for COVID-19. It is observed that after starting a vaccination process at a particular rate it should continue until the vaccinated population reaches a critical size.

Keywords: COVID-19, compartmental models, critical vaccination rate, disease control strategies, disease modelling, sensitivity Index.

INTRODUCTION

COVID-19 is a disease due to a virus named severe acute respiratory syndrome coronavirus 2 (SARS-COV-2 virus). It originated in Wuhan city China in late 2019, and spread throughout the world very rapidly. According to the World Health Organization (WHO) COVID-19 was reported to WHO on December 31, 2019. WHO declared the COVID-19 outbreak to be a global health emergency on January 30, 2020. Also, it declared COVID-19 a global pandemic on March 11, 2020. Maintaining social distancing, quarantining exposures, and isolating infectious people were the main control strategies until successful vaccinations were invented for the disease. The role of a vaccine is to prevent susceptible people from being infected for a time period or for their lifetime. However, according to WHO (2021a), the presently available vaccines for COVID-19 do not have fully immunizing ability but prevent people from getting seriously ill or dying from COVID-19. According to WHO, there is no confirmation about the full effectiveness of the vaccines in controlling COVID-19. Therefore, though vaccinated, people

* Corresponding author (lwsoma@gmail.com; <https://orcid.org/0000-0002-7276-1357>)



This article is published under the Creative Commons CC-BY-ND License (<http://creativecommons.org/licenses/by-nd/4.0/>). This license permits use, distribution and reproduction, commercial and non-commercial, provided that the original work is properly cited and is not changed in anyway.

need to take preventive measures (WHO, 2021c). The WHO updates the COVID-19 vaccine database regularly twice a week. According to updates on 17 June 2021, there are 287 total candidate vaccines and among these 102 are in the clinical phase and 185 are in the pre-clinical phase (WHO, 2021b). Recently, several kinds of vaccines were being developed by several countries. The WHO evaluated vaccines for COVID-19 by 3rd June 2021 are AstraZeneca/Oxford vaccine, Johnson and Johnson, Moderna, Pfizer/BionTech, Sinopharm, and Sinovac. Presently vaccines play an important role in avoiding serious illnesses due to COVID-19 and reducing the death toll.

Mathematical models are helpful in analyzing and forecasting the spread of infectious diseases and those results are useful for disease management policymakers and healthcare sectors to make their decisions on disease management processes. This paper proposes a mathematical model for the control process of COVID-19 by considering the control strategies quarantine, isolation, and vaccination. For this model seven population sub classes susceptible (S), exposed (E), quarantined (Q), infectious (I), isolated (J), removed (R) and vaccinated (V) are taken into account (SEQIJRV models). Several studies on mathematical models for infectious diseases considering vaccination factors are reported. SIR models with vaccinations (SIRV models) for infectious diseases are reported by Ledzewicz & Schättler (2011), and Chanprasopchai *et al.* (2018). Chanprasopchai *et al.* (2018) proposed an SIR mathematical model for dengue fever and the effect of the dengue vaccine was discussed. Optimal control analysis of an SIR model with vaccination and treatment was done by Ledzewicz & Schättler (2011). In that paper, an optimal strategy in terms of combined efforts of vaccination and treatment, such that the disease-specific death and the cost of vaccination and treatments are minimized, is described. An SIQR-type mathematical model for the spread of diseases considering vaccination, elimination, and quarantine strategies was proposed by Ma *et al.* (2018) and the model analyzed theoretically and numerically.

A mathematical model for the Ebola virus was proposed by Ahmad *et al.* (2016) considering quarantine, hospitalization, and vaccination components. The effect of the pulse vaccine strategy on the control of infectious disease was discussed by Shulgin *et al.* (1998). SEIR models with vaccinations (SEIRV models) were reported by Sun & Hsieh (2010), Biswas *et al.* (2014), d'Onofrio (2002), and Ghostine *et al.* (2021). An SEIR model with vaccination strategy was investigated by Biswas *et al.* (2014). The stability properties of the pulse vaccination strategy were discussed by d'Onofrio (2002) based on an SEIR epidemic model. The effects of the introduction of constraints for state variables on optimal control problem was studied by Ghostine *et al.* (2021) based on an SEIR model with vaccination. A mathematical model for Ebola virus disease was discussed by Ahmad *et al.* (2016) considering quarantine, hospitalization, and vaccination components. An SEQIJR mathematical model for the severe acute respiratory syndrome (SARS) was reported by Gumel *et al.* (2004). In that paper, the authors have examined the impact of isolation and quarantine on the control of SARS outbreaks. An extension of that model considering the imperfect vaccine effect was reported by Safi & Gumel (2011) and numerical and analytical studies of the model have been done by the authors. An SIQR type mathematical model for the spread of diseases considering vaccination, elimination, and quarantine strategies was proposed by Ma *et al.* (2018) who analyzed the model theoretically and numerically. A mathematical model considering quarantine, hospitalization, and vaccination components was proposed by Ahmad *et al.* (2016) for the Ebola virus. In that paper, their proposed model is used to predict resource utilization for disease control and the effectiveness of vaccination on infected populations, and the most sensitive parameters which effectively contribute to changing the disease dynamics are identified. Different types of deterministic compartmental mathematical models for COVID-19 for different purposes, such as parameter estimations Tang *et al.* (2020) & Anastassopoulou *et al.* (2020), studying the effects of control strategies Mishra *et al.* (2020), and predictions Agarwal & Jhaharia (2021).

MATERIAL AND METHODS

This section proposes a deterministic compartmental mathematical model for COVID-19 considering control strategies social distancing, quarantining, isolation, and vaccination.

Proposed mathematical model

A sketch for the transfer behaviour between compartments of the proposed model are shown in the Figure 1. In this figure *S*, *E*, *Q*, *I*, *J*, *R*, *V* and *M* represent susceptible, exposed, quarantined, infectious, isolated, recovered, vaccination and total population sizes respectively.

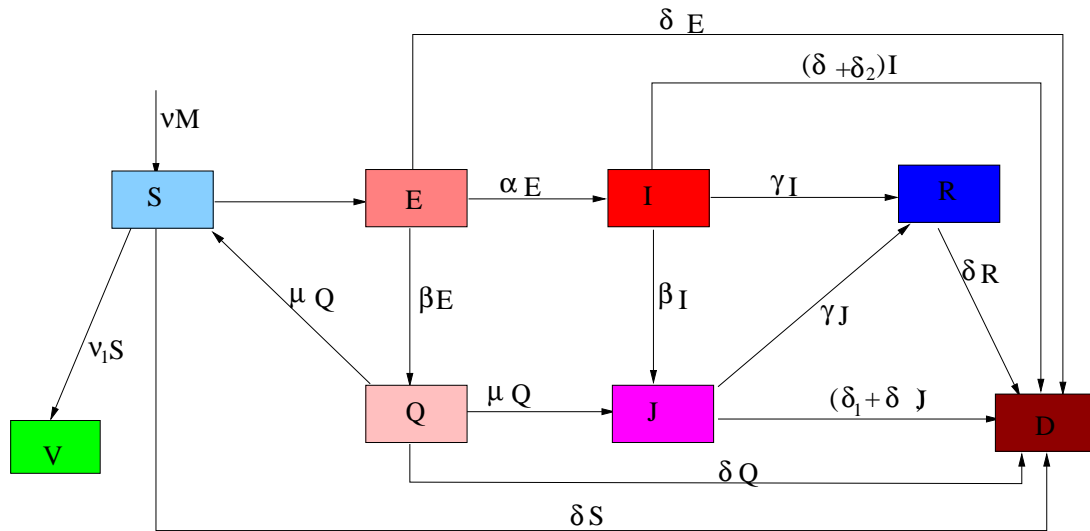


Figure 1: Schematic flow diagram for the SEQIJRV model.

Considering the schematic flow diagram in Figure 1, an SEQIJRV type mathematical model can be formulated as follows:

$$\begin{aligned}
 \frac{dS}{dt} &= vM - \sigma v_1 S - \alpha_1 \frac{(I + \epsilon_e E + \epsilon_q Q + \epsilon_j J)}{M} S - (v_1 + \delta_2) S + \mu_2 Q, \\
 \frac{dE}{dt} &= \alpha_1 \frac{(I + \epsilon_e E + \epsilon_q Q + \epsilon_j J)}{M} S - (\alpha_2 + \beta_1 + \delta_2) E, \\
 \frac{dQ}{dt} &= \beta_1 E - (\delta_2 + \mu_1 + \mu_2) Q, \\
 \frac{dI}{dt} &= \alpha_2 E - (\gamma_1 + \beta_2 + \delta_1 + \delta_2) I, \\
 \frac{dJ}{dt} &= \beta_2 I + \mu_1 Q - (\gamma_2 + \delta_1 + \delta_2) J, \\
 \frac{dR}{dt} &= \gamma_1 I + \gamma_2 J - \delta_2 R, \\
 \frac{dV}{dt} &= \sigma v_1 S - \delta_2 V.
 \end{aligned}
 \tag{1}$$

The initial conditions for the model are of the form

$$S(0) > 0, E(0) \geq 0, Q(0) \geq 0, I(0) \geq 0, J(0) \geq 0, R(0) \geq 0, V(0) \geq 0.
 \tag{2}$$

Table 1: Parameters interpretation of the proposed mathematical model

Parameter	Description
ν	Natural birth rate.
ν_1	Vaccination rate.
σ	Efficiency of the vaccination.
α_1	The transmission coefficient from the susceptible class to the exposed class.
α_2	The transfer rate from the exposed class to the infectious class.
β_1	The transfer rate from the exposed class to the quarantined class.
β_2	The transfer rate from the infected class to the isolated class.
μ_1	The transfer rate from the quarantined class to the isolated class.
μ_2	The transfer rate from the quarantined class to the susceptible class.
γ_1	The transfer rate from the infected class to the recovered class.
γ_2	The transfer rate from the quarantined class to the recovered class.
$\epsilon_e, \epsilon_q, \epsilon_j, \delta$	Exposing weights for the disease due to the classes E, Q and J respectively. Disease-specific and natural death rates respectively.

Equilibrium points of the system

There are two equilibrium points of the system:

$$\mathcal{E}_1^* \equiv (S_1^*, E_1^*, Q_1^*, I_1^*, J_1^*, R_1^*, V_1^*) \equiv \left(\frac{M\nu}{\delta_2 + \nu_1}, 0, 0, 0, 0, 0, \frac{M\nu\nu_1}{\delta_2(\delta_2 + \nu_1)} \right) \text{ and } \mathcal{E}_2^* \equiv (S_2^*, E_2^*, Q_2^*, I_2^*, J_2^*, R_2^*, V_2^*).$$

Here,

$$I_2^* = \frac{\alpha_2 A_2 M (A_2 (A_4 (\alpha_1 \nu (\alpha_2 + A_3 \epsilon_e) - A_1 A_3 (\delta_2 + \nu_1 \sigma)) + \alpha_1 \alpha_2 \beta_2 \nu \epsilon_j) + \alpha_1 A_3 \beta_1 \nu (A_4 \epsilon_q + \mu_1 \epsilon_j))}{\alpha_1 A_3 (A_1 A_2 - \beta_1 \mu_2) (A_2 (A_4 (\alpha_2 + A_3 \epsilon_e) + \alpha_2 \beta_2 \epsilon_j) + A_3 \beta_1 (A_4 \epsilon_q + \mu_1 \epsilon_j))},$$

$$S_2^* = \frac{\alpha_2 A_2 \nu M + A_3 \beta_1 \mu_2 I_2^* + A_1 A_2 A_3 (-I_2^*)}{\alpha_2 A_2 (\delta_2 + \nu_1 \sigma)}, E_2^* = \frac{A_3 I_2^*}{\alpha_2}, Q_2^* = \frac{A_3 \beta_1 I_2^*}{\alpha_2 A_2}, J_2^* = \frac{I_2^* (\alpha_2 A_2 \beta_2 + A_3 \beta_1 \mu_1)}{\alpha_2 A_2 A_4},$$

$$R_2^* = \frac{\gamma_1 I_2^* + \gamma_2 J_2^*}{\delta_2}, \text{ and } V_2^* = \frac{\sigma \nu_1 S_2^*}{\delta_2}. \text{ Here, } A_1 = \alpha_2 + \beta_1 + \delta_2, A_2 = \delta_2 + \mu_1 + \mu_2, A_3 = \beta_2 + \gamma_1 + \delta_1 + \delta_2, \text{ and}$$

$A_4 = \gamma_2 + \delta_1 + \delta_2$. Since $A_1 A_2 > \beta_1 \mu_2$, I_2^* is positive if and only if

$$\frac{\nu \alpha_1 (A_2 (A_4 (\alpha_2 + A_3 \epsilon_e) + \alpha_2 \beta_2 \epsilon_j) + A_3 \beta_1 (A_4 \epsilon_q + \mu_1 \epsilon_j))}{A_1 A_2 A_3 A_4 (\delta_2 + \nu_1 \sigma)} > 1 \implies \frac{\nu}{(\delta_2 + \nu_1 \sigma)} \mathcal{R}_0 > 1.$$

Here,

$$\mathcal{R}_0 = \frac{\alpha_1 (A_2 (A_4 (\alpha_2 + A_3 \epsilon_e) + \alpha_2 \beta_2 \epsilon_j) + A_3 \beta_1 (A_4 \epsilon_q + \mu_1 \epsilon_j))}{A_1 A_2 A_3 A_4}$$

$$= \frac{\alpha_1}{A_1} \left(\epsilon_e \delta_2 + \frac{\alpha_2}{A_3} + \frac{\beta_1 \epsilon_q}{A_2} + \frac{\epsilon_j \beta_1 \mu_1}{A_2 A_4} + \frac{\epsilon_j \alpha_2 \beta_2}{A_3 A_4} \right)$$

This implies that, the positive endemic equilibrium \mathcal{E}_2^* exists if and only if $\frac{\nu}{(\delta_2 + \nu_1 \sigma)} \mathcal{R}_0 > 1$. Also, if $\mathcal{R}_0 < 1$ then the disease free equilibrium state \mathcal{E}_1^* is stable. If $\mathcal{R}_0 > 1$ then the endemic equilibrium point is stable and the disease free equilibrium point becomes unstable.

Non-negativity of the solutions of the system

Let $M(t) = S(t) + E(t) + Q(t) + I(t) + J(t) + R(t) + V(t)$ be the total population size at time t . Summing up all the equations of the system (1) result in

$$\frac{dM}{dt} = M(v - \delta_2) - (u + v)\delta_1 \geq M(v - \delta_2 - \delta_1).$$

$M(t) \geq M(0)e^{(v-\delta_1-\delta_2)t}$, where $M(0)$ is the initial total population size.

Also $\frac{dM}{dt} \leq M(v - \delta_2) \implies M(t) \leq M(0)e^{(v-\delta_2)t}$.

$$M(0)e^{(v-\delta_1-\delta_2)t} \leq M(t) \leq M(0)e^{(v-\delta_2)t}.$$

Therefore at any finite time the total population size is bounded. From the second equation of the system (1) we have the inequality

$$\frac{dE}{dt} \geq -(\alpha_2 + \beta_1 + \delta_2)E.$$

$$\implies E(t) \geq E(0)e^{-(\alpha_2+\beta_2+\delta_2)t}.$$

This implies that $E(t)$ is non-negative. Similarly it can be shown that $Q(t), I(t), J(t), R(t)$ and $V(t)$ are non-negative. Since the total population size is non-negative $S(t)$ should also be non-negative.

Basic reproduction number and the effective reproduction number

The basic reproduction number (\mathcal{R}_0): The basic reproduction number of an infectious disease is a measure of the transmissibility of the disease. \mathcal{R}_0 defines as the average number of new cases produced by an infected individual during the individual’s infectious period in the absence of any prevention strategies. A measure for the average number of new cases produced by an infected individual when control strategies are implemented can be derived based on mathematical models formulated for the disease transmission process. Expressions for this reproduction number depend on the parameters of the mathematical model. One measure of the efficiency of a control strategy is its ability to reduce \mathcal{R}_0 . In order to control the spread of a disease, it is very important to take action to implement control strategies to gain the condition $\mathcal{R}_0 < 1$.

The effective reproduction number (\mathcal{R}_e): . In general the whole population would not be susceptible to an infectious disease. For some infectious diseases, infectious individuals become immunized for life to that disease. Also, individuals become partially or fully immunized by vaccinations. Therefore, not all contacts will become infected in such populations and an average number of secondary cases per infectious case will be lower than the basic reproduction number. The effective reproductive number (\mathcal{R}_e) is the average number of secondary cases per infectious individual in a population made up of both susceptible and non-susceptible hosts (Arenas *et al.*, 2020). If $\mathcal{R}_e > 1$, then the disease persists (secondary cases will increase) while disease dies out (secondary cases decrease) if $\mathcal{R}_e < 1$. When $\mathcal{R}_e = 1$, secondary cases remains unchanged. The effective reproduction number can be defined as the product of the basic reproductive number and the fraction of the host population that is susceptible (r). That is

$$r = \frac{\text{Susceptible population size}}{\text{Total population size}} \text{ and } \mathcal{R}_e = r\mathcal{R}_0.$$

If it is assumed that all the vaccinated people are immunized then $r = \frac{M - V}{M}$ and if the efficiency of the vac-

ination is σ then $r = \frac{M - \sigma V}{M}$, where V is the total vaccinated population size. For some infectious diseases recovered individuals become fully immunized for their lifetime. In such cases

$$r = \frac{\text{Total population size} - \text{Total recovered population size}}{\text{Total population size}} = \frac{(M - R)}{M}.$$

Time-dependent effective reproduction number ($R_e(t)$): The time-dependent effective reproduction number can be defined as

$$\mathcal{R}_e(t) = \mathcal{R}_0 \frac{(\text{Susceptible population size at time } t)}{\text{Total population size}} = \mathcal{R}_0 \frac{S(t)}{M}$$

Basic reproduction number of the model

The basic reproduction number of the proposed model is calculated using the *next-generation matrix* (NGM) method (Diekmann *et al.*, 2010, Gumel *et al.*, 2004, Yang, 2014). The infected subsystem (see Diekmann *et al.* (2010)) of the model system (1) is:

$$\begin{aligned} \frac{dE}{dt} &= \alpha_1 \frac{(I + \epsilon_E E + \epsilon_Q Q + \epsilon_J J)}{M} S - (\alpha_2 + \beta_1 + \delta_2) E \\ \frac{dQ}{dt} &= \beta_1 E - (\delta_2 + \mu_1 + \mu_2) Q \\ \frac{dI}{dt} &= \alpha_2 E - (\gamma_1 + \beta_2 + \delta_1 + \delta_2) I \\ \frac{dJ}{dt} &= \beta_2 I + \mu_1 Q - (\gamma_2 + \delta_1 + \delta_2) J \end{aligned} \tag{3}$$

In the process of calculating \mathcal{R}_0 using the next-generation method, the first step is to linearize the infected subsystem about the disease-free equilibrium point \mathcal{E}_1^* . The Jacobian matrix of the linearized infectious subsystem for disease-free equilibrium is

$$J = \begin{pmatrix} -A_1 + \frac{\alpha_1 v \epsilon_e}{\delta_2 + v_1 \sigma} & \frac{\alpha_1 v \epsilon_q}{\delta_2 + v_1 \sigma} & \frac{\alpha_1 v}{\delta_2 + v_1 \sigma} & \frac{\alpha_1 v \epsilon_j}{\delta_2 + v_1 \sigma} \\ \beta_1 & -A_2 & 0 & 0 \\ \alpha_2 & 0 & -A_3 & 0 \\ 0 & \mu_1 & \beta_2 & -A_4 \end{pmatrix}.$$

Now decompose the Jacobian matrix into two sub-matrices called the transmission matrix (see Diekmann *et al.* (2010)), J_T (*the production of new infections*) and transition matrix (see Diekmann *et al.* (2010)), J_M (*the changes in the state*). Then

$$J_T = \begin{pmatrix} \frac{\alpha_1 v \epsilon_e}{\delta_2 + v_1 \sigma} & \frac{\alpha_1 v \epsilon_q}{\delta_2 + v_1 \sigma} & \frac{\alpha_1 v}{\delta_2 + v_1 \sigma} & \frac{\alpha_1 v \epsilon_j}{\delta_2 + v_1 \sigma} \\ 0 & 0 & 0 & 0 \\ 0 & 0 & 0 & 0 \\ 0 & 0 & 0 & 0 \end{pmatrix} \text{ and } J_M = \begin{pmatrix} -A_1 & 0 & 0 & 0 \\ \beta_1 & -A_2 & 0 & 0 \\ \alpha_2 & 0 & -A_3 & 0 \\ 0 & \mu_1 & \beta_2 & -A_4 \end{pmatrix}.$$

The reproduction number for the disease-free equilibrium point, \mathcal{R}_{df} , is the maximum eigenvalue of the matrix $-J_T J_M^{-1}$. \mathcal{R}_{df} can be derived in the form:

$$\mathcal{R}_{df} = \frac{v\alpha_1}{A1(\delta_2 + v_1\sigma)} \left(\epsilon_e\delta_2 + \frac{\alpha_2}{A_3} + \frac{\beta_1\epsilon_q}{A_2} + \frac{\epsilon_j\beta_1\mu_1}{A_2A_4} + \frac{\epsilon_j\alpha_2\beta_2}{A_3A_4} \right).$$

The basic reproduction number of the model can be obtained by considering the fact that the susceptible population size is equal to the total population size. In order to keep the susceptible population size unchanged, the death rate and birth rate should be equal in the case of no vaccinations. That is \mathcal{R}_0 is the value of \mathcal{R}_{df} when $v = \delta_2$ and $v_1 = 0$. Then

$$\mathcal{R}_0 = \frac{\alpha_1}{A1} \left(\epsilon_e\delta_2 + \frac{\alpha_2}{A_3} + \frac{\beta_1\epsilon_q}{A_2} + \frac{\epsilon_j\beta_1\mu_1}{A_2A_4} + \frac{\epsilon_j\alpha_2\beta_2}{A_3A_4} \right).$$

In other words $\mathcal{R}_{df} = \frac{v}{(\delta_2 + v_1\sigma)}\mathcal{R}_0$. The time-dependent effective reproduction number of the model, subject to the assumption that recovered people are not immunized and the effectively vaccinated population is fully

immunized is $\mathcal{R}_e(t) = \mathcal{R}_0 \times \frac{(M - \sigma V(t))}{M}$.

If the recovered people are also immunized then the corresponding effective reproduction number is

$$\mathcal{R}_e(t) = \mathcal{R}_0 \times \frac{(M - \sigma V(t) - R(t))}{M}.$$

Sensitivity analysis

The sensitivity index provides information about the importance of each model parameter to a state variable that depends on the model parameters. The sensitivity index of a state variable (say \mathcal{V}) which depends on the model parameters is a measure of the relative change in \mathcal{V} when a parameter (say p) changes and it is defined as $\mathcal{S}_p^{\mathcal{V}} = \left(\frac{\partial \mathcal{V}}{\partial p} \right) \frac{p}{\mathcal{V}}$ (Siriprapaiwan *et al.*, 2018, Bajiya *et al.*, 2020). Sensitivity analysis is useful in determining parameters that have high impacts on \mathcal{V} . If a given change in a model parameter will cause a large change in the \mathcal{V} then it is said that the parameter is highly sensitive. The sensitivity index determines whether each parameter is sensitive (quite responsive), unit sensitive, or insensitive (not very responsive). The sensitivity index may be negative or positive. If the sensitivity index is positive (or negative) then the increases of the parameter increases (or decreases) the \mathcal{V} . The unitary sensitivity index implies that a change in the parameter leads to an equal change of the state variable \mathcal{V} .

Sensitivity index of the basic reproduction number \mathcal{R}_0

The initial disease transmission strength is related to the basic reproduction number. Therefore, sensitivity analysis of the basic reproduction number is helpful to identify model parameters which have a greater effect on the initial disease transmission. Identifying those parameters is helpful to take necessary actions to suppress the disease transmission. The sensitivity index of the basic reproduction number, \mathcal{R}_0 , relative to a model parameter, θ , is:

$$\begin{aligned} \mathcal{S}_\theta^{\mathcal{R}_0} &= \frac{\partial \mathcal{R}_0}{\partial \theta} \frac{\theta}{\mathcal{R}_0}. \text{ Accordingly } \mathcal{S}_{\alpha_1}^{\mathcal{R}_0} = 1, \mathcal{S}_{\alpha_2}^{\mathcal{R}_0} = \frac{\alpha_1\alpha_2}{A_1\mathcal{R}_0} \left(\frac{1}{A_3} + \frac{\epsilon_j\beta_2}{A_3A_4} \right) - \frac{\alpha_2}{A_1}, \mathcal{S}_{\epsilon_j}^{\mathcal{R}_0} = \frac{\alpha_1\epsilon_j}{A_1\mathcal{R}_0} \left(\frac{\beta_1\mu_1}{A_2A_4} + \frac{\beta_2\alpha_2}{A_3A_2} \right), \\ \mathcal{S}_{\beta_1}^{\mathcal{R}_0} &= \frac{\alpha_1\beta_1}{A_1\mathcal{R}_0} \left(\frac{\epsilon_q}{A_2} + \frac{\epsilon_j\mu_1}{A_2A_4} \right) - \frac{\beta_1}{A_1}, \mathcal{S}_{\beta_2}^{\mathcal{R}_0} = \frac{\alpha_1\beta_2\alpha_2}{A_1A_3\mathcal{R}_0} \left(\frac{\epsilon_j}{A_4} - \frac{\epsilon_j\beta_2}{A_3A_4} - \frac{1}{A_3} \right), \mathcal{S}_{\mu_1}^{\mathcal{R}_0} = \frac{\alpha_1\mu_1\beta_1}{A_1A_2\mathcal{R}_0} \left(\frac{\epsilon_j}{A_4} - \frac{\epsilon_j\mu_1}{A_2A_4} - \frac{\epsilon_q}{A_2} \right), \\ \mathcal{S}_{\mu_2}^{\mathcal{R}_0} &= -\frac{\alpha_1\mu_1\beta_1}{A_1A_2^2\mathcal{R}_0} \left(\epsilon_q + \frac{\epsilon_j\mu_1}{A_4} \right), \mathcal{S}_{\epsilon_e}^{\mathcal{R}_0} = \frac{\alpha_1\epsilon_e}{A_1\mathcal{R}_0}, \mathcal{S}_{\epsilon_q}^{\mathcal{R}_0} = \frac{\alpha_1\beta_1\epsilon_q}{A_1A_2\mathcal{R}_0}, \mathcal{S}_{\gamma_1}^{\mathcal{R}_0} = -\frac{\alpha_1\gamma_1}{A_1A_3^2\mathcal{R}_0} \left(\alpha_2 + \frac{\beta_2\alpha_2\epsilon_j}{A_4} \right), \text{ and} \\ \mathcal{S}_{\gamma_2}^{\mathcal{R}_0} &= -\frac{\alpha_1\gamma_2\epsilon_j}{A_4^2\mathcal{R}_0} \left(\frac{\beta_1\mu_1}{A_2} + \frac{\beta_2\alpha_2}{A_3} \right). \end{aligned}$$

Since $\mathcal{R}_{df} = \frac{\nu}{(\delta_2 + \nu_1 \sigma)} \mathcal{R}_0$, the sensitivity indices of \mathcal{R}_{df} against all the parameters except ν_1 are same as that of \mathcal{R}_0 . Also, $\mathcal{S}_{\nu_1}^{\mathcal{R}_{df}} = \frac{-\sigma \nu_1}{\delta_2 + \nu_1 \sigma}$. In the numerical simulations of the paper, parameters are chosen based on some assumptions. Those assumptions and relevant parameter values are tabulated in Table 2.

Table 2: Parameter values relevant to the assumptions/facts

Assumptions/facts	Parameter value relevant to the assumption (unit: per day)
The natural death rate and birth rate in Sri Lanka are 6.818 and 15.135 per thousand per year respectively	$\delta_2 = 6.818 / (365 \times 1000)$, $\nu = 15.135 / (365 \times 1000)$
Expose rate of COVID-19 is 0.19.	$\alpha_1 = 0.19$.
10% of the exposed people are quarantined and their average staying time in the exposed class is 2 days.	$\beta_1 = 0.1 / 2 = 0.05$.
90% of the exposed people may infect and the average staying time in the exposed class is 5 days (it is assumed incubation period of COVID-19 is 5 days).	$\alpha_2 = 0.90 / 5 = 0.18$.
5% of the quarantined people are infected and transferred to the isolated class and their average staying time in the quarantined class is 4 days.	$\mu_1 = 0.05 / 4$
During the 14 days quarantined period 95% of the quarantined class remain uninfected and they are transferred to the susceptible class	$\mu_2 = 0.95 / 14$
90% of the infectious people and 94% of isolated people recover and their average staying time in the infectious and isolated classes is 10 days.	$\gamma_1 = 0.9 / 10 = 0.09$ and $\gamma_2 = 0.94 / 10 = 0.094$.
3% of each infectious and isolated class died due to Covid-19 and their staying period in the respective class is 14 days.	$\delta_1 = 0.03 / 14$.
Infection transmission weights from classes E, Q, and J to the class S are 10%, 5% and 1% respectively.	$\epsilon_e = 0.1$, $\epsilon_q = 0.05$ and $\epsilon_j = 0.01$.
10% of the exposed people are quarantined and their average staying period in the exposed classes is 2 days.	$\beta_1 = 0.1 / 2 = 0.05$.
9% of the identified infectious people are hospitalized(isolated) and their average staying time in the infectious class is 3 days.	$\beta_3 = 0.09 / 3 = 0.03$.
The effective contact rate is 0.18.	$\alpha_1 = 0.18$.
The vaccination rate is 0.00002.	$\nu_1 = 0.00002$.

RESULTS AND DISCUSSION

This section discusses the effect of the control strategies, social distancing, quarantining, isolation and vaccination on the spread of COVID-19, based on the results obtained by the proposed mathematical model.

Sensitivity Analysis

This section explains the sensitivity of model parameters on the model’s state variables \mathcal{R}_{df} and endemic infectious population sizes I_2^* and J_2^* .

Table 3: Sensitivity indices of \mathcal{R}_{df} relevant to the model parameters

Parameter	Sensitivity indices of \mathcal{R}_{df}	Parameter	Sensitivity indices of \mathcal{R}_{df}	Parameter	Sensitivity indices of \mathcal{R}_{df}
α_1	1	β_1	-0.19755	μ_2	-0.016734
γ_1	-0.676366	α_2	0.135520	ϵ_j	0.0033575
ν_1	-0.461368	ϵ_e	0.0621130	γ_2	-0.003282
β_2	-0.22260	ϵ_q	0.0193196	μ_1	-0.00258

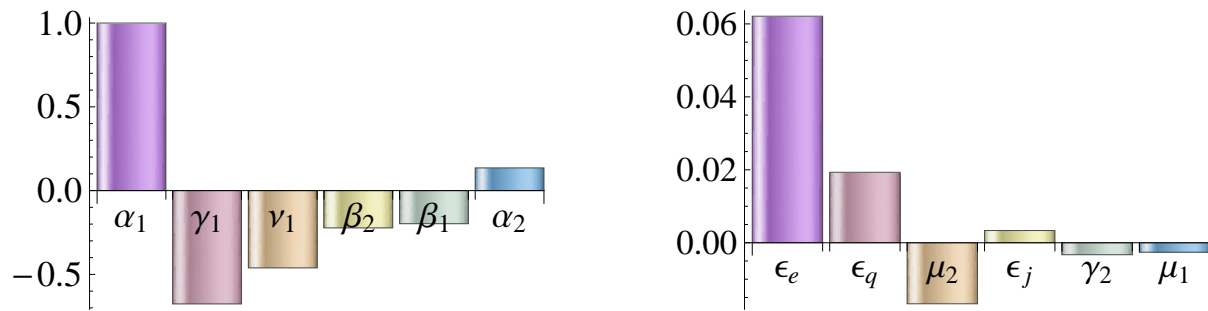


Figure 2: Graphical interpretation of sensitivity indices of \mathcal{R}_{df} .

Sensitivity of \mathcal{R}_{df}

Sensitivity analysis of \mathcal{R}_{df} is helpful to identify the model parameters which have a greater effect on the disease transmission when vaccination is started. For the above set of parameters $\mathcal{R}_{df} = 1.61314$. The sensitivity indices of \mathcal{R}_{df} is shown in Table 3. Graphical interpretation of the sensitivity indices of \mathcal{R}_{df} is shown in Figure 2.

Since the sensitivity indices of \mathcal{R}_{df} against $\alpha_1, \alpha_2, \epsilon_e, \epsilon_q,$ and ϵ_j are positive, \mathcal{R}_{df} increases as these parameters increase. \mathcal{R}_{df} decreases as the rest of the parameters increase since the corresponding sensitivity indices are negative. Also, the most sensitive parameter for \mathcal{R}_{df} is α_1 , and the least sensitive parameter is μ_1 for both \mathcal{R}_0 and \mathcal{R}_{df} . That is, the transmission rate from the susceptible class to the exposed class is the most dominant and the transmission rate from the quarantine class to the isolated class is the least effective parameter for the spread of the disease. In other words, maintaining social distancing and proper hygiene strategies are the most effective control strategy for controlling the spread of COVID-19. The next sensitive parameter for the \mathcal{R}_{df} is vaccination rate ν_1 for the considered set of parameters. Sensitivity indices of \mathcal{R}_{df} shown in Table 3 are arranged in decreasing order of their effectiveness. Since $S_{\alpha_1}^{\mathcal{R}_{df}} = 1$, a 10% increase (or decrease) in α_1 from the current value results in a 10% increase (or decrease) of \mathcal{R}_{df} . Also, since $S_{\nu_1}^{\mathcal{R}_{df}} = -0.461368$ a 10% increase of ν_1 ($0.00002 \times 10/100 = 0.000002$), results in a 4.6% decrease of \mathcal{R}_{df} . Similar interpretations can be given to other parameters.

Sensitivity of I_2^* and J_2^*

In the endemic equilibrium \mathcal{E}_2^* , especially I_2^* , and J_2^* are measures of the prevalence of the disease. Therefore, sensitivity analysis of I_2^* and J_2^* are helpful to identify more sensitive parameters on the disease prevalence. Sensitivity indices of I_2^* and J_2^* corresponding to parameter values are shown in the Table 4. Three consecutive more sensitive parameters of I_2^* and J_2^* are α_1, μ_2, ν_1 and $\alpha_1, \gamma_2, \beta_2$ respectively of the chosen set of parameters. Also, the third sensitive parameter for the total infectious population, $I_2^* + J_2^*$, is ν_1 . That is vaccination plays an important role in controlling the disease.

Table 4: Sensitivity indexes of I_2^* and J_2^* .

Parameter	Sensitivity index of			Parameter	Sensitivity index of		
	I_2^*	J_2^*	$(I_2^* + J_2^*)$		I_2^*	J_2^*	$(I_2^* + J_2^*)$
α_1	-1.4322	-1.4322	-1.4321	γ_1	-0.0552	0.0276	0.0136
α_2	-0.0784	-0.4393	-0.3780	γ_2	0.0351	-0.9424	-0.7762
β_1	0.2389	0.5998	0.5385	ϵ_e	-0.1605	-0.1605	-0.1605
β_2	-0.2069	0.7083	0.5527	ϵ_q	-0.4991	-0.4991	-0.4991
μ_1	-0.1879	0.1168	0.0651	ϵ_j	-0.0359	-0.0359	-0.0359
μ_2	0.6873	0.3826	0.4344	ν_1	0.6608	0.6608	0.6608

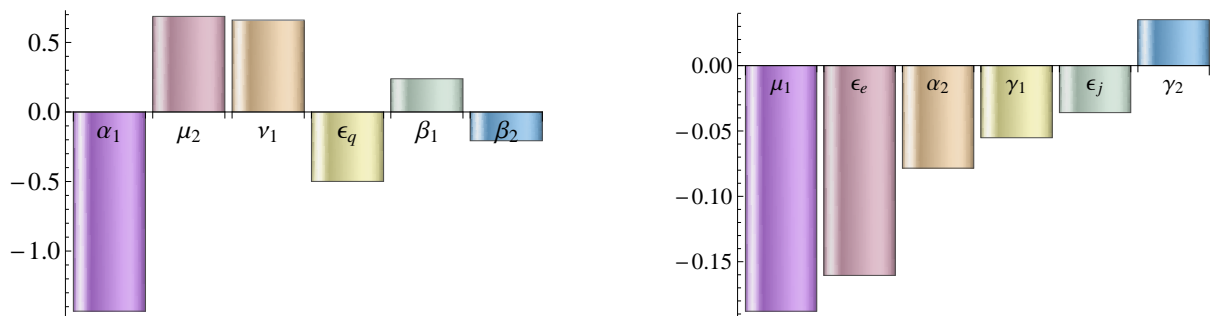


Figure 3: Graphical interpretation of sensitivity indices of I_2^* .

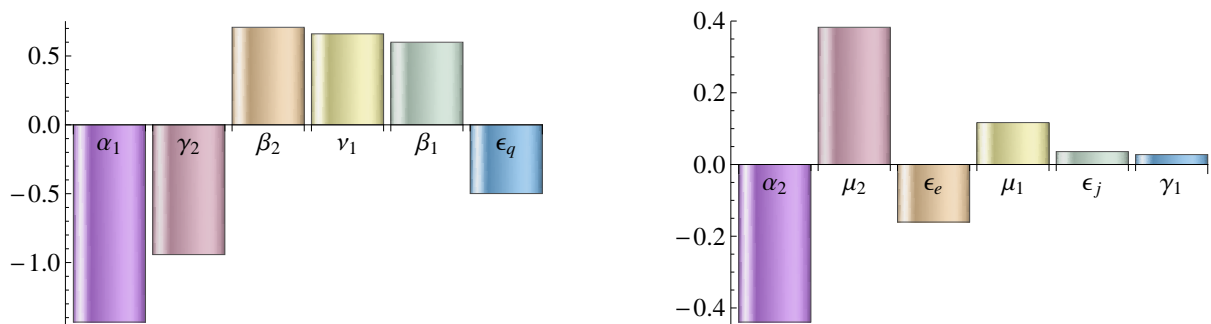


Figure 4: Graphical interpretation of sensitivity indices of J_2^* .

Identifying sufficient levels of control strategies in controlling the spread of a disease

Critical immunization population size

In order to prevent the disease, it is necessary to take actions to gain $\mathcal{R}_{ef} < 1$. Let V_c be the critical vaccinated population size. Then, $1 = \mathcal{R}_{ef} = \mathcal{R}_0 \frac{(M - V_c)}{M}$. That is $V_c = M \left(1 - \frac{1}{\mathcal{R}_0} \right)$. Suppose that the vaccination process is planned to complete within T_v days. Then it is needed to vaccinate a number of people $\lceil V_c/T_v \rceil$ per day to reach the disease dies-out level. If the health care sector's maximum vaccination capacity is V_0 per day then the vaccination campaign should continue $\lceil V_c/V_0 \rceil$ days to reach the disease dies-out level. Here, $\lceil x \rceil$ denotes the smallest integer greater than the real number x .

The effect of vaccination level and starting time

This section discusses the effect of vaccination level and vaccination starting time on the spread of the disease.

Critical immunization rate

Since $\mathcal{R}_{df} = \frac{v}{(\delta_2 + v_1\sigma)} \mathcal{R}_0$, the critical vaccination rate, v_{1c} satisfies

$$\frac{v}{(\delta_2 + v_{1c}\sigma)} \mathcal{R}_0 = 1. \text{ That is } v_{1c} = \frac{v\mathcal{R}_0 - \delta_1}{\sigma}.$$

Figures 5(a) and 5(b) shows the variation of percentage infectious and death population sizes when the vaccination strategy is started at different time levels, and 5 (c), and 5(d) shows the same for different strengths of vaccinations. For these simulations it is assumed that $\beta_1 = 0$, and $\beta_2 = 0$ and for Figures 5(a), 5(b), the vaccination rate, $v_1 = 0.001$. Also, the critical vaccination level for the considered set of parameters is $v_{1c} = 0.0000161147$.

According to Figures 5(a) and 5(b), the earlier vaccination process starts, the more helpful it is for the better control of the disease. According to Figures 5(c), and 5(d) we can conclude that there is no benefit in implementing a lesser vaccination strategy than v_{1c} in controlling the diseases since there is no significant decrease of death and infectious population sizes for implementing such control strategies (since infectious curves and death curves for $v < v_{1c}$ are almost overlapping). Vaccination strategies higher than v_{1c} help to control the disease and higher vaccination rates suppress the disease better. Figure 6 shows the variation of $\mathcal{R}_e(t)$ when vaccinations are applied at different time levels and when vaccination is started in different strengths. It is assumed that time is measured from the date of the first patient identified. Now we assume that the effective vaccinated population is fully immunized against the disease and any recovered people are not immunized. Then $\mathcal{R}_e(t) = \mathcal{R}_0 \frac{(M - V(t))}{M}$. Figure 6(a) and 6(b) shows the variation of $\mathcal{R}_e(t)$ against time for different levels of starting time of vaccination and different levels of vaccination rates respectively. The vaccination level for the results in Figure 6(a) is $v = 0.001$. The vaccination starting time for the results in Figure 6(b) is day 200. According to Figure 6(b) one can observe that $\mathcal{R}_e(t)$ reaches to one at a particular time, t_c , when $v_1 > v_{1c}$. Table 5 shows the t_c values for considered levels of v_1 . Approximately $(1 - \frac{1}{\mathcal{R}_0})100\% = 42\%$ people are vaccinated when $t = t_c$ at each vaccination level. The effect of vaccination on the reproduction number for the set of parameters shown in Table 2 is shown in Figure 7. According to this Figure, when the vaccination rate increases the reproduction number at the disease-free equilibrium point decreases and it reaches the critical value $\mathcal{R}_{df} = 1$ at $v_{1c} = 0.0000482191$. That is, for the chosen set of parameters, the vaccination rate should be increased up to v_{1c} to suppress the disease.

Figure 8 shows the $\mathcal{R}_{df} = 1$ surface against β_1 , β_2 and v_1 , that is the variation of v_{1c} against β_1 and β_2 . It can be observed that as β_1 and β_2 increase v_{1c} decreases. That is when quarantine and isolation rates increase the critical vaccination level decreases.

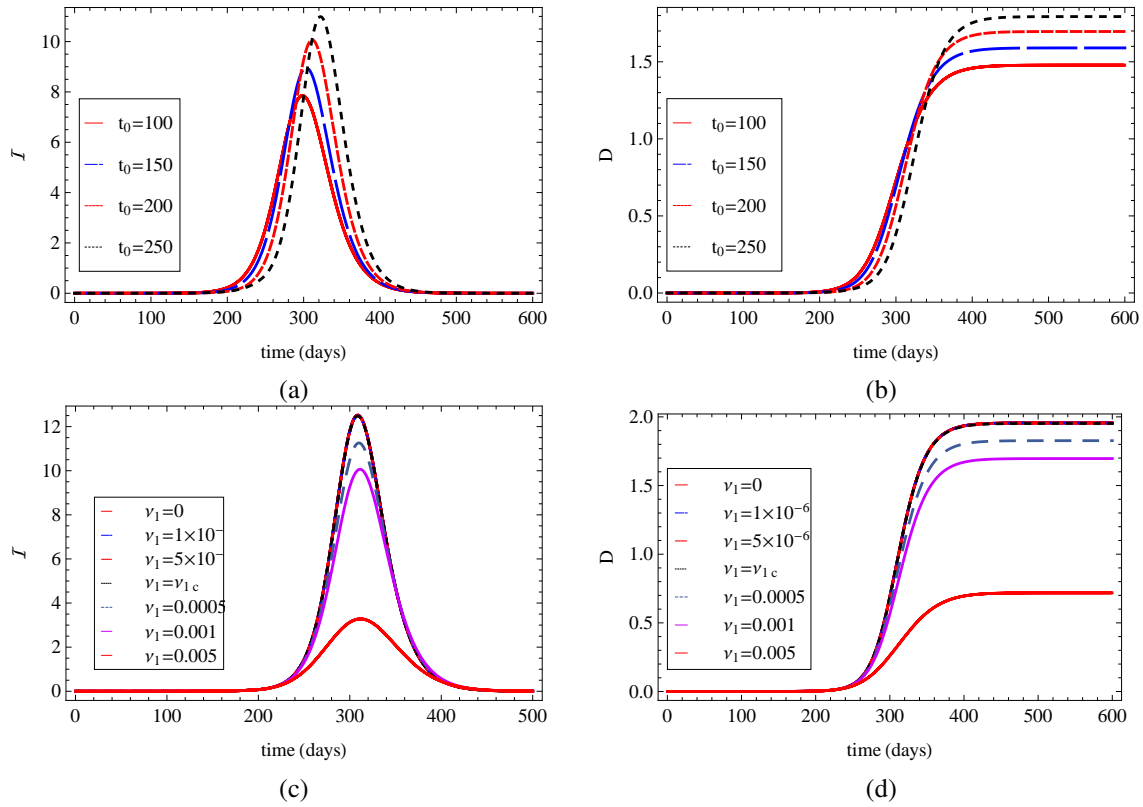


Figure 5: Variation of percentage infectious population size and death population size (a), (b): when vaccination starts at different time levels (t_0) and (c), (d): for different vaccination levels (v_1).

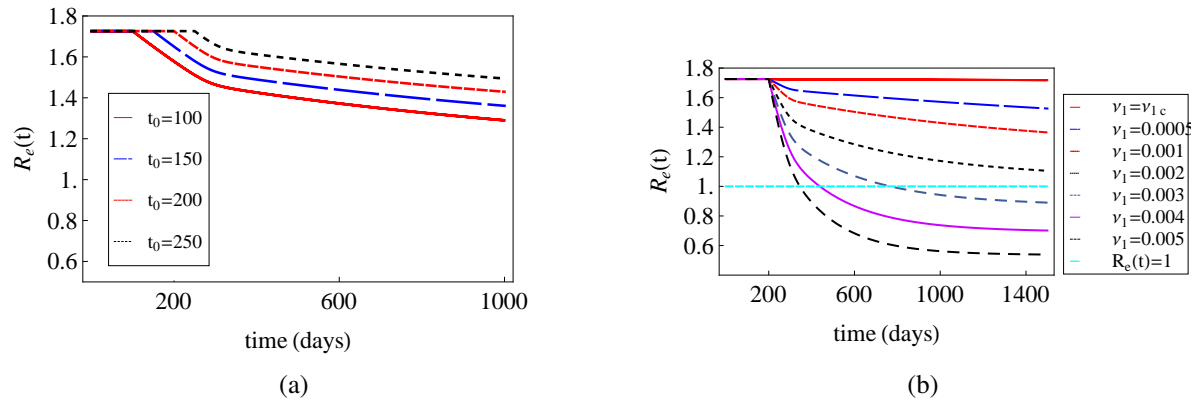


Figure 6: Variation of $\mathcal{R}_e(t)$ against time (a): when vaccination starts at different time and (b): for different vaccination levels.

Table 5: t_c correspond to v_1 .

v_1	0.002	0.003	0.004	0.005
t_c	≈ 6561	≈ 768	≈ 438	≈ 346

Table 6: Critical vaccination rates when both quarantine and isolation are applied, only one control strategy is applied and non of these control strategies is applied.

β_1	β_2	v_{1c}	β_1	β_2	v_{1c}
0.05	0.03	0.0000482191	0.05	0	0.0000707346
0	0.03	0.0000684917	0	0	0.0000980088

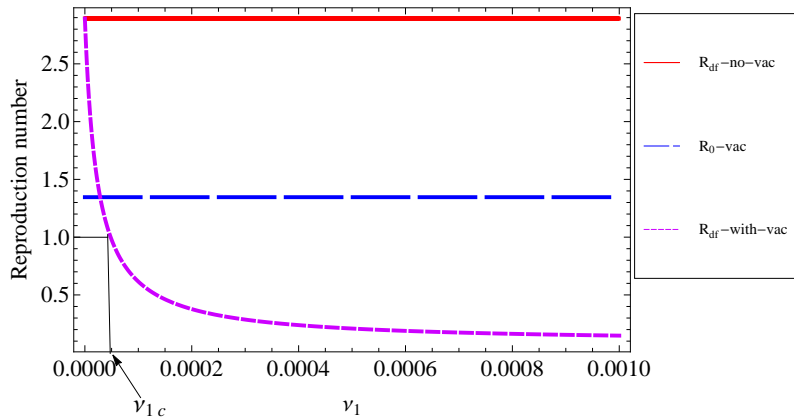


Figure 7: Variation of \mathcal{R}_{df} against v_1 . \mathcal{R}_0 -vac: Basic reproduction number considering vaccination. \mathcal{R}_{df} -no-vac: Disease-free reproduction number without vaccination. \mathcal{R}_{df} -with-vac: Disease-free reproduction number with vaccination.

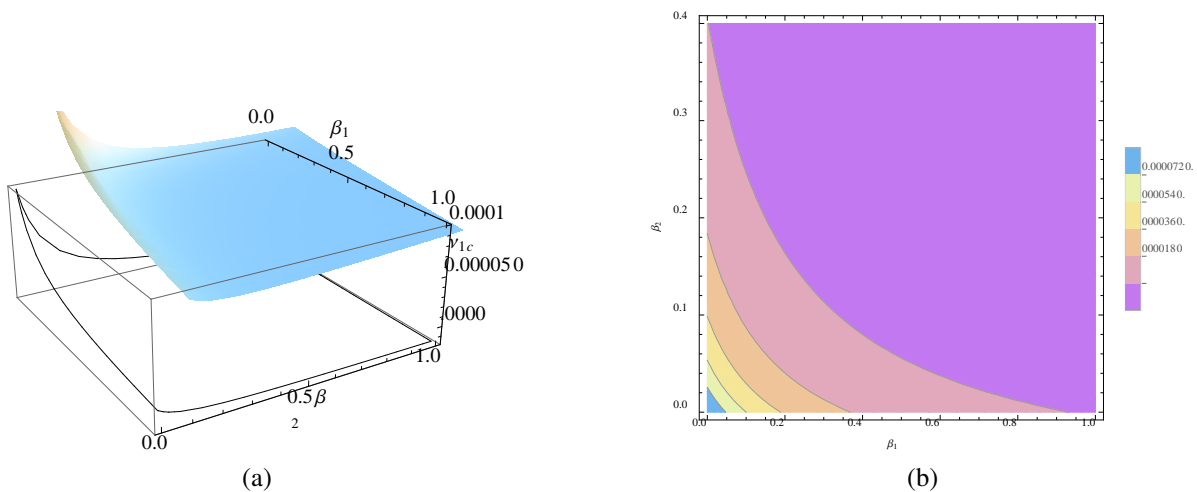


Figure 8: (a): v_{1c} surface against β_1 and β_2 , (b): contour plot of v_{1c} against β_1 and β_2 .

Table 6 shows the critical vaccination levels when both quarantine and isolation strategies are implemented, one of these is implemented, and none of these is applied. Based on the results shown in Figure 8 and Table 6, one can conclude that critical vaccination levels decrease when quarantine and isolation control strategies increase. This implies that even though vaccination started, maintaining the quarantining and isolation strategies is helpful for the suppression of the disease. Also, it is possible to suppress the disease only by a vaccination strategy if it is possible to maintain the vaccination rate greater than the critical value 0.0000980088.

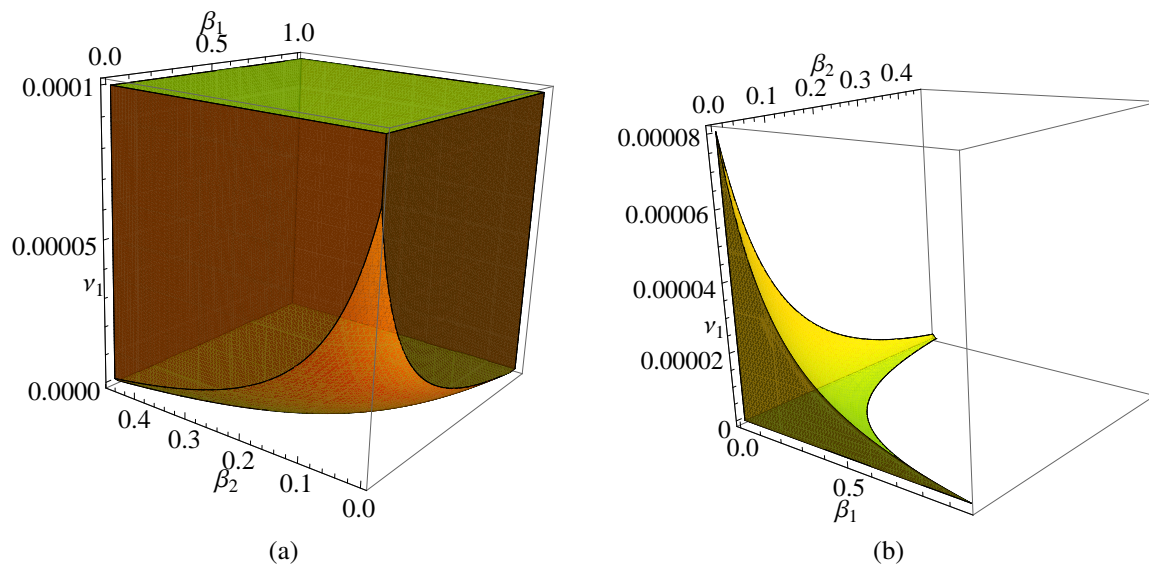


Figure 9: (a): $\mathcal{R}_{df} < 1$ parameter region (b): $\mathcal{R}_{df} > 1$ parameter region

Figure 9 shows the $\mathcal{R}_{df} < 1$ and $\mathcal{R}_{df} > 1$ parameter regions. In order to suppress the disease, it is needed to take actions to maintain control strategies such that control rates remain within the $\mathcal{R}_{df} < 1$ parameter region.

CONCLUSION

A deterministic mathematical model for COVID-19 is proposed considering the main control strategies of quarantine, isolation, and vaccination. Mostly using model-specific key terms in infectious disease modelling, the basic reproduction number, disease-free reproduction number, and effective reproduction number of the model are derived. Based on the sensitivity analysis of the reproduction number, it is observed that three most sensitive parameters of the model are transmission rates from the susceptible class to the exposed class, the recovery rate of infectious people, and the vaccination rate respectively for the chosen set of parameters. Since the sensitivity index of \mathcal{R}_{df} provides information about the importance of each model parameter on the spread of the disease, vaccination plays the third important role in the disease control process. Critical vaccination rate and critical percentage vaccination population size for the chosen set of parameters are $v_{1c} = 0.0000161147$ and $V_c = 42\%$ respectively. That is, to get full control of the disease, the vaccination process should be continued until 42% of the total population is vaccinated. For vaccination processes such that $v_1 > v_{1c}$, the minimum vaccination period to suppress the disease is determined. Disease die-out control parameter regions of the model are determined and a graphical interpretation of the region is presented. In order to suppress the disease, it is needed to strengthen the control strategies such that relevant parameters lie in the disease die-out parameter region. Based on the results of the proposed model it is found that earlier implementation of an effective vaccination process is helpful in properly controlling the disease. In the formulation of the model, it is assumed that all the vaccinated people are fully immunized to the diseases. But, the vaccinations investigated so far for COVID-19 do not fully immunize people to the disease. Therefore, the critical values derived here may be beyond the actual situation of COVID-19. Therefore, in future research, the author expects to modify the model by taking into account the immunization failure of the COVID-19 vaccinations.

REFERENCES

- Agarwal P. & Jhaharia K. (2021). Data analysis and modeling of covid-19. *Journal of Statistics and Management Systems* **24**(1):1–16.
DOI: <https://doi.org/10.1080/09720510.2020.1840076>
- Ahmad M.D., Usman M., Khan A. & Imran M. (2016). Optimal control analysis of ebola disease with control strategies of quarantine and vaccination. *Infectious Diseases of Poverty* **5**:72: 1–12.
DOI: <https://doi.org/10.1186/s40249-016-0161-6>
- Anastassopoulou C., Russo L., Tsakris A. & Siettos C. (2020). Data-based analysis, modelling and forecasting of the COVID-19 outbreak. *PLOS One* **15**(3): e0230405.
DOI: <https://doi.org/10.1371/journal.pone.0230405>
- Arenas A., Cota W., Gomez-Gardenes J., Gomez S., Granell C., Matamalas J.T., Soriano- Panos D. & Steinegger B. (2020). Derivation of the effective reproduction number r for covid-19 in relation to mobility restrictions and confinement. *medRxiv*.
- Bajjiya V.P., Bugalia S. & Tripathi J.P. (2020). Mathematical modeling of covid-19: Impact of non-pharmaceutical interventions in India. *Chaos: An Interdisciplinary Journal of Nonlinear Science* **30**(11): 113143.
DOI: <https://doi.org/10.1063/5.0021353>
- Biswas M.H.A., Paiva L.T. & De Pinho M. (2014). A SEIR model for control of infectious diseases with constraints. *Mathematical Biosciences and Engineering* **11**(4): 761.
DOI: <https://doi.org/10.3934/mbe.2014.11.761>
- Chanprasopchai P., Tang I. M. & Pongsumpun P. (2018). SIR model for dengue disease with effect of dengue vaccination. *Computational and Mathematical Methods in Medicine* **2018**: 9861572.
DOI: <https://doi.org/10.1155/2018/9861572>
- Diekmann O., Heesterbeek J. & Roberts M.G. (2010). The construction of next-generation matrices for compartmental epidemic model. *Journal of the Royal Society Interface* **7**(47): 873– 885.
DOI: <https://doi.org/10.1098/rsif.2009.0386>
- d’Onofrio A. (2002). Stability properties of pulse vaccination strategy in SEIR epidemic model. *Mathematical Biosciences* **179**(1): 57–72.
DOI: [https://doi.org/10.1016/S0025-5564\(02\)00095-0](https://doi.org/10.1016/S0025-5564(02)00095-0)
- Ghostine R., Gharamti M., Hassrouny S. & Hoteit I. (2021). An extended SEIR model with vaccination for forecasting the covid-19 pandemic in Saudi Arabia using an ensemble Kalman filter. *Mathematics* **9**(6): 636.
DOI: <https://doi.org/10.3934/mbe.2014.11.761>
- Gumel *et al.* (12 authors) (2004). Modelling strategies for controlling SARS outbreaks. *Proceedings of the Royal Society of London. Series B: Biological Sciences* **271**(1554): 2223–2232.
DOI: <https://doi.org/doi:10.1098/rspb.2004.2800>
- Ledzewicz U. & Schattler H. (2011). On optimal singular controls for a general SIR-model with vaccination and treatment. *Discrete and Continuous Dynamical Systems* **2011**: 981–990.
- Ma Y., Liu J.-B. & Li H. (2018). Global dynamics of an SIQR model with vaccination and elimination hybrid strategies. *Mathematics* **6**(328): 2–12.
DOI: <https://doi.org/10.3390/math6120328>
- Mishra B.K., Keshri A.K., Rao Y.S., Mishra B.K., Mahato B., Ayesha S., Rukhaiyyar P., Saini D.K. & Singh A.K. (2020). COVID-19 created chaos across the globe: Three novel quarantine epidemic models. *Chaos, Solitons and Fractals* **138**: 109928.
DOI: <https://doi.org/10.1016/j.chaos.2020.109928>
- Safi M.A. and Gumel A.B. (2011). Mathematical analysis of a disease transmission model with quarantine, isolation and an imperfect vaccine. *Computers and Mathematics with Applications* **61**(10): 3044–3070.
DOI: <https://doi.org/10.1016/j.camwa.2011.03.095>
- Shulgin B., Stone L. & Agur Z. (1998). Pulse vaccination strategy in the sir epidemic model. *Bulletin of Mathematical Biology* **60**(6): 1123–1148.
- Siriprapaiwan S., Moore E.J. & Koonprasert S. (2018). Generalized reproduction numbers, sensitivity analysis and critical immunity levels of an seqjr disease model with immunization and varying total population size. *Mathematics and Computers in Simulation* **146**:70–89.
- Sun C. & Hsieh Y.-H. (2010). Global analysis of an seir model with varying population size and vaccination. *Applied Mathematical Modelling* **34**(10): 2685–2697.
- Tang B., Bragazzi N.L., Li Q., Tang S., Xiao Y. & Wu J. (2020). An updated estimation of the risk of transmission of the novel coronavirus (2019-ncov). *Infectious Disease Modelling* **5**: 248–255.
DOI: <https://doi.org/10.1016/j.idm.2020.02.001>
- WHO (2021a). Covid-19 advice for the public: Getting vaccinated. Available at <https://www.who.int/publications/m/item/draft-landscape-of-covid-19-candidate-vaccines>, Accessed 30 July 2021.

- WHO (2021b). Covid-19 vaccine tracker and landscape. Available at <https://www.who.int/publications/m/item/draft-landscape-of-covid-19-candidate-vaccines>, Accessed 17 June 2021.
- WHO (2021c). Covid-19 vaccines. Available at <https://www.who.int/emergencies/diseases/novel-coronavirus-2019/covid-19-vaccines>, Accessed 17 June 2021.
- Yang H.M. (2014). The basic reproduction number obtained from jacobian and next generation matrices—a case study of dengue transmission modelling. *Biosystems* **126**:52–75.
DOI: <https://doi.org/10.1016/j.biosystems.2014.10.00>

RESEARCH COMMUNICATION

Plant Taxonomy

Two new additions and one confirmation of the occurrence of Lamiaceae (Lamiales) species from Northern dry zone in Sri Lanka

HD Jayasinghe^{1*} and HT Gamhewa²

¹National Institute of Fundamental Studies, Kandy, Sri Lanka.

²Department of Plant Science, Faculty of Science, University of Colombo, Sri Lanka.

Submitted: 26 October 2021; Revised: 10 September 2022; Accepted: 23 September 2022


Abstract: Sri Lanka abounds with a rich plant diversity, comprising 3087 species of flowering plants, of which 863 are endemic to the island. In Sri Lanka, the Lamiaceae plant family represents 70 indigenous species in 22 genera, distributed throughout the country in varied habitats. Since many of the species of the family are herbaceous and seasonal, less attention had been paid in field collections during the past. Here we document *Leucas diffusa* Benth. and *Orthosiphon pallidus* Royle ex. Benth. for the first time in Sri Lanka and further we confirm the existence of *Endostemon viscosus* (Roth) M.R. Ashby, a species that was included doubtfully in Sri Lankan flora, with field collected specimens. Each of these species is presented with a detailed taxonomic description, its ecology, places of occurrence in Sri Lanka, field photographs, and other relevant notes. All of these species were reported from the Northern dry zone of Sri Lanka, an area that was not accessible for botanists for 30 years due to civil war. This area has highly seasonal, rich herbaceous vegetation during the North Eastern monsoonal period. These findings, made during just two years, highlight that botanical explorations conducted in a timely manner in these seasonal habitats will reveal more undocumented herbaceous species.

Keywords: *Endostemon viscosus*, *Leucas diffusa*, new records, *Orthosiphon pallidus*.

INTRODUCTION

The family Lamiaceae is represented by more than 7000 species worldwide, being the sixth largest family after adding several species from the traditionally recognized family Verbenaceae, inferred by molecular studies (Harley *et al.*, 2004, Li *et al.*, 2016). Until then it was considered to be consisting of around 3500 species (Li & Hedge, 1994). This cosmopolitan family is currently represented by 236 genera (Royal Botanic Gardens, Kew, 2019), which are mainly concentrated in temperate zones and with a particular diversity in the Mediterranean region (Fernandes, 2005). In Sri Lanka, there are 70 indigenous species representing 22 genera, 13 of which are endemic (MOE, 2020). In addition, there are several cultivated species (Cramer, 1981; Moldenke & Moldenke, 1983).

In Sri Lanka, the genus *Leucas* R.Br. is represented by 6 species and the genus *Orthosiphon* Benth. is represented by 2 species (Cramer, 1981). No species of *Endostemon* N.E.Br. is represented in current Sri Lankan checklists or in recent family reviews (Cramer, 1981; Senaratna, 2001; MOE, 2020), though *Endostemon viscosus* (Roth) M.R. Ashby was included as a doubtful entry under the name *Orthosiphon diffusus* (Benth.) Benth. in Hooker (1885) and in Trimen (1895) based on a collection made by Walker, which is now deposited at Kew (Bar code: K000674643). Moreover, a specimen collected between 1973 and 1980 by Fagerlind and Klackenberg from Sri Lanka, deposited in the herbarium of the Swedish Museum of Natural History, was later identified as *E. viscosus* (Roth) M.R.Ashby (Emanuelsson & Klackenberg, 2001).

* Corresponding author (himesh.jayasinghe@gmail.com;  <https://orcid.org/0000-0001-5308-9158>)



This article is published under the Creative Commons CC-BY-ND License (<http://creativecommons.org/licenses/by-nd/4.0/>). This license permits use, distribution and reproduction, commercial and non-commercial, provided that the original work is properly cited and is not changed in anyway.

Here we provide for the first-time evidence for the occurrence of *Leucas diffusa* Benth. and *Orthosiphon pallidus* Royle ex. Benth. in Sri Lanka, where the first species was previously considered to be endemic to India and the latter was reported from other South-West Asian countries, including the Arabian peninsula, to Africa (The Royal Botanic Gardens, Kew, 2019; Sasidharan *et al.*, 2020). Moreover, the existence of *E. viscosus* (Roth) M. R. Ashby is further confirmed in Sri Lanka through field collected samples.

MATERIALS AND METHODS

Field surveys were conducted during the North-East Monsoon seasons of 2018 and 2019 in various parts of the Northern dry zone of Sri Lanka with the aim of recording the species diversity of less botanized parts of the country, especially focusing on the seasonal herbaceous species. Sampling sites were selected on an *ad hoc* basis, and the species of interest including many rare and data deficient species were collected. Plants that could not be identified in the field were also collected. All the collected specimens were deposited at National Herbarium, Peradeniya (PDA). Plants were photographed in detail in the field using a Canon 100 mm IS macro lens, fitted to a Canon 7D Mark II body. Relevant field notes were taken including morphological characters. Coordinates of the locations were taken from a Garmin 64S GPS. Specimens were identified from relevant publications (Hooker, 1885; Li & Hedge, 1994; Fernandes, 2005) and examining specimens online at Royal Botanic Gardens, Kew (K), Naturalis Biodiversity Center, Leiden (L), Royal Botanic Garden, Edinburgh (E), and Meise Botanic Garden (BR) [herbarium acronyms based on Thiers (2020)]. Collecting sites of three newly recorded Lamiaceae species are shown in Figure 1.

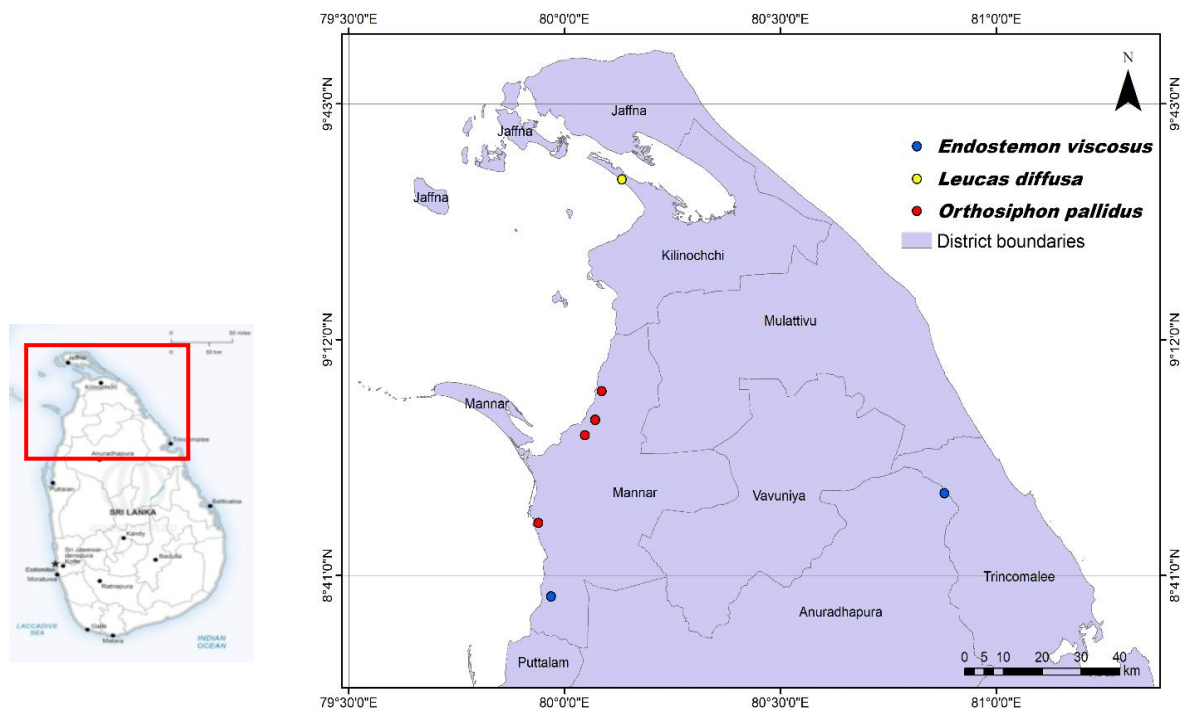


Figure 1: Distribution of the three newly recorded Lamiaceae species in the Northern dry zone, Sri Lanka.

RESULTS AND DISCUSSION

Taxonomic descriptions and photographs for all 03 newly recorded species are provided below.

- (1) *Leucas diffusa* Benth. in *Labitarum Genera et Species* (1834), pp. 615 — *Phlomis diffusa* Rottler ex Hook.f., nom. inval., *Fl. Brit. India* 4: 689 (1885), pp. 689; Figure 2

Taxonomic description: Decumbent herbs with radiating branches on sandy beaches, stem distinctly quadrangular with shallow longitudinal striation along each side, sparsely hirsute; leaves opposite, 1.2–2.5 × 0.3–0.8 cm, mostly pseudo-whorled, lanceolate to narrowly elliptic, obtuse, base cuneate, tapering to indistinct petiole, hirsute on both surfaces, more so along the midrib beneath, glandular-punctate, margin entire to faintly undulate, recurved, lateral veins (2) 3 pairs, ascending, prominulous, mid rib impressed above, obscurely raised below; inflorescences congested at pseudo-whorls of leaves, sessile, flowers almost sessile; calyx green, hirsute outside, tubular, 5–6 mm long, gradually expanding and curved towards the throat with almost equal, shortly triangular lobes tipped by a spinose hair, calyx throat ciliate, indistinctly longitudinally ridged; corolla white, 1–2 cm, densely long hirsute outside, glabrous inside, strongly 2-lipped, upper lip short, in-rolled and concealing the stamens, lower lip 3-lobed, lateral lobes small, acute, median lobe large, spatulate, slightly emarginate; stamens inserted, placed near the upper corolla lobe; filaments white; anthers reddish orange; nutlets oblong with a rounded apex, ca. 2 mm long, smooth, grey-brown.

Distribution and ecology: This species was found to be very common on the coastal, open sandy grounds at Pooneryn (9.5518 N, 80.1326 E). These plants were in healthy condition and most of them were in the flowering stage. The soil was full of moisture at the observation on January 29th, 2019, which provided a habitat for many other seasonal herb species such as *Utricularia* spp., *Drosera burmanni* Vahl, *Lindernia srilankana* L.H. Cramer & Philcox, *Murdannia striatipetala* Faden and *Eriocaulon quinquangulare* subsp. *quinquangulare* L. There were no other *Leucas* species occurring in this habitat, but *Leucas zeylanica* (L.) W.T. Aiton was found to be very common in adjacent inland habitats. Probably this species may be dying out at the onset of the dry season when the sand becomes very hot, a condition which usually last for about nine months until late November.

Specimens examined: Sri Lanka: Poonaryn, 2021 Dec 23, Himesh Jayasinghe *et al.*, HDJ 1327 **Other:** B. Heyne 605 (K!); Siliguri, North Bengal, C.B. Clarke 27035 (K!); Madras, India, s. coll. 60 (K!); India, N. Wallich, s.n. (K!), seen online.



Figure 2: *Leucas diffusa* A) habit; B) flower: front view; C) flower: lateral view; D) ventral view of leaf (Jayasinghe H. D.)

Revised taxonomic key to *Leucas* species in Sri Lanka.

- 1 Leaves linear to lanceolate, sessile to sub-sessile; calyx teeth not more than 1 mm long
 - 2 Verticils throughout the length of flowering stem, lax; calyx mouth straight, villous-annulate within; limb 10-toothed *L. longifolia*
 - 2 Verticils towards ends of flowering stem, dense; calyx mouth oblique, glabrous within; limb generally 7-8-toothed

- 3 Stem decumbent; leaves less than 2.6 cm long, glandular punctate, margin revolute; lateral veins prominulous *L. diffusa*
- 3 Stem erect; leaves more than 2.6 cm long, eglandular, margin flat; lateral veins prominent *L. zeylanica*
- 1 Leaves ovate, distinctly petiolate; calyx teeth at least 1.5 mm long
 - 4 Leaves lanate-tomentose beneath; calyx softly villous on nerves
 - 5 Stem + procumbent, straggling; verticils 6-10-flowered; leaves to 3 cm long; corolla tube exannulate within *L. decemdentata*
 - 5 Stem erect, verticils more than 10-flowered; leaves generally more than 3 cm long; corolla tube villous-annulate within *L. marrubioides*
 - 4 Leaves scabrid or hirtellous beneath; calyx strigose, hirtellous or hirsute on nerves
 - 6 Verticils lax, generally 2-4-flowered *L. biflora*
 - 6 Verticils dense, generally more than 4-flowered *L. angularis*
- (2) *Endostemon viscosus* (Roth) M.R.Ashby in Journal of Botany (1936), vol.74, pp. 126 — *Ocimum viscosum* Roth, Nov. Pl. Sp. (1821), pp. 274 — *Plectranthus viscosus* Spreng., Syst. Veg., ed. 16 [Sprengel] (1825), pp. 2: 691 ; Figure 3

Ocimum menthoides B.Heyne ex Roth, Nov. Pl. Sp. (1821), pp. 274.

Ocimum diffusum Benth., Pl. Asiat. Rar. (Wallich) (1830), 2: pp. 14 — *Orthosiphon diffusus* (Benth.) Benth., Prodr. [A. P. de Candolle] (1848), 12: pp. 50.

Orthosiphon tomentosus Benth., Pl. Asiat. Rar. (Wallich) (1830), 2: pp. 14.

Orthosiphon hispidus Benth., Prodr. [A. P. de Candolle] (1848), 12: pp. 50.

Ocimum adscendens Wight ex Hook.f., Fl. Brit. India [J. D. Hooker] (1885), 4(12): pp. 614.

Ocimum glaucum B.Heyne ex Hook.f., Fl. Brit. India [J. D. Hooker] (1885), 4(12): pp. 614.

Taxonomic description: Much branched, erect, stunted herbs to 0.3 m tall, appearing as *Ocimum tenuiflorum* L. at a glance; leaves 2 × 1.5 cm, opposite, elliptic, obtuse, broadly cuneate at base, margin crenate to sinuate, sometimes in-rolled; 4 pairs of lateral nerves, arching towards the tip; midrib and secondaries strongly impressed above, distinctly raised below; lamina distinctly glandular hairy on both sides; crushed leaves mint scented; petiole about half as long as the lamina; young stem and petiole covered with glandular hairs; inflorescence a terminal raceme, densely glandular hairy throughout except the corolla; rachis green, quadrangular with a longitudinal groove on middle of each side; bracts obtusely triangular, shorter than the pedicels; calyx tubular, down oriented, strongly 2-lipped, upper lip broadly obtuse, shortly decurrent, lower lip 4 lobed, acute, outer pair shorter than the inner pair; calyx throat densely covered with long, e-glandular hairs; corolla white to bright pink, corolla tube 4.5 x 2.5 cm wide, minutely hirsute outside on the tube, becoming glabrous towards lobes, 3 mm in size; obscurely 2 lipped; upper lip strongly emarginate, 3 mm, lower lip 3-lobed, 3.5 mm, lateral pair small, more long than wide, median lobe large, orbicular; stamens 4, inserted; anthers orangish; nutlets enclosed at the base of the accrescent calyx, oblong, white at immature stage, becoming blackish brown at maturity.

Distribution and ecology: We found this species from Kal Aru (8.6379 N, 79.9678 E) and from one of the resettlement sites of the Yan Oya irrigation project (8.8640 N, 80.8796 E). Both the locations were exposed rocky grounds and the plants were among the splits of these rocks. There were around 30 plants in each of these localities, and it was not a common species. This species was associated with some other seasonal species, which are capable of withstanding quite harsh conditions including *Platostoma menthoides* (L.) A.J. Paton,

Polycarpaea corymbosa (L.) Lam., *Chamaecrista mimosoides* (L.) Greene, and *Rostellularia procumbens* (L.) Nees.

Specimens examined: **Sri Lanka:** Yan Oya resettlement site H1, HDJ 70 (PDA); Ceylon, Walker s.n. (K!) seen online; **Other:** Tamil Nadu, R. Wight 2717 (K!); India, R. Wight 2494 (K!); Nagalur forest Narukkuparai, D.I. Arockiasamy 8090 (L!); Herb. Wight 2082 (L!), seen online.

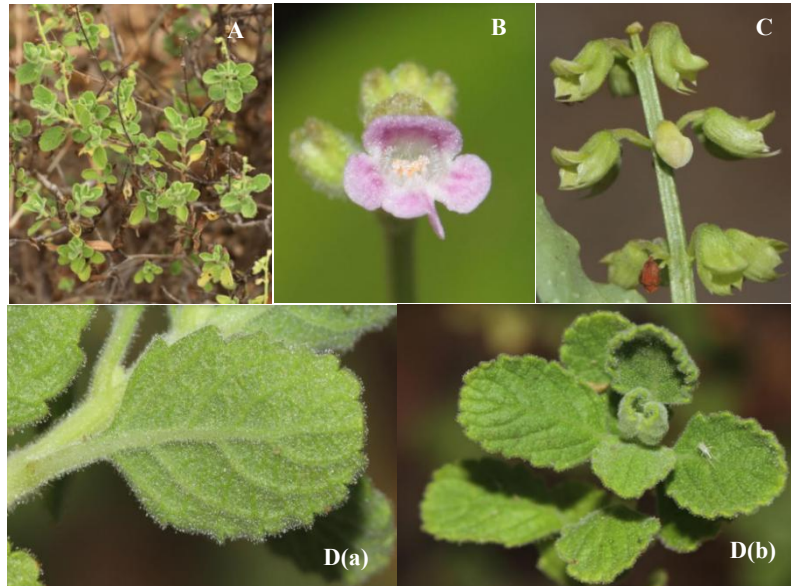


Figure 3: *Endostemon viscosus* A) habit; B) flower; C) inflorescence after anthesis; D (a) ventral side of leaf; D (b) dorsal side of leaf (Jayasinghe H.D.).

(3) *Orthosiphon pallidus* Royle ex. Benth. in Hooker (1833), Botanical Miscellany, vol. 3, pp. 370; Figure 4.

Ocimum reflexum Ehrenb. ex Schweinf., Beitr. Fl. Aethiop. (1867), pp. 126 - *Orthosiphon reflexum* (Ehrenb. ex Schweinf.) Vatke, Linnaea (1881), 43(2): pp. 85

Orthosiphon ehrenbergii Vatke, Linnaea (1872), 37(3): pp. 316

Ocimum somaliense Briq., Bull. Herb. Boissier (1903), Ser. 2 (3): pp. 985

Orthosiphon incisus A.Chev., Bull. Soc. Bot. France (1912), 58(Mém. 8d): pp. 199

Orthosiphon macrocheilus M.Ashby, J. Bot. (1938), 76: pp. 45

Taxonomic description: Mostly decumbent herb with many branches when growing in its preferred habitat of grazed mud flats, though it can grow erect at taller herbaceous vegetation. Stem green, sometimes with a dull red tinge at nodes, quadrangular, shortly pubescent; leaves opposite, 1.5–3 × 1–2 cm, coriaceous, oblong to narrowly ovate, obtuse at tip, base attenuate, margin undulate, sessile, midrib slightly impressed above, slightly raised below, lateral veins (2-) 3–4 pairs, upper ones connecting before the margin, prominulous, lamina glandular punctate on both sides; inflorescence a terminal raceme with 3–6 verticils of ca. 6 flowers, raceme 6–7 cm long mostly yellowish green sometimes tinged in dull red on pedicels, shortly pubescent throughout; flowers down oriented, 8 × 3 mm in size, pedicel slightly shorter than the calyx; calyx tubular, strongly 2-lipped, upper lip obtuse to apiculate, upturned, shortly decurrent, lower lip 4-lobed, inner pair longer than the outer, acuminate; outer pair with a straight inner margin and a curved outer margin; corolla white, shortly pubescent outside, tubular part slightly exceeding the calyx, strongly 2-lipped, upper lip much shorter, slightly 3-lobed, each lobe

obtuse, upturned, lower lip in-rolled, concealing the stamens, though the style shortly exceeding, which is white; nutlets orbicular-oblong, obtuse at both ends, pale brown, ca. 1 mm in diameter.

Distribution and ecology: This species was recorded from several places in coastal belt in Mannar district including Arippu (8.7986 N, 79.9389 E), Wedithalathivu (9.0245 N, 80.0703 E), Periyavilankuli (8.9905 N, 80.0465 E), and Iluppakadavai (9.0873 N, 80.0852 E). This is a species of very short vegetated, muddy ground, in flood plains and upper margins of salt marshes. It is a quite regular species in such micro-habitats, although such undisturbed habitats are rare due to paddy cultivation. This species is associated with other species such as *Basilicum polystachyon* (L.) Moench, *Bergia capensis* L., *Ammannia baccifera* L., and *Hydrolea zeylanica* (L.) Vahl etc. Some of the plants that were collected had a thick and deep root system, which is extraordinary when considering the size of the aboveground part, indicating that even though the leafy part is dying off in the dry season, the remaining root system makes sprouts in the next rainy season.

Specimens examined: Sri Lanka: Arippu, HDJ 47 (PDA!); Arippu, HDJ 203 (PDA!); Other: India, J.F. Royle s.n. (K!); India, V.V. Jacquemont 1427 (K!); Africa: Ethiopia, J.J.F.E. de Wilde 4659 (L!); Saudi Arabia, Waji Deli, Taku Miyazaki 990817WD5 (E!); s.l., W.G. Schimper 190 (BR!), seen online.



Figure 4: *Orthosiphon pallidus* A) habit; B) flower; C)(a) ventral side of leaf; C)(b) dorsal side of leaf (Jayasinghe H. D.).

Revised taxonomic key to *Orthosiphon* species in Sri Lanka.

1 Stamens included in lower lip of the corolla

2 Erect herbs to 100 cm tall; leaves ovate to ovate elliptic, coarsely crenate-serrate, to 7 cm long; raceme to 15 cm long *O. thymiflorus*

2 Decumbent herbs to 20 cm tall; leaves oblong to narrowly ovate, margin undulate, to 3 cm long; raceme to 7 cm long *O. pallidus*

1 Stamens much exerted beyond the lower lip of the corolla *O. aristatus*

CONCLUSION

The botanical explorations in the Northern dry zone should be timed appropriately, since most of the herbaceous plant species emerge with the Northeast monsoon and have a relatively short life span of 1-2 months from December to January. We were able to document *Leucas diffusa* Benth. and *Orthosiphon pallidus* Royle ex. Benth. for the first time in Sri Lanka through the explorations carried out at the appropriate time of the year. Further we confirm the existence of *Endostemon viscosus* (Roth) M.R. Ashby, a species that was included doubtfully in Sri Lankan flora. The results presented in our study indicate the need for further botanical explorations within this region as there are potentially other species to be recorded and described.

Acknowledgements

We wish to acknowledge Nuwan Chathuranga, Nimalka Sanjeevani, and Dineth Danushka for their help in field work. We also thank Dr R.K. Singh, Botanical Survey of India, and Southern Regional Centre for the help given in identification of the plants, and the staff of the Peradeniya Herbarium, who provided necessary facilities to deposit the voucher specimens.

REFERENCES

- Cramer L.H. (1981). Lamiaceae (Labiatae). In: *Revised handbook to the flora of Ceylon*, volume 3 (eds. M.D. Dassanayake & F.R. Fosberg), pp. 108–194. Oxford and IBH Publishing Co., New Delhi, India.
- Emanuelsson E. & Klackenbergh J. (2001). The occurrence of *Endostemon viscosus* (Lamiaceae) in Sri Lanka confirmed. *Kew Bulletin* **56**(4): 999–1001.
DOI: <https://doi.org/10.2307/4119313>
- Fernandes R. (2005). Lamiaceae. In: *Flora Zambesiaca*, volume 17 (eds. J.R. Timberlake & E.S. Martins), pp. 346. Royal Botanic Gardens, Kew, England.
- Harley *et al.* (13 authors) (2004). Labiatae. In: *The Families and Genera of Vascular Plants*, volume 7 (eds. K. Kubitzki & J.W. Kadereit), pp. 167–275. Springer, Berlin, Heidelberg, New York.
- Hooker J.D. (1885). *Flora of British India*, volume 4, pp. 612–691. L. Reeve & Co., London, UK.
DOI: <https://doi.org/10.5962/bhl.title.678>
- Li B., Cantino P.D., Olmstead R.G., Bramley G.L.C., Xiang C.L., Ma Z.H., Tan Y.H. & Zhang D.H. (2016). A large-scale chloroplast phylogeny of the Lamiaceae sheds new light on its subfamilial classification. *Scientific Reports* **6**: 1–18.
DOI: <https://doi.org/10.1038/srep34343>
- Li X. & Hedge I.C. (1994). Lamiaceae. In: *Flora of China*, volume 17 (eds. Z.Y. Wu & P.H. Raven), pp. 50–299. Missouri Botanical Garden Press, St. Louis, USA.
DOI: <https://doi.org/10.2307/2807882>
- MOE (2020). *The National Red List -2020: Conservation Status of the Flora of Sri Lanka*, pp. 75–79. Biodiversity Secretariat, Ministry of Environment, Colombo, Sri Lanka.
- Moldenke H.N. & Moldenke A.L. (1983). Verbenaceae. In: *Revised Handbook to the Flora of Ceylon*, volume 4 (eds. M.D. Dassanayake & F.R. Fosberg), pp. 196–487. Amerind Publishing Co. Pvt. Ltd., New Delhi, India.
- The Royal Botanic Gardens, Kew (2019). Plants of The World Online (POWO). Available at <http://www.plantsoftheworldonline.org/>, Accessed 25 April 2019.
- Sasidharan N., Renu G., Thilakar S.J. & Narasimhan D. (2020). India biodiversity portal: *Leucas diffusa* Benth., Available at <https://indiabiodiversity.org/species/show/263452>, Accessed 25 April 2020.
- Senaratna L.K. (2001). *A Check List of the Flowering Plants of Sri Lanka*. National Science Foundation, Colombo, Sri Lanka.
- Thiers B. (2020). *Index Herbarium, A Global Directory of Public Herbaria and Associated Staff*. The New York Botanical Garden, New York. Available at <http://sweetgum.nybg.org/science/ih/>, Accessed 25 April 2020.
- Trimen H. (1895). *A Handbook to the Flora of Ceylon*, volume 3, pp. 345 – 388. Dulau and Co., London, UK.
DOI: <https://doi.org/10.5962/bhl.title.10864>

GUIDANCE TO CONTRIBUTORS

Scope

The Journal of the National Science Foundation of Sri Lanka publishes the results of research in all aspects of Science and Technology. It is open for publication of Research Articles, Reviews, Research Communications and Correspondence.

IT related and other articles from formal sciences

The JNSF is a journal primarily devoted to natural sciences. It also considers for publication significant and novel contributions from formal sciences. Authors of emerging sub-disciplines of Computing and related areas such as Machine Learning, Artificial Intelligence and Data Sciences are requested to carefully adhere to the following guidelines when submitting manuscripts for this journal.

- Clear formulation of outcome-oriented **Research Objective/s** for targeted knowledge (sub)domain/s or (sub)discipline/s.
- Selection and comprehensive summarization of **appropriate Research Method/s** adopted to achieve the stated Research Objective/s.
- Sound reporting of research finding/s with Empirical Evaluation thereby arguing reliability, validity, and generalizability of research claim/s.

Categories of manuscripts

Research Articles: Research Articles are papers that present complete descriptions of original research. Research Articles should include an Abstract, Keywords, Introduction, Methodology, Results and Discussion, Conclusion and Recommendations where relevant. References should be prepared according to the “Guidelines for the preparation of manuscripts”. Maximum length of the article should be limited to 25 pages with a word count of 10,000 including references, figures and tables. Any articles above this limit will be returned.

Reviews: Reviews are critical presentations on selected topics of Science or Technology. They should be well focused and organized and avoid general “textbook” style. As reviews are intended to be critical presentations on selected topics, reviewers need to have had substantial leadership in research supported by a publication track record in the areas covered by the review. A person/s wishing to submit a Review Article should obtain prior approval from the Editorial Board by submitting a concise summary of the intended article, along with a list of the author’s publications in the related area (jnsf@nsf.gov.lk). Maximum length of the article should be limited to 40 pages with a word count of 12,000 including references, figures and tables. Any articles above this limit will be returned.

Research Communications: Research Communications are intended to communicate important new findings in a specific area of limited scope that are worthy of rapid dissemination among the scientific community. Authors are required to provide a statement justifying the suitability of the submission for a Research Communication. The article should include an Abstract, Keywords, Introduction, Methodology, Results & Discussion, Conclusion and References. Maximum length of the article should be limited to 10 pages with a word count of 2,500 including references, figures and tables. Any articles above this limit will be returned.

Correspondence: Correspondence will be accepted regarding one or more articles in the preceding four issues of the Journal, as well as Letters to the Editor. Articles covering important scientific events or any other news of interest to scientists, reviews of books of scientific nature, articles presenting views on issues related to science and scientific activity will also be considered. Publication will be made at the discretion of the Editor-in-Chief. Maximum length of the article should be limited to 05 pages with a word count of 1,500 including references, figures and tables. Any articles above this limit will be returned.

SUBMISSION OF MANUSCRIPT

Authors submitting articles to the JNSF should first create an account in the Sri Lanka Journals Online System (<https://jnsfsl.sljol.info/>). All manuscripts in MS Word format must be electronically submitted to the journal’s online platform at <https://jnsfsl.sljol.info/submit/start/>. Submissions via emails are not encouraged. Please make sure that no author information is mentioned in the article submitted. The names and details of affiliations of all authors and contact information of the corresponding author must be fed into the system during the online submission process. Authors (at least the corresponding author) are required to provide their personal, validated ORCID ID (by obtaining an ORCID ID from <https://orcid.org/>) when submitting the manuscript. No change to the authors or order of authors will be accepted after the submission. All those who have made significant contributions should be listed as co-authors. The corresponding author should ensure that all contributing co-authors are included in the author list and have approved the final version of the paper and have agreed to its submission for publication.

All submissions should be in English. If the manuscript conforms to the guidelines specified, the date received will be the date that the manuscript was submitted to the online system.

Submissions are accepted for processing on the understanding that they will be reviewed and that they have not been submitted for publication elsewhere (including publication as a full paper or extended abstract as a part of Conference Proceedings). The JNSF does not accept manuscripts that have already been submitted to pre-print servers.

Suggesting potential reviewers by authors

The authors may suggest up to three names of referees when submitting their manuscript, in the Cover Letter space provided at the bottom of the page in the first stage of online submission. Referees should not be from the institution where the work was carried out and should not have been co-authors in previous publications. The address, institutional affiliation and e-mail of the suggested referees should be supplied. Please note that the JNSF is not bound to select all or any of the suggested referees for sending the manuscript for reviewing

Authorship

All authors designated as authors should be eligible for authorship. Those who have made a substantial contribution to the concept or design of the work; or acquisition, analysis or interpretation of data are recognized as Authors.

The corresponding author should be prompt and ensure adherence to timelines when responding to requests, queries and recommendation of reviewers conveyed by or on behalf of the Editor-in Chief and Editorial Board.

Supplementary materials

Any experimental data necessary to evaluate the claims made in the paper but not included in the paper should be provided as supplementary materials. Supplementary materials will be sent to the reviewers and published online with the manuscript if accepted. The supplementary materials should conform to Journal guidelines and should be uploaded as separate files. Authors should number Supplementary Tables and Figures as, for example, 'Supplementary Table S1'. Refer to each piece of supplementary material at the appropriate point(s) in the main article. Supplementary Materials may include description of the materials and methods, controls, or tabulated data presented in Tables or Figures, and programming codes.

Peer review

The manuscripts submitted to the JNSF will initially be screened by the Editorial Board and, if suitable, will be referred to at least two subject experts in the relevant field. The peer-review process of the JNSF is double-blind.

When revision of a manuscript has been requested, the revised manuscript should be submitted on or before the stated deadline. If the revised manuscript is not received on time, the manuscript will not be processed further. The authors' response to the comments of referees should be tabulated with the comment, response and the line number/s for reference. The decision of the Editorial Board shall be final.

Accepted papers are subject to editing. The date of acceptance will be the date when the Editorial Board has decided it to be acceptable for publication.

Article publication fee

A total of US\$ 250 will be levied for each accepted manuscript for publication, except when the corresponding author is affiliated to a Sri Lankan Institute, in two stages as explained below.

- A processing fee of US\$ 20 will be levied for each manuscript at peer-review stage and the remaining US\$ 230 will be charged for accepted manuscripts at the time of publication.

Payments can be made online via NSF Payment Portal (<http://pg.nsf.gov.lk/>)

Authors' declaration

When an article is accepted for publication, the authors are required to submit the Authors' Declaration signed by all the authors.

Copyright

Articles in JNSF are published under the Creative Commons License CC-BY-ND. This license permits use, distribution and reproduction of articles for commercial and non-commercial purposes, provided that the original work is properly cited and is not changed in anyway. The copyright of the article is with the National Science Foundation of Sri Lanka. Therefore, authors are requested to check with institution's copyright and publication policy before submitting an article to the JNSF. Authors secure the right to reproduce any material that has already been published or copyrighted elsewhere. When an article is accepted for publication, the authors are required to submit the Transfer of Copyright document signed by all the authors.

Post-publication corrections

The Editorial Board reserves the right to take action on publishing an erratum or corrigendum. If serious errors are identified in a published article, the Journal may consider a retraction or publishing a correction.

STRUCTURE OF MANUSCRIPT

Manuscript

The manuscript should be free of errors and prepared in single column, using double-spaced text of Times New Roman 12 font throughout with line numbers, leaving at least 2 cm margins on both sides, and liberal spacing at the top and bottom of each page. Pages should be numbered consecutively.-

a. Style

The paper should be written clearly and concisely. The style of writing should conform to scholarly writing. Slang, jargon, unauthorized abbreviations, abbreviated phrasings should not be used. In general, the impersonal form should be used. Poor usage of language will result in rejection of the manuscript during initial screening.

b. Layout

Manuscripts other than review articles should be generally organized as follows: Title, Abstract, Keywords, Introduction, Methodology, Results and Discussion, Conclusions and Recommendations (where relevant), Acknowledgements and References. Pages should be arranged in the following order:

Title page should include the title of manuscript, and no author information should be mentioned in the title page. If a major part of the research has been published as an abstract in conference proceedings, it should be cited as a footnote on the title page. Authors must also indicate the **general and specific research area** of the manuscript in the title page. In order to highlight the significance of the manuscript, authors are required to provide the following highlights in brief. (1) Why was this study conducted? (2) What are the new findings? (3) Possible applications of the findings. Please limit your answers to 25-30 words for each.

Title: Should accurately and concisely reflect the contents of the article.

Running title: Should be a shortened title (limited to a maximum of 50 characters) that could be printed at the top of every other page of the Journal article.

Abstract: Should be between 200 - 250 words for full length articles and written as a single paragraph. It should not contain any references and should be able to stand on its own. It should outline objectives and methodology together with important results and conclusions. A Review Article should carry a summary of not more than 300 words.

Keywords: Include a maximum of six keywords, which may include the names of organisms (common or scientific), methods or other important words or phrases relevant to the study.

Introduction: This should state the reasons for performing the work with a brief review of related research studies in the context of the work described in the paper. Objectives of the study should be clearly stated.

Materials and Methods: This section should give the details of how you conducted your study. New methods may be described in detail with an indication of their limitations. Established methods can be mentioned with appropriate references. Sufficient details should be included to allow direct repetition of the work by others. Where human subjects are involved, they should be referred to by numbers or fictitious names. A paper reporting the results of investigations on human subjects or on animals must include a statement to the effect that the relevant national or other administrative and ethical guidelines have been adhered to, and a copy of the ethical clearance certificate should be submitted. Methods of statistical analyses used should be mentioned where relevant.

Results and Discussion: Results: the results should be concisely and logically presented. Repetition of the same results in figures, tables or text should be avoided.

Discussion: data essential for the conclusions emerging from the study should be discussed. Long, rambling discussions should be avoided. The discussion should deal with the interpretation of results. It should logically relate new findings to earlier ones. Unqualified statements and conclusions not completely supported by data should be avoided.

Molecular sequence data, such as gene or rDNA sequences, genome sequences, metagenomic sequences etc. must be deposited in a public molecular sequence repository, such as GenBank, that is part of the International Nucleotide Sequence Database Collaboration (INSDC). The accession numbers obtained must be cited in the text, Table or on Figures of phylogenetic trees of the manuscript.

Conclusion: The conclusion should be brief, highlight the outcomes of the study and should be aligned with the objectives of the study. It should not contain references.

Conflict of interest statement: All authors should include a statement on conflict of interest disclosing any financial or other substantive conflicts of interest that may be construed to influence the results or interpretation of their research. All sources of financial support for the project should be disclosed.

Acknowledgement: Should be brief and made for specific scientific, financial and technical assistance only. If a significant part of the research was performed in an institution other than in those indicated by the authors' affiliations given in the title page, this fact should be acknowledged. All those who have made substantial contribution to the research but do not qualify to be authors should be acknowledged.

References :

All research work of other authors, when used or referred to or cited, should be correctly acknowledged in the text and in the References.

Citing references in the text:

- References to the literature must be indicated in the text and tables as per the Author-Year System, by the author's last name and year, in parenthesis (i.e. Able, 1997) or (Able & Thompson, 1998).
- Citation to work by more than two authors should be abbreviated with the use of *et al.* (i.e. Able *et al.*, 1997).
- Multiple publications by the same first author in the same year should be coded by letters, (i.e. Thompson, 1991a; b).
- Multiple citations should be made in chronological order and separated by a semi-colon, (i.e. Zimmerman *et al.*, 1986; Able *et al.*, 1997).
- Reference to unpublished work, work in preparation or work under review should be cited in italics as (*unpublished data*) or, with the author's initials and surname given; such works should not be included in the Reference section.
- Personal communications may be mentioned in the text with the date of communication as (*Personal communication, 2 June 2000*).

List of references:

- The list of References should be arranged in alphabetical order based on the last name of the first author.
- Names of all the authors should be given except when there are more than 10 authors. When there are more than 10 authors, only the name of the first author can be given followed by *et al.*
- All the initials of the author must be given after the last name and the year of publication should follow in parentheses.
- This should be followed by the full title of the referred publication.
- When journal articles are listed, the journal name should be given in full and in italics and followed by the volume number in bold type, issue number in parentheses and then the inclusive pages.
- Where there are several publications by the same author(s) and published in the same year they should be differentiated by adding a lower-case letter after the year. When books are listed, the order should be: author(s), year, book title, volume number, edition, pagination/ inclusive pages, publisher and place of publication. The book title should be in italics. When sections of a book are listed, the order should be: author(s) of chapter, year, title of the section, title of the book, edition, inclusive pages, publisher and place of publication.
- Digital object identifiers (DOIs) should be included for all references where available.
- References should only be cited as 'in press' if the paper has been accepted for publication.

Examples of correct forms of references are given below.

Journal Articles

Boutin C. & Harper J.L. (1991). A comparative study of the population dynamics of five species of *Veronica* in natural habitats. *Journal of Ecology* 79(01): 199 – 221.

DOI: <https://doi.org/10.2307/2260793>

Books

Burnham K.P. & Anderson D.R. (2002). *Model Selection and Multimodal Inference*, 2nd edition, pp. 488. Springer Science and Business Media, Inc., New York, USA.

Book Chapters

Hinrichsen R.A. & Holmes E.E. (2009). Using multivariate state-space models to study spatial structure and dynamics. In: *Spatial Ecology* (eds. R.S. Cantrell, C. Cosner & S. Ruan), pp. 145 – 166. CRC/ Chapman Hall, Florida, USA.
DOI: <https://doi.org/10.1201/9781420059861.ch8>

Edited Books

Kimati H., Amorim L., Rezende J.A.M., Bergamin Filho A. & Camargo L.E.A. (eds.) (2005). *Manual de Fitopatologia*, volume 2. Doenças das Plantas Cultivadas, 4th edition. Ceres, São Paulo, Brazil.

Conference Papers

Weaver D. (2002). Implementation of a learning management system using an integrated approach to professional development. In: Winds of change in the sea of learning. *Proceedings of the 19th Annual Conference of the Australasian Society for Computers in Learning and Tertiary Education (ASCILITE)* (eds. A. Williamson, C. Gunn, A. Young & T. Clear), volume 2, Auckland, New Zealand, 8-11 December. Unitec Institute of Technology, Auckland, New Zealand, pp. 711-720.

Agency Publications

U.S. Census Bureau (2009). *World Population: 1950 – 2050*. U.S. Census Bureau, Washington DC, USA.

Department of Health (2008). *Health Inequalities: Progress and Next Step* (pdf). Department of Health, London, UK. Available at http://PublicationsPolicyAndGuidance/DH_08_5307, Accessed 9 June 2008.

Other

Robinson L.J. (2003) Spatial scale and depletion models of farmland birds in a fragmented landscape. *PhD thesis*, University of Reading, Reading, UK.

Efford M.G. (2008). Density 4.3: software for spatially explicit capture-recapture. Available at <http://www.otago.ac.nz/density>, Accessed 15 March 2009.

Abbreviations and Symbols: Unless common, these should be defined when first used, and not included in the abstract. The SI System of units should be used wherever possible. If measurements were made in units other than SI, the data should be reported in the same units followed by SI units in brackets, e.g. 5290 ft (1610 m).

Formulae and Equations: Equations should be typewritten and quadruple spaced. They should be started on the left margin and the number placed in parentheses to the right of the equation.

Nomenclature: Scientific names of plants and animals should be printed in italics. In the first citation, genus, species and authority must be given. e.g. *Borassus flabellifer* Linn. In latter citations, the generic name may be abbreviated, for example, *B. flabellifer* L.

Tables and figures: Tables and Figures should be clear and intelligible and kept to a minimum, and should not repeat data available elsewhere in the paper. Any reproduction of illustrations, tabulations, pictures etc. in the manuscript should be acknowledged.

Tables: Tables should be numbered consecutively with Arabic numerals and placed at the appropriate position in the manuscript. If a Table must be continued, a second sheet should be used and all the headings repeated. The number of columns or rows in each Table should be minimized. Each Table should have a title, which makes its general meaning clear, without reference to the text. All Table columns should have explanatory headings. Units of measurement, if any, should be indicated in parentheses in the heading of each column. Vertical lines should not be used and horizontal lines should be used only in the heading and at the bottom of the table. Footnotes to Tables should be placed directly below the Table and should be indicated by superscript lower case italic letters (^a, ^b, ^c, etc.).

Figures: All illustrations are considered as figures, and each graph, drawing or photograph should be numbered consecutively with Arabic numerals and placed at the appropriate position in the manuscript. Any lettering to appear on the illustrations should be of a suitable size for reproduction and uniform lettering should be used in all the Figures of the manuscript. Scanned figures or photographs should be of high quality (**300 dpi**), to fit the proportions of the printed page (12 × 17 cm). Each figure should carry a legend so that the general meaning of the figure can be understood without reference to the text. Where magnifications are used, they should be stated.

Units of measurement

Length: km, m, mm, µm, nm

Area: ha, km², m²

Capacity: kL, L, mL, µL

Volume: km³, m³, cm³

Mass: t, kg, g, mg, µg

Time: year(s), month(s), wk(s),
d(s), h, min, s

Concentration: M, mM, N, %, g/L, mg/L, ppm

Temperature: °C, K

Gravity: x g

Molecular weight: mol wt

Others: Radio-isotopes: 32P

Radiation dose: Bq

Oxidation-reduction potential: rH

Hydrogen ion concentration: pH

CONTENTS

EDITORIAL

- 01 **Predatory Journals; be aware of the spectrum!**
LP Jayatissa
-

RESEARCH ARTICLES

- 03 **Effect of oviposition-site deprivation on reproductive performance and life history parameters of dengue vector *Aedes aegypti***
KM Gunathilaka and SM Ganehiarachchi
- 13 **Quantification of metabolite cinnamic acid of cinnamon (*Cinnamomum zeylanicum*) in human plasma**
S Pigeera, P Ranasinghe, MN Kaumal and P Galappathy
- 21 **Temperature control in an exothermic continuous stirred tank reactor**
VA Rani, G Guna, D Prabhakaran and M Thirumarimurugan
- 37 **On recurrence relations for moments of dual generalized order statistics for a general transmuted power function distribution with characterizations**
SH Shahbaz and MQ Shahbaz
- 53 **Removal of methylene blue from aqueous solution using raw laterite: an adsorption study**
BM Gunathilake, D Jayawardana, PGH Pupulewatte, S Dissanayake and PM Manage
- 69 **Comparison of physicochemical and sensory properties of African butter seed (*Pentadesma butyracea*) and cocoa fats for potential use in future food applications**
NPS Jayathissa, ABG Silva, WMT Madhujith, PGSM De Silva and R Jayatissa
- 81 **Assessment of submergence stress responses and mining allelic variations of submergence tolerance gene *Sub1A* in Sri Lankan rice germplasm**
T Kariyawasam, D Nanayakkara, A Sumanarathna, D Weerasinghe, L Suriyagoda and D Jayatilake
- 93 **A comparison of model parameter estimation methods for complex survey survival data**
IT Jayamanne, A Ramanayake and RV Jayatillake
- 105 **Mechanically exfoliated graphene from Sri Lankan vein graphite for field effect transistor application**
M Thanishaichelvan, M Joy Karunya and U Sutharsini
- 113 **Assessment of transverse thermal conductivity of coir fibre using experimental, analytical, and numerical methods**
LG Chamath, LKT Srimal and GA Sewvandi
- 129 **Estimation of soil liquefaction potential in Colombo Port City (Sri Lanka) using several design earthquakes**
IACC Ilangakoon and AMRG Athapaththu
- 149 **Insights into the ecological roles of assembling genomes for stimulated methanogenic archaea *Methanoculleus* in coal seams**
BJ Liu and Y Li
- 159 **Analyzing the effects of quarantine, isolation, and vaccination on the spread of COVID-19 via a mathematical model**
LW Somathilake
-

RESEARCH COMMUNICATION

- 175 **Two new additions and one confirmation of the occurrence of Lamiaceae (Lamiales) species from Northern dry zone in Sri Lanka.**
HD Jayasinghe and HT Gamhewa
-